DETERMINATION OF THE SITE SYMMETRY OF Ni(0) AND Fe(0) ATOMS ISOLATED IN SOLID KRYPTON MATRIX VIA MAGNETIC CIRCULAR AND MAGNETIC LINEAR DICHROISM SPECTROSCOPY

BY

KAREN L. JENSEN

A DISSERTATION SUBMITTED TO THE GRADUATE SCHOOL
OF THE UNIVERSITY OF FLORIDA IN PARTIAL FULFILLMENT
OF THE REQUIREMENTS FOR THE DEGREE OF
DOCTOR OF PHILOSOPHY

UNIVERSITY OF FLORIDA

2003

I dedicate this composition to my mother, Dolores Eyring, a truly remarkable woman whose love for her child has been consistently demonstrated in both word and deed. I wish also to simultaneously dedicate this work to the memory of my best friend in this life, Steve Berman.

ACKNOWLEDGMENTS

I wish to thank my committee advisor, Martin Vala, Ph.D., for his incredible support and involvement in my academic pursuits. Similarly, I would like to recognize the tremendous assistance, guidance, and hospitality extended to me by both Bryce Williamson, Ph.D. (of the University of Canterbury, Christchurch, New Zealand) and Jean-Claude Rivoal, Ph.D. (of the Laboratoire d'Optique Physique, Paris, France).

Russell Pierce, the resident chemistry department electronics technician, is also deserving of my appreciation. His tenacious assistance in troubleshooting, designing, and repairing the complex electronics of our system enabled us to keep progressing forward. I also am indebted for the gracious help of Dennis Roser, who provided backup relief for the data acquisition during the many long periods of uninterrupted experiments along with many positive professional and sociable encounters during our years of working together.

I thank my sister Donna for her support over the years, and especially wish to thank my close friends Anita Berman and Rhonda Johnson for the constancy of their friendship.

TABLE OF CONTENTS

page

ACKNOWLEDGMENTS iii

LIST OF TABLES vi

LIST OF FIGURES viii

ABSTRACT xiv

CHAPTERS

1 INTRODUCTION 1

History 1
Previous Fe and Ni Work 9
Extension to MLD 11
Magnetic Saturation 12
Statement of Problem 13

2 THEORY OF MAGNETIC CIRCULAR AND MAGNETIC LINEAR DICHROISM 21

Production of Circularly Polarized Radiation 21
Magnetic Circular Dichroism 26
Magnetic Linear Dichroism 37

3 SATURATION THEORY OF MCD AND MLD FOR ORIENTATIONALLY AVERAGED SYSTEMS 47

MCD and MLD in the Nonlinear Regime 47
Development of Crystal Field Hamiltonian 53
Full State Eigenvectors 59
Laboratory vs. Molecular Reference Frame 60
Euler Transformation 61
Application of Euler Transform to MCD/MLD Equations 66
Wigner-Eckart Theorem 67
Final Reduced Expressions for MCD and MLD 69
Numerical Analysis 71

4 THE MCD AND MLD SPECTRA OF Fe(0) ATOMS IN KRYPTON MATRIX.......77

Introduction.......77
Electronic State Assignments via Complementary MCD/MLD Spectroscopy.......81
Experimental 81
Results 85
Discussion 86
Determination of Site Geometry via Magnetic Saturation Techniques.......87
Experimental 87
Data Reduction and Refinement 91
Results 94
Discussion 116
Summary.......129

5 THE MCD AND MLD OF Ni(0) ATOMS IN ARGON AND KRYPTON MATRICES.......196

Introduction.......196
Electronic State Assignments of Ni(0) in Argon.......199
Experimental 199
Results 200
Discussion 208
MCD and MLD Saturation Spectroscopy of Ni(0) in a Krypton Matrix.......209
Experimental 209
Data Reduction and Refinement 211
Results 213
$^3D_3$ Ground State Configuration of Ni(0) 213
$^3F_4$ Ground State Configuration of Ni(0) 218
Discussion 225
Summary.......229

6 CONCLUSIONS.......274

APPENDIX MATHEMATICAL MODELING SOFTWARE IN C^{++}.......283

LIST OF REFERENCES.......309

BIOGRAPHICAL SKETCH.......315

LIST OF TABLES

Table page

3-1. Basis set vectors for J = 3 ground state in octahedral, tetragonal, and trigonal crystal field symmetries 55

3-2. Basis set vectors for J = 4 ground state in octahedral, tetragonal, and trigonal crystal field symmetries 56

3-3. Crystal field energies for J = 3 and J = 4 atomic states in octahedral, tetragonal, and trigonal symmetries 57

3-4. Crystal field matrix for octahedral, tetragonal, and trigonal symmetries in the $|JM\rangle$ basis 58

4-1. MLD and MCD parametric expressions for the intensity and sign of atomic transitions for ΔJ = 1, 0, -1 78

4-2. MCD and MLD band positions and assignments for Fe(0) atoms isolated in a krypton matrix for the $^5D_4$ ground state configuration 85

4-3. Free atom and octahedral refinement parameters for the simultaneously-refined MCD and MLD experimental data sets 96

4-4. Free atom and octahedral refinement parameters for the individually-refined MCD and MLD experimental data sets 98

4-6. Tetragonal refinement parameters for the individually-refined MCD and MLD experimental data sets. 99

4-7. Tetragonal refinement parameters for the simultaneously-refined MCD and MLD experimental data sets 100

4-8. Tetragonal refinement parameters for the individually-refined MCD and MLD experimental data sets at different starting values of the crystal field parameters 113

4-9. Octahedral refinement parameters for the MCD and MLD experimental data sets determined from RMS vs. P plots for the lowest energy configuration over 250 theta increments 115

4-10. Relative transition intensities from the ground state J = 4 Zeeman sublevels to the excited state J' = 3 Zeeman sublevels....118

5-1. Gas phase absorption positions, observed argon matrix MCD and MLD positions and signs, and predicted relative intensities for MCD and MLD bands for Ni atoms with a $^3D_3$ ground state....201

5-2. Gas phase absorption positions, observed argon matrix MCD and MLD positions, signs, and predicted relative intensities for MCD and MLD bands for Ni atoms with a $^3F_4$ ground state....204

5-3. Relative intensities for the predicted MCD and MLD gas phase transitions between 339 and 352 nm....206

5-4. Free atom refinement parameters for the $^3D_3$ MCD and MLD experimental data sets....214

5-5. Octahedral refinement parameters for the $^3D_3$ MCD and MLD data sets....215

5-6. Tetragonal refinement parameters for the $^3D_3$ MCD and MLD data sets reduced by continuous scaling of the magnetization data....215

5-7. Tetragonal refinement parameters for the $^3D_3$ MCD and MLD data sets reduced by continuous scaling of the moments data....216

5-8. Trigonal refinement parameters for the $^3D_3$ MCD and MLD data sets reduced by continuous scaling of the magnetization data....217

5-9. Trigonal refinement parameters for the $^3D_3$ MCD and MLD data sets reduced by continuous scaling of the moments data....217

5-10. Free atom refinement parameters for the $^3F_4$ MCD and MLD experimental data sets for Ni(0) atoms in Kr....221

5-11. Octahedral refinement parameters for the $^3F_4$ MCD and MLD experimental data sets for Ni(0) atoms in Kr using one increment for numerical theta integration from 0 to $\pi/2$....221

5-12. Octahedral refinement parameters for the $^3F_4$ MCD and MLD experimental data sets for Ni(0) atoms in Kr using 250 increments for numerical theta integration over 0 to $\pi/2$....222

5-13. Octahedral refinement parameters for the $^3F_4$ MCD and MLD experimental data sets for Ni(0) atoms in Kr using 1000 increments for numerical theta integration over 0 to $\pi/2$....222

LIST OF FIGURES

Figure page

1-1. The MCD/MLD apparatus 15

1-2. Configuration for MCD experiment 16

1-3. Zeeman splitting and allowed transitions for circularly and linearly polarized radiation in a magnetic field **B** for a nondegenerate ground state 17

1-4. Zeeman splitting and allowed transitions for circularly and linearly polarized radiation in a magnetic field **B** for a degenerate ground state 18

1-5. Zeeman splitting and allowed transitions for circularly and linearly polarized radiation in a magnetic field **B** for a nondegenerate ground state to two nondegenerate excited states 19

1-6. Configuration for MLD Experiment 20

2-1. Configuration of polarizing filter and photoelastic modulator 41

2-2. Principle of photoelastic modulation 42

2-3. Components of electric and magnetic wave propagation through a photoelastic modulator 43

2-4. Origination of Faraday A term 44

2-5. Origination of Faraday C term 45

2-6. Origination of Faraday B term 46

3-1. MCD dependence on **B** and T. 72

3-2. Normalized Boltzmann population distribution for Fe(0) in free atom $^5D_4$ ground state at various temperatures (T °K) and magnetic field strengths (**B** Tesla) 73

3-3. Octahedral symmetry sites 74

3-4. Lower symmetry models of MX_{12} system 75

3-5. Relation of molecular xyz reference axes to laboratory XYZ axes via Euler angles ϕ, θ, and ψ 76

4-1. Splitting of Fe(0) by spin-orbit (SO) and octahedral crystal field (CF) perturbations 133

4-2. Diagram of Air Products closed-cycle helium cryostat 134

4-3. Diagram of Oxford superconducting split-coil magnet / liquid helium cryostat 135

4-4. Expanded View of Oxford Instruments magnet/cryostat cold finger 136

4-5. Plan view of furnace and Knudsen cell assembly for generating atomic beam 137

4-6. Temperature calibration data curves derived from a moments analysis 138

4-7. Superfluid ^{4}He vapor pressure calibration 139

4-8. Carbon-Glass thermistor calibration 140

4-9. Absorption spectrum of Fe(0) atoms isolated in Kr matrix 141

4-10. Magnetic circular dichroism (MCD) spectrum of Fe(0) atoms isolated in Kr matrix 142

4-11. Magnetic linear dichroism (MLD) spectrum of Fe(0) atoms isolated in a Kr matrix 143

4-12. Fe(0) atoms in Kr free atom MCD vs. **B** experimental and theoretical plots 144

4-13. Fe(0) atoms in Kr free atom MLD vs. $\mathbf{B}^2$ experimental and theoretical plots 147

4-14. Fe(0) atoms in Kr octahedral MCD vs. **B** experimental and theoretical plots 150

4-15. Fe(0) atoms in Kr octahedral MLD vs. $\mathbf{B}^2$ experimental and theoretical plots 153

4-16. Fe(0) atoms in Kr tetragonal MCD vs. **B** experimental and theoretical plots. 156

4-17. Fe(0) atoms in Kr tetragonal MLD vs. $\mathbf{B}^2$ experimental and theoretical plots. 159

4-18. Fe(0) atoms in Kr trigonal MCD vs. **B** experimental and theoretical plots 162

4-19. Fe(0) atoms in Kr trigonal MLD vs. $\mathbf{B}^2$ experimental and theoretical plots 165

4-20. RMS vs. D^{OCT} plots for actual MCD and MLD refinements at 1.61 K 168

4-21. RMS vs. D^{OCT} plots for actual MCD and MLD refinements at 4.22 K 169

4-22. The results of a structured incrementing of the D^{OCT} values at 1.74 and 4.22 K for MCD and MLD 170

4-23. Results of structured incrementing of D^{OCT} performed on all the data sets between 4.22 K and 1.48 K for octahedral geometry 171

4-24. Superimposed graphs for the MCD plots of Figure 4-23 for easier comparison ..174

4-25. Superimposed graphs for the MLD plots of Figure 4-23 for easier comparison ..175

4-26. The results of incrementing along one dimension (F_1^{TET}) of the tetragonal solution for the 4.22 K and 1.74 K MCD and MLD data sets 176

4-27. Plots of structured incrementing over all data sets for tetragonal symmetry 177

4-28. Simultaneous plots of MCD refinement data for all geometries based on numerically integrating theta over $\pi/2$ in one step for octahedral symmetry and initial starting parameters of $F_1^{TET} = F_2^{TET} = B^{TET} = 1.00$ for tetragonal and trigonal symmetry 180

4-29. Simultaneous plots of MLD refinement data for all geometries based on numerically integrating theta over p/2 in one step for octahedral symmetry and initial starting parameters of $F_1^{TET} = F_2^{TET} = B^{TET} = 1.00$ for tetragonal and trigonal symmetry 181

4-30. Splitting of Fe(0) by spin-orbit (S) and tetragonal crystal field (CF) perturbations........182

4-31. Fe(0) atoms in Kr tetragonal MCD vs. **B** experimental and theoretical plots. Initial input parameters to minimization routine: $F_1^{TET} = F_2^{TET} = B^{TET} = 0.05$. ...183

4-32. Fe(0) atoms in Kr tetragonal MLD vs. $\mathbf{B}^2$ experimental and theoretical plots. Initial input parameters to minimization routine: $F_1^{TET} = F_2T^{ET} = B^{TET} = 0.05$....186

4-33. Simultaneous plots of MCD refinement data for all geometries based on numerically integrating theta over $\pi/2$ in one step for octahedral symmetry and initial starting parameters of $F_1^{TET} = F_2^{TET} = B^{TET} = 0.05$ for tetragonal and trigonal symmetry 189

4-34. Simultaneous plots of MLD refinement data for all geometries based on numerically integrating theta over $\pi/2$ in one step for octahedral symmetry and initial starting parameters of $F_1^{TET} = F_2^{TET} = B^{TET} = 0.05$ for tetragonal and trigonal symmetry 190

4-35. Plots of structured incrementing of the MCD and MLD data under octahedral symmetry processing 250 steps of theta numerical integration from 0 to $\pi/2$ 191

4-36. Simultaneous plots of MCD refinement data for all geometries based on numerically integrating theta over $\pi/2$ in 250 steps for octahedral symmetry and initial starting parameters of $F_1^{TET} = F_2^{TET} = B^{TET} = 0.05$ for tetragonal symmetry 194

4-37. Simultaneous plots of MLD refinement data for all geometries based on numerically integrating theta over $\pi/2$ in 250 steps for octahedral symmetry and initial starting parameters of $F_1^{TET} = F_2^{TET} = B^{TET} = 0.05$ for tetragonal symmetry 195

5-1. Comparison of absorption spectrum of Fe(0) atoms in argon with Fe(0) gas phase atomic transitions from the $^5D_4$ ground state 230

5-2. The absorption spectrum of Ni(0) atoms matrix-isolated in argon and krypton contrasted with the Ni(0) atomic gas phase UV/Visible absorption spectrum from the $^3F_4$ ground state 231

5-3. The absorption spectrum of Ni(0) atoms matrix-isolated in argon and krypton constrasted with the Ni(0) atomic gas phase UV/Visible absorption spectrum from the $^3D_3$ ground state 232

5-4. Various mixtures of the gas-phase $^3F_4$ Ni(0) ground state transitions with those originating from a $^3D_3$ ground state 233

5-5. Absorption and MCD spectrum of Ni(0) atoms isolated in an argon matrix 234

5-6. Magnetic linear dichroism (MCD) and magnetic circular dichrosim (MCD) spectra of Ni(0) atoms isolated in argon matrix 235

5-7. Simulated spectra for gas phase Ni(0) with a $^3D_3$ ground state 236

5-8. Simulated MCD spectra in the ultraviolet region for gas phase Ni(0) atoms 237

5-9. Absorption, MCD, and MLD spectra for Ni(0) in Kr with both $^3D_3$ and $^3F_4$ ground states at 4.2 K 238

5-10. Ni(0) atoms in Kr free atom MCD vs. **B** experimental and theoretical plots for $^3D_3$ ground state 239

5-11. Ni(0) atoms in Kr free atom MLD vs. $\mathbf{B}^2$ experimental and theoretical plots for $^3D_3$ ground state 241

5-12. Ni(0) atoms in Kr octahedral MCD vs. **B** experimental and theoretical plots for $^3D_3$ ground state 244

5-13. Ni(0) atoms in Kr octahedral MLD vs. $\mathbf{B}^2$ experimental and theoretical plots for $^3D_3$ ground state 246

5-14. Ni(0) atoms in Kr tetragonal MCD vs. **B** experimental and theoretical plots for $^3D_3$ ground state....249

5-15. Ni(0) atoms in Kr tetragonal MLD vs. $\mathbf{B}^2$ experimental and theoretical plots for $^3D_3$ ground state....251

5-16. Ni(0) atoms in Kr trigonal MCD vs. **B** experimental and theoretical plots for $^3D_3$ ground state....254

5-17. Ni(0) atoms in Kr trigonal MLD vs. $\mathbf{B}^2$ experimental and theoretical plots plots for $^3D_3$ ground state....256

5-18. RMS deviation values as a function of temperature for all four geometry models for a $^3D_3$ ground state....259

5-19. Absorption, MCD, and MLD spectra of the principal ultraviolet transitions of Ni(0) atoms in krypton from the $^3F_4$ ground state....260

5-20. Ni(0) atoms in Kr free atom MCD vs. **B** experimental and theoretical plots for $^3F_4$ ground state....261

5-21. Ni(0) atoms in Kr free atom MLD vs. $\mathbf{B}^2$ experimental and theoretical plots for $^3F_4$ ground state....263

5-22. Ni(0) atoms in Kr octahedral MCD vs. **B** experimental and theoretical plots for $^3F_4$ ground state....264

5-23. Ni(0) atoms in Kr octahedral MLD vs. $\mathbf{B}^2$ experimental and theoretical plots for $^3F_4$ ground state....266

5-24. Ni(0) atoms in Kr tetragonal MCD vs. **B** experimental and theoretical plots for $^3F_4$ ground state....267

5-25. Ni(0) atoms in Kr tetragonal MLD vs. $\mathbf{B}^2$ experimental and theoretical plots for $^3F_4$ ground state....269

5-26. Ni(0) atoms in Kr trigonal MCD vs. **B** experimental and theoretical plots for $^3F_4$ ground state....270

5-27. Ni(0) atoms in Kr trigonal MLD vs. $\mathbf{B}^2$ experimental and theoretical plots for $^3F_4$ ground state....272

5-28. RMS deviation values as a function of temperature for all four geometry models for a $^3F_4$ ground state....273

6-1. Absorption (ABS), MCD, and MLD spectra of Fe(0) and Ni(0) isolated in solid krypton....279

6-2. Site symmetry configuration of $^5D_4$ ground state Fe(0) atoms matrix-isolated in solid krypton at 4.20 – 1.48 K 280

6-3. Site symmetry configuration of $^3F_4$ ground state Ni(0) atoms matrix-isolated in solid krypton at 4.00 – 1.48 K 281

6-4. Site symmetry configuration of $^3D_3$ ground state Ni(0) atoms matrix-isolated in solid krypton at 4.38 – 1.73 K 282

Abstract of Dissertation Presented to the Graduate School
of the University of Florida in Partial Fulfillment of the
Requirements for the Degree of Doctor of Philosophy

DETERMINATION OF THE SITE SYMMETRY OF Ni(0 AND Fe(0) ATOMS ISOLATED IN SOLID KRYPTON MATRIX VIA MAGNETIC CIRCULAR AND MAGNETIC LINEAR DICHROISM SPECTROSCOPY

By

Karen L. Jensen

May 2003

Chairperson: Martin Vala
Major Department: Chemistry

The techniques of magnetic circular dichroism (MCD) and magnetic linear dichroism (MLD) spectroscopy have been utilized to determine the absolute assignments of electronic state transitions for zero-valent Fe and Ni atoms isolated in krypton and/or argon rare gas matrices near, at, and below liquid He temperature. The different selection rules applying to MCD vs. MLD transitions and the differing oscillator intensities show the usefulness of sequential MCD/MLD for resolving transitions that may be otherwise unresolved or even unobservable by either of the techniques alone. In addition, sequential application of the techniques of magnetic circular and magnetic linear dichroism saturation spectroscopy was achieved on Fe(0) and Ni(0) atoms in krypton. Extension beyond the linear limits of MCD and MLD spectroscopy allows determination of the geometrical site symmetry of the embedded metal atom with high confidence levels.

The measurement of the MLD spectrum of $^5D_4$ Fe(0) in krypton was the first demonstrated application of the MLD technique to matrix isolated species and corroborated the assignments previously made by MCD spectroscopy. Several previously unobserved bands were detected in the MLD spectrum and assigned accordingly. The MLD technique was then applied to Ni(0) atoms isolated in an argon matrix to aid in the controversial assignment of the electronic absorptions thought to be attributable to two different isolable ground state configurations of Ni(0) in rare gas matrices. These energy states are ~205 cm^{-1} apart in the gas phase: the normal low energy $^3F_4$ and the higher energy $^3D_3$. The electronic assignments of transitions from these states were assigned unambiguously by applying the selection rules of the sequential MCD and MLD technique, establishing the validity of the dual ground state hypothesis.

By extensive theoretical development, the technique was extended to point groups lower than pseudo-isotropic symmetry. Refinement of the theoretical fit of a particular symmetry model to the observed experimental data yields both the actual site symmetry and the extent of crystal field splitting. An unexpected temperature dependent crystal field splitting was observed and is attributed to a unit cell contraction of the Kr matrix cage on cooling below liquid He temperature.

CHAPTER 1
INTRODUCTION

History

Matrix isolation methods have been used extensively to study species in unstable and intermediate states.[1-5] This technique involves freezing the unstable atom/molecule/ion in a solid nonreactive support so that the analyte's properties may be investigated. Condensation to the solid state, however, does not leave the unstable species unperturbed. Ideally, spectroscopic analysis would be conducted in the gas phase at low temperature, with a very dilute sample concentration, to minimize interactions with neighboring species. The limiting factors of dilute concentration and short lifetimes often makes gas-phase analysis impractical for detailed analysis of unstable species. Entrapping the species (commonly referred to as the solute) in a solid matrix permits the experimentalist to freeze out the short lifetime of a reactive or transitory state. Matrix isolation permits control over the concentration of the sample/matrix, allowing the use of many standard methods of analysis (UV/VIS, FTIR, Raman) as well as more sophisticated procedures (ESR, LIF, Mossbauer, MCD, MLD)[6]. Such investigations generally reveal extensive information about the trapped solute. However, to fully understand the solute analysis, the effects of the surrounding matrix cage on the solute must also be determined. For example, comparison of the gas phase electronic spectra of many atomic species with the electronic spectra of the same species isolated in solid rare gas matrices yields distinct differences in both the energy and multiplicity of spectral lines.[7-10] These discrepancies can be due to multiple site trapping, in which the local environment of some portion of the solute atoms is slightly different than the remaining solute atoms. Alternate sites are usually caused by condensation into a slightly unstable geometry. These unstable geometries will relax to the lower energy ground state geometry upon annealing (warming) the matrix sufficiently to permit rearrangement. Multiple lines remaining after careful annealing are indicative of perturbations due to spin-orbit coupling as well as lattice mode interactions. Analysis of such perturbations allows the determination of the presence or absence of Jahn-Teller effects which are caused by an external heavy atom (the matrix component).[11-15] Excessive annealing allows the solute atoms to migrate in a semi-fluid matrix medium resulting in generally uncontrollable cluster and bulk formation. Large cluster and bulk aggregates usually result in heavy clouding of the matrix leading to scattering of incident radiation and broad UV absorption.

Numerous accounts of research on matrix-isolated species can be found in the published literature. High molecular weight solvents have been used to stabilize reaction intermediates to control the formation of products. Spectroscopic studies of solvent-stabilized reaction intermediates trapped in a solid organic matrix, such as Ni-toluene,[16,17] give insight into the structure of the intermediate complex. From this structural information reaction mechanisms involving these intermediate states can be more readily understood. Such knowledge of intermediate or transition environments might better enable the experimentalist to predict and/or control reaction pathways. Using other solvents, such as SF_6 and CH_4 , allows expansion of the functional temperature range of the study because of their higher melting points.[2,18] These solvents can be frozen with liquid nitrogen baths at a temperature of approximately 77 K. However, solute-solvent interactions generally are much more extensive in these polyatomic matrices.

Co-condensation of the solute with monatomic rare gas solvents (Ne, Ar, Kr, Xe) requires refrigeration capabilities much lower, typically 10 – 40 K for Ar, Kr, and Xe, and approaching liquid He temperature (~4 K) for neon. Such temperatures are readily achievable using commercially available closed-cycle helium cryostats. The interactions between the trapped solute and rare gas solvent are minimal compared with other solvents, but are still not negligible.[2,9,19] Although such interactions may not be critical for understanding reaction pathways or electronic environments on a qualitative scale, a quantitative explanation of the solute species itself must include an analysis of perturbations to the solute's electronic structure caused by the solute-matrix interaction.

Much work has been done in the field of rare gas matrix-isolation of metal atoms, metal oxides, and small metal clusters.[20-23] Initially these efforts focused on determining the gross effects of matrix gas on the solute species; however, many of these studies ran into difficulty in fully explaining the spectral results. Especially difficult were the accurate assignments of the electronic transitions to the actual corresponding electronic states and the explanation of the unexpected multiplicity of some absorption lines. Some species demonstrated unusual spin-orbit splitting.

Magnetic circular dichroism (MCD) spectroscopy has proven very successful in assisting the accurate assignment of electronic transitions. MCD spectroscopy is accomplished by measuring the differential absorption of right and left circularly polarized light by a sample supported in a magnetic field collinear with the incident radiation (ultraviolet/visible range).[24-26] Figure 1-1 shows the experimental apparatus.

Figure 1-2 depicts the relation between the sample, applied magnetic field, and polarization geometry relative to the light propagation direction (z axis) for circularly polarized radiation in the MCD experiment. If no degenerate ground states exist (Figure 1-3), differential absorption occurs between the nondegenerate ground state and the Zeeman split excited states without any spectral temperature dependence. This type of band dispersion is designated a Faraday $\mathcal{A}$ term and is typical of diamagnetic species. Zeeman splitting[27,28] of degenerate ground states (Figures 1-4 and 1-5) by a magnetic field results in a temperature-dependent population distribution among the field-split ground-state levels, giving rise to temperature-dependent spectra designated as Faraday $\mathcal{C}$ terms. Faraday $\mathcal{C}$ terms are associated with paramagnetic species. These transitions and their related Faraday terms are discussed in Chapter 2, where they are linked to the total MCD dispersion function $f(\mathcal{E})$.

Previous work in this laboratory focused on MCD spectral analysis of transition metal atoms[22,24-26] and oxides[21] with degenerate ground states isolated in argon, krypton, or xenon solid matrices. Since these species were all paramagnetic in nature, the MCD dispersion spectra showed temperature dependence. The $^2P \leftarrow {}^2S$ transitions were the principal studies, as early theoretical analysis permitted treatment of only this type of transition.[27,28] Expansion of the theory now permits analysis for states of arbitrary multiplicity along with some matrix-enhanced forbidden transitions.[30-32] Analysis of the structural variation of a particular absorption band with temperature by the method of moments yields the magnitude of spin-orbit splitting. Detailed analysis of temperature dependent MCD transitions also permits derivation of spin-orbit coupling constants and the extent of matrix lattice interactions from cubic and noncubic vibrational modes, including determination of the extent (if any) of Jahn-Teller distortions to the solute. It is also possible to derive orbital *g*–factors and crystal field matrix perturbations from the MCD data.[10,28,30,32]

The MCD spectrum of a species often enables clarification of the assignments of excited-state transitions. For temperature dependent $\mathcal{C}$ terms the sign of the MCD transition is dependent on the sign of $\Delta\mathbf{J}$,[29,32] the signed change in the total orbital angular momentum during the transition. $\Delta\mathbf{L}$ is the signed change in the orbital angular momentum exclusive of **S**, the sum of the spin angular momenta m_s for the valence electrons. **L** is the sum of the ℓ quantum numbers of each of the valence shell electrons in an atom. **J** is the total orbital angular momentum including both **L** and **S** $(\mathbf{J} = \mathbf{L} + \mathbf{S})$. $\mathbf{M_J}$ delineates the individual 2J+1 degenerate orbitals once the degeneracy is lifted by either internal reference axes or an external field, as a magnetic field **B**. This is equivalent to specifying by the term J_z , as both $\mathbf{M_J}$ and J_z represent the component of **J** along the z axis. Various authors use these terms interchangeably. In this study, $\mathbf{M_J}$ is used predominantly, but J_z appears in some mathematical expressions to maintain consistency with the references from which the expressions were obtained. Selection rules for conventional electronic absorption spectroscopy (ABS) restrict electronic transitions to $\Delta\mathbf{J} = 0, \pm1$; $\Delta\mathbf{L} = \pm1$; $\Delta\mathbf{M_J} = 0, \pm1$. MCD selection rules are slightly more restrictive: $\Delta\mathbf{J} = 0, \pm1$; $\Delta\mathbf{L} = \pm1$; $\Delta\mathbf{M_J} = \pm1$. The sign convention for differential absorption (MCD) is, by definition, $\Delta A_C = A_- - A_+ = A_{LCP} - A_{RCP}$ where the subscript C represents MCD. ΔA_C is the signed resultant differential absorption of circularly polarized radiation. $A_- \equiv A_{LCP}$ is the absorption of left circularly polarized radiation moving in a negative (-) or counterclockwise helical arc along the z reference axis. $A_+ \equiv A_{RCP}$ is the absorption of right circularly polarized radiation moving in a positive (+) or clockwise helical arc along the z reference axis. Therefore, if $A_{LCP} > A_{RCP}$, then the MCD signal is positively signed. For electronic transitions from ground state J_i to excited state J_f in which $\Delta \mathbf{J} = 0, -1$, MCD $\mathcal{C}$ transitions are positive by definition, corresponding to preferential absorption of LCP radiation. For $\Delta \mathbf{J} = +1$, MCD $\mathcal{C}$ transitions are negative, corresponding to preferential absorption of RCP radiation. The sign of $\Delta \mathbf{J}$ corresponds to the sign of the $\mathcal{C}$ term MCD absorption, but in actuality it is the sum of the contributions from all of the possible $\Delta \mathbf{M_J}$ transitions that determines both the sign of the transition and the structure of the overall $\mathcal{C}$ band envelope. Altering the temperature of the matrix results in variations in the intensities of individual $\Delta \mathbf{M_J}$ transitions due to varying populations of the degenerate states. These variations are reflected in structural changes of the overall $\mathcal{C}$ band envelope. Angular-momentum coupling schemes and MCD/MLD dispersion spectra arising from electronic transitions between initial and final angular-momentum states are discussed in Chapter 2.

The magnetic fields referred to in this study will be represented by the variable **B**. Generally **B** and **H** are used somewhat interchangeably to represent magnetic field intensity. The symbol **E** is used almost exclusively among the options **E** and **D** to represent the electric field intensity in a region. In the strictest physical interpretation **B** and **E** are respectively the magnetic induction and electric field intensity defined in Maxwell's equations for 'free' or 'unbound' charge and current densities in a vacuum. Traditionally **H** (magnetic field intensity) and **D** (electric displacement) are derived quantities proportional to **B** and **E** by the isotropic tensors μ^{-1} and ε respectively:[34,35]

$$\mathbf{H} = \mu^{-1}\mathbf{B} = \mu_0^{-1}\mu_r^{-1}\mathbf{B} \tag{1-1}$$

$$\mathbf{D} = \varepsilon\mathbf{E} = \varepsilon_0\varepsilon_r\mathbf{E} \tag{1-2}$$

where μ_r^{-1} is defined as the inverse isotropic magnetic permeability of the medium, and ε_r as the isotropic dielectric permittivity of the medium the fields exist across. The variables μ_r and ε_r are the relative permeability and permittivity defined as

$$\mu_r = \frac{\mu}{\mu_0} = \frac{\mathbf{B}}{\mathbf{H}} \tag{1-3}$$

$$\varepsilon_r = \frac{\varepsilon}{\varepsilon_0} = \frac{\mathbf{D}}{\mathbf{E}} \tag{1-4}$$

where $\mu_0 = 4\pi \times 10^{-7}$ Volt-seconds/Ampere-meter
≡ magnetic permeability of free space

$\varepsilon_0 = 8.854 \times 10^{-12}$ Ampere-seconds/Volt-meter
≡ dielectric permittivity of free space

$\mu \equiv$ magnetic permeability of medium

$\varepsilon \equiv$ dielectric permittivity of medium

Note that it is not required that the medium be isotropic. This assumption relates to many real applications and is valid in this study with high vacuum [< 1 x 10^{-6} Torr] as the medium. The perturbation of the magnetic field by the copper cold finger and sapphire window with the deposited metal atom/noble gas matrix (Figures 1-1 to 1-3) is regarded as negligible. However, the presence of diagmagnetic impurities in the matrix can significantly affect higher order moments analyses, especially in the low magnetic-field limit regime.

Conventionally, **B** is expressed in terms of **H** by the direct permeability of the medium μ to represent the effective microscopic magnetic flux density in a medium accounting for modification of the macroscopic **H** by the medium:

$$\mathbf{B} = \mu\, \mathbf{H} \tag{1-5}$$

In a physical medium, induced polarization and magnetization of the medium creates 'bound' charge and current densities across the medium either opposing the applied **B** and **E** fields or enhancing them.[34] Thus alteration of the **B** and **E** fields depends on the significance of μ and ε. In a vacuum, the proportionality constant $\mu = \varepsilon = 1$. In air, the values of μ and ε are generally assumed to be equal to the vacuum value of one, which is accurate to a high degree of approximation. The parameters μ and ε are also functions of frequency and wavevector, but confinement within the visible light region of the electromagnetic spectrum (as in this study) negates any need to compensate for these effects.[35] Throughout this study the applied magnetic field is expressed as **B** and its component along the z axis as B_z. Since the experiments are performed in high vacuum [$< 1 \times 10^{-6}$ Torr], for all practical purposes **B** = **H**.

In Figure 1-3 an electronic transition from ground state $^1S_0\,(ns^2)$ to excited state $^1P_1\,(ns^1np^1)$ is represented for the magnetic fields **B** = 0 and **B** > 0 for MCD. When **B** = 0, there is no Zeeman effect and the three sub-levels of the ^1P excited state ($^1P_{-1}$, $^1P_0$, $^1P_1$) are degenerate in energy. The subscripts -1, 0, and 1 denote the magnetic component of total angular momentum $\mathbf{M_J}$ of the degenerate energy sub-levels. When **B** > 0, the states $^1P_{-1}$, $^1P_0$, and $^1P_1$ are split in energy from each other by a magnitude of $\mu_B g B_z$ due to their relative orthogonal orientations in the magnetic field; μ_B is the Bohr magneton ($\mu_B = 9.27 \times 10^{-24}$ JT^{-1}), and g is the magnetic moment of a free electron.[33] Transitions from the ground $^1S_0$ state to each of these excited state sub-levels are characterized by different energies of absorption corresponding to their magnitude of separation by the Zeeman energy, $\mu_B g B_z$.

Reiterating, Faraday $\mathcal{C}$ transitions in which $\Delta\mathbf{M}_J = +1$ absorb LCP radiation. Transitions in which $\Delta\mathbf{M}_J = -1$ absorb RCP radiation. The sign of the sum of the dominant transitions (LCP or RCP) determines the resultant sign of $\Delta A_C = A_{LCP} - A_{RCP}$ and is established by the total angular momentum of the lowest magnetically split Zeeman sub-level ($\mathbf{M}_J = -\mathbf{J}$) coupled with the selection rules $\Delta\mathbf{J} = 0, \pm1$, $\Delta\mathbf{L} = \pm1$, $\Delta\mathbf{M}_J = \pm1$. The shape of the dispersion $f(\mathcal{E})$ is proportional to the relative populations of the Zeeman sublevels (determined by T), the energy separations to excited state sub-levels (determined by **B**), and the MCD selection rules $\Delta\mathbf{M}_J = \pm1$. In the case of transitions which remain unresolved in the UV/VIS spectrum, this difference in MCD sign often aids in clarification of the assignment of the excited states when overlapping ABS transitions are resolved in the MCD spectrum. Also, transitions which may have weak or even unobservable absorption intensity may exhibit significant intensity in the MCD spectrum.

The application of both ABS and MCD techniques have enabled accurate assignment of previously ambiguous or even unobserved electronic transitions. However, when the two techniques (ABS and MCD) are applied separately in time, even between the short duration of a single scan (~30 minutes), transitions for the same band may no longer have the same integrated band area due to matrix or site decay by thermal or photolytic processes. The apparatus used in this study is capable of acquiring simultaneous ABS/MCD spectra, thus eliminating fluctuations of the integrated intensities and moments of transition bands due to decay or site shifting phenomena.

Previous Fe and Ni Work

An MCD study of Fe atoms condensed in Ar, Kr, and Xe by Shaks-Emanpour, Vala, and co-workers concluded that spin-orbit coupling was the principal interaction causing the observed electronic spectra.[22] Calculated MCD parameters for Fe/Kr agreed within experimental error with the expected values for the free atom model in which there is no matrix effect. The Jahn-Teller effect was deemed inactive (or at least negligible) in both the ground and excited states since there was no observable reduction in the orbital angular momentum as determined from the experimental data. The magnitude of the spin-orbit coupling constant, 104 cm^{-1}, is large enough to preclude the preeminence of a Jahn-Teller effect. Absolute assignments of the states of electronic transitions were made utilizing the sign dependence of the MCD transitions. The lack of observable splitting of the spectral bands implied a small or negligible crystal field effect. Comparison of the calculated free atom and octahedral site models showed variances between the experimental and calculated theoretical data of 2% at 10 K and 0.5% at 20 K, which are both less than the experimental error. It was concluded that the existence of an octahedral field site geometry in Fe/Kr instead of the free atom environment would have a negligible effect on the MCD spectral parameters at these temperatures. Consequently, no inferences can be made from their data about the site symmetry of Fe(0) in Kr matrices.

Previous MCD spectral analyses of Ni atoms isolated in rare gas matrices demonstrate ambiguities in the assignment of electronic transitions. A low lying gas phase $^3D_3$ excited state ($4s^13d^7$ electronic configuration) just 205 cm^{-1} above the gas phase $^3F_4$ ground state ($4s^23d^6$) may simultaneously exist as a stable ground state configuration in Ar, Kr, and Xe matrices along with Ni atoms in a $^3F_4$ ground state configuration.[7,36-39] The simultaneous presence of both ground states has not been absolutely confirmed, since transitions from both ground states to excited states complicate the absorption and MCD spectra. The spectral transitions need to be assigned absolutely. Subsequently, determination of the site symmetry of each ground state environment, if indeed both do exist, would be very beneficial in understanding the stabilization of the $^3D_3$ site relative to the $^3F_4$ site.

Extension to MLD

The complementarity of magnetic linear dichroism (MLD) spectroscopy can assist in the assignment of excited states not confirmed by MCD. MLD spectroscopy, as shown in Figure 1-6, differs from MCD spectroscopy in two principle ways:[33]

- Orientating the sample and incident radiation in relation to the magnetic field.
- Using linearly polarized radiation instead of circularly polarized radiation.

In MLD experiments, the magnet coil is rotated so that the magnetic field is perpendicular to the propagation direction of the incident linearly polarized radiation (Figure 1-6 A), which is then modulated between orientations parallel and perpendicular to the magnetic field (Figure 1-6 B).

The signs of MLD transitions are also dependent on $\Delta\mathbf{J}$,[29] but in a slightly different manner: for $\Delta\mathbf{J} = 0$, temperature dependent MLD Faraday $\mathcal{G}$ term transitions are positively signed, while for $\Delta\mathbf{J} = \pm 1$, they are negatively signed (Figures 1-3 to 1-5). Perpendicular transitions correspond to $\Delta\mathbf{M}_J = \pm 1$ and parallel transitions to $\Delta\mathbf{M}_J = 0$. As with MCD, the overall sign of $\Delta\mathbf{J}$ transitions along with the bandshape is determined by the combination of $\Delta\mathbf{M}_J = \pm 1$ and $\Delta\mathbf{M}_J = 0$ absorptions. The resultant differential absorption of parallel and perpendicular linearly polarized radiation for MLD is $\Delta A_L = A_{\parallel} - A_{\perp} = A_z - A_x$. The subscript L in ΔA_L represents differential absorption for MLD as opposed to C in ΔA_C for MCD. Also, whereas MCD $\mathcal{C}$ term intensities will be seen in the derivations of Chapter 2 to be directly proportional to **B** and inversely proportional to

T, MLD intensities are directly proportional to $\mathbf{B}^2$ and inversely proportional to T^2.[33] Thus, some transitions unresolved in the MCD spectrum of a particular species may be resolved in the MLD spectrum simply due to their enhanced intensity at the same T and **B**. Utilization of both MCD and MLD spectroscopy can lead to unambiguous assignment of the excited state transitions of complicated electronic spectra. As with MCD, the instrumentation used in this study is capable of simultaneously collecting ABS and MLD spectra to eliminate scaling difficulties. MCD and MLD are both greatly enhanced in the information that can be extracted from matrices by extending the techniques to very low temperatures and high magnetic fields.

Magnetic Saturation

The method of moments analysis has been applied to temperature dependent MCD transitions to assist determination of the site symmetry of the solute-matrix environment. Potential flaws in this approach arise mostly from the large experimental errors present in the data, leading to errors in the MCD parameter determinations. The presence of diamagnetic impurities affects the dipole strength of the solute-matrix environment, directly affecting the MCD moments analysis. If magnetic saturation techniques are applied to temperature dependent transitions, a more accurate determination of the site symmetry is possible by determining the mathematical model which best fits the experimental data: octahedral, trigonal, tetragonal, or lower symmetry if the model is adequate. Saturation analysis avoids the complications of diamagnetic impurities. The more extensive data sets acquired during the saturation experiment, along with the increased sensitivity of the refinement of experimental data relative to the model applied, increase the confidence level of the assignments.

The magnetic saturation technique involves collection of temperature dependent electronic transition data, and also of magnetic field dependent data. The practical region for this study requires the data be collected at liquid helium temperatures (~4 K) and below to achieve saturation or near saturation at the fields being utilized (0 – 4 Tesla).[29,40] Fitting of the 3-dimensional surface data to the predicted results for various symmetry configuration models permits inference of the actual site symmetry to a high degree of confidence.

Theoretical analysis of the MCD and MLD spectra for a system approaching or in saturation has been developed from the basic theory for application to metal atoms in weak octahedral crystal field matrices by Rivoal, Vala, and coworkers.[30] Previous experimental studies suggest that such sites are probably octahedral in nature, although dodecahedral, tetrahedral, and distorted axial configurations have not been ruled out.[22,40,41] The individual metal atoms may occupy either a substitutional site, in which the metal atom physically replaces a matrix atom in the lattice, or an interstitial site, where it 'crowds' between existing matrix atoms in the lattice. Whether sites are substitutional or interstitial in nature has been difficult to determine.

Statement of Problem

The objective was to demonstrate the advantage of sequential ABS/MCD and ABS/MLD spectroscopic studies for the unequivocal assignment of electronic states in Fe(0)/Kr and Ni(0)/Kr matrices. The MCD was obtained simultaneously with ABS for proper scaling, then the MLD acquired simultaneously with ABS. Uncertainties and ambiguities in previous MCD assignments were clarified by MLD methods. The state transitions for Fe(0) in Kr have been previously assigned by Zeringue et al via MCD spectroscopy at ~0.5 Tesla and 12 – 30 Kelvin.[10] An MLD spectrum of Fe(0) in Kr was obtained under similar conditions and electronic state assignments from its $^5D_4$ ground state analyzed according to MLD theoretical criteria.[29] In doing so, the validity of applying magnetic linear dichroism spectroscopy simultaneously with a magnetic circular dichroism analysis to arrive at an unambiguous assignment of the states was proven. The complementary MCD/MLD methods was then applied to Ni(0) atoms isolated in Ar and Kr matrices. Using the properties of the signed MCD and MLD transitions, theoretical spectra for Ni(0) residing in both $^3D_3$ and $^3F_4$ ground states were calculated and compared with the experimentally obtained spectra. Absolute reconciliation of the dual ground state controversy was made based on these comparisons, and the electronic energy states assigned accordingly.

Being fully confident of the state assignments to the Fe(0) and Ni(0) transitions, the method of MCD/MLD saturation spectroscopy will subsequently be applied to Fe(0) and Ni(0) in a Kr matrix. Analysis of data obtained for temperatures from 4.2 K – 1.5 K and magnetic fields of 0 to 4 Tesla will permit conclusions to be drawn about the symmetry of the Fe(0) and Ni(0) species in their ground-state configurations within the Kr matrix cage.

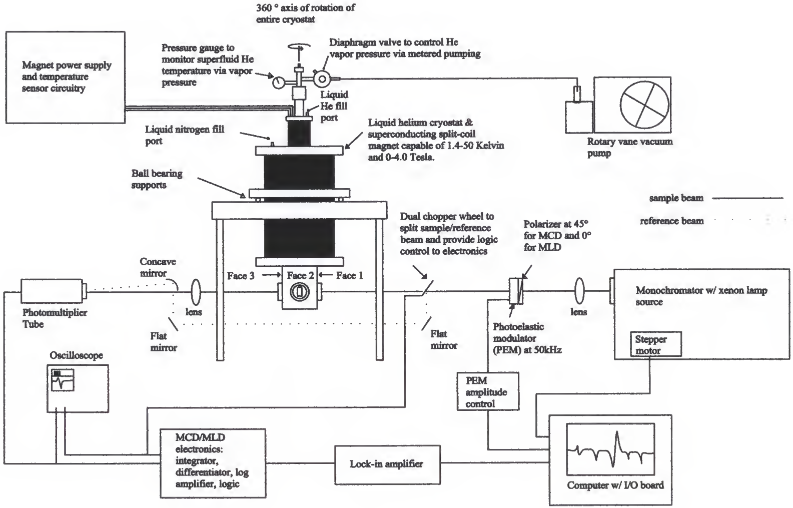
360 ° axis of rotation of entire cryostat
Magnet power supply and temperature sensor circuitry
Pressure gauge to monitor superfluid He temperature via vapor pressure
Diaphragm valve to control He vapor pressure via metered pumping
Liquid He fill port
Liquid nitrogen fill port
Liquid helium cryostat & superconducting split-coil magnet capable of 1.4-50 Kelvin and 0-4.0 Tesla.
Rotary vane vacuum pump
Ball bearing supports
sample beam
reference beam
Dual chopper wheel to split sample/reference beam and provide logic control to electronics
Polarizer at 45° for MCD and 0° for MLD
Concave mirror
Face 3
Face 2
Face 1
Monochromator w/ xenon lamp source
Photomultiplier Tube
lens
lens
Flat mirror
Flat mirror
Photoelastic modulator (PEM) at 50kHz
Stepper motor
Oscilloscope
PEM amplitude control
MCD/MLD electronics: integrator, differentiator, log amplifier, logic
Lock-in amplifier
Computer w/ I/O board

Figure 1-1. The MCD/MLD apparatus. The rotary vacuum pump is used to achieve matrix temperatures below 4.2 Kelvin by exploiting the properties of superfluid helium. Matrix temperatures between 4.2-50 K are achieved by use of a vapor displacement bubble insert.

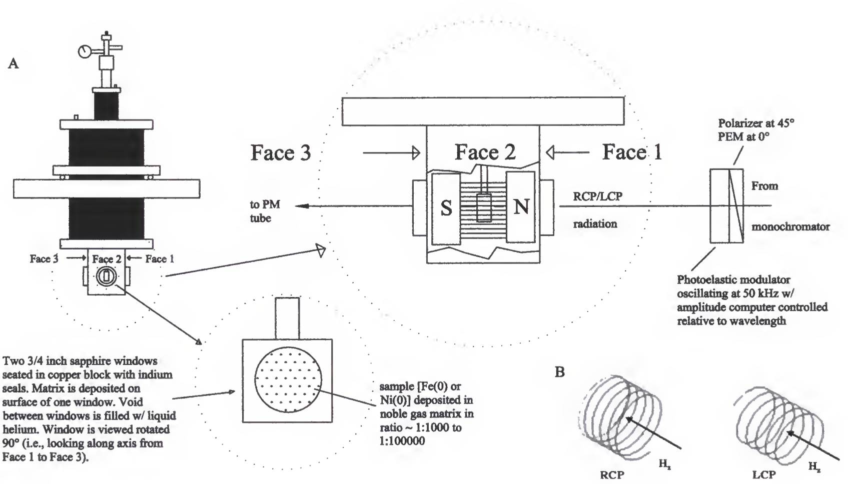
A
Face 3
Face 2
Face 1
Face 3
Face 2
Face 1
to PM tube
S
N
RCP/LCP
radiation
Polarizer at 45°
PEM at 0°
From
monochromator
Photoelastic modulator oscillating at 50 kHz w/ amplitude computer controlled relative to wavelength
Two 3/4 inch sapphire windows seated in copper block with indium seals. Matrix is deposited on surface of one window. Void between windows is filled w/ liquid helium. Window is viewed rotated 90° (i.e., looking along axis from Face 1 to Face 3).
sample [Fe(0) or Ni(0)] deposited in noble gas matrix in ratio ~ 1:1000 to 1:100000
B
RCP
H_z
LCP
H_z

Figure 1-2. Configuration for MCD experiment. A) Detailed view of the configuration for MCD using right and left circularly polarized radiation. The polarizing filter is set 45° from the vertical plane and the vertical axis of the PEM is at 0° from the vertical plane. The radiation is coaxial with the magnetic field. B) Illustration depicting right and left circularly polarized radiation (RCP and LCP) propagating collinearly along magnetic field **B=μH.**

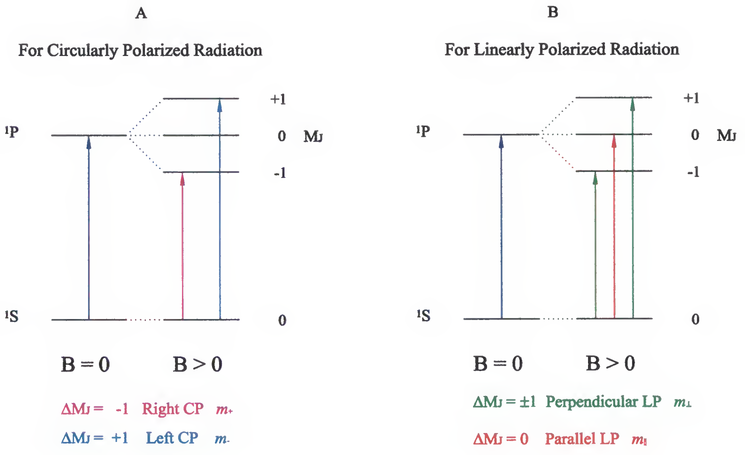
A
For Circularly Polarized Radiation
^1P
^1S
+1
0
-1
0
M_J
B = 0
B > 0
$\Delta M_J = -1$ Right CP m_+
$\Delta M_J = +1$ Left CP m_-
B
For Linearly Polarized Radiation
^1P
^1S
+1
0
-1
0
M_J
B = 0
B > 0
$\Delta M_J = \pm 1$ Perpendicular LP $m_\perp$
$\Delta M_J = 0$ Parallel LP $m_\parallel$

Figure 1-3. Zeeman splitting and allowed transitions for circularly and linearly polarized radiation in a magnetic field **B** for a nondegenerate ground state. In this example $\Delta J = +1$. A) Transitions for circularly polarized radiation. B) Transitions for linearly polarized radiation.

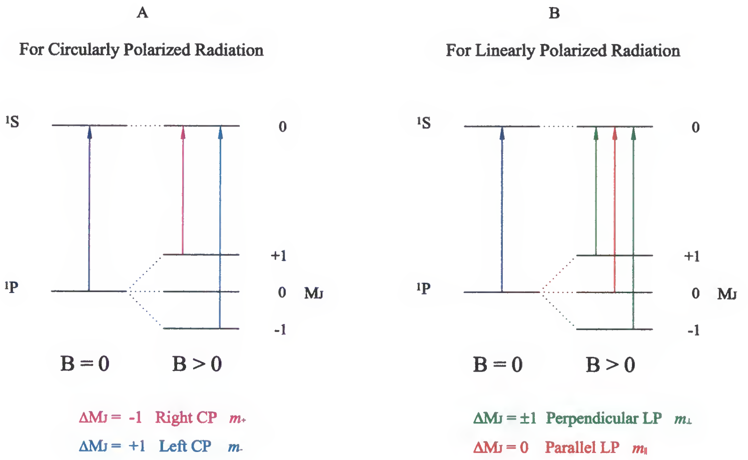
A
For Circularly Polarized Radiation
^1S
^1P
0
+1
0
-1
M_J
B = 0
B > 0
$\Delta M_J = -1$ Right CP m_+
$\Delta M_J = +1$ Left CP m_-
B
For Linearly Polarized Radiation
^1S
^1P
0
+1
0
-1
M_J
B = 0
B > 0
$\Delta M_J = \pm1$ Perpendicular LP $m_\perp$
$\Delta M_J = 0$ Parallel LP $m_\parallel$

Figure 1-4. Zeeman splitting and allowed transitions for circularly and linearly polarized radiation in a magnetic field **B** for a degenerate ground state. In this example $\Delta J = -1$. A) Transitions for circularly polarized radiation. B) Transitions for linearly polarized radiation.

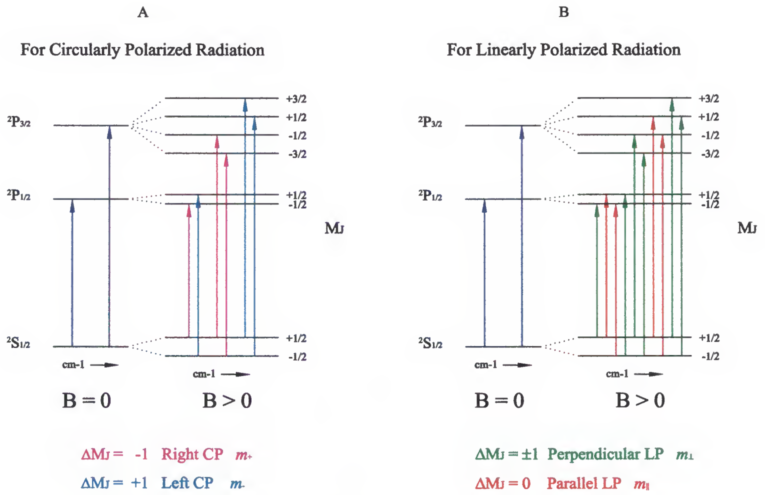

Figure 1-5. Zeeman splitting and allowed transitions for circularly and linearly polarized radiation in a magnetic field **B** for a nondegenerate ground state to two nondegenerate excited states. In this example ΔJ = 0, +1. A) Transitions for circularly polarized radiation. B) Transitions for linearly polarized radiation.

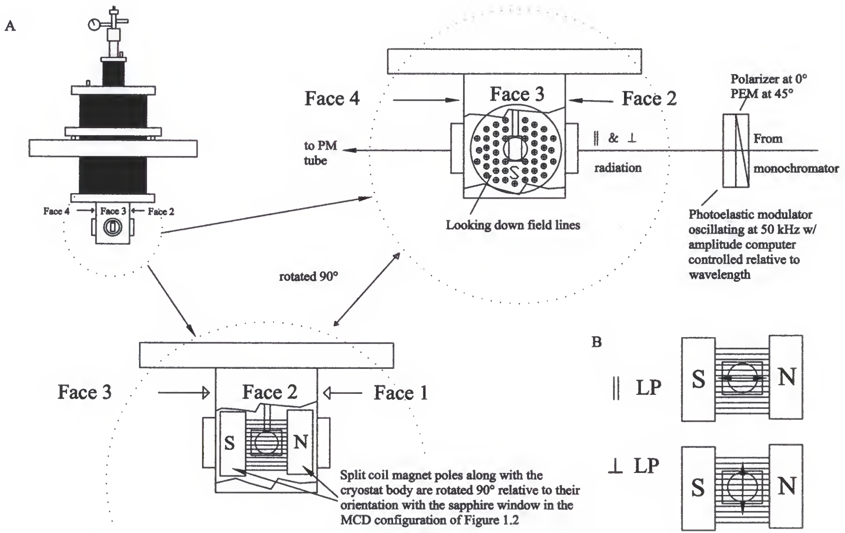
A
Face 4
Face 3
Face 2
Face 4
Face 3
Face 2
to PM tube
|| & ⊥
radiation
Polarizer at 0°
PEM at 45°
From
monochromator
S
Looking down field lines
Photoelastic modulator oscillating at 50 kHz w/ amplitude computer controlled relative to wavelength
rotated 90°
Face 3
Face 2
Face 1
S
N
Split coil magnet poles along with the cryostat body are rotated 90° relative to their orientation with the sapphire window in the MCD configuration of Figure 1.2
B
|| LP
S
N
⊥ LP
S
N

Figure 1-6. Configuration for MLD experiment. A) Detailed view of the configuration for MLD using parallel and perpendicular linearly polarized radiation. The incident radiation is perpendicular to the magnetic field lines. B) Illustration depicting orientation of the resultant electric field vector of incident radiation propagating parallel and perpendicular to the magnetic field **B**=μ**H**.

CHAPTER 2
THEORY OF MAGNETIC CIRCULAR AND MAGNETIC LINEAR DICHROISM

Production of Circularly Polarized Radiation

Electronic absorption spectroscopy is generally utilized to measure the energies of electronic transitions in chemical absorbers in the ultraviolet/visible (UV/VIS) region of the electromagnetic spectrum. All species exhibit an electronic absorption spectrum, which arises from the absorption of randomly polarized radiation causing an electron to undergo a transition from its ground state energy level to an allowable excited state.[42] The technique of circular dichroism (CD) spectroscopy measures the difference in absorption of right and left circularly polarized radiation in the UV/VIS region by an absorber in the absence of a magnetic field. In order to exhibit circular dichroism, an absorber needs to be of a low symmetry configuration.[43,44] Isolated solute molecules such as a solution of +d-10 camphorsulfonic acid and crystalline solids as tris-ethylenediamine cobalt(III) chloride and potassium iron ferrocyanate readily exhibit CD.[45,46] As the absorber tends toward higher symmetry and thus an isotropic spatial configuration, preferential absorption of right or left circularly polarized radiation is no longer favored and natural CD disappears.

Application of a magnetic field collinear with the propagating circularly polarized radiation will produce a magnetically induced circular dichroism in all species due to Zeeman splitting of degenerate ground and/or excited electronic states by the field. The field creates a separation of equivalent energy levels along the field axis (Figures 1-3 to 1-5). This Zeeman splitting effect is the basic mechanism underlying magnetic circular dichroism (MCD) spectroscopy.[27,28,33,43] Central to the determination of a circular dichroism effect in a species, either natural or magnetically induced, is the production of circularly polarized (CP) radiation. Earlier technology utilized Pockels or Kerr cells to produce circularly polarized radiation.[47,48] Adaptation of the piezo-optic or photoelastic effect in an isotropic transparent material is now commonly utilized to generate CP radiation. Advantage is taken of the stress-induced birefringence created in a uniform solid block (glass, uniaxial quartz, CaF_2, etc.) by a sustained acoustic vibration induced by a mechanical transducer (Figure 2-1). The typical vibration frequency is in the audio - 100 kHz range. In an unstressed state, the solid block would have x and y components of its index of refraction equal, i.e., $n_x = n_y$ (Figure 2-2) and a beam of plane linearly polarized light impinging at an angle of rotation of 45° to the block axes would experience no rotation upon passing through the block. Static compression of the block along the x axis would cause an increase in the magnitude of n_x resulting in an absolute retardation of the velocity of the component of radiation (E_x) along the axis of compression. The phase difference or retardation φ in radians is given as

$$\varphi = \frac{2\pi l(n_x - n_y)}{\lambda} \tag{2-1}$$

where: $l \equiv$ path length of photoelastic medium

$n_x \equiv$ x component of refractive index

$n_y \equiv$ y component of refractive index

$\lambda \equiv$ wavelength of radiation

If the retardation $\varphi = N\pi$, where $N = 0, 2, 4, \ldots$, then the resultant total electric field radiation vector remains in phase (Figure 2-3 A). If the retardation $\varphi = N\pi$, where $N = 1, 3, 5, \ldots$, then E_x will be 180° out of phase with E_y. The plane of the resultant exiting radiation $\bar{\mathbf{E}} = E_x + E_y$ is perpendicular to the plane of the impinging radiation (Figure 2-3 B). Oscillating between 0 and π retardation of E_x provides parallel ($\parallel$) and perpendicular ($\perp$) linearly polarized radiation $\bar{\mathbf{E}}$ for MLD spectroscopy.

The amount of compression necessary to produce a specific retardation of E_x by $\varphi = \pi$ is necessarily wavelength dependent. Considering Figures 2-1, 2-2 and 2-3, a retardation of π corresponding to $\varphi = N\pi$, $N = 1$ for monochromatic polarized light of wavelength λ_1 is created by a specific amplitude of compression along the x axis. If the thickness of the photoelastic medium in the z direction is an integral value of λ_1 within the medium, say $m\lambda_1$, ($m = 1, 2, 3 \ldots$), then the number of oscillations parallel to the y axis (E_y component) made by a photon passing through the block is exactly m, since there is no retardation along the y axis. Retardation of the E_x component along the x axis caused by a compression specific enough to produce a rotation of 90° in the resultant radiation vector $\bar{\mathbf{E}}$ requires there be $(m\text{-}\frac{1}{2})\lambda_1$ oscillations of the photon along the x axis (E_x component). The E_x component lags one-half wavelength behind the E_y component on exit from the medium, and the resultant $\bar{\mathbf{E}}$ is rotated 90 degrees from the impinging $\bar{\mathbf{E}}$. Thus the retardation is termed $\lambda/2$ and is specific for λ_1 at n_{x1}.

For a different monochromatic radiation of wavelength λ_2 as is encountered while scanning the UV/Visible spectrum, the retardation $\varphi_{\lambda 2}$ of the E_x component of radiation at n_{x1} will differ from $\varphi_{\lambda 1}$ upon exiting the block. The phase difference of the x-component of the radiation vector $\bar{\mathbf{E}}$ will no longer be exactly π. To compensate for this, the amplitude of mechanical compression on the block along the x axis needs to be altered to achieve n_{x2}, thus either further increasing n_x for longer wavelengths by increasing the amplitude of compression, or decreasing n_x for shorter wavelengths by decreasing the amplitude of compression.

Extending this concept of static compression to a dynamic oscillation allows the generation of light which essentially rotates its plane of polarization around the axis of propagation in synchronization with the oscillation frequency of the birefringent block, first in one direction, then the other. This device is known as a photoelastic modulator (PEM). With nonspecific amplitude control applied to the modulated block, the output is typically elliptical in cross-section. If the amplitude of compression (and corresponding rarefaction) is controlled such that for monochromatic radiation of wavelength λ the retardation of the x component of radiation (E_x) is $\pm\frac{1}{4}\lambda$ (equivalent to a phase shift of $\pi/2$), then the resultant of E_x and E_y exiting the block at maximum compression ($+\frac{1}{4}\lambda$) and distension ($-\frac{1}{4}\lambda$) will have constant amplitude and thus a circular cross-section (Figure 2-3 C). This is defined as circularly polarized radiation. Experimentally this amplitude control requires electronic circuitry which adjusts the oscillation amplitude of the acoustic transducer axially distorting the photoelastic block. The amplitude required is a function of the wavelength of monochromatic light impinging on the PEM. The modulation of the block oscillates through a phase of compression (elliptically polarized radiation (EP)) to n_x maximum (circularly polarized (CP) radiation), rarefaction through neutral ($n_x = n_y \equiv$ plane polarization), to distension (elliptically polarized (EP) radiation) to n_x minimum (circularly polarized (CP) radiation), then back to neutral and repeats itself. The plane of polarization of radiation exiting the block rotates first in one direction (right EP or CP) during the phase when $n_x > n_y$ and then in the other direction (left EP or CP) during the period when $n_x < n_y$.[47,48] Mathematical expressions describing the electric and magnetic field vectors of CP radiation propagating along z are given as follows from the solutions of Maxwell's equations of electrodynamics[28,33-35]. Propagation is along the z axis (Figures 2-1, 2-2 and 2-3) and the system is isotropic in the x-y plane.

$$\vec{\mathbf{E}}_{\pm}(z,t) = E_0^0 \exp[2\pi i\nu(t - \frac{\hat{n}\pm z}{c})](\vec{\mathbf{i}} \pm i\vec{\mathbf{j}}) \tag{2-2}$$

$$\vec{\mathbf{H}}_{\pm}(z,t) = (\frac{\hat{n}\pm}{\hat{\mu}}) E_0^0 \exp[2\pi i\nu(t - \frac{\hat{n}\pm z}{c})](\mp i\vec{\mathbf{i}} + \vec{\mathbf{j}}) \tag{2-3}$$

where: $\vec{\mathbf{E}} \equiv$ electric field vector of radiation

$\vec{\mathbf{H}} \equiv$ magnetic field vector of radiation

$\vec{\mathbf{i}}, \vec{\mathbf{j}} \equiv$ unit vectors along x and y axes respectively

$E_0^0 \equiv$ amplitude of electric displacement

$\nu \equiv$ frequency of radiation

$t \equiv$ time

$\hat{n}_{\pm} \equiv$ complex refractive index for RCP and LCP, respectively

$\hat{\mu} \equiv$ complex magnetic permeability in x-y plane

$z \equiv$ path length

$c \equiv$ velocity of light in vacuo

Again, the radiation is circularly polarized only at maximum compression and maximum distension for amplitude modulation appropriate to produce ±¼ λ retardation. It is at these positions that an appropriate lock-in amplifier must be synchronized with the transmitted intensity collected at the photomultiplier (PM) tube at the PEM frequency (50 kHz) to detect differential absorption for purposes of MCD. For MLD the lock-in synchronization is at twice the PEM frequency (100 kHz) and the wavelength retardation is ±½ λ.

Magnetic Circular Dichroism

The Lambert (Equations 2-4, 2-5) and Beer Laws (Equations 2-6, 2-7) describe the relationship between the absorbed radiation and the sample concentration and path length. Applying these laws to an absorbing system requires consideration of the limitations of the laws.[27,33,49]

$$\ln\frac{I_0}{I} = \kappa z = \frac{4\pi v k z}{c} \tag{2-4}$$

$$I = I_0 \exp\left(\frac{-4\pi v k z}{c}\right) \tag{2-5}$$

$$\ln\frac{I_0}{I} = \kappa'[c] \tag{2-6}$$

$$I = I_0 \exp\left(-\kappa'[c]\right) \tag{2-7}$$

where κ, κ' ≡ frequency dependent absorption coefficients

z ≡ path length of the sample along z axis of radiation propagation

$[c]$ ≡ concentration of the absorbing solute in the sample

I_0 ≡ initial intensity of radiation entering the sample

I ≡ intensity of radiation at any point within the sample

k ≡ absorption coefficient of medium in z direction

v ≡ frequency of radiation

c ≡ velocity of light in vacuo

In order for Equations 2-4 and 2-6 to be valid, κ must be independent of the path length and radiation intensity and κ' must be independent of the concentration and radiation intensity. Uniform distribution of the absorber throughout the sample to achieve homogeneity should preclude any dependence on path length. The interaction between adjacent absorbers and between absorbers and solvent must be zero for κ' to apply exactly. Ideally this means the absorber must be isolated in dilute gas phase infinitely separated from its nearest neighbor. Sufficiently low concentrations of absorbing solute in solution (gas, liquid, or solid phase) can approach a very good approximation to ideality. Independence of the effects of radiation intensity requires the normal Boltzmann distribution of populated energy levels not be perturbed by the applied radiation. This is not a problem at typically applied radiation intensities in spectroscopic measurements. Combining Equations 2-4 and 2-6 gives the classic Beer-Lambert Law

$$\ln\frac{I_0}{I} = \alpha[c]z \tag{2-8}$$

where $\alpha \equiv$ absorption coefficient independent of concentration and path length

In common logarithm base the expression is

$$\log\frac{I_0}{I} = \varepsilon[c]z \equiv \mathrm{A} \tag{2-9}$$

where $\varepsilon \equiv$ molar extinction coefficient

A ≡ absorbance or optical density (OD)

Magnetic circular dichroism is induced by a magnetic field and is the difference in absorption by a substance within the field of left and right circularly polarized light propagating parallel to and coaxially with the magnetic field. It is a manifestation of the

Faraday effect[41] (magnetic optical rotation (MOR)) in which the plane of polarization of linearly polarized light is rotated on passage through a substance in a magnetic field with nonzero magnetic component parallel to the light beam. Since linearly polarized light can be separated into components of left and right circularly polarized light (Equations 2.2 and 2.3), the MOR effect is the difference in refractive indices between left and right circularly polarized radiation. Natural optical activity is measured similarly and is known as optical rotatory dispersion (ORD) as a function of wavelength. The counterpart measurement of differential absorption of LCP and RCP radiation as a function of wavelength is called natural circular dichroism (CD) in the absence of a magnetic field, magnetic circular dichroism in the presence of one. If the ORD is known explicitly, then the CD can be calculated from Kramers-Kronig transforms,[43] and vice versa. An attempt to relate the natural optical activity to a physical interpretation at the atomic/molecular level visualizes the coercion of electrons of dissymmetric species to move in a helical path on excitation. The direction of rotation of this helix then preferentially favors either LCP or RCP absorption[28]. In natural optical activity, however, LCP and RCP radiation both interact equivalently with the absorber and the differential absorption is a consequence of molecular asymmetry. Magnetic optical activity results from perturbation of the electronic states of the absorber by the magnetic field and although the mechanism of interaction may be the same, the necessity of molecular asymmetry to produce the effect is no longer required.

Development of the theoretical treatment of magnetic circular dichroism is restricted to dilute, rigid impurities (absorbers) isolated in crystalline solids. The absorption is considered localized at the impurity. Application of the Beer-Lambert Law to the measurement of absorption phenomena in low temperature solid matrices requires that the experimental parameters be controlled to remain satisfactorily within the assumptions inherent in the law. Solute concentrations are a function of the rate of codeposition of the solute with the solvent. Control of these rates to give a solute:solvent ratio of $1{:}10^3$ to $1{:}10^5$ results in concentrations adequate for study without any indication of solute-solute interaction. Solute-solvent interactions, although considered minimal at first approximation, nevertheless exist. It is precisely these interactions that are the focus of the present study. Fluctuations in the rate of deposition to solid phase can also create local inhomogeneities in the matrix. Control of the solute/solvent ratios to $1{:}10^3$ - $1{:}10^5$ has not demonstrated any observable problem due to these local inhomogeneities.

The approach to describing MCD theory is typically semi-classical: classical radiation theory is applied to quantum-mechanical absorbers. It has been thoroughly addressed by Piepho and Schatz,[33] Schatz and McCaffery,[43] Stephens,[27,28] and Osborne and Stephens[49] as extensions of the theory of Henry, Schnatterly, and Schlichter[50] and Mort, Luty, and Brown.[51] In this thesis it will be described in terms of the Faraday effect[41] coupled with the closely related Zeeman effect.[30]

The degeneracy of an atom in electronic state **J** is $2J + 1$ when no external magnetic field is present. Angular momentum in atomic systems is specified by **J** and $\mathbf{M_J}$ quantum numbers, where **J** is the total angular momentum of the atom and $\mathbf{M_J}$ is the z component of the total angular momentum.[42,43,52] The total orbital angular momentum is specified by **L**, the sum of the individual orbital angular momenta. The total spin angular momentum is denoted by **S**, the sum of the individual spin angular momenta. There are two methods for describing the angular momentum attributable to movement of the electrons in an atom:

- Russell-Saunders coupling, also known as **L-S** coupling
- **J, J** coupling.

Russell-Saunders coupling sums the total **L** and **S** angular momenta separately and considers their effects as independent of each other. **L-S** coupling is generally applicable to atoms of low to moderate atomic weight and permits separate consideration of the individual orbital angular momentum of an electron from its spin angular momentum. In heavy atoms ($Z > \sim 85 - 90$) the interactions of electrons to produce a total spin for each state has a significant perturbation on the energy levels of each state relative to those implied by Russell-Saunders coupling. Consideration of these effects is required to accurately describe the atomic angular momentum in terms of the total angular momentum of each electron. This method is referred to as **J, J** coupling. The Russell-Saunders **L-S** coupling scheme will be utilized to describe the angular momentum of the atoms discussed in this thesis (Fe, Ni, and Kr) due to their moderate atomic weights. The coupling scheme according to the Russell-Saunders method is

$$\mathbf{J} = \Sigma l_i + \sum s_i = \mathbf{L} + \mathbf{S} \tag{2-10}$$

$$\mathrm{M_J} = \mathbf{J}, \mathbf{J} - 1, \mathbf{J} - 2, \mathbf{J} - 3, \ldots, 0, \ldots, -\mathbf{J} + 1, -\mathbf{J} \tag{2-11}$$

where: $l_i \equiv$ orbital angular momentum of individual electron i

$s_i \equiv$ spin angular momentum of individual electron i

Application of an external magnetic field alters the potential energy of the 2J + 1 degenerate orbitals, rendering them nonequivalent under the field perturbation. Electronic transitions between these nondegenerate ground and/or excited states are restricted by quantum theory to $\Delta\mathbf{L} = \pm1$, $\Delta\mathbf{J} = \pm1$, $\Delta\mathbf{M}_J = 0, \pm1$. In order to understand the selection rules for Zeeman splitting, consider the three possible transitions between states $\mathbf{J}_{\text{initial}} = 0$ and $\mathbf{J}_{\text{final}} = 1$ for linearly polarized electric dipole radiation both parallel and perpendicular to the magnetic field (Figure 1-4). The transition for $\Delta\mathbf{J} = +1$, $\Delta\mathbf{M}_J = 0$ in a magnetic field along the z axis is not changed in energy from the same transition in an unperturbed system in zero magnetic field exhibiting absorption with parallel radiation. This reflects total electronic polarization in the z direction of the applied field, i.e., for $\Delta\mathbf{J} = +1$, $\Delta\mathbf{M}_J = 0$, there is no transverse component of the orbital angular momentum vector and thus no interaction with the magnetic field is possible. The transitions for $\Delta\mathbf{M}_J = \pm1$ both exhibit energy changes consistent with electronic polarization components perpendicular to the magnetic field and of opposite direction, absorbing energy when radiation is applied perpendicular to the z axis. These results can be quantitatively determined from quantum-mechanical calculations. This phenomenon is the basis for magnetic linear dichroism, which will be discussed in the following pages.

Figure 1-4 also displays the selection rules based on circularly polarized light for $\Delta\mathbf{L} = +1$, $\Delta\mathbf{J} = +1$. Again, quantum-mechanical methods may be used to arrive at the appropriate selection rules, but a qualitative assessment presents a better physical understanding of the process. Thermodynamic considerations requiring the conservation of angular momentum within a system imply that RCP and LCP photons possess angular momentum of $\mathbf{J} = 1$, $\mathbf{M}_J = +1$ and $\mathbf{J} = 1$, $\mathbf{M}_J = -1$ respectively. When absorbed radiation is spontaneously emitted from a system, there must be a change of at least 1 unit of total angular momentum (i.e., $\Delta\mathbf{J} = \pm 1$). The emitted radiation must necessarily possess that difference in energy as a net increase of its own angular momentum. Extending the previous discussions to a $^{1}\mathbf{P}\leftarrow{}^{1}\mathbf{S}$ transition allows prediction of the spectral dispersion $f(\mathcal{E})$, which describes the bandshape of the absorption as a function of radiation wavelength. Figure 2-4 shows the origin of the spectral dispersion $f(\mathcal{E})$ which is designated the Faraday $\mathcal{A}$ term (Figure 2-4 C). It can be seen in the figure how the relation between signs of transitions reflect the energy levels of the system. It is necessary for at least one state in the transition, either initial or final, or both, to be degenerate to produce an $\mathcal{A}$ term. If the ground state is nondegenerate, the term is temperature independent. If the ground state is normally degenerate in the absence of a magnetic field, as in Figure 2-5 for $^{1}\mathbf{S}_{0}\leftarrow{}^{1}\mathbf{P}_{1,0,-1}$, then the presence of an external magnetic field **B** splits that degeneracy and thus a temperature dependence based on a Boltzman population distribution of the ground state levels is reflected in the spectrum. As T decreases, the population of the lowest state $^{1}\mathbf{P}_{-1}$ increases and that of $^{1}\mathbf{P}_{0}$ and $^{1}\mathbf{P}_{+1}$ decreases. The intensity of the transition $^{1}\mathbf{S}_{0}\leftarrow{}^{1}\mathbf{P}_{-1}$ increases proportional to the inverse of temperature while that of $^{1}\mathbf{S}_{0}\leftarrow{}^{1}\mathbf{P}_{+1}$ decreases. The net dispersion $f(\mathcal{E})$ shifts in both intensity and average energy. Although this type of absorption band due to transitions from a temperature dependent differentially populated ground state is basically of type $\mathcal{A}$, the significant contribution made to its shape by the temperature dependence justifies classifying it separately as a Faraday $\mathcal{C}$ term (Figure 2-5 C). It should also be noted that $\mathcal{C}$ terms show a magnetic field dependence on population since increasing the field strength

strength at a given temperature increases the Zeeman separation between **M_J** levels of the ground state, thereby increasing the population of the lowest states. This effect is especially appreciable as the magnitude of the Zeeman energy, $g\mu_B B_z$, approaches and then surpasses kT.

A third Faraday parameter, the $\mathcal{B}$ term in Figure 2-6 B, is identified with transitions arising from magnetic field mixing of nearby energy levels with the excited state **J** **(J_f)** or ground state **A** **(J_i)**. These nearby states (**K, L, M, N** in Figure 2-6 A) have a magnetic dipole transition moment between themselves and excited state **J** which is induced by the magnetic field. This transition moment varies as the inverse of the energy difference between the states (i.e., very nearby states mix more strongly than those farther away in energy). Thus, they 'mix', or combine linearly with state **J** resulting in an induced degeneracy of mixed states in the excited state. This results in a weak absorption (Figure 2-6 B). The structure of the $\mathcal{B}$ term is like the $\mathcal{C}$ term, but is typically much weaker in intensity. It has no temperature dependence. The normal energy separations between adjacent electronic levels (ΔW) is on the order of 10^4 cm^{-1}. Bandwidths measured at half maximum intensity (FWHM $\equiv \Gamma$) are typically around 10^3 cm^{-1} at room temperature. Setting the Zeeman energy $E_z = 1$ cm^{-1} for a typical magnetic field intensity field of ~ 0.1 T, $\Gamma = 10^3$ cm^{-1}, $\Delta W = 10^4$ cm^{-1} and $kT = 200$ cm^{-1} at room temperature, the theoretical relative intensities of the terms for a paramagnetic species are[29]

$$\mathcal{A} : \mathcal{B} : \mathcal{C} :: \approx \frac{E_z}{\Gamma} : \frac{E_z}{\Delta W} : \frac{E_z}{kT} :: \approx 10^{-3} : 10^{-4} : 5 \text{ x } 10^{-3} :: 10 : 1 : 50 \qquad (2\text{-}12)$$

The resultant general expression for MCD is given as

$$\frac{\Delta A_c}{\mathcal{E}} = \gamma_{\pm} \sum_{a,j} \frac{N_a}{N} \left[\left|\langle a|\hat{m}_-|j\rangle\right|_2 - \left|\langle a|\hat{m}_+|j\rangle\right|^2 \right] \delta\ (\mathcal{E}_{ja} - \mathcal{E})\ [c]\, z \qquad (2\text{-}13)$$

where $\gamma_{\pm} = \dfrac{2N_0\,\pi^3\,\alpha^2\, c\, l \log_{10} e}{250\, h\, c\, n}$

A parametric description of the MCD dispersion which is applicable to the linear limit region is

$$\frac{\Delta A_C}{\mathcal{E}} = \gamma \left\{ A_1 \left(-\frac{\partial f(\mathcal{E})}{\partial \mathcal{E}} \right) + \left(B_0 + \frac{C_0}{kT} \right) f(\mathcal{E}) \right\} \mu_B B_z\, [c]\, z \qquad (2\text{-}14)$$

The parameters A_1, B_0, and C_0 (Equations 2-15) are representative of the contributions from the Faraday $\mathcal{A}$, $\mathcal{B}$, and $\mathcal{C}$ transitions depicted in Figures 2-4, 2-5, and 2-6 for electronic MCD transitions from ground state A_α to excited state J_λ. The subscripts 0 and 1 are indicative of the contribution to the bandshape, with 0 representing a bandshape that is proportional to the zeroth order derivative of $f(\mathcal{E})$ and 1 representing proportionality to the first derivative of $f(\mathcal{E})$. The first derivative structure of the $\mathcal{A}$ term is clearly evident in Figure 2-4 C, while in the $\mathcal{C}$ term of Figure 2-5 C the derivative structure from any pure $\mathcal{A}$ term contribution is diluted by the more intense contribution of the temperature dependence of the lower energy transition from the lowest ground state.

$$A_1 = \frac{1}{d_A} \sum_{\alpha,\lambda} \left[\left|\langle A_\alpha|\hat{m}_-|\ J_\lambda\rangle^0\right|^2 - \left|\langle A_\alpha|\hat{m}_+|\ J_\lambda\rangle^0\right|^2 \right] \left[\langle J_\lambda|L_z + 2S_z|\ J_\lambda\rangle^0 - \langle A_\alpha|L_z + 2S_z|A_\alpha\rangle^0 \right]$$

$$B_0 = -\frac{2}{d_A} \sum_{\alpha,\lambda} \Re e \left\{ \sum_{K_\kappa \neq J} \left[\langle A_\alpha|\hat{m}_-|\ J_\lambda\rangle^0 \langle K_\kappa|\hat{m}_+|A_\alpha\rangle^0 - \langle A_\alpha|\hat{m}_+|\ J_\lambda\rangle^0 \langle K_\kappa|\hat{m}_-|A_\alpha\rangle^0 \right] \frac{\langle J_\lambda|L_z + 2S_z|K_\kappa\rangle^0}{W_K^0 - W_J^0} \right.$$

$$\left. + \sum_{K_\kappa \neq A} \left[\langle A_\alpha|\hat{m}_-|\ J_\lambda\rangle^0 \langle J_\lambda|\hat{m}_+|\ K_\kappa\rangle^0 - \langle A_\alpha|\hat{m}_+|\ J_\lambda\rangle^0 \langle J_\lambda|\hat{m}_-|\ K_\kappa\rangle^0 \right] \frac{\langle K_\kappa|L_z + 2S_z|A_\alpha\rangle^0}{W_K^0 - W_J^0} \right\}$$

$$C_0 = \frac{1}{d_A} \sum_{\alpha,\lambda} \left[\left|\langle A_\alpha|\hat{m}_-|J_\lambda\rangle^0\right|^2 - \left|\langle A_\alpha|\hat{m}_+|J_\lambda\rangle^0\right|^2 \right] \langle A_\alpha|L_z + 2S_z|A_\alpha\rangle^0$$

(2-15)

where $\hat{m}_{\pm} = \frac{1}{\sqrt{2}}(\hat{m}_x \pm i\hat{m}_y)$

$\hat{m}_x \equiv$ electric dipole transition moment along x axis (for **B** along z)

$\hat{m}_y \equiv$ electric dipole transition moment along y axis (for **B** along z)

$\hat{m}_- \equiv$ electric dipole transition moment for left CP radiation

$\hat{m}_+ \equiv$ electric dipole transition moment for right CP radiation

$d_A \equiv$ degeneracy of state A

$W_K^0, W_J^0 \equiv$ energies of state levels K_κ and J_λ

A treatise by Henry, Schnatterly, and Slichter[50] depicts an approach to analyzing the band shapes in terms of moments values similar to the approach of Van Vleck's application to nuclear magnetic resonance studies.[53] Actual determination of an expression for the line shape $f(\mathcal{E})$ may be impractical, or impossible, but determinations of moments values can be computed exactly since they can be expressed as diagonal sums. Moments apply a weighted analysis to the asymmetrical structure of a band centered about its mean and characterized by its asymmetry, skewness, kurtosis, etc. The higher the order of the moment, the more significant the contribution to the magnitude of the moment due to asymmetry in the wings of the transition band.[28,32]

$$\langle A \rangle_n = \int \left(\frac{A}{\nu}\right) (\nu - \nu_0)^n \, d\nu \tag{2-16}$$

$$\langle \Delta A \rangle_n = \int \left(\frac{\Delta A}{\nu}\right) (\nu - \nu_0)^n \, d\nu \tag{2-17}$$

$$\nu_0 = \frac{\int A \, d\nu}{\int \frac{A}{\nu} \, d\nu} \tag{2-18}$$

where n signifies the order of the moment

The reduced moment expression for MCD is arrived at by dividing $\langle \Delta \mathrm{A} \rangle_n$ by the zeroth moment of absorption, which is simply the integrated area under the band

$$\frac{\langle \Delta \mathrm{A}_c \rangle_n}{\langle \mathrm{A} \rangle_0} = \left(A_n + B_n + \frac{C_n}{kT} \right) \frac{\mu_\mathrm{B} \mathrm{B}_\mathrm{z}}{D_0} \tag{2-19}$$

D_0 is determined from the zero field absorption

$$\frac{\mathrm{A}_\pm^0}{\varepsilon} = \gamma_\pm \, D_0 \, f(\mathscr{E})[c]z$$

$$D_o = \frac{1}{2d_\mathrm{A}} \sum_{\alpha,\lambda} \left[\left| \langle \mathrm{A}_\alpha | \hat{\mathrm{m}}_+ | \mathrm{J}_\lambda \rangle^0 \right|^2 - \left| \langle \mathrm{A}_\alpha | \hat{\mathrm{m}}_- | \mathrm{J}_\lambda \rangle^0 \right|^2 \right] \tag{2-20}$$

The application of these equations to linear limit MCD data permits the evaluation of contributions due to spin-orbit coupling and cubic or noncubic lattice mode vibrations. The magnitude of the excited state g_{orb} value can also be approximated. As an example , consider the moments ratios for the $^2\mathrm{P} \leftarrow {}^2\mathrm{S}$ transition for Cu, Ag, and Au[41]

$$\frac{\langle \Delta \mathrm{A}_\mathrm{C} \rangle_1}{\langle \mathrm{A} \rangle_0} = 2\mu_\mathrm{B} \mathrm{B}_\mathrm{z} \left(\mathrm{g}_\mathrm{orb} - \frac{a_s \, \zeta}{kT} \right) \tag{2-21}$$

$$\frac{\langle \mathrm{A}_\mathrm{C} \rangle_2}{\langle \mathrm{A} \rangle_0} = \langle \mathrm{E}^2 \rangle_\mathrm{C} + \langle \mathrm{E}^2 \rangle_\mathrm{NC} + a_S \, \zeta^2 \tag{2-22}$$

$$\frac{\langle \Delta \mathrm{A}_\mathrm{C} \rangle_3}{\langle \mathrm{A} \rangle_0} = 6\mu_\mathrm{B} \mathrm{B}_\mathrm{z} \left(\mathrm{g}_\mathrm{orb} - \frac{a_S \zeta}{kT} \right) \left(\langle \mathrm{E}^2 \rangle_\mathrm{C} + \frac{\langle \mathrm{E}^2 \rangle_\mathrm{NC}}{2} + \frac{a_S \zeta^2}{2} \right) \tag{2-23}$$

where $\mathrm{g}_\mathrm{orb} \equiv$ excited state orbital Landè g factor

$\zeta \equiv$ spin orbit coupling constant between $^2\mathrm{P}_{1/2}$ and $^2\mathrm{P}_{3/2}$

$\langle \mathrm{E}^2 \rangle_\mathrm{C} \equiv$ cubic lattice mode contribution

$\langle \mathrm{E}^2 \rangle_\mathrm{NC} \equiv$ noncubic lattice mode contribution

$$a_\mathrm{S} = \left(\frac{kT}{\mu_\mathrm{B} \mathrm{B}_\mathrm{z}} \right) \left(\frac{1}{(2\mathrm{S}+1)} \right) \sum_{m_\mathrm{S}} m_\mathrm{S} \, \exp\left(- \frac{m_s g \mu_\mathrm{B} \mathrm{B}_\mathrm{z}}{kT} \right)$$

$\mathrm{m_s} \equiv$ z component of spin orbit quantum number

The MCD intensity is proportional to **B** and 1/T. Changes in these are followed directly by experiment as a perturbation is applied. Henry, Schnatterly, and Slichter[50] formulated their approach concentrating on orbitally singlet ground states undergoing electronic transitions to degenerate excited states. The dependence of the interaction between the excited electrons and the lattice atoms was assumed to be linear, and mixing of nondegenerate electronic states was ignored. The information about the embedded solute atom obtainable from this method is broad in scope. The band area remains constant and electron-lattice interactions have no effect on the first and second moments. The first moment is dependent on the magnitude of the spin orbit coupling and thus leads to the determination of the SO coupling constant ζ. Any *f*-band broadening caused by cubic and noncubic lattice vibrations permits determination of the relative contributions made by each of these modes from the second moment and changes in the third moment.

Magnetic Linear Dichroism

The extension to linear dichroism (LD) is made by accounting for the differential absorption of linearly polarized light parallel and perpendicular with respect to the absorbing center. In the presence of a magnetic field perpendicular to the incident radiation it is termed magnetic linear dichroism (MLD) given by the general expression

$$\frac{\Delta \mathrm{A_L}}{\mathcal{E}} = \gamma_{\pm} \sum_{\mathrm{a,j}} \frac{\mathrm{N_a}}{\mathrm{N}} \left[\left| \langle \mathrm{A}_\alpha | \hat{\mathrm{m}}_{\parallel} | \mathrm{J}_\lambda \rangle^0 \right|^2 - \left| \langle \mathrm{A}_\alpha | \hat{\mathrm{m}}_{\perp} | \mathrm{J}_\lambda \rangle^0 \right|^2 \right] \delta(\mathcal{E}_{ja} - \mathcal{E})\ [c]\, z \qquad (2\text{-}24)$$

Development of a parametric expression for the MLD dispersion is characterized by six parameters (A_2, B_1, C_1, E_0, F_0, and G_0) as opposed to the three (A_1, B_0, and C_0) for MCD.[29,33] Each is representative of the contributions to $f(\mathcal{E})$ by the Faraday parameters $\mathfrak{A}$, $\mathfrak{B}$, $\mathfrak{C}$, $\mathfrak{E}$, $\mathfrak{F}$, and $\mathfrak{G}$ for MLD, the subscript denoting the order of differentiation (2 for second order, etc).

$$\frac{\Delta \mathrm{A_L}}{\mathscr{E}} = \gamma \left\{ A_2 \left(\frac{1}{2} \frac{\partial^2 f(\mathscr{E})}{\partial \mathscr{E}^2} \right) + \left[B_1 + \frac{C_1}{kT} \right] \left(- \frac{\partial f(\mathscr{E})}{\partial \mathscr{E}} \right) + \left[E_0 + \frac{F_0}{kT} + \frac{G_0}{k^2T^2} \right] f(\mathscr{E}) \right\} \mathrm{B_z}^2 [c] z \tag{2-25}$$

where

$$A_2 = \frac{1}{d_\mathrm{A}} \sum_{\alpha,\lambda} \left(\left| \langle \mathrm{A}_\alpha | \hat{\mathrm{m}}_\parallel | \mathrm{J}_\lambda \rangle^0 \right|^2 - \left| \langle \mathrm{A}_\alpha | \hat{\mathrm{m}}_\perp | \mathrm{J}_\lambda \rangle^0 \right|^2 \right) \left(\langle \mathrm{J}_\lambda | \hat{\mu}_z | \mathrm{J}_\lambda \rangle^0 - \langle \mathrm{A}_\alpha | \hat{\mu}_z | \mathrm{A}_\alpha \rangle^0 \right)^2$$

$$B_1 = \frac{2}{d_\mathrm{A}} \sum_{\alpha,\lambda} \Re\mathrm{e} \left[\langle \mathrm{A}_\alpha | \hat{\mathrm{m}}_\parallel | \mathrm{J}_\lambda \rangle^0 \left(\sum_{\mathrm{K}_\kappa \neq \mathrm{J}} \frac{\langle \mathrm{A}_\alpha | \hat{\mathrm{m}}_\parallel | \mathrm{K}_\kappa \rangle^0 \, \langle \mathrm{K}_\kappa | \hat{\mu}_z | \mathrm{J}_\lambda \rangle^0}{\mathrm{W}_\mathrm{K}^0 - \mathrm{W}_\mathrm{J}^0} + \sum_{\mathrm{K}_\kappa \neq \mathrm{A}} \frac{\langle \mathrm{A}_\alpha | \hat{\mu}_z | \mathrm{K}_\kappa \rangle^0 \, \langle \mathrm{K}_\kappa | \hat{\mathrm{m}}_\parallel | \mathrm{J}_\lambda \rangle^0}{\mathrm{W}_\mathrm{K}^0 - \mathrm{W}_\mathrm{A}^0} \right) \right.$$

$$\left. - \langle \mathrm{A}_\alpha | \hat{\mathrm{m}}_\perp | \mathrm{J}_\lambda \rangle^0 \left(\sum_{\mathrm{K}_\kappa \neq \mathrm{J}} \frac{\langle \mathrm{A}_\alpha | \hat{\mathrm{m}}_\perp | \mathrm{K}_\kappa \rangle^0 \, \langle \mathrm{K}_\kappa | \hat{\mu}_z | \mathrm{J}_\lambda \rangle^0}{\mathrm{W}_\mathrm{K}^0 - \mathrm{W}_\mathrm{J}^0} + \sum_{\mathrm{K}_\kappa \neq \mathrm{A}} \frac{\langle \mathrm{A}_\alpha | \mu_z | \mathrm{K}_\kappa \rangle^0 \, \langle \mathrm{K}_\kappa | \hat{\mathrm{m}}_\perp | \mathrm{J}_\lambda \rangle^0}{\mathrm{W}_\mathrm{K}^0 - \mathrm{W}_\mathrm{A}^0} \right)^2 \langle \mathrm{A}_\alpha | \mu_z | \mathrm{A}_\alpha \rangle^0 \right]$$

$$\mathrm{x} \ \left(\langle \mathrm{J}_\lambda | \hat{\mu}_z | \mathrm{J}_\lambda \rangle^0 - \langle \mathrm{A}_\alpha | \hat{\mu}_z | \mathrm{A}_\alpha \rangle^0 \right)$$

$$C_1 = \frac{1}{d_\mathrm{A}} \sum_{\alpha,\lambda} \left(\left| \langle \mathrm{A}_\alpha | \hat{\mathrm{m}}_\parallel | \mathrm{J}_\lambda \rangle^0 \right|^2 - \left| \langle \mathrm{A}_\alpha | \hat{\mathrm{m}}_\perp | \mathrm{J}_\lambda \rangle^0 \right|^2 \right) \left(\langle \mathrm{J}_\lambda | \hat{\mu}_z | \mathrm{J}_\lambda \rangle^0 - \langle \mathrm{A}_\alpha | \hat{\mu}_z | \mathrm{A}_\alpha \rangle^0 \right) \langle \mathrm{A}_\alpha | \hat{\mu}_z | \mathrm{A}_\alpha \rangle^0$$

$$E_0 = \frac{1}{d_\mathrm{A}} \sum_{\alpha,\lambda} \left[\left(\sum_{\mathrm{K}_\kappa \neq \mathrm{J}} \frac{\langle \mathrm{A}_\alpha | \hat{\mathrm{m}}_\parallel | \mathrm{K}_\kappa \rangle^0 \, \langle \mathrm{K}_\kappa | \hat{\mu}_z | \mathrm{J}_\lambda \rangle^0}{\mathrm{W}_\mathrm{K}^0 - \mathrm{W}_\mathrm{J}^0} + \sum_{\mathrm{K}_\kappa \neq \mathrm{A}} \frac{\langle \mathrm{A}_\alpha | \hat{\mu}_z | \mathrm{K}_\kappa \rangle^0 \, \langle \mathrm{K}_\kappa | \hat{\mathrm{m}}_\parallel | \mathrm{J}_\lambda \rangle^0}{\mathrm{W}_\mathrm{K}^0 - \mathrm{W}_\mathrm{A}^0} \right)^2 \right.$$

$$\left. - \left(\sum_{\mathrm{K}_\kappa \neq \mathrm{J}} \frac{\langle \mathrm{A}_\alpha | \hat{\mathrm{m}}_\perp | \mathrm{K}_\kappa \rangle^0 \, \langle \mathrm{K}_\kappa | \hat{\mu}_z | \mathrm{J}_\lambda \rangle^0}{\mathrm{W}_\mathrm{K}^0 - \mathrm{W}_\mathrm{J}^0} + \sum_{\mathrm{K}_\kappa \neq \mathrm{A}} \frac{\langle \mathrm{A}_\alpha | \hat{\mu}_z | \mathrm{K}_\kappa \rangle^0 \, \langle \mathrm{K}_\kappa | \hat{\mathrm{m}}_\perp | \mathrm{J}_\lambda \rangle^0}{\mathrm{W}_\mathrm{K}^0 - \mathrm{W}_\mathrm{A}^0} \right)^2 \right]$$

$$F_0 = \frac{2}{d_\mathrm{A}} \sum_{\alpha,\lambda} \Re\mathrm{e} \left[\langle \mathrm{A}_\alpha | \hat{\mathrm{m}}_\parallel | \mathrm{J}_\lambda \rangle^0 \left(\sum_{\mathrm{K}_\kappa \neq \mathrm{J}} \frac{\langle \mathrm{A}_\alpha | \hat{\mathrm{m}}_\parallel | \mathrm{K}_\kappa \rangle^0 \, \langle \mathrm{K}_\kappa | \hat{\mu}_z | \mathrm{J}_\lambda \rangle^0}{\mathrm{W}_\mathrm{K}^0 - \mathrm{W}_\mathrm{J}^0} + \sum_{\mathrm{K}_\kappa \neq \mathrm{A}} \frac{\langle \mathrm{A}_\alpha | \hat{\mu}_z | \mathrm{K}_\kappa \rangle^0 \, \langle \mathrm{K}_\kappa | \hat{\mathrm{m}}_\parallel | \mathrm{J}_\lambda \rangle^0}{\mathrm{W}_\mathrm{K}^0 - \mathrm{W}_\mathrm{A}^0} \right) \right.$$

$$\left. - \langle \mathrm{A}_\alpha | \hat{\mathrm{m}}_\perp | \mathrm{J}_\lambda \rangle^0 \left(\sum_{\mathrm{K}_\kappa \neq \mathrm{J}} \frac{\langle \mathrm{A}_\alpha | \hat{\mathrm{m}}_\perp | \mathrm{K}_\kappa \rangle^0 \, \langle \mathrm{K}_\kappa | \hat{\mu}_z | \mathrm{J}_\lambda \rangle^0}{\mathrm{W}_\mathrm{K}^0 - \mathrm{W}_\mathrm{J}^0} + \sum_{\mathrm{K}_\kappa \neq \mathrm{A}} \frac{\langle \mathrm{A}_\alpha | \hat{\mu}_z | \mathrm{K}_\kappa \rangle^0 \, \langle \mathrm{K}_\kappa | \hat{\mathrm{m}}_\perp | \mathrm{J}_\lambda \rangle^0}{\mathrm{W}_\mathrm{K}^0 - \mathrm{W}_\mathrm{A}^0} \right)^2 \right]$$

$$G_0 = \frac{1}{2d_\mathrm{A}} \sum_{\alpha,\lambda} \left(\left| \langle \mathrm{A}_\alpha | \hat{\mathrm{m}}_\parallel | \mathrm{J}_\lambda \rangle^0 \right|^2 - \left| \langle \mathrm{A}_\alpha | \hat{\mathrm{m}}_\perp | \mathrm{J}_\lambda \rangle^0 \right|^2 \right) \left| \langle \mathrm{A}_\alpha | \hat{\mu}_z | \mathrm{J}_\lambda \rangle^0 \right|^2$$

(2-26)

D_0 is calculated from the zero field absorption the same as with MCD accounting for linearly polarized radiation

$$\frac{A^0_{\parallel,\perp}}{\mathcal{E}} = \gamma_{\parallel,\perp}\, D_0 f(\mathcal{E})[c]z$$

$$D_0 = \frac{1}{2\,d_{\mathrm{A}}}\sum_{\alpha,\lambda}\left[\left|\langle \mathrm{A}_\alpha|\hat{\mathrm{m}}_{\parallel}|\mathrm{J}_\lambda\rangle^0\right|^2 - \left|\langle \mathrm{A}_\alpha|\hat{\mathrm{m}}_{\perp}|\mathrm{J}_\lambda\rangle^0\right|^2\right] \tag{2-27}$$

Moments expressions for zeroth, first, and second order are

$$\langle \mathrm{A}_{\mathrm{L}}\rangle_0 = \gamma\,\frac{1}{kT}\left(F_0 + \frac{G_0}{kT}\right)\mathrm{B_z}^2\,[c]z \tag{2-28}$$

$$\langle \Delta\mathrm{A}_{\mathrm{L}}\rangle_1 = \gamma\left(B_1 + \frac{C_1}{kT}\right)\mathrm{B_z}^2\,[c]z \tag{2-29}$$

$$\langle \Delta\mathrm{A}_{\mathrm{L}}\rangle_2 = \gamma\left[A_2 + \;\rho\,\frac{1}{kT}\left(F_0 + \frac{G_0}{kT}\right)\right]\mathrm{B_z}^2\,[c]z \tag{2-30}$$

where for a band shape function $f(\mathcal{E})$ which is Gaussian

$$\rho = \frac{\Gamma^2}{(8\ \ln 2)} \tag{2-31}$$

where Γ is the band full width at half maximum (FWHM). Since $\langle \mathrm{A}_{\mathrm{L}}\rangle_0$ is the integrated area of the MLD absorption, it is seen from Equations 2-28 – 2-30 that the intensity of an MLD transition is proportional to both the square of the magnetic field and the inverse square of the temperature. Setting the Zeeman energy $E_z = 1\ \mathrm{cm}^{-1}$, $\Gamma = 10^3\ \mathrm{cm}^{-1}$, $\Delta W = 10^4\ \mathrm{cm}^{-1}$ and $kT = 200\ \mathrm{cm}^{-1}$ at room temperature gives

$$\mathfrak{A}:\mathfrak{B}:\mathfrak{C}:\mathfrak{E}:\mathfrak{F}:\mathfrak{G} \approx \frac{5\mathrm{E_z}}{\Gamma^2}:\frac{\mathrm{E_z}}{\Delta\mathrm{W}\,\Gamma}:\frac{\mathrm{E_z}}{\mathrm{kT}\,\Gamma}:\frac{\mathrm{E_z}}{(\Delta\mathrm{W})^2}:\frac{\mathrm{E_z}}{\mathrm{kT}\,\Delta\mathrm{W}}:\frac{\mathrm{E_z}}{(\mathrm{kT})^2}::500:10:500:1:50:2500 \tag{2-32}$$

The equations for MCD and MLD presented in this chapter are no longer valid at high magnetic fields and very low temperatures. The linearity of Equations 2-13, 2-20, 2-22, 2-24, and 2-28 – 2-30 breaks down under these conditions. In order to obtain an accurate analysis of experimental data collected in a low T/high **B** regime, extension to the concept of magnetic saturation is indicated. MCD and MLD spectral data acquired in the magnetic saturation regime permit evaluation of the metal-host environment at a much more sensitive level. In the following chapter the basic MCD and MLD theory just presented for the linear limit applications of low magnetic fields and moderately low temperatures is extended to liquid helium temperatures and below and to moderately high magnetic fields.

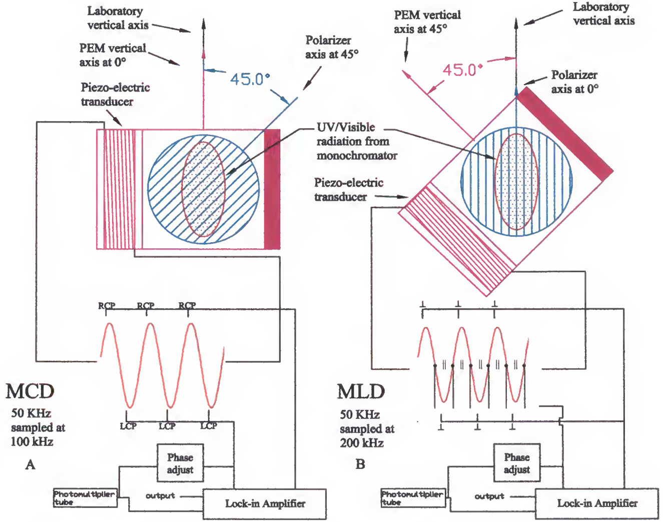

Figure 2-1. Configuration of polarizing filter and photoelastic modulator [PEM]. A) Orientation for MCD for RCP and LCP radiation with PEM modulation frequency of 50 kHz, locked at 50 kHz, sampled at 100 kHz. B) Orientation for MLD for parallel (||) and perpendicular (⊥) radiation with PEM modulation frequency of 50 kHz, locked at 100 kHz, sampled at 200 kHz.

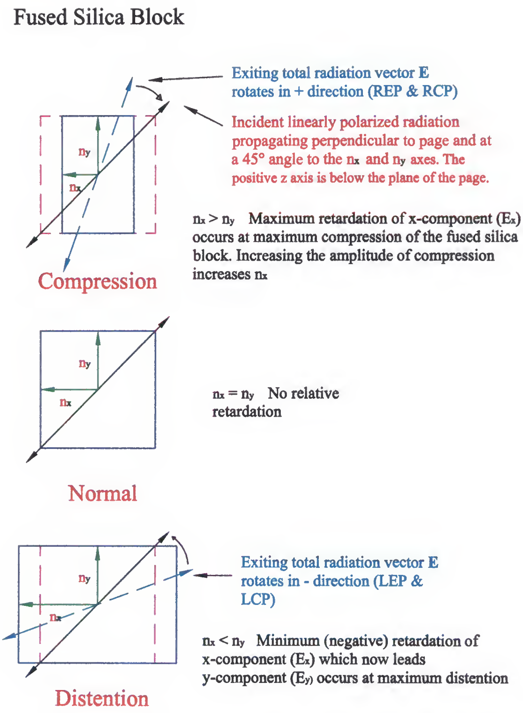

Exiting total radiation vector **E** rotates in + direction (REP & RCP)

Incident linearly polarized radiation propagating perpendicular to page and at a 45° angle to the n_x and n_y axes. The positive z axis is below the plane of the page.

$n_x > n_y$ Maximum retardation of x-component (E_x) occurs at maximum compression of the fused silica block. Increasing the amplitude of compression increases n_x

$n_x = n_y$ No relative retardation

Exiting total radiation vector **E** rotates in - direction (LEP & LCP)

$n_x < n_y$ Minimum (negative) retardation of x-component (E_x) which now leads y-component (E_y) occurs at maximum distention

Figure 2-2. Principle of photoelastic modulation. The generation of elliptically and circularly polarized radiation by acoustic modulation (50 kHz) of a fused silica block. The positive z axis extends below the plane of the page.

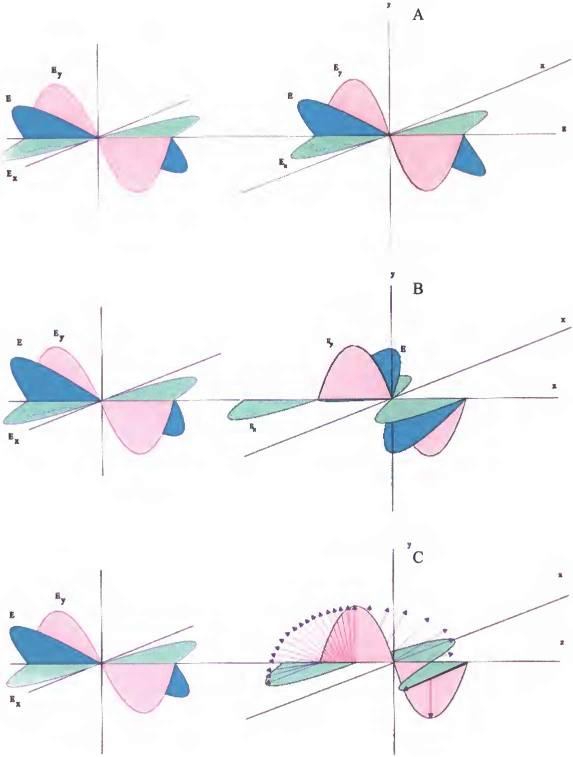

Figure 2-3. Components of electric and magnetic wave propagation through a photoelastic modulator. A) No relative retardation. B) λ/2 retardation for production of 90° phase-shifted LP radiation. C) λ/4 retardation for production of CP radiation.

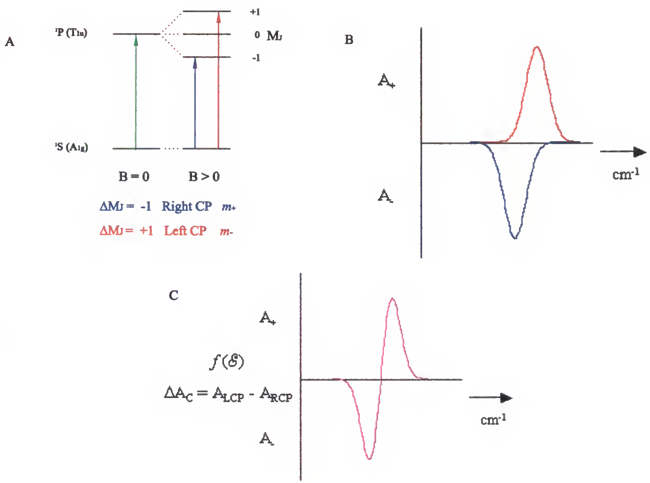

Figure 2-4. Origination of Faraday $\mathcal{A}$ term. A) Electronic transitions from a nondegenerate ^{1}S ground state to a degenerate ^{1}P excited state. B) Dispersions due to individual + and – transitions. C) Sum of + and – terms which appears in a spectrum as an $\mathcal{A}$ term, the resultant of which can be overall + or -, depending on the system under investigation.

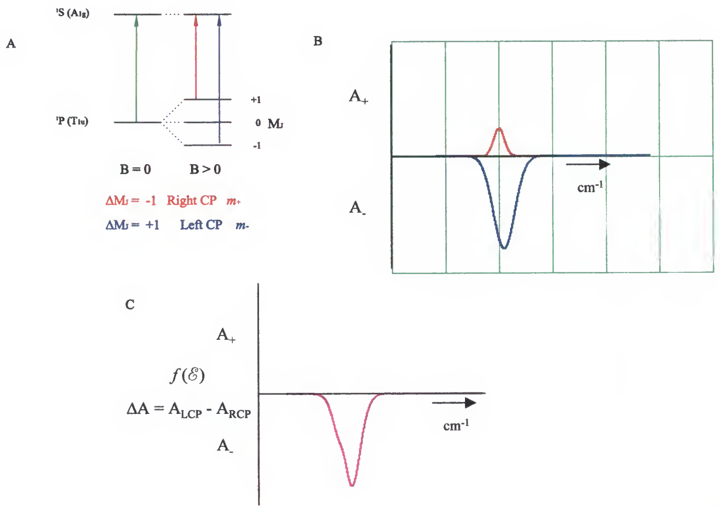

Figure 2-5. Origination of Faraday 𝒞 term. A) Electronic transitions from a degenerate ^1P ground state to a nondegenerate ^1S excited state. B) Dispersions due to individual + and – transitions. C) Sum of + and – terms which appears in a spectrum as a 𝒞 term, the resultant of which can be overall + or -. Note the asymmetric structure of the band.

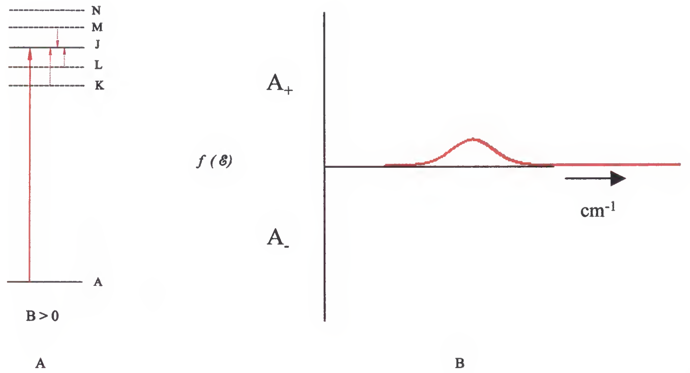

Figure 2-6. Origination of Faraday $\mathcal{B}$ term. A) Electronic transitions from ground state A to excited state j. Nearby states K, L, M, and N may mix under the influence of the magnetic field **B** if they are related to J by a magnetic dipole moment. Mixing may occur for state A as well. B) Weak $\mathcal{B}$ term absorption which may be + or -.

CHAPTER 3
SATURATION THEORY OF MCD AND MLD FOR ORIENTATIONALLY AVERAGED SYSTEMS

MCD and MLD in the Non-linear Regime

Previous analyses in this laboratory have focused on determination of atomic spin-orbit coupling constants, excited state g values, and cubic/non-cubic contributions of lattice mode vibrations to the MCD dispersion. Evaluation of the dispersion expressions A_1, B_0, C_0, and D_0 given in Equations 2-14, 2-15, and 2-20 can give estimations of these values, but often there is a large uncertainty present due to experimental errors. The application of these dispersion expressions is only valid in the linear limit of MCD absorption, that is, where the MCD absorption varies linearly with applied magnetic field **B**. Assumption of linearity requires that the magnitude of Zeeman splittings be small relative to kT and the MCD dispersion bandwidth. These conditions also hold for the MLD dispersion parameters A_2, B_1, C_1, D_0, E_0, F_0, and G_0 given in Equations 2-25 – 2-27. It is important to note that Equations 2-13 and 2-24 are only applicable for isotropic molecules or for anisotropic molecules oriented with the molecular z-axis parallel to the laboratory Z-axis. The eigenfunctions must be diagonal in the magnetic dipole transition moment operator $\hat{\mu}_Z$ in the laboratory reference frame. Extension to randomly oriented systems within linear limits can be found in Piepho and Schatz.[32] Also paramount in the theoretical derivation is the assumption of validity for applying first order perturbation theory to the Zeeman splittings. A full treatment of the bandwidth dependence when the Zeeman splitting $\mu_B g B_z$ is comparable to the bandwidth becomes necessary when sharp bandwidths appear at higher temperatures above approximately 4 – 5 K. The theoretical treatment of the bandwidth adjustment necessary at higher temperatures also can be found in Piepho and Schatz.[33] The experimental approach of the present study was limited to temperatures at and below liquid He temperature, so considerations of bandwidth compensation are not included. The energy of Zeeman splitting E_Z for an electron in a magnetic field is given by

$$E_Z = g\mu_B B_z \mathbf{M}_J \tag{3-1}$$

$$g = 1 + \frac{J(J+1) + S(S+1) - L(L+1)}{2J(J+1)} \tag{3-2}$$

where $g \equiv$ Lande' g value (≈ 2.00232 for free electron)

$\mu_B \equiv$ Bohr magneton ($0.4669\ \mathrm{cm}^{-1}$ /Tesla)

$B_z \equiv$ Magnetic field strength (Tesla)

$\mathbf{M}_J \equiv -J, -J+1, -J+2, \ldots 0, J-2, J-1, J$

For a free electron in a 5 Tesla **B** field the Zeeman splitting is approximately 4.7 cm^{-1}. Separations between atomic and molecular electronic states are of the order $10^3\ \mathrm{cm}^{-1}$ and the magnitude of electronic transition energies is typically $10^4\ \mathrm{cm}^{-1}$, implying the feasibility of using a first order perturbation derivation since the Zeeman splitting is approximately 0.5% of the band separation and 0.05% of the transition energy. Born-Oppenheimer (BO), Franck-Condon (FC) and Rigid Shift (RS) approximations are assumed valid for the electronic transitions between ground and excited states. Nearby electronic states may mix under the influence of the magnetic field requiring the inclusion of higher order terms in the perturbation solution. If this is necessary, the initial zero-field eigenfunctions can be adjusted to include these effects and still be diagonalized in $\hat{\mu}_Z$.

For the Zeeman splitting to become comparable with kT, the effects of **B** and T must be considered. Figure 3-1 illustrates the MCD dependence on **B** and T. Increasing **B** directly increases the magnitude of Zeeman splitting by Equation 3-1, but for E_Z to be approximately equal to kT for a given T of 20 K at k = 0.69509 cm^{-1} K^{-1} would require an applied magnetic field **B** of 14.9 Tesla (T). At 10 K, a field **B** of 7.44 T would be necessary and at liquid helium temperature of 4.2 K the field requirement would be only 3.13 T. The normal operating configuration of our instrumentation for linear limit data collection utilizes an electromagnet capable of ≈0.55 T. The lower limit of the standard Air Products closed cycle helium cryostat is 10 K at best. This gives a kT of 6.95 cm^{-1} and $\mu_B g B_z$ of 0.514 cm^{-1} or ≈7.4% of kT. Utilization of an Oxford superconducting magnet/liquid helium cryostat capable of 4 Tesla and ≈1.4 K permits data collection on systems where kT ≈ 0.973 cm^{-1} and $\mu_B g\, B_z \approx 3.74\ cm^{-1}$ for a free electron. Where g becomes less for real atomic systems (g = 1.5 for Fe atoms, 1.33 for Ni atoms), the Zeeman energy will be proportionately smaller ($\mu_B g\, B_z = 2.80\ cm^{-1}$ for $g = 1.5$ at 4 T), but will still be significantly greater than kT at low T. Physically, the population distribution within the ground state manifold shifts toward increasing concentration of the lower Zeeman states with increasing **B** and/or decreasing T until eventually only the lowest Zeeman level is populated at sufficiently large values **B**/T (Figure 3-2). The required condition of $E_Z \ll kT$ for the linear limit dispersion equations to apply is no longer realized. First order expansion no longer applies in the general development of Equations 2-13 and 2-24. The expression for MCD instead becomes[33]

$$\frac{\Delta A_C}{\mathcal{E}} = \frac{\gamma \mu_B B_z}{\sum_{\alpha,\lambda} \exp\left(\frac{\langle A_\alpha|\hat{\mu}_Z|A_\alpha\rangle^0 B_z}{kT}\right)} \left\{ \sum_{\alpha,\lambda} \exp\left(\frac{\langle A_\alpha|\hat{\mu}_Z|A_\alpha\rangle^0 B_z}{kT}\right) \left[A_1(\alpha\lambda)\left(\frac{\partial f(\mathcal{E})}{\partial \mathcal{E}}\right) \right.\right.$$

$$\left.\left. + B_0(\alpha\lambda) f(\mathcal{E}) + \left(\left|\langle A_\alpha|\hat{m}_{-1}|J_\lambda\rangle^0\right|^2 - \left|\langle A_\alpha|\hat{m}_{+1}|J_\lambda\rangle^0\right|^2 \right) \frac{f(\mathcal{E})}{\mu_B B_z} \right] \right\} \qquad (3\text{-}3)$$

Random molecular orientation is not accounted for in Equation 3-3. The ground state eigenfunctions are still required to be diagonal in the laboratory $\hat{\mu}_Z$. The $\mathcal{A}$ and $\mathcal{B}$ terms are usually not of importance in an MCD saturation study of paramagnetic samples since the C term is dominant in most cases. Consider then the third term of Equation 3-3, which corresponds to the MCD $\mathcal{C}$ Faraday parameter. Dispersion including saturation becomes

$$\left(\frac{\Delta A'}{\mathcal{E}}\right)_{C_{sat}} = \frac{\gamma \sum_{i\ pairs} \Delta\alpha_i \left[\exp\left(\frac{\langle A_{\alpha_i}|\hat{\mu}_Z|A_{\alpha_i}\rangle^0 B_z}{kT}\right) - \exp\left(-\frac{\langle A_{\alpha_i}|\hat{\mu}_Z|A_{\alpha_i}\rangle^0 B_z}{kT}\right)\right]}{\sum_{i\ pairs} \left[\exp\left(\frac{\langle A_{\alpha_i}|\hat{\mu}_Z|A_{\alpha_i}\rangle^0 B_z}{kT}\right) + \exp\left(-\frac{\langle A_{\alpha_i}|\hat{\mu}_Z|A_{\alpha_i}\rangle^0 B_z}{kT}\right)\right]} \qquad (3\text{-}4)$$

where $\Delta\alpha_i \equiv \sum_{\lambda}\left(\left|\langle A_{\alpha_i}|\hat{m}_{-1}|J_\lambda\rangle^0\right|^2 - \left|\langle A_{\alpha_i}|\hat{m}_{+1}|J_\lambda\rangle^0\right|^2 \right)$

The summations are over a single member of a ground state Kramers pair. A Kramers pair represents eigenstates which are diagonal in $\hat{\mu}_Z$ and transform reciprocally under time reversal[32]. Complete population saturation for Zeeman level $|A_{\alpha_i}\rangle$ representing the lowest energy configuration results in

$$\left(\frac{\Delta A'}{\mathcal{E}}\right)_{C_{sat}} = \gamma \Delta\alpha_i f(\mathcal{E}) \qquad (3\text{-}5)$$

For a single Kramers pair ground state

$$\left(\frac{\Delta A'}{\mathscr{E}}\right)_{C_{sat}} = \gamma \Delta\alpha f(\mathscr{E}) \tanh\left(\frac{\langle A_\alpha|\hat{\mu}_z|A_\alpha\rangle^0 B_z}{kT}\right)$$

$$= \gamma \Delta\alpha f(\mathscr{E}) \tanh\left(\frac{g\hat{\mu}_B B_z}{2kT}\right) \qquad (3\text{-}6)$$

This is the mathematical description of the curve graphed in Figure 3-1. Again it is only explicitly valid for a single ground state Kramers pair as Cu or Ag atoms, but serves to illustrate the approach to utilizing saturation theory to extract useful information about the ground state configuration. Determination of the ground state magnetic moment $\langle A_\alpha|\hat{\mu}_z|A_\alpha\rangle^0$ of an absorber could be arrived at by determination of the C_0/D_0 value from a linear limit MCD experiment. By obtaining an MCD saturation curve and fitting the theoretical expression of Equation 3-4 to the experimental data by varying the value of the magnetic moment in a least squares analysis, an accurate value of the moment may be obtained and the *g* value determined directly.

Application of the general expression for MCD and MLD to saturation in the case of large Zeeman splitting must be made for non-Kramers pairs on an individual basis and for quantitative dispersion descriptions this becomes quite complex. The focus of this study is to arrive at expressions for the MCD and MLD saturation as a function of symmetry which are proportional to the actual quantitative curves and then scale and compare these proportional curves to the experimentally obtained saturation curves for Fe and Ni atoms isolated in solid Kr matrix. The basic theory has been presented by Piepho and Schatz[33] and developed for application to experimental data by Pellow and Vala for pseudo-isotropic molecules in which the high-order symmetry of individual molecular orientations does not affect the results.[40,54] The expression for MCD given by Equations 2-13 and 3-3 for large Zeeman splitting is

$$\Delta A_C = \left(\frac{\sigma \mathscr{E} f[c]l}{Z}\right)\sum_{\alpha}\sum_{\beta}\exp\left(-\frac{\langle A_\alpha|\mathscr{H}_{eff}|A_\alpha\rangle}{kT}\right)\left[\left|\langle A_\alpha|\hat{m}_-|B_\beta\rangle\right|^2 - \left|\langle A_\alpha|\hat{m}_+|B_\beta\rangle\right|^2\right] \tag{3-7}$$

where $\sigma \equiv 2N_0\pi^3 \log_{10}e/(250\ h\ c)$

$\mathscr{E}$ ≡ photon energy

Z ≡ electronic partition function

f ≡ bandshape function

$[c]$ ≡ concentration

l ≡ path length

A ≡ irreducible representation symmetry label of electronic ground state in crystal field [CF] symmetry (component α)

B ≡ irreducible representation symmetry label of electronic ground state in CF symmetry (component β)

$\hat{m}_- \equiv (\hat{m}_x - i\hat{m}_y)/\sqrt{2}$: transition moment electric dipole operator LCP

$\hat{m}_+ \equiv (\hat{m}_X + i\hat{m}_Y)/\sqrt{2}$: transition moment electric dipole operator RCP

$\mathscr{H}_{eff}$ ≡ total Hamiltonian operator $\mathscr{H}_Z + \mathscr{H}_{CF}$

$\mathscr{H}_Z = \hat{\mu}_Z = g\mu_B B_z J_Z$ ≡ Zeeman operator $[J_Z \equiv M_J]$

$\mathscr{H}_{CF}$ ≡ diagonal crystal field Hamiltonian operator

N_0 ≡ Avogadro's number

h = 6.626 x 10^{-34} J s ≡ Planck's constant

Development of Crystal Field Hamiltonian

The theoretical developments of Pellow, Vala, and Rivoal[40,55] are extended in an insightful collaboration with B. Williamson to account for the effects of high **B**, low T, and random orientation of atoms in anisotropic site geometries. The application of a weak crystal field as caused by matrix atoms surrounding an absorbing center permits expansion of the eigenfunctions for the ground state in a $|\mathrm{JM}\rangle$ basis at zero applied magnetic field as

$$|\mathrm{A}_\alpha\rangle = \sum_M c_{JM}^{A_\alpha} \, |\mathrm{JM}\rangle \tag{3-8}$$

J is the irreducible representation (irrep) symmetry label from group theory[57] with component M in the JM basis, which is the SO_3 symmetry group in Butler's notation convention[56] denoting the group of all rotations. The $\langle \mathrm{A}_\alpha | \mathrm{JM} \rangle$ coefficients are tabulated in Butler for various symmetry groups and are quantized along the crystal field's symmetry axis (axis of principle rotation) if such an axis exists. Thus the component M values refer to the molecular z-axis, ***which does not necessarily coincide*** with the laboratory Z-axis along which the magnetic field is applied. The crystal field eigenvectors $|\mathrm{A}_\alpha\rangle$ are subsequently determined and diagonalized in the crystal field for zero magnetic field via the equivalent operator methods of Watanabe.[57] Expressions are derived for the three likely symmetry classifications which a zero-valent medium-sized metal atom might occupy in a rare gas matrix of Ar, Kr, or Xe. The high symmetry configuration is one in which the metal atom occupies an octahedral site, either substitutional (MX_{12}) or interstitial (MX_6) as shown in Figure 3-3. Watanabe's equivalent operator methods provide an algebraic expression descriptive of the site geometries for a variety of crystal fields based on the point groups representative of a particular symmetry. The equivalent operator $\mathscr{H}_{CF}$ which can be substituted to describe the perturbation caused by an octahedral crystal field distortion is

$$V_{OCT} = \frac{D^{OCT}}{60}\left[\left\{35J_z^4 - 30\,J(J+1)J_z^2 + 25J_z^2 + 3J^2(J+1)^2 - 6J(J+1)\right\} + \frac{5}{2}\left(J_+^4 + J_-^4\right)\right] \quad (3\text{-}9)$$

Figure 3-4 depicts the distortions by the cage atoms around a centrally located metal atom that would result in lower tetragonal or trigonal symmetry environments. Several possible lower symmetry configurations can be envisioned within these two groups. Only the D_{4h} and D_{3h} point groups are considered. Application of the operator equivalent method to provide tetragonal and trigonal crystal field energies gives

$$V_{TET} = \frac{B^{TET}}{3}\left[3J_z^2 - J(J+1)\right] + \frac{F_1^{TET}}{60}\left[35J_z^4 - 30J(J+1)J_z^2 + 25J_z^2 + 3J^2(J+1)^2\right.$$

$$\left. - 6J(J+1)\right] + F_2^{TET}(J_+^4 + J_-^4) \quad (3\text{-}10)$$

$$V_{TRI} = \frac{G^{TRI}}{3}\left[(3J_z^2 - J(J+1)\right] + \frac{K^{TRI}}{60}\left[(35J_z^4 - 30J(J+1)J_z^2 + 25J_z^2 + 3J^2(J+1)^2\right.$$

$$\left. - 6J(J+1)\right] + \frac{M^{TRI}}{12}\left[J_z\left(J_+^3 + J_-^3\right) + \left(J_+^3 + J_-^3\right)J_z\right] \quad (3\text{-}11)$$

Note that only one parameter, D^{OCT}, needs to be derived to establish the crystal field splitting for the octahedral environment, while three are necessary for the tetragonal and trigonal models. Tables 3-1 and 3-2 contain the basis state vectors from Butler[56] for initial J = 3 for the multiple site geometries. The state vectors for the J = 4 ground state are in Tables 3-3 and 3-4. The expressions for the crystal field energies are listed in Tables 3-5, 3-6, and 3-7, respectively, for ground states with J = 4 (for Fe(0): $^5D_4$; for Ni(0): $^3F_4$) and J = 3 (for Ni(0): $^3D_3$). Table 3-8 depicts the crystal field matrix resulting for H_{CF} in generalized form for all three symmetries for a $^3D_3$ ground state. A determination of the theoretical MCD and MLD is also derived for the free atom environment in which there is no crystal field perturbation for comparison with the perturbed environment.

Table 3-1. Basis set state vectors for J = 3 ground state in a trigonal crystal field

$SO_3 - O - D_3 - C_3$ Symmetry Partners as JM Partners

State vector	D_3	JM Eigenvector Coefficients
$\|3\,1\,\tilde{0}\,0\rangle$	$A_2(1)$	$\|3\;\;3\rangle+\sqrt{5}/3\sqrt{2}+\|3\;\;0\rangle+2/3+\|3\;\;-3\rangle-\sqrt{5}/3\sqrt{6}$
$\|3\,1\,1\,1\rangle$	E(1)	$\|3\;\;1\rangle+1/\sqrt{6}+\|3\;\;-2\rangle-\sqrt{5}/\sqrt{6}$
$\|3\,1\,1\,-1\rangle$	E(1)	$\|3\;\;2\rangle+\sqrt{5}/\sqrt{6}+\|3\;\;-1\rangle-1/\sqrt{6}$
$\|3\,\tilde{1}\,0\,0\rangle$	A_1	$\|3\;\;3\rangle-1/\sqrt{2}+\|3\;\;-1\rangle-1/\sqrt{6}$
$\|3\,\tilde{1}\,1\,1\rangle$	E(2)	$\|3\;\;1\rangle+\sqrt{5}/\sqrt{6}+\|3\;\;-2\rangle+1/\sqrt{6}$
$\|3\,\tilde{1}\,1\,-1\rangle$	E(2)	$\|3\;\;2\rangle-1/\sqrt{6}+\|3\;\;-1\rangle+\sqrt{5}/\sqrt{6}$
$\|3\,\tilde{0}\,\tilde{0}\,0\rangle$	$A_2(2)$	$\|3\;\;3\rangle+\sqrt{2}/3+\|3\;\;0\rangle-\sqrt{5}/3+\|3\;\;-3\rangle-\sqrt{2}/3$

Source: Philip H. Butler, "Point Group Symmetry Applications", $SO_3 - O - D_4 - C_4$ Symmetry Partners as JM Partners, pp. 522–527, Plenum Press, New York (1981).

Table 3-2. Basis set state vectors for J = 3 ground state in octahedral and tetragonal crystal fields

$SO_3 - O - D_4 - C_4$ Symmetry Partners as JM Partners

State vector	O	D_4	JM Eigenvector Coefficients
$\|3\,1\,\tilde{0}\,0\rangle$	T_1	A_2	$\|3\;\;0\rangle-1$
$\|3\,1\,1\,1\rangle$	T_1	E(1)	$\|3\;\;1\rangle-\sqrt{3}/2\sqrt{2}+\|3\;\;-3\rangle-\sqrt{5}/2\sqrt{2}$
$\|3\,1\,1\,-1\rangle$	T_1	E(1)	$\|3\;\;3\rangle-5/2\sqrt{2}+\|3\;\;-1\rangle-\sqrt{3}/2\sqrt{2}$
$\|3\,\tilde{1}\,1\,1\rangle$	T_2	E(2)	$\|3\;\;1\rangle-\sqrt{5}/2\sqrt{2}+\|3\;\;-3\rangle-\sqrt{3}/2\sqrt{2}$
$\|3\,\tilde{1}\,1\;-1\rangle$	T_2	E(2)	$\|3\;\;3\rangle+\sqrt{3}/2\sqrt{2}+\|3\;\;-1\rangle-1/\sqrt{2}$
$\|3\,\tilde{1}\,\tilde{2}\,2\rangle$	T_2	B_2	$\|3\;\;2\rangle-1/\sqrt{2}+\|3\;\;-2\rangle-1/\sqrt{2}$
$\|3\,\tilde{0}\,2\,2\rangle$	A_2	B_2	$\|3\;\;2\rangle-1/\sqrt{2}+\|3\;\;-2\rangle+1/\sqrt{2}$

Source: Philip H. Butler, "Point Group Symmetry Applications", $SO_3 - O - D_4 - C_4$ Symmetry Partners as JM Partners, pp. 527–531, Plenum Press, New York (1981).

Table 3-3. Basis set state vectors for J = 4 ground state in a trigonal crystal field

$SO_3 - O - D_3 - C_3$ Symmetry Partners as JM Partners

State vector	D_3	JM Eigenvector Coefficients
$\lvert 4\,0\,0\,0\rangle$	$A_1(1)$	$\lvert 4\;\;3\rangle - \sqrt{10}/3\sqrt{3} + \lvert 4\;\;0\rangle - \sqrt{7}/3\sqrt{3} + \lvert 4\;\;-3\rangle - \sqrt{10}/3\sqrt{3}$
$\lvert 4\,1\,\tilde{0}\,0\rangle$	A_2	$\lvert 4\;\;3\rangle - 1/\sqrt{2} + \lvert 4\;\;-3\rangle - 1/\sqrt{2}$
$\lvert 4\,1\,1\,1\rangle$	$E(1)$	$\lvert 4\;\;4\rangle - \sqrt{2}/3 + \lvert 4\;\;1\rangle - \sqrt{7}/3\sqrt{2}$
$\lvert 4\,1\,1\,-1\rangle$	$E(1)$	$\lvert 4\;\;2\rangle + \sqrt{7}/3\sqrt{2} + \lvert 4\;\;-1\rangle + \sqrt{7}/3\sqrt{2}$
$\lvert 4\,2\,1\,1\rangle$	$E(2)$	$\lvert 4\;\;4\rangle - \sqrt{7}/3\sqrt{3} + \lvert 4\;\;1\rangle - 2/3\sqrt{3} + \lvert 4\;\;-2\rangle - 4/3\sqrt{3}$
$\lvert 4\,2\,1\,-1\rangle$	$E(2)$	$\lvert 4\;\;2\rangle - 4/3\sqrt{3} + \lvert 4\;\;-1\rangle + 2/3\sqrt{3} + \lvert 4\;\;4\rangle - \sqrt{7}/3\sqrt{3}$
$\lvert 4\,\tilde{1}\,0\,0\rangle$	$A_1(2)$	$\lvert 4\;\;3\rangle + \sqrt{7}/3\sqrt{6} + \lvert 4\;\;0\rangle - 2\sqrt{5}/3\sqrt{3} + \lvert 4\;\;-3\rangle - \sqrt{7}/3\sqrt{3}$
$\lvert 4\,\tilde{1}\,1\,1\rangle$	$E(3)$	$\lvert 4\;\;4\rangle - \sqrt{14}/3\sqrt{3} + \lvert 4\;\;1\rangle + 5/3\sqrt{6} + \lvert 4\;\;-2\rangle + 1/3\sqrt{6}$
$\lvert 4\,\tilde{1}\,1\,-1\rangle$	$E(3)$	$\lvert 4\;\;2\rangle + 1/3\sqrt{6} + \lvert 4\;\;-1\rangle - 5/3\sqrt{6} + \lvert 4\;\;-4\rangle - \sqrt{14}/3\sqrt{3}$

Source: Philip H. Butler, "Point Group Symmetry Applications", pp. 522–523, Plenum Press, New York (1981).

Table 3-4. Basis set state vectors for J = 4 ground state in octahedral and tetragonal crystal fields

$SO_3 - O - D_4 - C_4$ Symmetry Partners as JM Partners

State vector	O	D_4	JM Eigenvector Coefficients
$\lvert 4\,0\,0\,0\rangle$	A_1	$A_1(1)$	$\lvert 4\;\;4\rangle + \sqrt{5}/\sqrt{6} + \lvert 4\;\;0\rangle + \sqrt{7}/2\sqrt{3} + \lvert 4\;\;-4\rangle + \sqrt{5}/2\sqrt{6}$
$\lvert 4\,1\,\tilde{0}\,0\rangle$	T_1	A_2	$\lvert 4\;\;4\rangle + 1/\sqrt{2} + \lvert 4\;\;-4\rangle - 1/\sqrt{2}$
$\lvert 4\,1\,1\,1\rangle$	T_1	$E(1)$	$\lvert 4\;\;1\rangle + \sqrt{7}/2\sqrt{2} + \lvert 4\;\;-3\rangle + 1/2\sqrt{2}$
$\lvert 4\,1\,1\,-1\rangle$	T_1	$E(1)$	$\lvert 4\;\;3\rangle - 1/2\sqrt{2} + \lvert 4\;\;-1\rangle - \sqrt{7}/2\sqrt{2}$
$\lvert 4\,2\,0\,0\rangle$	E	$A_1(2)$	$\lvert 4\;\;4\rangle - \sqrt{7}/2\sqrt{6} + \lvert 4\;\;0\rangle + \sqrt{5}/2\sqrt{3} + \lvert 4\;\;-4\rangle - \sqrt{7}/2\sqrt{6}$
$\lvert 4\,2\,2\,2\rangle$	E	B_1	$\lvert 4\;\;2\rangle - 1/\sqrt{2} + \lvert 4\;\;-2\rangle - 1/\sqrt{2}$
$\lvert 4\,\tilde{1}\,1\,1\rangle$	T_2	$E(2)$	$\lvert 4\;\;1\rangle + \sqrt{1}/2\sqrt{2} + \lvert 4\;\;-3\rangle - \sqrt{7}/2\sqrt{2}$
$\lvert 4\,\tilde{1}\,1\,-1\rangle$	T_2	$E(2)$	$\lvert 4\;\;3\rangle - \sqrt{7}/2\sqrt{2} + \lvert 4\;\;-1\rangle - 1/2\sqrt{2}$
$\lvert 4\,\tilde{1}\,\tilde{2}\,2\rangle$	T_2	B_2	$\lvert 4\;\;2\rangle + 1/\sqrt{2} + \lvert 4\;\;-2\rangle - 1/\sqrt{2}$

Source: Philip H. Butler, "Point Group Symmetry Applications", pg. 528, Plenum Press, New York (1981).

Table 3.5 Crystal field energies for the J = 3 and J = 4 atomic states in octahedral symmetry

Octahedral			
J = 3		J = 4	
State	Crystal field energy	State	Crystal field energy
T_1	6D	A_1	28D
T_2	-2D	T_1	14D
A_2	-12D	E	4D
		T_2	-26D

Source: Hiroshi Watanabe, "Operator Methods in Ligand Field Theory," Appendix 4.2, pp. 171-173, Prentice-Hall, Inc., Englewood, New Jersey (1966)

Table 3.6 Crystal field energies for the J = 3 and J = 4 atomic states in tetragonal symmetry

Tetragonal			
J = 3		J = 4	
State	Crystal field energy	State	Crystal field energy
A_2	$-4B + 6F_1$	$A_1(1)$	$49F_1/3 + 7F_2/3$
E(1)	$2B + 9F_1/4 + 3F_2/4$	A_2	$28B/3 + 14F_1$
E(2)	$7F_1/4 - 3F_2/4$	E(1)	$-14B/3 + 21F_1/4 + 7F_2/4$
B_2	$-7F_1 + F_2$	E(2)	$4B/3 - 69F_1/4 - 7F_2/4$
B_1	$-7F_1 + F_2$	$A_1(2)$	$8B/3 + 47F_1/3 - 7F_2/3$
		B_1	$8B/3 - 11F_1 + 3F_2$
		B_2	$8B/3 - 11F_1 - 3F_2$

Source: Hiroshi Watanabe, "Operator Methods in Ligand Field Theory," Chapter 4, Prentice-Hall, Inc., Englewood, New Jersey (1966)

Table 3.7 Crystal field energies for the J = 3 and J = 4 atomic states in trigonal symmetry

Trigonal			
J = 3		J = 4	
State	Crystal field energy	State	Crystal field energy
$A_2(1)$	$G + 13K/3 + 20\sqrt{2}\,M$	$A_1(1)$	$-98K/9 + 140\sqrt{2}\,M/9$
$E(1)$	$-G/2 - 17K/3 + 5\sqrt{2}$	A_2	$7G/3 - 21K$
A_1	$5G + 3K$	$E(1)$	$-7G/6 + 7K/3 + 35\sqrt{2}\,M/3$
$E(2)$	$-5G/2 - K/3 - 5\sqrt{2}\,M/3$	$E(2)$	$-14K/9 + 20\sqrt{2}\,M/9$
$A_2(2)$	$14K/3 - 20\sqrt{2}\,M$	$A_1(2)$	$-13G/3 + 71K/9 - 140\sqrt{2}\,M/9$
		$E(3)$	$13G/3 + 101K/9 - 125\sqrt{2}\,M/9$

Source: Hiroshi Watanabe, "Operator Methods in Ligand Field Theory," Chapter 4, Prentice-Hall, Inc., Englewood, New Jersey (1966)

.

Table 3.8 Crystal field matrix for octahedral, tetragonal, and trigonal symmetries in the $|JM\rangle$ basis.

J = 3							
Basis Vectors	$\|3\ 3\rangle$	$\|3\ 2\rangle$	$\|3\ 1\rangle$	$\|3\ 0\rangle$	$\|3\ -1\rangle$	$\|3\ -2\rangle$	$\|3\ -3\rangle$
$\|3\ 3\rangle$	3(D+F+K) +5(B+G)			$3\sqrt{5}\,M$	$\sqrt{15}\,D$		
$\|3\ 2\rangle$		-7(D+F+K)			$\sqrt{10}\,M$	5D	
$\|3\ 1\rangle$			D+F+K -3(B+G)			$\sqrt{10}\,M$	$\sqrt{15}\,D$
$\|3\ 0\rangle$	$3\sqrt{5}\,M$			6(D+F+K) -4(B+G)			$3\sqrt{5}\,M$
$\|3\ -1\rangle$	$\sqrt{15}\,D$	$\sqrt{10}\,M$			D+F+K -3(B+G)		
$\|3\ -2\rangle$			$\sqrt{10}\,M$			-7(D+F+K)	
$\|3\ -3\rangle$			$\sqrt{15}\,D$	$3\sqrt{5}\,M$			3(D+F+K) +5(B+G)

Source: Hiroshi Watanabe, "Operator Methods in Ligand Field Theory," Chapter 4, Prentice-Hall, Inc., Englewood, New Jersey (1966)

Note: Octahedral symmetry: F=B=K=G=M=0; $D=D^{OCT}$; Tetragonal symmetry: D=K=G=M=0; $F=F^{TET}$, $B=B^{TET}$; Trigonal symmetry: D=F=B=0; $K=K^{TRI}$, $G=G^{TRI}$, $M=M^{TRI}$

Full State Eigenvectors

Application of an external magnetic field **B** then mixes the crystal field eigenvectors to produce a new set of eigenvectors which are a linear combination of the crystal field eigenvectors, and therefore they are also a linear combination of the JM basis eigenvectors. For the total effective Hamiltonian

$$\mathscr{H}_{\mathrm{eff}} = \mathscr{H}_{\mathrm{CF}} + \hat{\mu}_{\mathrm{Z}} \tag{3-12}$$

the Zeeman matrix elements mixing crystal field eigenvectors $|\mathrm{A}_\alpha\rangle$ and $|\mathrm{B}_\beta\rangle$ are determined in the JM basis as

$$\langle \mathrm{A}_\alpha | \hat{\mu}_{\mathrm{Z}} | \mathrm{B}_\beta \rangle = \sum_{\mathrm{M}_1} \sum_{\mathrm{M}_2} c_{\mathrm{JM}_1}^{\mathrm{B}_\beta} c_{\mathrm{JM}_2}^{\mathrm{A}_\alpha^*} \langle \mathrm{JM}_2 | \hat{\mu}_{\mathrm{Z}} | \mathrm{JM}_1 \rangle \tag{3-13}$$

Designating the eigenvectors for $\mathscr{H}_{\mathrm{eff}}$ using coefficients $\langle \mathrm{i} | \mathrm{A}_\alpha \rangle$ in the $|\mathrm{A}_\alpha\rangle$ basis as

$$|\mathrm{i}\rangle = \sum_{\mathrm{A}} \sum_{\alpha} c_{\mathrm{A}_\alpha}^{\mathrm{i}} |\mathrm{A}_\alpha\rangle \tag{3-14}$$

and then expanding in the $|\mathrm{JM}\rangle$ basis gives

$$|\mathrm{i}\rangle = \sum_{\mathrm{A}} \sum_{\alpha} \sum_{\mathrm{M}} c_{\mathrm{A}_\alpha}^{\mathrm{i}} c_{\mathrm{JM}}^{\mathrm{A}_\alpha^*} |\mathrm{JM}\rangle = \sum_{\mathrm{M}} c_{\mathrm{JM}}^{\mathrm{i}} |\mathrm{JM}\rangle \tag{3-15 a}$$

which appears in Dirac notation as

$$|\mathrm{i}\rangle = \sum_{\mathrm{M}} \sum_{\mathrm{A}_\alpha} \langle \mathrm{JM} | \mathrm{A}_\alpha \rangle \langle \mathrm{A}_\alpha | \mathrm{i} \rangle |\mathrm{JM}\rangle = \sum_{\mathrm{M}} \langle \mathrm{JM} | \mathrm{i} \rangle |\mathrm{JM}\rangle \tag{3-15 b}$$

The eigenvalue $\mathrm{E_i}$ for the total effective Hamiltonian $\mathscr{H}_{\mathrm{eff}}$ corresponds to the eigenvector $|\mathrm{i}\rangle$ representing the combined crystal field and Zeeman eigenvectors as expressed in the $|\mathrm{JM}\rangle$ basis. Retaining the $|\mathrm{JM}\rangle$ basis for the excited state energy level as allowed by the principle of spectroscopic stability permits writing the electric dipole transition moments as

$$\langle \mathrm{i} | \hat{\mathrm{m}} | \mathrm{J'M'} \rangle = \sum_{\mathrm{M}} \langle \mathrm{i} | \mathrm{JM} \rangle \langle \mathrm{JM} | \hat{\mathrm{m}} | \mathrm{J'M'} \rangle \tag{3-16}$$

Laboratory vs. Molecular Reference Frames

The laboratory reference frame will be designated by capital letters X, Y, and Z and is oriented such as to define Z as the axis collinear with the applied magnetic field **B** (Figure 3-5), that is, Z is parallel to **B**. X is taken as the vertical axis, orthogonal to Z and normal to the earth's surface. Y is therefore orthogonal to both X and Z and lies in the horizontal plane parallel to the earth's surface in the localized laboratory reference frame. Vector components of the electric dipole operator and the magnetic dipole operator in the laboratory (or space fixed) X Y Z reference frame are designated by capital M and μ respectively with upper case

$$\hat{M}_Z \quad \hat{M}_X \quad \hat{M}_Y \qquad\qquad \hat{\mu}_Z \quad \hat{\mu}_X \quad \hat{\mu}_Y$$

$$\hat{M}_{\pm 1} = \mp \frac{1}{\sqrt{2}} \left(\hat{M}_X \pm i\hat{M}_Y \right) \qquad \hat{\mu}_{\pm 1} = \mp \frac{1}{\sqrt{2}} \left(\hat{\mu}_X \pm i\,\hat{\mu}_Y \right) \tag{3-17}$$

subscripts

The MCD can then be expressed as follows with γ as a collection of constants and partition function Z

$$\Delta A_C = \frac{\gamma}{Z} \sum_{i} \sum_{M'} e^{-\frac{E_i}{kT}} \left[\left| \left\langle i \middle| \hat{M}_{-1} \middle| J'M' \right\rangle \right|^2 - \left| \left\langle i \middle| \hat{M}_{+1} \middle| J'M' \right\rangle \right|^2 \right] \tag{3-18}$$

Performing a double summation over JM for each of the dipole terms gives the general expression for MCD

$$\Delta A_C = \frac{\gamma}{Z} \sum_{i} e^{-\frac{E_i}{kT}} \sum_{M'} \sum_{M_1} \sum_{M_2} \langle JM_1 | i \rangle \langle i | JM_2 \rangle \Big[\langle JM_2 | \hat{M}_{+1} | J'M' \rangle \langle J'M' | \hat{M}_{-1} | JM_1 \rangle - \left\langle JM_2 \middle| \hat{M}_{-1} \middle| J'M' \right\rangle \left\langle J'M' \middle| \hat{M}_{+1} \middle| JM_1 \right\rangle \Big] \tag{3-19}$$

In this expression it is important to note that M_1 and M_2 represent the components of the $|JM\rangle$ basis in the molecular reference frame while the electric dipole operators $\hat{M}_{+1}$ and $\hat{M}_{-1}$ in Equations 3-18 and 3-19 (and $\hat{M}_Z$ and $\hat{M}_X$ in Equations 3-21 and 3-22 below) and the magnetic dipole operator $\hat{\mu}_Z$ of Equation 3-12 are referenced to the laboratory (space fixed) reference frame. The general expression for MLD is developed similarly as Equation 3-7 from Equation 2-24 substituting the parallel $\hat{m}_{\parallel} = \hat{M}_Z$ and perpendicular $\hat{m}_{\perp} = \hat{M}_X$ electric dipole transition moment operators associated with MLD transitions

$$\Delta A_L = \left(\frac{\sigma \mathscr{E} f\,[c] l}{Z} \right) \sum_{\alpha} \sum_{\beta} \exp\left(\frac{\langle A_\alpha | \mathscr{H}_{eff} | A_\alpha \rangle}{kT} \right) \left[\left| \langle A_\alpha | \hat{m}_{\parallel} | B_\beta \rangle \right|^2 - \left| \langle A_\alpha | \hat{m}_{\perp} | B_\beta \rangle \right|^2 \right] \tag{3-20}$$

Expansion in the $|JM\rangle$ basis results in

$$\Delta A_L = \frac{\gamma}{Z} \sum_{i} \sum_{M'} e^{-\frac{E_i}{kT}} \left| \langle i | \hat{M}_Z | J'M' \rangle \right|^2 - \left| \langle i | \hat{M}_X | J'M' \rangle \right|^2 \tag{3-21}$$

where $$\hat{M}_X = \frac{\hat{m}_+ + \hat{m}_-}{\sqrt{2}}$$

and the general expression is

$$\Delta A_L = \frac{\gamma}{Z} \sum_{i} e^{-\frac{E_i}{kT}} \sum_{M'} \sum_{M_1} \sum_{M_2} \langle JM_1 | i \rangle \langle i | JM_2 \rangle \Big[\langle JM_2 | \hat{M}_Z | J'M' \rangle \langle J'M' | \hat{M}_Z | JM_1 \rangle$$
$$- \langle JM_2 | \hat{M}_X | J'M' \rangle \langle J'M' | \hat{M}_X | JM_1 \rangle \Big] \tag{3-22}$$

Euler Transformation

These equations have been developed on the molecular level, that is, the crystal field distortion is uniquely applied to each molecule, not to the collection of molecules. The molecular z-axis has been assumed to coincide with the laboratory Z-axis. If the symmetry of the systems of study is restricted to isotropic or cubic point groups (SO_3, O_h, T_d) then random molecular orientation poses no problem in the MCD/MLD theoretical calculations since all orientations are equivalent. If the high symmetry is broken due to molecular distortion, then some restrictions are imposed on the theory. The assumption of an orientation of the molecular z-axis (lower case letters will be used for molecular axes) parallel to the laboratory Z-axis (coincident with the applied magnetic field **B**) is inconsequential for the cubic point group systems. For lower symmetry as D_4 and D_3 where there is now present a unique rotation axis defined as the molecular z-axis, non-alignment of the molecular z-axis with the laboratory Z-axis for random molecular orientation results in a variation in the mixing of the crystal field eigenvectors under the influence of an external magnetic field. An assumed alignment of the molecular z-axis with the laboratory Z-axis still results in zero theoretical CD intensity at zero applied magnetic field, but a non-zero LD would be expected theoretically via this constraint. This is consistent with the observed results for oriented molecules of low symmetry but is inconsistent for a random orientation of such molecules.

It is necessary to transform the laboratory reference coordinates to the molecular reference frame to account for random orientation in non-cubic systems. This will adapt the electric and magnetic dipole operator expressions in the laboratory X Y Z reference frame to the molecular x y z frame where they can be applied to each individual orientation. A summation over all orientations will then give the correct MCD/MLD expressions. The matrix elements in the laboratory frame to be determined in the molecular frame are

$$\langle A\alpha|\hat{\mu}_0|B\beta\rangle \qquad \left|\langle i|\hat{M}_{\pm 1}|J'M'\rangle\right|^2 \qquad \left|\langle i|\hat{M}_X|J'M'\rangle\right|^2 \qquad \left|\langle i|\hat{M}_Z|J'M'\rangle\right|^2 \qquad (3\text{-}23)$$

The method of classical mechanics' Euler transformation as depicted in Piepho and Schatz[33] and Goldstein[58] proceeds by developing a transformation matrix between the laboratory X, Y, Z reference frame and the molecular x, y, z reference frame in terms of Euler angles defined as follows and illustrated in Figure 3-5 where ccw is counterclockwise rotation.

$$\phi \equiv ccw\ about\ Z \quad \begin{pmatrix} X \\ Y \\ Z \end{pmatrix} \rightarrow \begin{pmatrix} X' \\ Y' \\ Z \end{pmatrix} \Rightarrow \mathbf{D} = \begin{pmatrix} \cos\phi & \sin\phi & 0 \\ -\sin\phi & \cos\phi & 0 \\ 0 & 0 & 1 \end{pmatrix} \qquad (3\text{-}24\text{ a})$$

$$\theta \equiv \mathit{ccw\ about}\ \mathrm{X'} \quad \begin{pmatrix} \mathrm{X'} \\ \mathrm{Y'} \\ \mathrm{Z} \end{pmatrix} \rightarrow \begin{pmatrix} \mathrm{X'} \\ \mathrm{Y''} \\ \mathrm{z} \end{pmatrix} \Rightarrow \mathbf{C} = \begin{pmatrix} 1 & 0 & 0 \\ 0 & \cos\theta & \sin\theta \\ 0 & -\sin\theta & \cos\theta \end{pmatrix} \qquad \text{(3-24 b)}$$

$$\psi \equiv \mathit{ccw\ about}\ \mathrm{z} \quad \begin{pmatrix} \mathrm{X'} \\ \mathrm{Y''} \\ \mathrm{z} \end{pmatrix} \rightarrow \begin{pmatrix} \mathrm{x} \\ \mathrm{y} \\ \mathrm{z} \end{pmatrix} \Rightarrow \mathbf{B} = \begin{pmatrix} \cos\psi & \sin\psi & 0 \\ -\sin\psi & \cos\psi & 0 \\ 0 & 0 & 1 \end{pmatrix} \qquad \text{(3-24 c)}$$

Therefore the transformation from X Y Z to x y z is accomplished by the orthogonal transformation matrix **A**

$$\begin{pmatrix} \mathrm{x} \\ \mathrm{y} \\ \mathrm{z} \end{pmatrix} = \mathbf{A} \begin{pmatrix} \mathrm{X} \\ \mathrm{Y} \\ \mathrm{Z} \end{pmatrix} \qquad \text{(3-25 a)}$$

$$\begin{pmatrix} \mathrm{X} \\ \mathrm{Y} \\ \mathrm{Z} \end{pmatrix} = \mathbf{A}^{\mathrm{T}} \begin{pmatrix} \mathrm{x} \\ \mathrm{y} \\ \mathrm{z} \end{pmatrix} \qquad \text{(3-25 b)}$$

where **A** is given by the products of the matrices in Equations 3-24 a-c

$$\mathbf{A{=}BCD} \qquad \text{(3-26)}$$

resulting in

$$\mathbf{A} = \begin{pmatrix} \cos\psi\cos\phi - \cos\theta\sin\phi\sin\psi & \cos\psi\sin\phi + \cos\theta\cos\phi\sin\psi & \sin\psi\sin\theta \\ -\sin\psi\cos\phi - \cos\theta\sin\phi\cos\psi & -\sin\psi\sin\phi + \cos\theta\cos\phi\cos\psi & \cos\psi\sin\theta \\ \sin\theta\sin\phi & -\sin\theta\cos\phi & \cos\theta \end{pmatrix}$$

$$\text{(3-27)}$$

Therefore, for a vector operator **V(X,Y,Z)** in the laboratory reference frame, the Euler transformation to molecular x y z coordinates becomes via Equation 3-25 b

$$\mathrm{V_X} = \mathrm{A_{11}V_x} + \mathrm{A_{21}V_y} + \mathrm{A_{31}V_z} \qquad \text{(3-28 a)}$$

$$\mathrm{V_Y} = \mathrm{A_{12}V_x} + \mathrm{A_{22}V_y} + \mathrm{A_{32}V_z} \qquad \text{(3-28 b)}$$

$$\mathrm{V_Z} = \mathrm{A_{13}V_x} + \mathrm{A_{23}V_y} + \mathrm{A_{33}V_z} \qquad \text{(3-28 c)}$$

Spherical transformation of the V laboratory components in terms of Cartesian molecular coordinates gives

$$V_{\pm 1} = \mp \frac{1}{\sqrt{2}}\,(V_X \pm i V_Y)$$

$$= \mp \frac{1}{\sqrt{2}}((A_{11} \pm i A_{12})V_x + (A_{21} \pm i A_{22})V_y + (A_{31} \pm i A_{32})V_z) \qquad \text{(3-29 a)}$$

$$V_0 = V_Z \qquad \text{(3-29 b)}$$

Using similar reciprocal transformations from spherical to Cartesian coordinates in the molecular reference frame

$$v_x = \frac{1}{\sqrt{2}}\,(v_{-1} - v_{+1}) \qquad \text{(3-30 a)}$$

$$v_y = \frac{i}{\sqrt{2}}\,(v_{-1} + v_{+1}) \qquad \text{(3-30 b)}$$

$$v_z = v_0 \qquad \text{(3-30 c)}$$

Substituting Equations 3-30 into Equations 3-28 and 3-29 gives

$$V_X = \frac{1}{\sqrt{2}}\,(A_{11} + i A_{21})\,v_{-1} - \frac{1}{\sqrt{2}}\,(A_{11} - i A_{21})\,v_{+1} + A_{31}\,v_0 \qquad \text{(3-31 a)}$$

$$V_Y = \frac{1}{\sqrt{2}}\,(A_{12} + i A_{22})\,v_{-1} - \frac{1}{\sqrt{2}}\,(A_{12} - i A_{22})\,v_{+1} + A_{32}\,v_0 \qquad \text{(3-31 b)}$$

$$V_{\pm 1} = \mp \frac{1}{\sqrt{2}}\left[\,\frac{1}{\sqrt{2}}(A_{11} \pm i A_{12} + i A_{21} \mp A_{22})v_{-1} - \frac{1}{\sqrt{2}}\,(A_{11} \pm i A_{12} - i A_{21} \pm A_{22})v_{+1}\right.$$

$$\left. + \,(A_{31} \pm A_{32})\,v_0\right] \qquad \text{(3-31 c)}$$

$$V_0 = V_Z = \frac{1}{\sqrt{2}}\,(A_{13} + i A_{23})v_{-1} - \frac{1}{\sqrt{2}}\,(A_{13} - i A_{23})v_{+1} + A_{33}v_0 \qquad \text{(3-31 d)}$$

The orientational average of a function $F(\theta, \phi, \psi)$ over the Eulerian angles is

$$\langle F(\theta, \phi, \psi)\rangle = \frac{\int_{\psi=0}^{2\pi}\int_{\phi=0}^{2\pi}\int_{\theta=0}^{2\pi} F(\theta, \phi, \psi)\, d\tau}{\int_{\psi=0}^{2\pi}\int_{\phi=0}^{2\pi}\int_{\theta=0}^{2\pi} d\tau} \tag{3-32}$$

Referring to the diagrams of the Euler angles (Figure 3-5) and Equations 3-24 a-c, matrix **D** is applied to the laboratory reference frame followed by matrix **C,** then matrix **B.** Axis X', which is angle ϕ away from axis X about axis Z, remains perpendicular to Z and z. The angle between X and the projection of z on the XY plane is $\pi/2 - \phi$. In a molecular system of axial symmetry (as D_{4h}, D_{3h}) molecular x and y (both perpendicular to z) are equivalent, thus arbitrary linear combinations of x and y are allowable. Angle ψ is then chosen contingent on the presence of axial symmetry along molecular z as $\pi/2$ for convenience. This results in molecular y being perpendicular to both molecular z and laboratory Z, i.e., it coincides with X' resulting from the application of **D.**

The magnetic dipole matrix element $\langle \mathrm{A}_\alpha | \hat{\mu}_Z | \mathrm{B}_\beta \rangle$ is independent of ϕ since Zeeman splitting is along laboratory Z, therefore

$$\langle F(\phi)\rangle = \frac{\int_0^{2\pi} F(\phi)\, d\phi}{\int_0^{2\pi} d\phi} = \frac{1}{2\pi}\int_0^{2\pi} F(\phi)\, d\phi \tag{3-33}$$

from which follows

$$\langle \cos^2\phi \rangle = \frac{1}{2\pi}\int_0^{2\pi} \cos^2\phi \; d\phi = \frac{1}{2} \tag{3-34 a}$$

$$\langle \sin^2\phi \rangle = \frac{1}{2\pi}\int_0^{2\pi} \sin^2\phi \; d\phi = \frac{1}{2} \tag{3-34 b}$$

$$\langle \sin\phi \; \cos\phi \rangle = \frac{1}{2\pi}\int_0^{2\pi} \sin\phi \; \cos\phi \; d\phi = 0 \tag{3-34 c}$$

Application of Euler Transforms to MCD/MLD Equations

Application of Equations 3-31 and 3-27 to the magnetic dipole transition moment results in

$$\left\langle \mathrm{A}_\alpha \middle| \hat{\mu}_\mathrm{Z} \middle| \mathrm{B}_\beta \right\rangle = \frac{i \sin\theta}{\sqrt{2}} \left[\mathrm{e}^{-i\psi} \left\langle \mathrm{i} \middle| \hat{\mu}_{-1} \middle| \mathrm{J'M'} \right\rangle + \mathrm{e}^{i\psi} \left\langle \mathrm{i} \middle| \hat{\mu}_{+1} \middle| \mathrm{J'M'} \right\rangle \right] + \cos\theta \left\langle \mathrm{i} \middle| \hat{\mu}_0 \middle| \mathrm{J'M'} \right\rangle \tag{3-35}$$

Since $\psi = \pi/2$ (arbitrarily)

$$ie^{\pm i\psi} = i\,(\cos\psi \pm i \sin\psi) = i\cos\frac{\pi}{2} \pm \sin\frac{\pi}{2} = \mp 1 \tag{3-36}$$

giving

$$\left\langle \mathrm{A}_\alpha \middle| \hat{\mu}_\mathrm{Z} \middle| \mathrm{B}_\beta \right\rangle = \frac{\sin\theta}{\sqrt{2}} \left[\left\langle \mathrm{i} \middle| \hat{\mu}_{-1} \middle| \mathrm{J'M'} \right\rangle - \left\langle \mathrm{i} \middle| \hat{\mu}_{+1} \middle| \mathrm{J'M'} \right\rangle \right] + \cos\theta \left\langle \mathrm{i} \middle| \hat{\mu}_0 \middle| \mathrm{J'M'} \right\rangle \tag{3-37}$$

Applying Equations 3-13, 3-14, 3-15, and 3-16

$$\left\langle \mathrm{A}_\alpha \middle| \hat{\mu}_\mathrm{Z} \middle| \mathrm{B}_\beta \right\rangle = \sum_{\mathrm{M}_1} \sum_{\mathrm{M}_2} \left\langle \mathrm{A}_\alpha \middle| \mathrm{JM}_2 \right\rangle \left\langle \mathrm{JM}_1 \middle| \mathrm{B}_\beta \right\rangle \left[\frac{\sin\theta}{\sqrt{2}} \left(\left\langle \mathrm{JM}_2 \middle| \hat{\mu}_{-1} \middle| \mathrm{JM}_1 \right\rangle - \left\langle \mathrm{JM}_2 \middle| \hat{\mu}_{+1} \middle| \mathrm{JM}_1 \right\rangle \right) \right. \\ \left. + \cos\theta \left\langle \mathrm{JM}_2 \middle| \hat{\mu}_0 \middle| \mathrm{JM}_1 \right\rangle \right] \tag{3-38}$$

Evaluating the general MCD expression of Equation 3-18 with Equations 3-31 c and 3-27

gives

$$\left[\left| \left\langle \mathrm{i} \middle| \hat{\mathrm{M}}_{-1} \middle| \mathrm{J'M'} \right\rangle \right|^2 - \left| \left\langle \mathrm{i} \middle| \hat{\mathrm{M}}_{+1} \middle| \mathrm{J'M'} \right\rangle \right|^2 \right] = \cos\theta \left[\left| \left\langle \mathrm{i} \middle| \hat{\mathrm{m}}_{-1} \middle| \mathrm{J'M'} \right\rangle \right|^2 - \left| \left\langle \mathrm{i} \middle| \hat{\mathrm{m}}_{+1} \middle| \mathrm{J'M'} \right\rangle \right|^2 \right] \\ - \sqrt{2}\, \sin\theta\, \Re e \left[ie^{-i\psi} \left(\left\langle \mathrm{i} \middle| \hat{\mathrm{m}}_{-1} \middle| \mathrm{J'M'} \right\rangle \left\langle \mathrm{i} \middle| \hat{\mathrm{m}}_0^{*} \middle| \mathrm{J'M'} \right\rangle + \left\langle \mathrm{i} \middle| \hat{\mathrm{m}}_0 \middle| \mathrm{J'M'} \right\rangle \left\langle \mathrm{i} \middle| \hat{\mathrm{m}}_{+1}^{*} \middle| \mathrm{J'M'} \right\rangle \right) \right] \tag{3-39}$$

Since $\hat{\mathrm{m}}_0^{*} = \hat{\mathrm{m}}_\mathrm{z} = \hat{\mathrm{m}}_0$ and $\hat{\mathrm{m}}_{\pm 1}^{*} = \left(\mp 1/\sqrt{2}\right)\left(\hat{\mathrm{m}}_\mathrm{x} \mp i\hat{\mathrm{m}}_\mathrm{y}\right) = -\hat{\mathrm{m}}_{\mp 1}$ and $\psi = \pi/2$, with $\Re\mathrm{e}$ representing the real part of the argument, expansion as in Equation 3-19 gives

$$\Delta \mathrm{A}_C = \frac{\gamma}{Z} \sum_{\mathrm{i}} e^{-\frac{E_\mathrm{i}}{kT}} \sum_{\mathrm{M'}} \sum_{\mathrm{M}_1} \sum_{\mathrm{M}_2} \left\langle \mathrm{JM}_1 \middle| \mathrm{i} \right\rangle \left\langle \mathrm{i} \middle| \mathrm{JM}_2 \right\rangle \left\{ \cos\theta \left[\left\langle \mathrm{JM}_2 \middle| \hat{\mathrm{m}}_{+1} \middle| \mathrm{J'M'} \right\rangle \left\langle \mathrm{J'M'} \middle| \hat{\mathrm{m}}_{-1} \middle| \mathrm{JM}_1 \right\rangle \right. \right. \\ \left. - \left\langle \mathrm{JM}_2 \middle| \hat{\mathrm{m}}_{-1} \middle| \mathrm{J'M'} \right\rangle \left\langle \mathrm{J'M'} \middle| \hat{\mathrm{m}}_{+1} \middle| \mathrm{JM}_1 \right\rangle \right] \sqrt{2} \sin\theta\, \Re\mathrm{e} \left[\left\langle \mathrm{JM}_2 \middle| \hat{\mathrm{m}}_{-1} \middle| \mathrm{J'M'} \right\rangle \left\langle \mathrm{J'M'} \middle| \hat{\mathrm{m}}_0 \middle| \mathrm{JM}_1 \right\rangle \right. \\ \left. \left. - \left\langle \mathrm{JM}_2 \middle| \hat{\mathrm{m}}_0 \middle| \mathrm{J'M'} \right\rangle \left\langle \mathrm{J'M'} \middle| \hat{\mathrm{m}}_{-1} \middle| \mathrm{JM}_1 \right\rangle \right] \right\} \tag{3-40}$$

A similar evaluation of the general operator expression for MLD in Equation 3-20 using Equations 3-31 a, 3-31 b, and 3-27 then equating $C + C^{*} = 2\ \Re\mathrm{e}\ (C)$ leads to

$$\begin{gathered}
\left|\langle \mathrm{i}|\hat{\mathrm{M}}_{Z}|\mathrm{J'M'}\rangle\right|^{2} - \left|\langle \mathrm{i}|\hat{\mathrm{M}}_{X}|\mathrm{J'M'}\rangle\right|^{2} = \frac{1}{2}\left[\sin^{2}\theta - \cos^{2}\phi - \cos^{2}\theta\sin^{2}\phi\right]\Big(\left|\langle \mathrm{i}|\hat{\mathrm{m}}_{-1}|\mathrm{J'M'}\rangle\right|^{2} \\
\left|\langle \mathrm{i}|\hat{\mathrm{m}}_{+1}|\mathrm{J'M'}\rangle\right|^{2}\Big) + \left[\ \cos^{2}\theta - \sin^{2}\phi\sin^{2}\theta\ \right] \left|\langle \mathrm{i}|\hat{\mathrm{m}}_{0}|\mathrm{J'M'}\rangle\right|^{2}\ \Re\mathrm{e}\ \big[\ \cos(2\psi) \\
(\cos^{2}\theta\sin^{2}\phi - \cos^{2}\phi - \sin^{2}\theta) + 4\cos\psi\ \sin\psi\ \cos\phi\ \sin\phi\ \cos\theta \\
+ 2i(\sin\psi\cos\psi\,(\cos^{2}\theta\sin^{2}\theta - \cos^{2}\theta\sin^{2}\phi) + \cos\phi\sin\phi\cos(2\psi))\ \langle \mathrm{i}|\hat{\mathrm{m}}_{-1}|\mathrm{J'M'}\rangle \\
\langle \mathrm{i}|\hat{\mathrm{m}}^{*}_{+1}|\mathrm{J'M'}\rangle\ \big] - \sqrt{2}\ \Re e\ \big[\ e^{-i\psi}\sin\theta\big(\sin\phi\cos\phi - i\cos\theta\,[1+\sin^{2}\varphi]\big)\langle \mathrm{i}|\hat{\mathrm{m}}_{-1}|\mathrm{J'M'}\rangle \\
\langle \mathrm{i}|\hat{\mathrm{m}}^{*}_{0}|\mathrm{J'M'}\rangle\ +\ \langle \mathrm{i}|\hat{\mathrm{m}}_{0}|\mathrm{J'M'}\rangle\ \langle \mathrm{i}|\hat{\mathrm{m}}^{*}_{+1}|\mathrm{J'M'}\rangle\ \big]
\end{gathered} \tag{3-41}$$

Application of the relations of Equations 3-34 and 3-35 and expressing generally as Equation 3-22 gives

$$\begin{gathered}
\Delta \mathrm{A}_{L} = \frac{\gamma}{Z}\sum_{\mathrm{i}} e^{-\frac{E_{\mathrm{i}}}{kT}}\ \sum_{\mathrm{M'}}\sum_{\mathrm{M_1}}\sum_{\mathrm{M_2}}\langle \mathrm{J\,M_1}|\mathrm{i}\rangle\langle \mathrm{i}|\mathrm{JM_2}\ \rangle\Big\{\ \frac{1}{2}\Big[\ \sin^{2}\theta\ \text{-}\ \frac{1}{2}(1\ +\cos^{2}\theta\,)\Big] \\
\big(\ \text{-}\ \langle \mathrm{JM_2}|\hat{\mathrm{m}}_{-1}|\mathrm{J'M'}\rangle\ \langle \mathrm{J'M'}|\hat{\mathrm{m}}_{+1}|\mathrm{JM_1}\rangle\ -\ \langle \mathrm{JM_2}|\hat{\mathrm{m}}_{+1}|\mathrm{J'M'}\rangle\ \langle \mathrm{J'M'}|\hat{\mathrm{m}}_{-1}|\mathrm{JM_1}\rangle\ \big) \\
+(\cos^{2}\theta - \frac{1}{2}\sin^{2}\theta\,)\langle \mathrm{JM_2}|\hat{\mathrm{m}}_{0}|\mathrm{J'M'}\rangle\ \langle \mathrm{J'M'}|\hat{\mathrm{m}}_{0}|\mathrm{JM_1}\rangle - \Re\mathrm{e}\ \Big[\ (\frac{1}{2}(\cos^{2}\theta - 1) - \sin^{2}\theta) \\
\langle \mathrm{JM_2}|\hat{\mathrm{m}}_{-1}|\mathrm{J'M'}\rangle\ \langle \mathrm{J'M'}|\hat{\mathrm{m}}_{-1}|\mathrm{JM_1}\rangle\ \Big] + \sqrt{2}\ \Re\mathrm{e}\ \Big[\frac{3i}{2}\sin\theta\cos\theta(<\langle \mathrm{JM_2}|\hat{\mathrm{m}}_{-1}|\mathrm{J'M'}\rangle\ \langle \mathrm{J'M'}|\hat{\mathrm{m}}_{0}|\mathrm{JM_1}\rangle \\
\langle \mathrm{JM_2}|\hat{\mathrm{m}}_{0}|\mathrm{J'M'}\rangle\ \langle \mathrm{J'M'}|\hat{\mathrm{m}}_{-1}|\mathrm{JM_1}\rangle\ )\Big]\Big\}
\end{gathered} \tag{3-42}$$

Wigner-Eckart Theorem

Application of these quite general expressions for the magnetic dipole moment (Equation 3-35), MCD dispersion (Equation 3-40), and MLD dispersion (Equation 3-42) requires evaluation of the transition moment integrals (matrix elements) for the specific J'←J transitions. Simplification of this task can be achieved by taking advantage of all molecular point group symmetry operations for the absorbing center. High symmetry coefficients derived from vector coupling coefficients are utilized in the method of Wigner-Eckart reduction to derive the transition moment integrals. The resultant is a product of symmetry related coefficients and a constant 'reduced' matrix element which is symmetry independent. Derivations of the Wigner-Eckart Theorem can be found in Piepho and Schatz,[33] Watanabe,[57] Griffith[59] and Wigner.[60]

For functions ϕ_α^{a} and ψ_β^{b} belonging to the same basis in a particular point group,

$$\int \phi_\alpha^{*\mathrm{a}}\, \psi_\beta^{\mathrm{b}}\, \delta\, \tau = \left\langle \phi_\alpha^{\mathrm{a}} \mid \psi_\beta^{\mathrm{b}} \right\rangle = \left\langle \mathrm{a}_\alpha \mid \mathrm{b}_\beta \right\rangle \tag{3-43}$$

Perform an orthogonal transformation $\mathfrak{R}$ on both functions

$$\left\langle \mathrm{a}_\alpha \mid \mathrm{b}_\beta \right\rangle = \left\langle \mathfrak{R}\mathrm{a}_\alpha \mid \mathfrak{R}\mathrm{b}_\beta \right\rangle \tag{3-44}$$

$$= \sum_{\alpha',\beta'} \mathbf{D}^{\mathrm{a}}(\mathrm{R})^{*}_{\alpha',\alpha}\; \mathbf{D}^{\mathrm{b}}(\mathrm{R})_{\beta',\beta} \left\langle \mathrm{a}_{\alpha'} \mid \mathrm{b}_{\beta'} \right\rangle \tag{3-45}$$

where $\mathbf{D}^{\mathrm{a}}$ and $\mathbf{D}^{\mathrm{b}}$ are unitary irreps. Summing both sides for group order h over dimension l_{a} of irrep a and applying the Great Orthogonality Theorem and then summing over β'

$$\sum_{\mathfrak{R}} \left\langle \mathfrak{R}\mathrm{a}_\alpha \mid \mathfrak{R}\mathrm{b}_\beta \right\rangle = h \left\langle \mathrm{a}_\alpha \mid \mathrm{b}_\beta \right\rangle$$

$$= \sum_{\alpha'\,\beta'} \frac{h}{l_{\mathrm{a}}} \delta_{\mathrm{ab}}\, \delta_{\alpha'\beta'}\, \delta_{\alpha\beta} \left\langle \mathrm{a}_{\alpha'} \mid \mathrm{b}_{\beta'} \right\rangle \tag{3-46}$$

$$\left\langle \mathrm{a}_\alpha \mid \mathrm{b}_\beta \right\rangle = \delta_{\mathrm{ab}}\, \delta_{\alpha\beta}\, l_{\mathrm{a}}^{-1} \sum_{\alpha'}^{l_a} \left\langle \mathrm{a}_{\alpha'} \mid \mathrm{a}_{\alpha'} \right\rangle \tag{3-47}$$

This result is the basis for the Wigner-Eckart Theorem[33,57] and states that functions in different rows of nonequivalent irreps are orthogonal. The general Wigner-Eckart Theorem is

$$\left\langle \mathrm{a}_\alpha \left| O_\phi^f \right| \mathrm{b}_\beta \right\rangle = \sum_r \left(r\, \mathrm{a}_\alpha \middle| f\phi, \mathrm{b}_\beta \right) |\mathrm{a}|^{-\frac{1}{2}} \left\langle \mathrm{a} \middle\| O^f \middle\| \mathrm{b} \right\rangle_r$$

$$= \sum_r (f\phi\,, \mathrm{b}_\beta | r\, \mathrm{a}_\alpha)^{*}\; |\mathrm{a}|^{-\frac{1}{2}}\; \left\langle \mathrm{a} \middle\| O^f \middle\| \mathrm{b} \right\rangle \tag{3-48}$$

Final Reduced Expressions for MCD and MLD

The final derived expressions for the three critical terms for saturation analysis are obtained Wigner-Eckart reductions (vide infra). Each is a phased product of a symmetry independent reduced matrix element, the JM basis wavefunctions, and the appropriate 3JM or 3JM^2 Wigner-Eckart coefficients reflecting the symmetry environment.

Magnetic dipole expression after Wigner-Eckart reductions:

$$\langle A_\alpha | \hat{\mu}_Z | B_\beta \rangle = \langle J \| \hat{\mu} \| J \rangle \sum_{M_1}\sum_{M_2} \langle A_\alpha | J M_2 \rangle \langle J M_2 | B_\beta \rangle (-1)^{J-M} \left[\frac{\sin\theta}{\sqrt{2}} \left(\begin{pmatrix} J & 1 & J \\ -M_2 & -1 & M_1 \end{pmatrix} \delta_{M_1,M_2+1} - \begin{pmatrix} J & 1 & J \\ -M_2 & +1 & M_1 \end{pmatrix} \delta_{M_1,M_2-1} \right) + \cos\theta \begin{pmatrix} J & 1 & J \\ -M_2 & 0 & M_1 \end{pmatrix} \delta_{M_1,M_2} \right] \tag{3-49}$$

To solve for the reduced matrix element, begin with a diagonal matrix element in the ground state manifold. The Zeeman perturbation is applied to the ground state only, since under normal conditions population of only the ground state energy level occurs (i.e., ΔJ = 0).

$$\langle JM | \hat{\mu}_0 | JM \rangle = -g\mu_B M = \left(\frac{J}{M} \right) \begin{pmatrix} J & 1 & J \\ -M & 0 & M \end{pmatrix} \langle JM \| \hat{\mu} \| JM \rangle \tag{3-50}$$

$$\langle JM \| \hat{\mu} \| JM \rangle = -\left(\frac{J}{M} \right) \begin{pmatrix} J & 1 & J \\ -M & 0 & M \end{pmatrix}^{-1} g\mu_B M \tag{3-51}$$

Choosing M = J arbitrarily

$$\langle J \| \hat{\mu} \| J \rangle = [J(2J+1)(J+1)]^{-\frac{1}{2}} \; g\mu_B \tag{3-52}$$

Final Magnetic Dipole Expression:

$$\langle A_\alpha | \hat{\mu}_z | B_\beta \rangle = -(-1)^{J-M_2} \, [J(2J+1)(J+1)]^{\frac{1}{2}} \, g\,\mu_B \sum_{M_1}\sum_{M_2} \langle A_\alpha | J M_2 \rangle \langle J M_1 | B_\beta \rangle \times \left[\frac{\sin\theta}{\sqrt{2}} \left(\begin{pmatrix} J & 1 & J \\ -M_2 & -1 & M_1 \end{pmatrix} \delta_{M_1,M_2+1} - \begin{pmatrix} J & 1 & J \\ -M_2 & 1 & M_1 \end{pmatrix} \delta_{M_1,M_2-1} \right) + \cos\theta \begin{pmatrix} J & 1 & J \\ -M_2 & 0 & M_1 \end{pmatrix} \delta_{M_1,M_2} \right] \tag{3-53}$$

Contrast this with Equation 3-1 for the Zeeman splitting independent of orientation

$$E_z = g\,\mu_B\,\mathbf{B}\,M_J \tag{3-1}$$

Further application of the Wigner-Eckart reductions to the general MCD and MLD expressions allows the theoretical dispersion to be expressed purely in terms of the JM basis set wavefunctions independent of symmetry considerations. The reduced MCD and MLD expressions are given as follows:

Reduced MCD Expression:

$$\begin{aligned}\Delta A_C = \frac{\gamma}{Z}\left|\langle J\|\hat{m}\|J'\rangle\right|^2 \sum_{i} e^{-\frac{E_i}{kT}} \sum_{M'} \Bigg[& \sum_{M_1}\left|\langle JM_1|i\rangle\right|^2 \cos\theta \left\{ \begin{pmatrix} J & 1 & J' \\ -M_1 & -1 & M' \end{pmatrix}^2 \delta_{M_1,M'-1} \right. \\ & \left. - \begin{pmatrix} J & 1 & J' \\ -M_1 & 1 & M' \end{pmatrix}^2 \delta_{M_1,M'+1} \right\} + \sum_{M_1}\sum_{M_2} \langle JM_1|i\rangle\langle i|JM_2\rangle\ \sqrt{2}\,\sin\theta \begin{pmatrix} J & 1 & J' \\ -M_1 & 0 & M' \end{pmatrix} \delta_{M_1,M'} \\ & \times \left[\begin{pmatrix} J & 1 & J' \\ -M_2 & -1 & M' \end{pmatrix} \delta_{M_2,M'-1} + \begin{pmatrix} J & 1 & J' \\ -M_2 & 1 & M' \end{pmatrix} \delta_{M_2,M'+1} \right] \Bigg]\end{aligned}$$

(3-54)

Reduced MLD Expression:

$$\begin{aligned}\Delta A_L = \frac{\gamma}{Z}\left|\langle J\|\hat{m}\|J'\rangle\right|^2 \sum_{i} e^{-\frac{E_i}{kT}} \sum_{M'} \Bigg[& \sum_{M_1}\left|\langle JM_1|i\rangle\right|^2 \left\{ \left(\cos^2\theta - \frac{\sin^2\theta}{2}\right) \begin{pmatrix} J & 1 & J' \\ -M_1 & 0 & M' \end{pmatrix}^2 \right. \\ & \times\ \delta_{M_1,M'} + \left(\frac{1}{4}\sin^2\theta - \frac{1}{2}\cos^2\theta\right) \left[\begin{pmatrix} J & 1 & J' \\ -M_1 & -1 & M' \end{pmatrix}^2 \delta_{M_1,M'+1} + \begin{pmatrix} J & 1 & J' \\ -M_1 & 1 & M' \end{pmatrix}^2 \delta_{M_1,M'-1} \right] \Bigg\} \\ & - \sum_{M_1}\sum_{M_2} \langle JM_1|i\rangle\langle i|JM_2\rangle \frac{3}{2}\sin^2\theta \begin{pmatrix} J & 1 & J' \\ -M_2 & -1 & M' \end{pmatrix} \begin{pmatrix} J & 1 & J' \\ -M_1 & 1 & M' \end{pmatrix} \delta_{M_1,M'+1}\,\delta_{M_2,M'-1} \Bigg]\end{aligned}$$

(3-55)

Numerical Analysis

Equation 3-30 requires an integration over all three Eulerian angles, θ, ψ, and ϕ to account fully for orientational averaging of the entire system. The procedure just completed integrates over the angles ϕ and ψ, but not over θ. There is no apparent way to perform an integration analytically over θ. It is therefore necessary to perform the integration numerically in sufficient intervals to mimic the molecular environment. Since it is assumed the 'supermolecule' systems being dealt with in either of the symmetry classifications (octahedral, tetragonal, or trigonal) will maintain at least axial symmetry (i.e., D_{4h} or D_{3h} as the lowest symmetry configurations), then this restriction to axial symmetry with a molecular horizontal mirror plane permits the limits of integration to be set from 0 to $\pi/2$ radians.

The number of increments required to closely approximate the actual behavior of the molecular system to be confident about the symmetry assignments is not readily obvious. A reasonable conclusion would dictate sufficiently small intervals to become microscopic in size -- $\sim 10^3$ increments. The extreme would certainly be on the atomic scale, which would require approximately 10^{14}-10^{15} increments. A calculation based on reasonable parameters justified by previous experiments[61] to determine the amounts of metal vs. rare gas present in a typical matrix demonstrated at least 250 increments were necessary to gain accuracy to two significant figures and 10^3 increments were necessary to gain accuracy to three significant figures. Preference would be for 10^4 increments, but this proved costly in computer CPU requirements.

Computer software has been written to apply the above equations to an analysis of experimental data. The software was written originally in compiled basic [QuickBASIC 4.5] and FORTRAN 77 / VS2. It was then ported to the C^{++} computer language. Appendix A provides a listing of the C^{++} code.

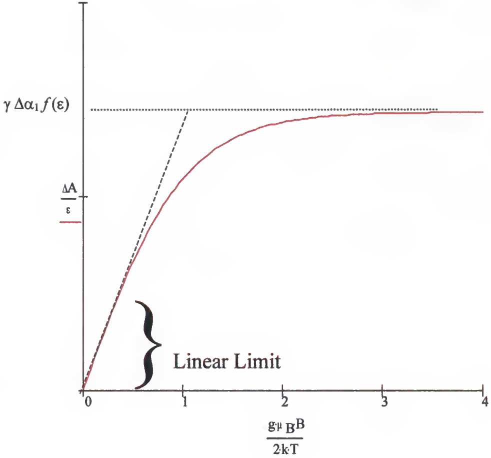

$$\left(\frac{\Delta A'}{\varepsilon}\right)_{C_{sat}} = \gamma \Delta\alpha_1 f(\varepsilon) \tanh\left(\frac{g\mu_B B}{2kT}\right)$$

Figure 3-1. MCD dependence on **B** and T. Depicted is the saturation of a Kramers doublet and the linear limit region of **B**/T.

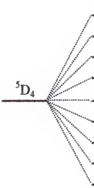

T	20 K	10 K	4.2 K	1.4 K	Zeeman
kT	13.9 cm^{-1}	6.95 cm^{-1}	2.92 cm^{-1}	0.973 cm^{-1}	Energy
	8.00E-01	6.41E-01	3.48E-01	4.21E-02	1.541 cm^{-1}
	8.24E-01	6.79E-01	3.97E-01	6.27E-02	1.156 cm^{-1}
	8.48E-01	7.18E-01	4.53E-01	9.31E-02	0.771 cm^{-1}
	8.72E-01	7.56E-01	5.19E-01	1.38E-01	0.385 cm^{-1}
	8.96E-01	8.01E-01	5.92E-01	2.05E-01	0.000
	9.20E-01	8.46E-01	6.72E-01	3.04E-01	-0.385 cm^{-1}
	9.44E-01	8.91E-01	7.70E-01	4.53E-01	-0.771 cm^{-1}
	9.68E-01	9.42E-01	8.78E-01	6.73E-01	-1.156 cm^{-1}
	1.00E+00	1.00E+00	1.00E+00	1.00E+00	-1.541 cm^{-1}

0.55 T $g\mu_B B = 0.385\ cm^{-1}$

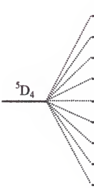

	1.99E-01	3.97E-02	4.62E-04	9.90E-11	11.208 cm^{-1}
	2.43E-01	5.96E-02	1.21E-03	1.76E-09	8.406 cm^{-1}
	2.99E-01	8.90E-02	3.15E-03	3.14E-08	5.604 cm^{-1}
	3.65E-01	1.33E-01	8.23E-03	5.59E-07	2.802 cm^{-1}
	4.46E-01	2.00E-01	2.15E-02	9.96E-06	0.000
	5.46E-01	2.98E-01	5.62E-02	1.77E-04	-2.802 cm^{-1}
	6.67E-01	4.46E-01	1.47E-01	3.16E-03	-5.604 cm^{-1}
	8.17E-01	6.68E-01	3.83E-01	5.62E-02	-8.406 cm^{-1}
	1.00E+00	1.00E+00	1.00E+00	1.00E+00	-11.208 cm^{-1}

4 T $g\mu_B B = 2.802\ cm^{-1}$

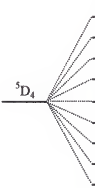

	2.36E-03	5.59E-06	3.12E-13	3.02E-38	42.02 cm^{-1}
	5.04E-03	2.54E-05	1.14E-11	1.48E-33	31.52 cm^{-1}
	1.07E-02	1.15E-04	4.17E-10	7.25E-29	21.02 cm^{-1}
	2.28E-02	5.21E-04	1.53E-08	3.53E-24	10.51 cm^{-1}
	4.86E-02	2.36E-03	5.58E-09	1.74E-19	0.00
	1.04E-01	1.07E-02	2.04E-05	8.52E-15	-10.51 cm^{-1}
	2.21E-01	4.86E-02	7.48E-04	4.17E-10	-21.02 cm^{-1}
	4.70E-01	2.20E-01	2.74E-02	2.04E-05	-31.52 cm^{-1}
	1.00E+00	1.00E+00	1.00E+00	1.00E+00	-42.02 cm^{-1}

15 T $g\mu_B B = 10.5\ cm^{-1}$

Figure 3-2. Normalized Boltzmann population distribution for Fe(0) in free atom $^5D_4$ ground state at various temperatures (T °K) and magnetic field strengths (**B** Tesla).

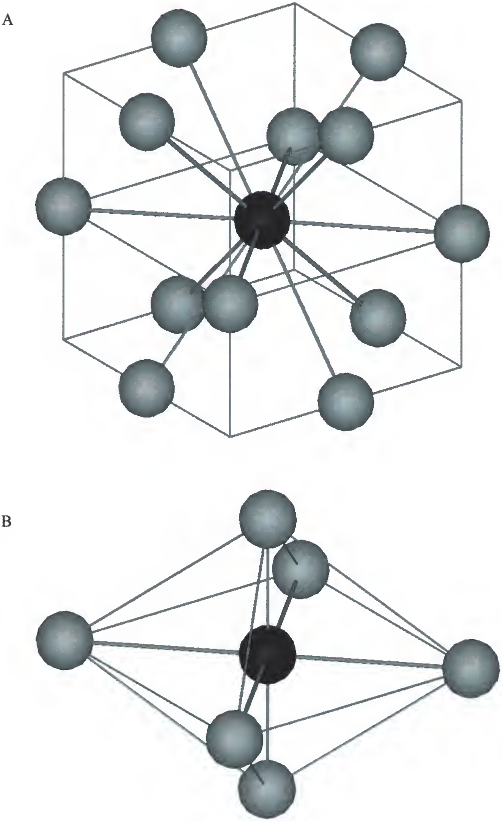

Figure 3-3. Octahedral symmetry sites. A) MX_{12} substitutional. B) MX_6 interstitial.

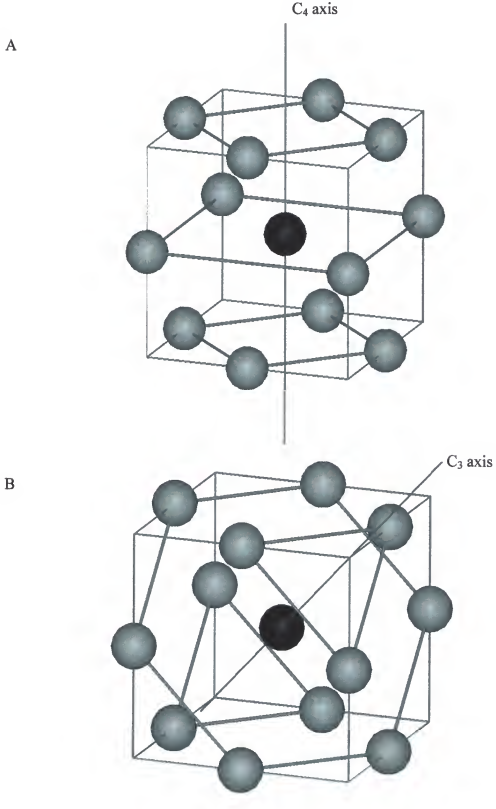

Figure 3-4. Lower symmetry models of MX_{12} system. A) Tetragonal: relative extension or compression along the C_4 axis. B) Trigonal: relative extension or compression along the C_3 axis.

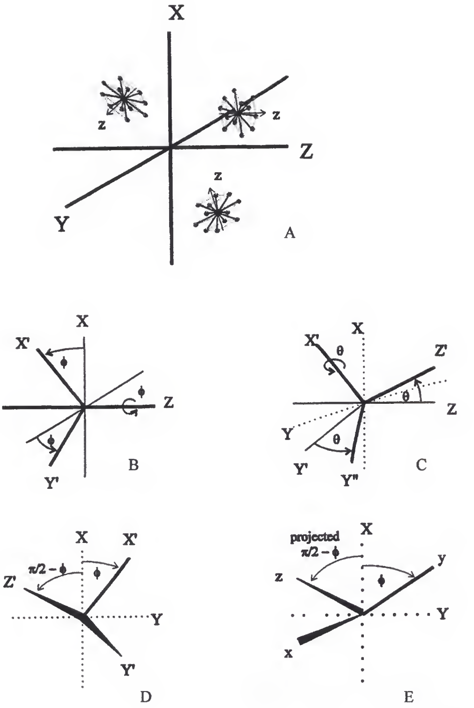

Figure 3.5. Relation of molecular xyz reference axes to laboratory XYZ axes via Euler angles, ϕ, θ, and ψ. A) Randomly oriented MX_{12} 'supermolecules' of D_{4h} symmetry. B) Euler matrix **D** rotates about Z by ϕ. C) Euler matrix **C** rotates about X′ by θ. D) Projection of Z′ in XY plane. E) $\psi = \pi/2$ arbitrarily for axial symmetry which maps $Y' \Rightarrow X'$.

CHAPTER 4
THE MCD AND MLD SPECTRA OF Fe(0) ATOMS IN KRYPTON MATRIX

Introduction

The MCD analysis of Fe(0) atoms isolated in argon, krypton, and xenon matrices has been previously reported by J. ShahksEmampour et al.[22] Their research addressed the complexity of the electronic absorption spectra observed for Fe(0) isolated in these matrix environments. The objective was to investigate the magnitude of spin-orbit coupling and the extent of matrix lattice interactions with the Fe(0) atom. Perturbations of the Fe(0) electronic energy levels caused by rare gas atoms comprising the lattice cage surrounding the Fe(0) atom could result in a Jahn-Teller effect and/or line broadening/splitting due to geometrical distortion of the Fe(0) atomic orbitals. Earlier investigations of Fe(0) in Ar, Kr, Xe, and N_2 by Mann and Broida[7] provided an incomplete assignment of the electronic transitions using gas phase data[11] as a guide for correlation. The MCD spectra obtained by ShahksEmampour et al. permitted absolute state assignments of the transitions. Temperature dependent studies and moments analyses of Fe(0) absorption bands in a Kr matrix by Micklitz and Barrett[62] allowed them to conclude there was no quenching of the Fe atoms' orbital angular momentum which would present as a Jahn-Teller effect. The matrix crystal field effect was deemed negligible. The MCD data of ShahksEmampour et al. supported these conclusions.

Table 4-1. MLD and MCD parametric expressions for the intensity and sign of atomic transitions for $\Delta J = 1, 0, -1$.

J'	$\mathcal{G}_0/\mathcal{D}_0$ MLD[a,c]	$\mathcal{C}_0/\mathcal{D}_0$ MCD[b,c]
J	$\frac{(2J+3)(2J-1)}{20} g_A^2$	g_A
J+1	$\frac{-J(2J-1)}{20} g_A^2$	$-Jg_A$
J-1	$-\frac{(J+1)(2J+3)}{20} g_A^2$	$(J+1)g_A$

Adapted from: Marek Kreglewski and Martin Vala. Theory of magnetic linear dichroism. Application to matrix-isolated atomic transitions. Tables I and II, pg. 5418, J. Chem. Phys. 74, 5411 (1981)

[a] Units μ_B^2 ($\mu_B \equiv$ Bohr magneton)

[b] Units μ_B ($\mu_B \equiv$ Bohr magneton)

[c] $\mathcal{D}_0 = (1/27)\left|\langle {}^5LJ'\|m\|{}^5D_4\rangle\right|^2$

Table 4-1 lists the calculated Faraday parametric ratios for $\mathcal{G}_0/\mathcal{D}_0$ and $\mathcal{C}_0/\mathcal{D}_0$ utilized in determining the assignment of transitions for paramagnetic species. Note the sign of each term, which is dependent on ΔJ. The predicted transitions from Table 4-1 do indeed appear in the experimental samples analyzed in this study. Experimentally, increasing the magnitude of the magnetic field greatly affects the MLD spectrum making it possible to observe otherwise very weak transitions. This technique has allowed the assignment of a few previously unseen or undetermined weak absorptions in the Fe/Kr ${}^5D_4$ ground state spectrum, as the z^5F_4, y^5F_4, x^5F_4, and w^5D_4 transitions. A weak MCD shoulder on the x^5D_3 transition appears sharply in the analog MLD spectrum.

Spin-orbit interaction splits the gas phase ${}^5D$ ground term ($3d^64s^2$) resulting in a ${}^5D_4$ ground state with spin-orbit constant $\lambda \approx 104$ cm^{-1} (Figure 4-1). The separation between the ${}^5D_4$ ground state and the ${}^5D_3$ state is 416 cm^{-1}. The results of Micklitz and

Barrett and laser induced fluorescence (LIF) studies by McKenzie et al.[63] support the conclusion that matrix crystal field effects and/or Jahn-Teller effects are small compared to the spin-orbit splitting. They deduced that the total difference in the ^5D ground terms due to crystal field or Jahn-Teller effects was less than 9 cm^{-1}, i.e., significantly less than the splitting due to free atom spin-orbit interactions. The experimental bandwidths of ~50 cm^{-1} preclude the resolution of such small splitting. The $\mathcal{C}_0$ and $\mathcal{D}_0$ MCD terms were calculated for transitions from the ground state J = 4 to excited states J' = 3, 4, and 5. A moments analysis was performed on the $z^5P_3 \leftarrow {}^5D_4$ transition[22], resulting in determination of $\mathcal{C}_0/\mathcal{D}_0$ from the slope of $\langle \Delta A \rangle_0 / \langle A \rangle_0$ vs 1/T as 8.2 ± 0.8. This compares well with the theoretical value of 7.5.[22] Since this ratio is linearly proportional to the ground state Lande g value, it was concluded that there is no obvious quenching of the orbital angular momentum, indicating there is no Jahn-Teller effect operative in the ground state.

Comparing the free atom theoretical $\mathcal{C}_0$ and $\mathcal{D}_0$ values with values calculated for an octahedral crystal field model showed a variance of only 2% at 10 K and of 0.5% at 20 K. The coefficients are from Griffith (Table A19)[59] and were applied to a $|JM_J\rangle$ basis. The effect caused by an octahedral field would have little impact on MCD parameters derived from spectra obtained at these temperatures. It should be noted the experimental conditions involved data collection at ~12 – 30 K and a magnetic field of 0.55 Tesla. Thus, the MCD data falls within the linear limit regime of MCD theory (Figure 3-1) and permits evaluation of the $\mathcal{C}_0/\mathcal{D}_0$ ratio from the slope of $\langle \Delta A \rangle_0 / \langle A \rangle_0$ vs 1/T.

Equations 3-4 and 3-6 show that large deviation from these limits occurs at low T and high **B**. It is precisely these non-linear effects that will be exploited to establish the actual site symmetry of Fe(0) in krypton matrices. The absence of the Jahn-Teller effect in the excited state is inferred from the lack of observable splitting in the experimental spectra obtained. The matrix crystal field effect is considered minimal and non-observable within the experimental bandwidths obtained. Thus the authors drew no conclusions about the actual site symmetry of the Fe(0) atom embedded in Ar, Kr, and Xe matrices.

The complementary nature of magnetic linear dichroism spectroscopy has been utilized to corroborate the assignments of the MCD atomic transitions made for Fe in Kr. This first utilization of MLD on a matrix-isolated sample illustrates the validity of the MLD theory and the usefulness of sequential MCD/MLD data collection to establish transition assignments to a much higher degree of confidence. Additionally, several transitions not resolved in the MCD spectrum of Fe(0) in Kr appear in the MLD spectrum, even though the MLD intensity is ~16 times weaker in magnitude at equivalent field strengths. The MLD signal is easily increased since it is proportional to $\mathbf{B}^2$ while the MCD is proportional only to **B** (Equations 2-43 and 2-49). Also, the $J' = 4 \leftarrow J = 4$ transitions are strongly positive in the MLD while they are only weakly positive in the MCD (Table 4-1). The MLD $\mathcal{G}_0/\mathcal{D}_0$ term dominates the spectrum. The extension of MCD and MLD data collection past the linear limit regime to achieve near saturation has been accomplished and permits one to deduce quantitative conclusions about the site symmetry of the Fe(0) atom in its nobel gas lattice.

Electronic State Assignments via Complementary MCD/MLD Spectroscopy

Experimental

The previous data of ShahksEmanpour et al.[22] were obtained utilizing an Air Products closed cycle helium cryostat (Figure 4-2) operating on the Joule-Thomson principle of cooling. The Air Products cryostat is only capable of achieving temperatures as low as ~10-12 K. In order to acquire usable MLD spectra due to the intrinsic weakness of MLD transitions, a specially designed combination split-coil superconducting magnet / liquid helium cryostat was built for these experiments by Oxford Instruments of Oxford, England. It is capable of significantly higher magnetic field strengths as well as lower temperatures (Figures 4-3 and 4-4).

High purity Fe powdered metal (Spex) was effused as an atomic beam from a tantalum Knudsen cell (Figure 4-5) resistively heated for 1 hour in high vacuum ($< 1 \times 10^{-6}$ Torr) at 1450 °C, as measured using an infrared pyrometer. Pure research grade krypton (Kr) gas (> 99.9995%, Matheson) was inlet parallel to the Fe atomic beam path to provide a co-condensing matrix lattice to entrap the Fe atoms. Both components (Fe and Kr) were co-condensed onto a three-quarter inch diameter sapphire window maintained at ~ 4.2 K at the end of a copper cold finger inside the Oxford Instruments magnet/cryostat (Figures 1-1 – 1-2, 4-3 and 4-4). The Oxford instrument has an upper magnetic field capability of 4 Tesla. It is not a Joule-Thompson instrument, but relies instead on liquid helium filled inner canisters to supercool the magnet windings. These are insulated by a surrounding liquid nitrogen canister and a high vacuum shroud. There

---

is a separate liquid helium chamber encompassing the interior of the cold finger and allowing liquid helium to fill the void between two 0.750 inch diameter by 0.250 inch thick sapphire windows providing the optical path and surfaces for matrix deposition. There are two distinct and separate sets of sapphire windows, one set above the other, allowing for independent depositions. The cold finger vertical axis is moveable up and down via a threaded attachment and rotates 360° about its axis to allow either set to be placed in the path of the Knudsen cell atomic beam for matrix deposition and aligned in the optical path for spectroscopic analysis. The matrix is deposited on the exterior surface of one window of one pair of sapphire windows. The second completely separate set of windows can be used for a separate deposition experiment, and was generally used for temperature calibration.

The location of the matrix on the outer surface of the 0.250 thick inch sapphire window does create a concern regarding the actual matrix temperature. Heat flow across the sapphire window to the liquid helium behind it precludes the outer surface of the window along with the matrix on its surface from achieving exactly the same temperature as the liquid helium coolant; it is reasonable to predict it will be somewhat warmer in actual temperature than the temperature of the liquid helium. The achievable temperature range of the cryostat for cooling the matrix window is approximately 4.2 - 50 Kelvin utilizing a vapor displacement bubble insert. Temperatures below 4.2 K are achieved by removing the insert and applying a metered vacuum to the liquid helium used as a coolant for the sample window (Figures 1-1, 4-3, and 4-4). Liquid He cools further under such conditions, attaining superfluid state. This permits temperatures as low as ~1.4 - 1.5 K to be attained. Measurements of the window/matrix temperature were accomplished by simultaneously monitoring the temperature vs. liquid helium vapor pressure curve along with two thermistors mounted in close proximity to the exterior surface of the sapphire window, one a Fe/Rh junction thermistor and the other a carbon-glass (CG) junction thermistor.

The true matrix temperature is likely higher at the actual exterior surface of the sapphire window where the matrix is deposited. Calibrations of the window exterior surface temperature are performed periodically utilizing either a film of $Fe(CN)_6^{-3}$/PVA (polyvinyl alcohol) or a matrix of a well-characterized $^2P \leftarrow {}^2S$ transition (as Cu or Ag in Ar or Kr).[10,24,26] These methods permit the temperature determination of the matrix to be made directly from the MCD absorption spectra due to their known response to temperature. The temperature calibration during this specific series of experiments was accomplished following the temperature dependent variation of the Cu $^2P \leftarrow {}^2S$ transition in a krypton matrix centered at 312.4 nm (Figure 4-6). Although the temperature as determined by the He vapor pressure over the liquid He is a very accurate measure of the liquid helium temperature, it does not allow for thermal variations or the thermal gradient through the thickness of the window (Figure 4-7). Once calibrated, temperature-monitoring using the more sensitive carbon-glass thermistor proved to be the most stable and reproducible means of measuring the matrix temperature (Figure 4-8). Temperature determination using the CG thermistor was accomplished by measuring the voltage (in

---

millivolts) across the thermistor, applying the manufacturer's calibration to the voltage to compensate for magnetic field effects, then converting to temperature based on the Cu/Kr moments calibration illustrated in Figure 4-6.

The Fe/Kr sample was characterized according to its previously recorded ABS/MCD spectra (Figures 4-9 and 4-10) now utilizing optics and new electronics specifically designed and built to acquire simultaneous ABS/MCD or ABS/MLD spectra[41]. The matrix was then annealed to 35-37 K for ~5 minutes to permit relaxation of the various weakly stable geometrical sites to one dominant ground state site. It was then re-cooled to liquid helium temperature (~4 K) and simultaneous ABS/MCD spectra were recorded again to verify the integrity of the matrix. The Oxford superconducting magnet was then isolated from its high vacuum pump, appropriate optics were installed, and the magnet was rotated about its vertical axis 90° so that its magnetic field axis was perpendicular to the incident light path. The modulation of the light beam exiting the photoelastic modulator was adjusted for $\lambda/2$ retardation, which provides linearly polarized radiation with its resultant electric field vector $\vec{\mathbf{E}}$ alternating between orientations parallel and perpendicular to the magnetic field axis (Figures 1-3, 2-2, 2-3, 4-3 and 4-4). The photoelastic modulator (Morvue Model C-3) reference signal to the lock-in amplifier (Ithaco Model 353) was set at 100 KHz. The magnetic field was ramped to 1 Tesla and scans were made from 400 to 200 nm to acquire the simultaneous ABS/MLD spectra. Additional MLD scans were made over the range 350 – 300 nm at various temperatures from ~1.4 – 22 K and at magnetic fields between 0 and 4 Tesla.

Results

A representative MLD spectrum is illustrated in Figure 4-11. Table 4-2 contains the band positions and assignments for the MCD and MLD spectra of Fe(0) in Kr matrices. Column one lists the upper electronic excited states. Columns two and three contain the approximate measured intensities of the MCD transitions along with their frequency. Columns three and four list the approximate measured MLD transition intensities and their corresponding frequencies of differential absorption.

Table 4-2. MCD and MLD band positions and assignments for Fe(0) atoms isolated in a krypton matrix for the $^5D_4$ ground state configuration.

Transition	$\mathcal{C}_0/\mathcal{D}_0$[a,b]	MCD λ^{Kr} (nm)	$\mathcal{G}_0/\mathcal{D}_0$[b]	MLD λ^{Kr} (nm)
z^5D_4	+1.4	374.0	+0.5	372
z^5D_3	+2.6	370.0	+0.8	--
z^5F_5	-1.5	359.6	-0.1	357.9
z^5F_4	w(+)	353.5	w(+)	352
z^5P_3	+8.2	335.5	-0.6	331.6
y^5D_4	+1	302	+1.8	300.8
y^5D_3	+5	298.3	-0.8	297.2
y^5F_5	-6	293.8	-0.3	292.4
y^5F_4	w(+)	290.5	w(+)	289.2
y^5F_3	w(+)	288.0	w(+)	286
y^5P_3	+4.4	270.5	-1.3	268.6
x^5D_4	w(+)	251.0	-0.6	249.2
x^5D_3	--	--	w(-)	247.2
x^5F_5	vs(-)	246	vs(-)	245.5
x^5F_4	--	--	w(+)	243.5
w^5D_4	--	--	w(+)	224.7

[a] Adapted from: J. ShakhsEmampour, R. Pyzalski, M. Vala, and J.C. Rivoal. Magnetic circular dichroism study of matrix-isolated iron atoms. Table 5, J. Physique 45, 953 (1984).
[b] Values estimated from the ratio of MCD/MLD peak height to absorption intensity

Four transitions which were previously unobserved in the MCD/ABS spectra of ShahksEmampour et al.[22] are visible in these spectra. Two weakly positive bands are found in the MCD spectrum: the $z^5F_4 \leftarrow {}^5D_4$ transition at 353.5 nm and the $y^5F_4 \leftarrow {}^5D_4$ transition at 290.5 nm. These two transitions also appear in the MLD spectrum at 352 nm and 289.2 nm, respectively, as weakly positive bands. In addition, the transitions $x^5F_4 \leftarrow {}^5D_4$ and $w^5D_4 \leftarrow {}^5D_4$ are also visible in the MLD spectrum and are located, respectively, at 243.5 nm and 224.7 nm. Both are weak in intensity and positive in sign. The band structure near 250 nm contains three transitions, two of which were identified by ShaksEmampour et al.[22] in their MCD study: the weakly positive $x^5D_4 \leftarrow {}^5D_4$ transition at 251.0 nm and the weakly negative $x^5F_5 \leftarrow {}^5D_4$ transition at 246 nm. There is obviously a third transition intermediate between the two, but it is not resolved adequately in the MCD spectrum to assign as either a positive or negative transition. The MLD spectrum shows a greatly enhanced absorption by the $x^5D_4 \leftarrow {}^5D_4$ transition with a positive sign, and a clearly visible negatively signed shoulder located at 247.2 nm, on the long wavelength side of the $x^5F_5 \leftarrow {}^5D_4$ transition. This band is assigned as due to the $x^5D_3 \leftarrow {}^5D_4$ transition.

Discussion

The utilization of MLD as a method for corroborating or independently assigning electronic transitions seen in absorption and MCD spectra is seen to be of great value. The complementarity of MCD/MLD spectral transitions permits the analysis of complex absorption spectra to be accomplished with relative simplicity, since the direction of transitions dictates which states can be assigned. Table 4-1 gives the calculated Faraday parametric ratios for $\mathcal{B}_0/\mathcal{D}_0$ and $\mathcal{C}_0/\mathcal{D}_0$ which are essential in determining the assignment of transitions. Note the sign of each term, which is dependent on ΔJ. It was demonstrated that the predicted transitions from Table 4-1 do indeed appear in the actual sample.

The inherent magnitude of MLD transitions is small. However, increasing the magnitude of the applied magnetic field strength greatly affects the MLD spectrum due to its $\mathbf{B}^2$ dependence, making it possible to reveal otherwise very weak transitions. This technique has allowed the assignment of a few previously unseen or undetermined weak absorptions in the Fe/Kr $^5D_4$ ground state spectrum. The newly revealed z^5F_4, y^5F_4, x^5F_4, and w^5D_4 transitions are annotated in Figure 4-11 and listed Table 4-2. A weak shoulder for the x^5D_3 transition in the MCD appears sharply in the MLD analog. It will be very useful to apply the complementarity of MCD/MLD to more complex systems, as Ni(0) appearing in dual ground states in rare gas matrices.

Determination of Site Geometry via Magnetic Saturation Techniques

Experimental

Subsequent experiments were performed under similar temperature and field conditions of the previous section. Sample preparation involved deposition of Fe(0) in Kr for 30 minutes at ~1520 °C on a 0.75 inch diameter sapphire window (Figures 4-3 and 4-4) at liquid helium temperature (approximately 4.2 K). Powdered iron metal (Spex) was heated in a Knudsen cell furnace (Figure 4-5), creating a directed beam of atomic iron exiting a small circular orifice drilled in the tantalum cell containing the Fe powder. The krypton gas was from Matheson (99.9995% pure) and was inlet parallel to the effusing Fe(0) atomic beam. After the deposition period, absorption and MCD spectra were obtained to characterize the quality of the matrix. Typically, as in this case, newly deposited matrices exhibited low-energy shoulders on many transition bands. These were indicative of alternative matrix trapping sites. These sites reflect a slightly perturbed geometry distortion of the Fe(0) lattice, shifting the observed electronic transition energies. Generally, they are unstable, and easily eliminated by annealing the matrix to approximately 35 K for several minutes to permit site stabilization. After annealing, absorption and MCD spectra of the Fe(0)/Kr matrix were again acquired to verify dissipation of the unstable alternate sites.

The Oxford superconducting magnet was controlled by a PC interfaced to the magnet power supply via an analog voltage input connector. A software program written in QuickBasic 4.5 drove the input and output for a Metrabyte DASH-16 I/O card having both digital and analog input/output channels. Increasing the output analog signal from the computer to the magnet power supply produced a linear response in the current output from the magnet power supply to the input terminals of the superconducting magnet's coils sufficient to change the filed to the predetermined level. The current was then removed as the magnet remained in persistent mode until the next required field change.

Both the temperature and magnetic field dependence of a single specific isolated transition with strong MCD and MLD absorption were monitored ($z^5P_3 \leftarrow {}^5D_4$ at ~331.7 nm). The purpose of these scans was to achieve or approach magnetic saturation as described in Chapter 3 by steadily increasing the magnetic field **B** from 0 to 3 T while maintaining the temperature of the matrix at a constant value. Although some temperature and field-dependent scans were obtained at temperatures from 4.2 – ~22 K, most of the data was collected between ~1.5 – 4.2 K at magnetic field strengths between 0 – 2.88 Tesla. The additional time required to ramp the magnet beyond 3 T to 4 T (~ 30 minutes) proved to be impractical in regard to our limited supply of liquid helium, which restricted the experiments to a total duration of approximately 35 hours. This 3 Tesla upper bound of the magnetic field at the superfluid helium temperatures achieved was well into the non-linear regime of the magnetic saturation phenomenon, and generated abundant valid experimental data for analysis.

Superfluid helium temperatures were achieved by connecting a high volume rotary vacuum pump to the top of the He filled inner cold finger chamber via a flexible stainless steel hose. A pressure gauge (0.5 $\mathrm{mm_{Hg}}$ resolution) was inserted via a tee at the top of the inner He chamber to monitor the magnitude of the He vapor pressure. The vacuum pump line was throttled with a coarse metering valve to roughly control the vacuum level over the liquid He. Fine control of the He vapor pressure was accomplished by use of a balanced diaphragm valve assembly designed by Bryce Williamson and built in our machine shop. The diaphragm valve was placed in-line with the rotary vacuum pump and mounted at the top of the cryostat inner liquid He chamber access port. This diaphragm valve assembly, once set and stabilized, compensated for irregularities in the rotary vacuum pump, allowing fine control of the liquid He vapor pressure. The stability of the He vapor pressure was controlled to better than ~ ±1–2 $\mathrm{mm_{Hg}}$ at 1.5 K. At ~3 K and above, the variation in the He vapor pressure stability was less than ±0.5 $\mathrm{mm_{Hg}}$.

This research was conducted in collaboration with J.C. Rivoal, and co-workers at the Laboratoire d'Optique Physique, Paris, France[64]. Magnetization scans were acquired in Florida, while bandshape scans and moments analyses were performed in Paris. Graham and Grinter[65] utilized magnetization scans to study Fe(0) atoms in xenon, tracking the peak intensities instead of moment measurements of the bandshapes. They deduced the existence of a rather large axial crystal field with $|M_J| = 4$ components [of the $J = 4$ state] approximately 100 cm^{-1} below the $|M_J| = 3$ level. Their results conflicted sharply with early results from the Florida and Paris laboratories.

To perform magnetization scans, the monochromator was scanned to the maximum intensity of the $z^5P_3 \leftarrow {}^5D_4$ transition at 335.5 nm for the MCD and 331.6 nm for the MLD (Table 4-2). The temperature was stabilized at 4.22 K and then the magnetic field was ramped from 0 T to 2.88 T in 0.1 T increments and back down to 0 T again. The field was allowed to stabilize two minutes at each of 31 field intensities prior to recording the peak intensity for 30 seconds at each **B** for a particular T. The recorded saturation plateaus were continuously digitized and then averaged across the recorded time interval. This data was corrected for baseline variations (minimal) and scaled relative to all data of that type (MCD or MLD). The 1008 MCD and 1030 MLD corrected data points were sorted into sets of the same **B** and T and then averaged to provide an MCD data set consisting of 403 averaged data points and an MLD data set of 465 averaged data points. These data sets covered the magnetic field range 0 – 2.88 T and the temperature range 4.22 – 1.48 K.

Saturation scans were conducted by the Paris group on Fe/Kr and Fe/Xe matrices by scanning the $z^5P_3 \leftarrow {}^5D_4$ transition (331.4 nm in Kr, 340.1 nm in Xe) and the $y^5P_3 \leftarrow {}^5D_4$ transition (268.6 nm in Kr, 275.5 nm in Xe). Both were scanned at a specific temperature with the magnetic field ramped from 0 T to 1.50 Tesla. The temperature range was 2.3 – 22 K, thus complementing the results of this research. Digitization of the bandshape was acquired in the saturation scans, while only the transition intensity at fixed wavelengths was acquired for the magnetization scans.

Since the magnetization scans are more quickly obtained, many more data points can be recorded. However, using the entire bandshape results in more accurate data because the ratio of the MCD or MLD $\langle \Delta A \rangle_0$ band moment and the absorption $\langle A \rangle_0$ band moment are collected simultaneously. This compensates for any matrix effects, including decay of the matrix integrity.

The field ramp was software controlled by an IBM PC 286 clone, which was used to control the entire ABS/MCD/MLD instrument. The magnetic field was ramped in increments of 0.1 Tesla and allowed to stabilize 2 minutes prior to the acquisition of each spectrum. The bandshapes were digitally recorded by the computer software relative to the zero magnetic field signal. Saturation spectra were acquired for both MCD and MLD simultaneously with the absorption spectrum.

Data Reduction and Refinement

The MCD and MLD relative intensity data was then used as the experimental framework for comparison with theoretical models of various symmetries representing

Fe(0) atoms isolated in a crystal field lattice. Theoretical MCD and MLD intensities for each symmetry model were calculated using the methods described in Chapter 3. Initially FORTRAN computer software written in version 77 for the Physics Department's SPARC computer and in the slightly modified IBM version VS2 (to support vector and parallel processing) for the Northeast Regional Data Center's IBM 3090/600J Supercomputer or IBM RSC6000 was utilized to process the refinements. Further refinements were later accomplished using a routine written in C^{++} (Appendix A), executing on a dual 500 MHz Pentium 3 Xeon processor system.

The goal of the magnetic saturation measurements is to determine the site symmetry of Fe(0) atoms in Kr. To accomplish this, the parameters defining a particular symmetry are refined until the best per cent root-mean-square deviation (RMS) fit of the experimental data to the theoretical data is achieved. This symmetry model must simultaneously fit both the MCD and MLD data within reasonable confidence limits. The parameters varied are the symmetry dependent crystal field parameters D^{OCT}, B^{TET}, F^{TET}, K^{TRI}, L^{TRI}, and M^{TRI} (Equations 3-9 – 3-11, Tables 3-3 and 3-4) which describe the extent of mixing of the $|JM_J\rangle$ free atom states for each symmetry classification.[57] The temperature range is 1.57 - 4.22 K for MCD and 1.48 - 4.22 K for MLD spectra. The magnetic field strengths are 0 to 2.88 Tesla. A total of 1008 MCD and 1030 MLD data points were obtained and averaged to give 403 averaged MCD points [at thirteen temperatures] and 465 MLD points [at fifteen temperatures]. Individual data groupings were made for refinement as follows:

- A single MCD set of 403 data points and a single MLD data set of 465 data points were processed, both separately and simultaneously.
- Thirteen sets of 31data points at each temperature, obtained for MCD, and fifteen sets, for MLD, were processed both separately and simultaneously (31 is the number of magnetic field levels for which data was collected).

Simulations at various theta increments (Chapter 3) to establish the extent of refinement necessary using lower symmetry models were performed on the MCD 403 point data set with theta increments of 1, 10, 20, and 50 for tetragonal crystal field symmetry. The results show large variation in the refined crystal field parameter values, with the RMS actually increasing. Additionally, MCD data sets MCD at 1.48 K (31 data points) and at 1.48 K (10 data points) were calculated at theta increments of 1000 and 10000 (Table 4-5), again modeling tetragonal symmetry. The resulting value for the Group 2 set gave an RMS value of 0.446 and B^{TET}, F_1^{TET}, F_2^{TET} of 1.036, 1.000, 1.000, respectively, at $\Delta\theta = 1000$. The result for the 10 point data set data set ($\Delta\theta = 10000$) resulted in an RMS of 0.458, B^{TET}, F_1^{TET}, F_2^{TET} of 1.043, 1.000, 1.000, respectively. This indicates reasonably good convergence of the refinement. Refinement of the 31 point data set at 4.22 K ($\Delta\theta = 1000$) gave an RMS error = 3.29% and B^{TET}, F_1^{TET}, F_2^{TET} of 1.749, 2.015, 1.000. Processing the same data set at $\Delta\theta = 10000$ resulted in: RMS = 3.22% and B^{TET}, F_1^{TET}, F_2^{TET} of 1.765, 2.008, 1.000. Calculations on the NERDC IBM 3090/600J and RSC6000 were of comparable duration in actual central processor time utilized, however allocation of the extensive amounts of CPU time required to process these data sets was not permitted by the NERDC staff. These results justify limiting the numerical incrementation of theta in the calculation of the Zeeman energies and theoretical MCD and MLD expressions of Chapter 3 to 1000 intervals, corresponding to incrementing by $\pi/2\text{x}10^{-3}$ radian per interval. After numerous refinements, 250 increments proved viable.

Computations made utilizing a much faster dual 500 MHz Xeon processor system running C++ executable code under the Windows NT 4.0 O/S proved much more economical. Refinements of individual Group 2 data sets required typically 12 to 18 hours for each for tetragonal and trigonal convergence using 1000 theta increments. Integration over 250 theta increments was compared on several data sets and demonstrated results consistent with the 1000 increment runs to at least two and often three significant figures. These refinements took typically 3 to 4 hours. Thus, after a number of calculations were made over 1000 theta increments, most subsequent refinements were integrated over only 250 theta increments due to the faster run times involved providing nearly the same precision in results.

Results

The simulated data calculated for the free atom model of Fe(0) in krypton matrix with Landé g value = 1.5 (Equation 3-2) are plotted against the experimental data in Figures 4-12 and 4-13 for the Group 2 data set. Both MCD and MLD data sets were computed simultaneously to arrive at the best theoretical fit for both sets together. The simultaneously-refined free atom RMS deviation vs. temperature (T) values are collected in Table 4-3. The octahedral results for the individually-refined Group 2 data point sets are depicted in Figures 4-14 and 4-15, and the D^{OCT} vs. T and RMS vs. T values are in collected in Tables 4-3 and 4-4. Figures 4-16 and 4-17 include the results of the simultaneous refinements using the tetragonal symmetry model, refining over 1000 theta increments between 0 and $\pi/2$. The trigonal data sets, also refined over 1000 theta increments, are graphed in Figures 4-18 and 4-19. The numerical results for the tetragonal symmetry model are listed in Tables 4-5 and 4-6, while Table 4-7 contains the trigonal results.

The Group 1 free atom results of 4.46% for the 403 MCD data points and 8.23% for the 465 MLD data points lead to the conclusion that the free atom model isn't very favorable. The average RMS of 10.96% (15.49% for MCD and 6.43% for MLD) for both complete MCD and MLD data sets (Group 1 with 868 data points total) refined simultaneously under octahedral symmetry leads to the initial conclusion that an octahedral symmetry environment for the Fe(0) atom in Kr lattice is unlikely. The free atom comparison cannot be refined, since there is no 'adjustable' crystal field. Since the 3-dimensional calculations of the Group 1 data sets for tetragonal and trigonal symmetry would be very expensive computationally, it was deemed reasonable to investigate first the behavior of the free atom and octahedral models across the span of individual temperature sets. These results, found in Table 4-4, indicate much better mathematical correlation at many of the temperatures for the free atom and octahedral models, especially for the MLD data. As a matter of specific interest, the data trends show a favoritism for the free atom model at the higher temperatures (~2.5 – 4.22 K) and a

Table 4-3. Free atom and octahedral refinement parameters for the simultaneously-refined MCD and MLD experimental data sets. Theta integration for octahedral refinements is in one step over 0 to $\pi/2$.

		Free atom symmetry				Octahedral Symmetry				
Number of Data Points	T_{MCD}/T_{MLD} T(K)	MCD RMS (%)	MLD RMS (%)	average RMS (%)	std dev (%)	MCD RMS (%)	MLD RMS (%)	average RMS (%)	std dev (%)	D^{OCT}
403/465	All	--	--	--	--	15.49	6.43	10.96	6.41	0.087
31/31	4.22/4.22	2.36	0.78	1.57	1.12	2.94	2.74	2.84	0.14	0.129
31/31	3.82/3.78	2.33	1.30	1.82	0.73	2.94	3.47	3.21	0.37	0.106
31/31	3.82/3.74	2.33	2.41	2.37	0.06	2.94	2.92	2.93	0.01	0.106
31/31	3.34/3.23	2.15	1.01	1.58	0.81	2.88	2.74	2.81	0.10	0.092
31/31	2.98/2.91	1.49	1.66	1.58	0.12	2.11	2.32	2.22	0.15	0.081
31/31	2.58/2.53	1.42	2.76	2.09	0.95	1.53	2.10	1.82	1.82	0.070
31/31	2.31/2.29	2.36	5.21	3.79	2.02	2.27	1.99	2.13	0.20	0.072
31/31	2.18/2.11	1.82	4.83	3.37	2.06	2.12	1.57	1.90	0.46	0.059
31/31	2.08/2.11	1.91	4.83	3.33	2.13	2.22	1.57	1.85	0.39	0.059
31/31	1.95/1.91	2.69	6.61	4.87	2.47	2.13	1.17	1.65	0.68	0.058
31/31	1.83/1.79	3.12	7.70	5.41	3.24	2.09	1.23	1.66	0.61	0.058
31/31	1.74/1.74	4.44	8.24	6.34	2.69	2.78	1.32	2.83	0.71	0.058
31/31	1.74/1.68	4.44	8.70	6.57	3.01	2.78	1.32	3.26	0.10	0.058
31/31	1.61/1.61	5.44	9.73	7.59	3.03	3.39	1.29	2.34	1.48	0.059
31/31	1.57/1.55	5.79	9.67	7.73	2.74	3.90	1.72	2.77	1.60	0.056
31/31	1.57/1.48	5.79	11.10	8.45	3.75	3.90	1.64	2.81	1.54	0.056

Table 4-4. Free atom and octahedral refinement parameters for the individually-refined MCD and MLD experimental data sets. Theta integration for octahedral refinements is in one step over 0 to π/2.

			Free Atom Symmetry software minimization		Octahedral Symmetry software minimization				Octahedral Symmetry RMS vs. D^{OCT} plot			
Number of Data Points	T_{MCD}(K)	T_{MLD}(K)	MCD RMS (%)	MLD RMS (%)	MCD RMS (%)	MLD RMS (%)	MCD D^{OCT}	MLD D^{OCT}	MCD RMS (%)	MLD RMS (%)	MCD D^{OCT}	MLD D^{OCT}
403/465	All	All	4.46	8.23	3.14	1.8	0.112	0.077	--	--	--	--
31	4.22	4.22	2.36	0.78	2.94	2.81	0.137	0.130	2.94	2.81	0.14	0.13
31	3.82	3.78	2.30	1.25	2.93	3.53	0.127	0.111	2.93	2.93	0.13	0.11
31	--	3.74	--	2.39	--	3.08	--	0.104	--	3.15	--	0.10
31	3.34	3.23	2.15	1.01	2.87	2.79	0.117	0.093	2.81	2.85	0.11	0.09
31	2.98	2.91	1.49	1.66	2.06	2.46	0.028	0.083	2.07	2.51	0.03	0.08
31	2.58	2.53	1.42	2.76	1.34	2.16	0.172	0.071	1.34	2.17	-0.01	0.07
31	2.31	2.29	2.36	5.21	--	2.00	diverges	0.073	1.98	2.07	-0.04	0.07
31	2.18	2.11	1.82	4.83	--	1.60	diverges	0.061	1.31	1.63	-0.04	0.06
31	2.08	--	1.91	--	--	--	diverges	--	1.40	--	-0.04	--
31	1.95	1.91	2.69	6.61	1.25	1.18	2.460	0.060	1.25	1.19	-0.10	0.06
31	1.83	1.79	3.12	7.70	0.85	1.22	-0.125	0.059	0.85	1.27	-0.12	0.06
31	1.74	1.74	4.44	8.24	0.96	1.30	-0.159	0.058	0.96	1.41	-0.16	0.06
31	--	1.68	5.44	8.70	1.34	1.24	-0.171	0.057	1.34	1.52	-0.17	0.06
31	1.61	1.61	5.79	9.73	1.89	1.23	-0.170	0.057	1.89	1.40	-0.17	0.06
31	1.57	1.55	--	9.67	--	1.14	--	0.054	--	1.54	--	0.05
31	--	1.48	--	10.56	--	1.34	--	0.056	--	1.77	--	0.06

Table 4-5. Tetragonal refinement parameters for the simultaneously-refined MCD and MLD experimental data sets

			Tetragonal Symmetry Primary Refinement							Secondary Refinement				
Number of Data Points	MCD T(K)	MLD T(K)	MCD RMS (%)	MLD RMS (%)	average RMS (%)	std dev (%)	F_1^{TET}	F_2^{TET}	B^{TET}	MCD RMS (%)	MLD RMS (%)	F_1^{TET}	F_2^{TET}	B^{TET}
31/31	4.22	4.22	3.96	2.30	3.13	0.59	1.61	1.01	0.98					
31/31	3.82	3.78	3.68	2.61	3.15	0.38	5.11	3.92	1.77	3.82	2.85	1.62	1.00	1.00
31/31	3.82	3.74	3.59	3.26	3.42	0.12	18.82	13.85	7.72	3.82	3.59	1.61	1.01	0.99
31/31	3.34	3.23	3.56	1.28	2.42	0.81	3.02	2.00	1.60	3.68	1.45	1.63	1.01	1.00
31/31	2.98	2.91	2.33	1.39	1.86	0.33	29.61	21.50	12.49	2.64	1.12	1.64	1.01	0.98
31/31	2.58	2.53	1.61	1.82	1.71	0.08	1.81	1.52	0.50	1.68	1.67	1.67	1.01	1.00
31/31	2.31	2.29	2.29	2.91	2.60	0.22	1.88	1.05	0.94	2.35	2.74	1.88	1.00	1.00
31/31	2.18	2.11	2.02	2.89	2.46	0.31	1.86	1.05	0.94	2.05	2.84	1.86	1.00	1.00
31/31	2.08	2.11	1.45	0.57	1.01	0.31	3.84	26.48	-35.93	1.99	3.07	1.83	1.00	1.00
31/31	1.95	1.91	1.95	2.64	2.30	0.24	2.01	1.17	0.78	1.96	2.68	1.99	1.00	0.99
31/31	1.83	1.79	1.59	2.40	1.99	0.29	3.20	6.10	-5.23	1.71	2.53	2.04	1.00	1.00
31/31	1.74	1.74	1.31	2.16	1.74	0.30	2.12	1.00	1.00					
31/31	1.74	1.68	1.41	2.07	1.74	0.23	2.13	1.00	1.00					
31/31	1.61	1.61	1.55	1.78	1.67	0.08	2.18	1.00	1.00					
31/31	1.57	1.55	2.22	2.17	2.19	0.02	2.17	1.00	1.00					
31/31	1.57	1.48	2.32	2.13	2.23	0.07	2.20	1.00	1.00					

Note: Theta integration for the refinements is in 250 steps over 0 to π/2. Initial values for refinement: $F_1^{TET} = F_2^{TET} = B^{TET} = 1.0$

Table 4-6. Tetragonal refinement parameters for the individually-refined MCD and MLD experimental data sets

			Tetragonal Symmetry software minimization						RMS vs. F_1^{TET} plot					
Number of Data Points	MCD T(K)	MLD T(K)	MCD RMS (%)	MLD RMS (%)	MCD F_1^{TET}	MLD F_1^{TET}	F_2^{TET}	B^{TET}	MCD RMS (%)	MLD RMS (%)	MCD F_1^{TET}	MLD F_1^{TET}	F_2^{TET}	B^{TET}
31	4.22	4.22	---	4.32	---	0.09	1.00	1.00	3.96	2.29	1.62	1.58	1.00	1.00
31	3.82	3.78	---	4.12	---	0.67	1.01	1.00	3.82	2.85	1.62	1.58	1.01	1.00
31	---	3.74	---	3.10	---	0.72	1.00	1.00	---	3.59	---	1.58	1.00	1.00
31	3.34	3.23	---	3.55	---	0.90	1.00	1.00	3.68	2.75	1.64	1.26	1.00	1.00
31	2.98	2.91	---	3.06	---	1.00	1.00	1.00	2.56	1.11	1.64	1.56	1.00	1.00
31	2.58	2.53	---	2.92	---	1.11	1.00	1.00	1.68	0.90	1.64	1.38	1.00	1.00
31	2.31	2.29	---	3.47	---	1.11	1.00	1.00	2.05	1.02	1.64	1.26	1.00	1.00
31	2.18	2.11	---	2.39	---	1.18	1.00	1.00	1.65	0.93	1.64	1.30	1.00	1.00
31	2.08	---	---	---	---	---	---	---	1.96	---	1.48	---	1.00	1.00
31	1.95	1.91	---	2.16	---	1.20	1.00	1.00	1.44	0.93	1.48	1.26	1.00	1.00
31	1.83	1.79	---	2.29	---	1.21	1.00	1.00	1.10	0.77	1.42	1.26	1.00	1.00
31	1.74	1.74	---	2.09	---	1.22	1.00	1.00	1.12	1.32	1.34	1.26	1.00	1.00
31	---	1.68	---	1.94	---	1.23	1.00	1.00	---	1.02	---	1.26	1.00	1.00
31	1.61	1.61	---	2.14	---	1.23	1.00	1.00	1.35	0.97	1.32	1.24	1.00	1.00
31	1.57	1.55	---	1.61	---	1.25	1.00	1.00	2.04	1.27	1.32	1.26	1.00	1.00
31	---	1.48	---	1.95	---	1.24	1.00	1.00	---	1.13	---	1.24	1.00	1.00

Note: Theta integration for the refinements is in 250 steps over 0 to $\pi/2$. Initial values for refinement: $F_1^{TET} = F_2^{TET} = B^{TET} = 1.0$

Table 4-7. Trigonal refinement parameters for the simultaneously-refined MCD and MLD experimental data sets

				Trigonal Symmetry						
Number of Data Points	T_{MCD}(K)	T_{MLD}(K)	T_{ave}(K)	RMS_{MCD} (%)	RMS_{MLD} (%)	RMS_{ave} (%)	std dev (%)	K^{TRI}	L^{TRI}	M^{TRI}
31/31	4.22	4.22	4.22	6.03	3.93	4.98	0.74	0.374	0.004	0.070
31/31	3.82	3.78	3.80	5.79	3.57	4.68	0.78	0.343	0.003	0.035
31/31	3.82	3.74	3.78	5.72	3.44	4.58	0.81	0.323	0.003	-0.042
31/31	3.34	3.23	3.29	5.78	4.35	5.07	0.51	0.315	0.008	-0.029
31/31	2.98	2.91	2.95	4.89	4.66	4.78	0.08	0.302	0.012	-0.065
31/31	2.58	2.53	2.56	4.57	5.23	4.90	0.23	0.266	0.014	-0.141
31/31	2.31	2.29	2.30	4.85	6.55	5.70	0.60	0.265	0.013	-0.203
31/31	2.18	2.11	2.15	4.61	6.75	5.68	0.76	0.226	0.015	-0.224
31/31	2.08	2.11	2.10	4.40	6.75	5.58	0.83	0.226	0.015	-0.224
31/31	1.95	1.91	1.93	3.62	5.58	4.60	0.69	0.256	-0.001	-4.067
31/31	1.83	1.79	1.81	3.48	6.11	4.80	0.93	0.260	-0.002	-2.516
31/31	1.74	1.74	1.74	2.89	7.29	5.09	1.56	0.239	0.003	-2.345
31/31	1.74	1.68	1.71	2.89	7.07	4.98	1.48	0.312	-0.014	-1.555
31/31	1.61	1.61	1.61	3.20	7.56	5.38	1.54	0.411	-0.033	-0.798
31/31	1.57	1.55	1.56	3.40	8.21	5.81	1.70	0.419	-0.036	-0.603
31/31	1.57	1.48	1.53	3.40	8.94	6.17	1.96	0.453	-0.039	-0.494

Note: Theta integration for the refinements is in 250 steps over 0 to $\pi/2$. Initial values for refinement: $F_1^{TET} = F_2^{TET} = B^{TET} = 1.0$

preference for the octahedral model at the lower temperatures (below ~2.5 K). It was decided to forego the expensive Group 1 computations under the more extensive tetragonal and trigonal symmetries and focus on refining the Group 2 individual temperature data sets. From the Group 2 results it can be seen that the average D^{OCT} of 0.087 cm^{-1} arrived at for the Group 1 results is in reasonable agreement with the values obtained for the individual Group 2 refinements, even though the Group 1 RMS values are in poor agreement for the overall data sets.

Figure 4-20 shows the RMS vs. D^{OCT} plots for actual MCD and MLD refinements at 1.61 K. Figure 4-20 A shows the results of simultaneous refinement of the MCD and MLD data sets at 1.61 K, while Figure 4-20 B plots the results of separately refining the same MCD and MLD data sets. In Figure 4-20 A, the MLD plot refines to a sharp minimum slightly above zero with a low RMS deviation ($D^{OCT} = 0.059cm^{-1}$, RMS = 1.29 %), but the MCD data displays a long positive plateau from zero upwards, refining only to an RMS deviation of 3.39 %. Although there is a minimum to the curve at $D^{OCT} = 0.37$, it is quite broad and flat relative to the MLD refinement. Comparing the MCD locus of Figure 4-20 A to the MCD of Figure 4-20 B, the minimization routine 'missed' the minimum near –0.9 cm^{-1} entirely. When refining simultaneously, the results are obviously dominated by the MLD data.

The plots of Figure 4-20 show the output of the minimization routine used, which attempts to bracket a minimum, check for other minima, then establish the depth of each minimum via a parabolic interpolation method,[66] finally selecting the most extreme minimum. Figure 4-21 plots similar results for the MCD and MLD data sets at 4.22 K. It is possible for this method to 'skip' minima if the incrementing method is less than optimal. Figure 4-22 plots the results of a structured incrementing of the D^{OCT} values at 1.74 K and 4.22 K for MCD and MLD. The minimization routine is not utilized. Instead, the D^{OCT} value is set to a specific value, the theoretical MCD and MLD are calculated, then the RMS deviation is determined at that value. D^{OCT} is then incremented to the next step and the process repeated. This is the 'brute force' method of determining the minima over a pre-determined range, and is practical only for a one-dimensional problem or over a short range. The increment applied $[\Delta D^{OCT} = 0.01 \text{ cm}^{-1}]$ and the previously hypothesized lack of necessity for integrating numerically over a quarter radius (0 - $\pi/2$) for the one-dimensional octahedral refinement model (as opposed to the three-dimensional tetragonal and trigonal models) requires only 500 calculations for a D^{OCT} range of –2.5 to +2.5. The length of a single computational cycle for a small data set (~15 data points) is on the order of a fraction of a second. For example, using a cycle time of ~0.5 sec, 500 cycles require approximately 4 minutes of central processor time on a 500 MHz PIII Xeon processor. Thus these calculations are computationally practical.

Figure 4-22 illustrates the presence of multiple minima for three of the four curves, but each curve has a distinct extreme minimum. The 4.22 K MCD has a single minimum, not as sharply defined as in the 1.74 K MCD and both MLD curves. The structure of the MCD curves obviously changes significantly from 4.22 K to 1.74 K. Exploring this further, similar calculations were performed on all the data sets between

4.22 K and 1.48 K and plotted in Figure 4-23. The principal minimum for each curve is noted on the graphs. Figures 4-24 and 4.25 show superimposed graphs for the MCD and MLD plots of Figure 4-23 for easier comparison. The MCD plots of Figures 4-23 and 4-24 demonstrate a shallow well with positive D^{OCT} of 0.13 – 0.14 cm^{-1} at 3.82 – 4.22 K, corresponding to an energy differential across the T_2-A levels (Figure 4-1) of ~7.56 cm^{-1}. The 3.34 K plot shows a flattening in this region which bifurcates in the 2.98 K plot, developing into two distinct minima through the 1.58 K plot. The principal D^{OCT} minimum shifts from the positive region between 0.10 and 0.20 cm^{-1} to the negative side of the axis, exhibiting a value of -0.01 cm^{-1} at 2.58 K ($\Delta E = 0.54$ cm^{-1}) growing more negative to –0.17 cm^{-1} at 1.58 K ($\Delta E = 9.18$ cm^{-1}). A third shallow minimum appears at 1.95 K between $D^{OCT} = 0.05 – 0.07$ cm^{-1} ($\Delta E = 3.2$ cm^{-1}) which continues to grow with decreasing temperature. It is consistent with the D^{OCT} values calculated for the MLD data, but does not refine as the primary minimum. This shift to the negative region for the primary minimum is troublesome, as it is indicative of an inversion in the ordering of the crystal field split levels, i.e., the T_2 level of Figure 4-1 would now be the most energetic level instead of the least energetic, with the A level lying lowest. This contradicts the MLD results. Also, Mossbauer studies by P. Montano, P. Barrett, and Z. Shanfield[67] pointed to a positive crystal field parameter (D^{OCT}) with the T_2 level being lowest in energy. They deduced this from a determination of a 70 T magnetic hyperfine field at the ^{57}Fe nucleus due to hyperfine splitting in an external magnetic field. This was not definitive, and suggested that the range of the splitting was between 10 and 100 cm^{-1}.

Inspection of Figures 4-23 and 4-25 demonstrate remarkable stability in the D^{OCT} value obtained from the MLD refinements. Although there is a slight formation of a secondary minimum around $D^{OCT} = -0.3$ cm^{-1} at 1.83 K and below ($\Delta E = 16.2$ cm^{-1}), its RMS value is very high (approximately 23 %), indicating it is a very poor candidate for a representation of the structure. The principal low energy minimum of the MLD plots is very sharp and is confined to a very narrow range, decreasing from $D^{OCT} = 0.13$ cm^{-1} at 4.22 K ($\Delta E = 7.02$ cm^{-1}) to $D^{OCT} = 0.07$ cm^{-1} at 2.31 K ($\Delta E = 3.78$ cm^{-1}), then leveling at $D^{OCT} = 0.06$ cm^{-1} from 2.18 K – 1.47 K ($\Delta E = 3.24$ cm^{-1}). All of these energies are low, and indicative of only very slight perturbation of the Fe atom energy configuration by the matrix lattice.

Since the refinement under octahedral symmetry displays some ambiguity in the resolution of minima with the minimization scheme utilized, it is certainly reasonable to expect similar problems with the lower tetragonal and trigonal symmetry models as well. These problems may be expected to be more difficult to localize as the lower symmetry models extend to three-dimensions, increasing the size of the grid under consideration to the cubed power of the one-dimensional grid. Additionally, numerical integration over the theta angle from 0 to $\pi/2$ is now required. However, refining similar small data sets (as in the octahedral approach) to identical range and resolution over three dimensions while integrating numerically from 0 to $\pi/2$ over 1000 theta intervals would be computationally prohibitive, requiring an estimated 3.5×10^5 days, or over 950 years with the technology utilized!! Thus, either the resolution and/or volume grid must be drastically reduced in (practical to some extent) or dependence placed on an effective minimization routine. Consideration of the refinement results will demonstrate that there is some difficulty in locating and/or distinguishing between multiple minima unresolved by the minimization routine, depending on the starting parameters. The routine utilized, Powell's direction set methods in multidimensions, implements a 'golden search' using Brent's bracketing method, followed by a parabolic interpolation in one dimension to establish the minimum. The routines are found in "Numerical Recipes in C^{++}" by W.H. Press et al.[66]

Figure 4-26 plots the results incrementing along one dimension (F_1^{TET}) of the tetragonal solution for the 4.22 K and 1.74 K MCD and MLD data sets while maintaining the other two dimensions (F_2^{TET} and B^{TET}) at the constant value of 1.000 cm^{-1}. The F_1^{TET} increment spacing was 0.02 cm^{-1} and each cycle was calculated over 250 theta increments between 0 and $\pi/2$. The initial input 'guess' provided to the minimization routine for the crystal field parameters was set at $F_1^{TET} = F_2^{TET} = B^{TET} = 1.000$ cm^{-1}. The refinements for the simultaneous MCD/MLD data sets at all temperatures resolved to minima with F_1^{TET} between 1.6 and 2.2 cm^{-1}, F_2^{TET} between 1.00 – 1.01 cm^{-1}, and B^{TET} between 0.98-1.00 cm^{-1} (Table 4-5). Note that there are two separate sections for the results in Table 4-5 for the MCD/MLD simultaneous refinements: primary refinements and secondary refinements. In many of the primary refinement cases, the result of the minimization routine resolved to crystal field parameters that varied dramatically, as the table indicates. However, inspection of the intermediate RMS values output by the routine and cataloged in a separate data file showed reasonably rapid convergence to crystal field parameters with F_2^{TET} and B^{TET} close to or equal to 1.0 cm^{-1} in all cases. Once this point was arrived at, several of the refinements progressed beyond, creeping slowly down what appears to be a long, broad valley to a slightly lower RMS value, but with results for the crystal field parameters and the corresponding energy of splitting being wildly variant. The minimization routine fails to find a unique minimum.

The final value of the RMS deviation when allowed to go to completion was not much improved in either case over the values obtained at F_2^{TET} and B^{TET} close to or equal to 1.0 cm^{-1}, but often the energy separation across the resulting crystal field perturbation became very large, in some cases over 100 or even 200 cm^{-1}. It is interesting to note that at temperatures 1.83 K and below, the refinements stopped on their own at F_2^{TET} and B^{TET} equal to 1.000 cm^{-1}. In Table 4-6 for the MCD/MLD individual refinements, in each case, computer software minimization of the individual MLD data sets proceeded to a conclusion of F_2^{TET} and B^{TET} equal to 1.00 cm^{-1} (1.01 in the single case at 3.78 K).

In order to further understand the complications arising here, additional computations over all data sets were made similar to those for the 'brute force' octahedral solutions, bypassing the minimization routine and incrementing the F_1^{TET} parameter from –0.5 to +2.5 in increments of 0.02 cm^{-1} while holding the F_2^{TET} and B^{TET} crystal field parameters constant at 1.00. The results of those calculations are shown in Figure 4-27. It is seen that there is a singular minimum from 4.22 K down to 3.23 K, hovering between F_1^{TET} = 1.5 to 1.6 cm^{-1}. At 2.98/2.91 K, there is a broadening and flattening of the MLD curve at its minimum as it bifurcates at 2.53 K into two distinct minima of nearly equal depth. The primary minimum is at $F_1^{TET} = 1.38$ cm^{-1} while the secondary lies higher at close to 2.0 cm^{-1}. These two minima remain distinct throughout the remainder of the data from 2.53 – 1.48 K, with the primary leveling at $F_1^{TET} = 1.26$ to 1.24 cm^{-1}and the secondary residing between 2.1– 2.2 cm^{-1}. The MCD plots shown in Figure 4-27 behave very similarly, the only exception being that the bifurcation of the single minimum around $F_1^{TET} = 1.62$-1.64 occurs at a slightly lower temperature of 1.95 K, resulting in the primary minimum tracking close to the MLD primary minimum and the MCD secondary minimum following closely with the MLD secondary minimum.

It is tempting to conclude that since the minimization routine resolved consistently with parameters F_2^{TET} and B^{TET} equal to 1.00 with reasonable RMS values, that the results are reliable. However, the existence of the multiple deep minima, and the fact that some of the refinements proceed beyond these minima, creeping along a broad, flat valley which slowly descended only slightly to give large variations in the crystal field parameters, suggests that these results may be less credible than desired. It is necessary to look closer at what the predicted behavior of the tetragonal model may be based on what has been learned from the free atom and octahedral calculations to this point.

Figures 4-28 and 4-29 illustrate comparisons of the RMS values calculated for the free atom, octahedral, and tetragonal symmetries for the MCD and MLD data sets, respectively, found in Tables 4-3 – 4-6. The free atom refinements tabulated in Tables 4-3 and 4-4 indicate reasonable confidence in a free atom model for the ‘crystal field symmetry’, at least around 4.2 K. There is no crystal field perturbation present in the free atom model and the Fe(0) atom behaves as if it is a 'free atom', unaffected by the matrix lattice. The 'crystal field separation' under this model is then 0 cm^{-1}. This model appears to hold reasonably well at the 'warmer' temperatures from 4.22 K down to about 2.3 K (RMS values ranging between 0.71-2.76 %), but the RMS values climb sharply as the temperature decreases below 2.3 K, indicating a worsening of the fit of the free atom theoretical model to the experimental data. The octahedral model RMS fit remains fairly consistent throughout the temperature range though, and the D^{OCT} crystal field parameter shows an initial value of 0.13 cm^{-1} at 4.22 K ($\Delta E = 7.02$ cm^{-1}) decreasing steadily to a plateau with $D^{OCT} = 0.06$ cm^{-1} extending from 2.18 K down to 1.48 K ($\Delta E = 3.24$ cm^{-1}). These are small perturbations, having an energy spread of only a few wavenumbers. The tetragonal RMS results using the initial guesses of $F_1^{TET} = F_2^{TET} = B^{TET} = 1.000$ cm^{-1} demonstrate slightly worse agreement with the experimental data at 4.22 K (~ 3.1 %) than the free atom or octahedral symmetries, but the fit improves significantly as the temperature decreases. The MCD tetragonal data of Figure 4-28 below ~2.5 K is only slightly worse than the octahedral fit, and rivals the octahedral fit near the lowest temperatures. The MLD tetragonal data of Figure 4-29, however, indicates a clear preference for the tetragonal symmetry model at temperatures below about 2.9 K. No conclusions will be drawn at this point about the preferred symmetry, as there is pending a question about the confidence of the tetragonal results.

The data of Table 4-7 demonstrates the much poorer fit associated with the trigonal refinement symmetry, ranging from 2.9 - 6.0 RMS deviation for MCD and 3.4 -

8.9% RMS deviation for the MLD data. Unlike some of the tetragonal refinements, all of the trigonal refinements each located a distinct minimum. Since these values are significantly larger across the entire temperature range from 1.48 to 4.22 K than the results for the free atom, octahedral, or tetragonal results, trigonal symmetry is ruled out as a viable geometry for the crystal field symmetry of Fe(0) atoms in Kr matrix.

A bit of rational speculation is now presented. The free atom results are obviously favored at the higher temperatures of 4.22 K down to ~ 2.5 – 3 K, where either octahedral or tetragonal symmetry seems to become the preferential environment (trigonal symmetry has been ruled out). In the free atom environment, there is no crystal field separation, i.e., the crystal field splitting is 0 cm^{-1}. In the octahedral environment at 4.22 K, where the RMS fit is worse than the free atom fit for both MCD and MLD, the crystal field parameter $D^{OCT} = 0.13$ corresponds to an energy separation between the T_2 and A levels of Figure 4-1 of only 7.02 cm^{-1}. At 2.4 – 2.6 K, where the octahedral model, in which there is reasonable confidence, begins to dominate over the free atom model. The crystal field parameter of $D^{OCT} = 0.06$ cm^{-1} represents a T_2-A energy separation of 3.24 cm^{-1}, a barely discernible amount of energy. However, if the tetragonal symmetry refinement prevails at the transition point of ~2.6 – 2.9 K, where its RMS is indicative of the best fit of theoretical data to the experimental data, then the derived crystal field parameters of $F_1^{TET} = 1.6$ cm^{-1}, $F_2^{TET} = 1.00$ cm^{-1}, $B^{TET} = 1.00$ cm^{-1} correspond to a total energy spread across the seven tetragonal crystal field energy levels (Figure 4-30) of 56.7 cm^{-1}. This is an abrupt jump in energy over a very short temperature interval. It would seem more reasonable that the transition would continue smoothly at a much lower energy of total splitting. Otherwise, on re-warming higher than ~2.5 K it would seem feasible that energy should be emitted in a re-arrangement back to an abrupt octahedral symmetry environment.

Furthermore, the equivalent operator expression for the octahedral symmetry environment (Equation 3-9) is essentially a subset of the expression for the tetragonal environment (Equation 3-10). If $B^{TET} = 0.0$, then Equation 3-10 becomes Equation 3-9.

$$V_{OCT} = \frac{D^{OCT}}{60}\left[\left\{35J_z^4 - 30\,J(J+1)J_z^2 + 25J_z^2 + 3J^2(J+1)^2 - 6J(J+1)\right\} + \frac{5}{2}\left(J_+^4 + J_-^4\right)\right] \tag{3.9}$$

$$V_{TET} = \frac{B^{TET}}{3}\left[3J_z^2 - J(J+1)\right] + \frac{F_1^{TET}}{60}\left[35J_z^4 - 30\,J(J+1)J_z^2 + 25J_z^2 + 3J^2(J+1)^2\right.$$

$$\left. - 6J(J+1)\right] + F_2^{TET}(J_+^4 + J_-^4) \tag{3.10}$$

The same crystal field eigenvectors are used. The only distinction is the representation of the coefficient of the last term of each equation. Close inspection will show that $F_2^{TET} = D^{OCT}/24$ and $F_1^{TET} = D^{OCT}$. Thus, Equation 3-10, the equivalent operator for tetragonal crystal field symmetry, should be just as valid for refining an octahedral site, although less efficient. If the site symmetry being tested is indeed octahedral, using Equation 3-10 should result in $B^{TET} = 0.0$ and $F_2^{TET} = F_1^{TET}/24$. The resultant RMS should be identical for application of each operator to the same octahedral environment. Therefore, if the tetragonal results have an equivalent RMS value, then the F_1^{TET} crystal field parameter arrived at from the use of Equation 3-10 in the Hamiltonian should be equal to the D^{OCT}

value obtained from the use of Equation 3-9. The same inference can be made regarding the free atom model: either Equation 3-9 should refine to $D^{OCT} = 0.0$ or Equation 3-10 should refine to $F_1^{TET} = F_2^{TET} = B^{TET} = 0.0$. It seems implausible that in any case the tetragonal model RMS should be worse than the octahedral refinement model results, since it is the superset of the octahedral model. Yet, this is what the results of Tables 4-5 and 4-6 display. It is understandable that a better refinement (lower RMS) would result in different crystal field parameters, as this would be a valid indication of a preference of tetragonal symmetry over the octahedral model, presenting as distortions in the crystal field parameters B^{TET} , F_1^{TET} and F_2^{TET} from D^{OCT}. It also raises a concern to have the refined parameters F_2^{TET} and B^{TET} end up refining to exactly their starting values: 1.00.

Knowing from the octahedral results that the minimization routine may well skip by one minimum to a neighboring minimum of greater or less depth, and evoking the argument of the preceding paragraph, it was necessary to re-calculate all the data sets under tetragonal symmetry using different initial 'guesses' for the starting crystal field parameters. The values of $F_1^{TET} = 0.05$ cm^{-1}, $F_2^{TET} = 0.05$ cm^{-1}, $B^{TET} = 0.05$ cm^{-1} were utilized, parameters that start the refinement out close to zero total crystal field splitting. Close monitoring of the refinement by tracking the intermediate RMS values vs. crystal field parameters in a separate data output file demonstrated that the routine did perform a search for minima far from the low energy starting point, but this time, in all data sets, the final results were even lower RMS than the first reported results listed in Tables 4-5 and 4-6, with the resultant crystal field parameters usually, but not always, indicative of a low total energy separation consistent with the expectation of a smooth transition from a free atom state to or through a low energy octahedral configuration. These results are collected in Table 4-8 and graphed in Figures 4-31 and 4-32. Again there are several refinements which demonstrate a stable intermediate refinement stage, with parameters leveling at reasonable low energy values and RMS deviation values not far above the final values, yet creeping along a shallow valley ending in unrealistic large and deviant results. Thus, the primary and secondary refinement parameters are reported for comparison as in Tables 4-5 and 4-6.

Plotting these new values against the octahedral and free atom results already obtained demonstrates a early favoritism of a free atom or tetragonal environment near 4.2 K which proceeds to a marked tetragonal preference with decreasing temperature (Figures 4-33 and 4-34). These conclusions may still be deceptive, as comparison of the tetragonal parameters of Table 4-8 with the octahedral parameters of Tables 4-3 and 4-4 still shows a large difference in the refinement parameters. Recall again that the octahedral equivalent operator is a subset of the tetragonal equivalent operator. D^{OCT} values from Tables 4-3 and 4.4 at 4.22 K and 3.82 K for the simultaneous MCD/MLD refinements are 0.129 and 0.106 cm^{-1}, respectively. These values are still an order of magnitude greater than the values obtained from the tetragonal refinement, if the geometry were to be octahedral. The tetragonal values are $F_1^{TET} = 0.015$, $F_2^{TET} = 0.087$, and $B^{TET} = -0.041$ at 4.22 K. Since, for an octahedral model refined under tetragonal symmetry, $F_1^{TET} = D^{OCT}$, $F_2^{TET} = D^{OCT}/24$, and $B^{TET} = 0.0$, it is implied that $D^{OCT} = 0.015$

Table 4-8. Tetragonal refinement parameters for the individually-refined MCD and MLD experimental data sets at different initial starting values of the crystal field parameters

			Tetragonal Symmetry primary minimization						secondary minimization					
Number of Data Points	MCD T (K)	MLD T (K)	MCD RMS (%)	MLD RMS (%)	F_1^{TET}	F_2^{TET}	B^{TET}	ΔE_{CF} (cm^{-1})	MCD RMS (%)	MLD RMS (%)	F_1^{TET}	F_2^{TET}	B^{TET}	ΔE_{CF} (cm^{-1})
31	4.22	4.22	1.99	1.29	0.015	0.087	-0.041	2.61	---	---	---	---	---	---
31	3.82	3.78	2.13	1.43	0.005	0.047	0.021	1.46	---	---	---	---	---	---
31	3.82	3.74	---	---	---	---	---	---	---	---	---	---	---	---
31	3.34	3.23	1.85	0.86	0.008	0.057	-0.020	1.66	---	---	---	---	---	---
31	2.98	2.91	1.42	0.71	0.013	0.060	-0.018	1.90	---	---	---	---	---	---
31	2.58	2.53	1.27	0.73	0.080	-0.032	-0.193	2.48	---	---	---	---	---	---
31	2.31	2.29	2.07	1.24	0.074	0.238	-0.613	10.01	2.07	1.34	0.133	0.126	-0.414	7.59
31	2.18	2.11	1.72	0.60	0.068	-0.024	-0.227	2.47	1.73	0.61	0.085	-0.022	-0.206	2.75
31	2.08	2.11	1.70	0.60	0.064	-0.015	-0.214	2.45	1.71	0.72	0.106	-0.001	-0.080	3.64
31	1.95	1.91	1.58	0.89	0.660	1.452	1.185	31.22	1.71	0.88	0.300	0.073	0.123	11.39
31	1.83	1.79	1.18	1.05	0.839	0.021	1.531	39.63	1.37	1.01	0.394	0.031	0.264	14.68
31	1.74	1.74	0.94	1.13	5.921	0.008	9.623	263.60	1.28	1.09	0.405	0.046	0.035	14.48
31	1.74	1.68	0.94	0.92	5.658	0.010	9.226	252.30	1.33	0.91	0.391	0.032	0.062	13.70
31	1.61	1.61	1.42	0.79	-0.117	0.131	-0.117	5.77	1.46	0.74	-0.265	0.053	0.061	8.31
31	1.57	1.55	1.90	0.68	6.537	-0.015	10.451	289.10	2.19	0.94	0.463	0.408	0.064	16.28
31	1.57	1.48	1.90	0.86	-0.117	0.129	0.158	3.87	2.34	0.83	-0.226	0.074	0.063	7.56

Note: Theta integration for the refinements is in 250 steps over 0 to $\pi/2$. Initial values for refinement: $F_1^{TET} = F_2^{TET} = B^{TET} = 0.05$

via its relationship with F_1^{TET} and that $D^{OCT} = 2.09$ via its relationship with F_2^{TET}. These are obviously inconsistent with an octahedral model, yet it must be noted that very small energies are involved: 2.61 cm^{-1} for the above parameters. These are very minor distortions overall, and may well lie within the error of experiment.

A further check of calculation accuracy was pursued by numerically integrating the octahedral refinements over 250 theta increments. Subsequent to the theoretical development of Chapter 3 it had been surmised, perhaps erroneously, that an octahedral crystal field symmetry imposed about the central metal atom by a surrounding rare gas atom lattice would behave similarly as a totally symmetric isotropic field for purposes of refinement. In fact, an octahedral field is not totally symmetric, and is often categorized as 'pseudo-isotropic', denoting its less than completely spherical symmetry. Thus it was desired to compare the results of octahedral refinements over theta integration with those absent theta integration. Since the octahedral refinement is, again, a one-dimensional problem, instead of involving the complications of multiple energy wells resolution as seen previously in the use of the minimization routine, the minimization routine was again bypassed and the RMS deviation values vs. D^{OCT} calculated directly via the 'brute force' method from $D^{OCT} = -0.40$ to $D^{OCT} = +0.40$ in increments of 0.01 cm^{-1}. The resultant plots are illustrated in Figure 4-35 and the data tabulated in Table 4-9. Contrasting this diagram with Figure 4-23 graphing the octahedral results for no theta integration (i.e., one theta increment) shows the presence of slightly more complicated multiple minima dilemma at lower temperatures. At 2.58 K (MCD) and 2.53 K (MLD) the MCD locus has bifurcated and has minima at points which are practically 180 degrees out of phase with the MLD locus. Figures 4-36 and 4-37 graph respectively plots for the MCD and MLD RMS deviations vs. temperature for the theta integrated octahedral plots of Figure 4-35 along with the tetragonal and free atom results. The theta integrated octahedral refinements are improved over the similar plots illustrated in Figures 4-33 and 4-34, and rival again the tetragonal model for the designated symmetry. The RMS values plotted are for the lowest minimum in Figure 4-35.

Table 4-9. Octahedral refinement parameters for the MCD and MLD experimental data sets determined from RMS vs P plots for the lowest energy configuration over 250 theta increments.

MCD/MLD
Simultaneous Refinements

Number of			Symmetry Octahedral			ΔE_{CF}		ΔE_{CF}
Data Points	T_{MCD} (K)	T_{MLD} (K)	RMS_{MCD} (%)	RMS_{MLD} (%)	D^{OCT}_{MCD}	(cm^{-1})	D^{OCT}_{MLD}	(cm^{-1})
31/31	4.22	4.22	2.07	0.63	0.060	3.24	-0.02	1.08
31/31	3.82	3.78	2.13	0.83	0.050	2.70	-0.06	3.24
31/31	3.34	3.23	1.90	0.79	0.040	2.16	0.03	1.62
31/31	2.98	2.91	1.41	0.72	0.010	0.54	0.05	2.70
31/31	2.58	2.53	1.22	0.88	-0.070	3.78	0.05	2.70
31/31	2.31	2.29	1.99	1.67	-0.090	4.86	0.09	4.86
31/31	2.18	2.11	1.50	0.95	-0.080	4.32	0.06	3.24
31/31	2.08	2.11	1.43	0.95	-0.070	3.78	0.06	3.24
31/31	1.95	1.91	1.38	1.35	-0.120	6.48	0.07	3.78
31/31	1.83	1.79	0.98	1.79	-0.140	7.56	0.08	4.32
31/31	1.74	1.74	0.98	1.94	-0.170	9.18	0.08	4.32
31/31	1.74	1.68	0.98	1.94	-0.170	9.18	0.08	4.32
31/31	1.61	1.61	1.25	2.44	-0.180	9.72	0.08	3.78
31/31	1.57	1.55	1.91	2.07	-0.180	9.72	0.07	3.78
31/31	1.57	1.48	1.91	2.88	-0.180	9.72	0.07	3.78

There is a tendency to view some of the data as 'reasonable' due to its low RMS deviation, as the octahedral results at 4.22 K. However, when looking at the various results it must be kept in mind that if indeed one geometry is dominant over a particular temperature range, then becomes invalid over another temperature range, it is not unreasonable for the data plots of that geometry over the invalid range to display inconsistencies or irregularities. It is interesting to note that the octahedral and tetragonal RMS deviation results plot almost identically for the MCD results, both indicating a very slight preference over the free atom model. The MLD octahedral results are very comparable with the free atom results initially, indicating very slightly better refinement than the tetragonal model. However, in both MCD and MLD the free atom model becomes less encouraging as a possible solution, while the preference for either octahedral or tetragonal symmetry is favored. The difficulty lies in distinguishing between these two symmetries. The MCD RMS deviation data allows for no discrimination between the two competing solutions. However, the more sensitive MLD data does indicate a shift toward tetragonal symmetry as the favorable model below about 2.5, with a total crystal field splitting energy of ~7 – 15 cm^{-1}. The irregularities apparent in the plots of Figure 4-35 at and below ~2.5 K lend credence to discounting octahedral symmetry as a viable model below ~2.5 K

Discussion

A point of interpretation to be dealt with in the discussion section is the weight given the MCD and MLD results, considering them equally (as with the average of both values) or to judge perhaps that the MLD plots are a more sensitive indicator of the true geometry. From statistical considerations, a root mean square (RMS) deviation of greater

---

than 5% is generally regarded as “not probable” as a solution. RMS values between approximately 3-5 % may be regarded as possible, with some degree of confidence. Values less than 3% are candidates to be regarded as highly possible, with decreasing RMS per cent deviation directly reflecting the increase in confidence level of the theoretical model representing the true physical site geometry. This does not guarantee that the model is accurate however -- it is in reality only a measure of the deviation of the actual experimental data from the calculated theoretical data for the assumed model. It can be seen from Tables 4-3 – 4-9 that although the MLD refinements frequently appear quite good, the corresponding MCD refinement for the same symmetry at the identical temperature should be rejected based on the large magnitude of RMS deviation values. The greater dependency of the MLD on $\mathbf{B}^2$ as opposed to **B** for MCD often results in much more intense MLD spectra for analysis. This translates directly to improved accuracy in the measured magnitudes and band moments of the transitions.

There is an inherent problem in utilizing magnetization scans for the symmetry modeling by the methods of this research. Referring to Table 4-10, it can be seen that the bandshape for the MLD $^5P_3 \leftarrow {}^5D_4$ transition has a constant barycenter, i.e., the peak wavelength of the band remains constant due to the symmetry of the J transitions distributed about the central wavelength. A more significant concern is the shift in barycenter of the MCD $^5P_3 \leftarrow {}^5D_4$ transition band peak due to asymmetrical transitions about the center absorption frequency (Table 4-10). The asymmetry of the band causes slight changes in the bandshape with increasing **B** and decreasing T, causing a shift of the transition peak's center frequency. The consequence is a magnetization locus that deviates to some extent from the true peak intensity across all **B** and T.

Table 4-10. Relative transition intensities from the ground state J = 4 Zeeman sublevels to the excited state J' = 3 Zeeman sublevels

	π	σ^+	σ^-
M_J	$\Delta M_J{}^a = 0$	$\Delta M_J = +1$	$\Delta M_J = -1$
+4	0	0	28
+3	7	0	21
+2	12	1	15
+1	15	3	10
0	16	6	6
-1	15	10	3
-2	12	15	1
-3	7	21	0
-4	0	28	0

[a] $\Delta M_J = M'_J$ (excited state) - M_J (ground state)

Analyses of the MCD/MLD saturation data focused on the obvious assumption that the crystal field environment must be the same for both MCD and MLD determinations, i.e., refinement of both MCD and MLD individually should fit the same appropriate symmetry and yield the same crystal field parameters within experimental error. It has been assumed previously that this symmetry was valid over the entire temperature range, i.e., the crystal field symmetry was constant. This implies the refined parameters (D^{OCT}, B^{TET}, F^{TET}, G^{TRI}, K^{TRI}, and M^{TRI}) would remain constant over the entire temperature range in a given matrix. The possibility of a transition in the relative positions of the surrounding lattice cage rare gas atoms was regarded as unlikely. That hypothesis has been invalidated by this research, as inspection of Tables 4-4, 4-8, and 4-9 and Figures 4-36 and 4-37 demonstrate a rather smooth variation of the crystal field parameters with decreasing temperature from a 'near' free atom state, to octahedral symmetry, to tetragonal symmetry.

The refinement simulations for the free atom, octahedral, and tetragonal symmetry models (Figures 4-12 – 4-15, 4-31, 4-32, Tables 4-3, 4-4, 4-8, and 4-9) show excellent fits at and just below liquid helium temperature. The individual refined MCD data at these temperatures indicates a small octahedral crystal field parameter (T = 4.22 K, $D^{OCT} = 0.06\ cm^{-1}$, RMS = 2.07%, $\Delta E_{CF} = 3.24\ cm^{-1}$; T = 3.82 K, $D^{OCT} = 0.05\ cm^{-1}$, RMS = 2.13%, $\Delta E_{CF} = 2.70\ cm^{-1}$) as had been seen in several earlier limited studies. Rivoal et al., our Paris collaborators, also determined the crystal field symmetry to be slightly octahedral in the temperature range 4.2 K – 22 K for Fe(0) in Kr and Xe.[65] They calculated $D^{OCT} \cong 0.06\ cm^{-1}$, in exact agreement with our initial MCD results. Our individual MLD refinements, however, do not support this conclusion at 3.82 and 4.22 K (T = 4.22 K, $D^{OCT} = -0.02$, RMS = 0.63, $\Delta E_{CF} = 1.08\ cm^{-1}$; T = 3.82 K, $D^{OCT} = -0.06$, RMS = 0.83, $\Delta E_{CF} = 3.24\ cm^{-1}$). The negative sign of the crystal field parameter indicates an inversion of the crystal field energy levels, with the singlet A residing lowest in energy and the triplet T_2 state highest in energy. This contradicts the Mossbaüer results of Coufal, Lüscher, and Micklitz.[68] The combined refinement suggests an environment consistent with a near free atom state in which $D^{OCT} \approx 0.00\ cm^{-1}$ or a very slightly octahedrally perturbed state where $D^{OCT} \approx 0.02\ cm^{-1}$ at and just below liquid helium temperature (4.2 – 3.8 K). The associated separation energy ΔE_{CF} is approximately 1.1

cm^{-1}. Rivoal et al. assumed the octahedral symmetry field to be 'totally isotropic' in their software calculations, paralleling the calculations of Tables 4-3 and 4-4 and Figures 4-14 and 4-15 of this study. Recall that the octahedral data of Table 4.9 was calculated under the assumption that the octahedral model is sufficiently anisotropic to preclude being treated mathematically as isotropic.

Support for the octahedral and tetragonal models increases with decreasing temperature, although it is difficult to distinguish an octahedral perturbation from a slight tetragonal distortion initially ($T = 4.22$ K, $F_1^{TET} = 0.015\ cm^{-1}$, $F_2^{TET} = 0.087\ cm^{-1}$, $B^{TET} = -0.041\ cm^{-1}$, $RMS_{MCD} = 1.99$, $RMS_{MLD} = 1.29$, $\Delta E_{CF} = 2.61\ cm^{-1}$). It is concluded that there is indeed a crystal field perturbation of some form, however, and thus the free atom model, though a good approximation at these temperatures, is rejected in favor of the octahedral/tetragonal symmetry. The free atom model breaks down dramatically at ≤ 3.5 K for the MLD results and ≤ 2.3 K for the MCD. At ≤ 2.5 K, the MLD octahedral fits worsens with decreasing T from RMS = 0.88% at ~2.53 K to RMS = 2.88% at ~1.48 K. The tetragonal model remains stable and indicative of a better theoretical fit than the octahedral symmetry at low temperature. The tetragonal MLD RMS ranges from 1.34 % at 2.29 K to 0.83 % at 1.48 K. The MCD results are ambiguous and supportive of either model.

Nuclear gamma resonance spectroscopy (Mossbaüer spectroscopy) has been performed on ^{57}Fe isolated in argon, krypton, and xenon rare gas matrices by H. Coufal, E. Lüscher, and H. Micklitz.[68] The spectra in all three rare gases consist of a distinct inverse-temperature-dependent absorption with an isomer shift of –0.75 ± 0.03 mm s^{-1} relative to metallic Fe at 300 K. The T dependence is linear from 4.4 to 20.5 K. They concluded the ^{57}Fe atoms reside in a magnetic ground state (a triplet state) indicating the crystal field parameter is positive in sign. The constancy of the isomer shift across the Ar-Kr-Xe series implies the existence of a nearly free atom state for the ^{57}Fe atoms in the rare gas solid. The lack of a quadrupole line-broadening effect is indicative of cubic (octahedral or tetrahedral) site symmetry.

Montano, Barrett, and Schanfield[67] acquired additional Mossbaüer spectra of Fe in Xe at 2.8 T and measured a $\mathbf{B}_{eff}$ at the Fe nucleus of 70 ± 1.5 T from the observed magnetic hyperfine splitting. They concluded a T_2 ground state was responsible for this based on close agreement with predicted spectra, thus establishing the ground state **J** as a 'good', or valid, quantum number for Fe isolated in the heavy rare gas solids. This directly implies the separation energy ΔE_{CF} is less than the spin-orbit splitting constant of 104 cm^{-1}. They also concluded no excited states were occupied at 4.4 K and 2.8 T, implying the separation energy must be greater than the Zeeman energy at 2.8 T, approximately 10 cm^{-1}. The results of this study via magnetic saturation methods support the predominance of a T_2 ground state. The separation is also found to be much less than the spin-orbit coupling constant, as expected. The results of this srudy show that at 4.2 K and 2.88 T the T_2 ground state is populated to a high degree, but not solely populated. Observe the theoretical hyperbolic tangent curve of Figure 3-1 and compare it with the curvature of the experimental data of Figures 4-12 and 4-13. At 2.88 T, the experimental

---

curves are approaching an asymptote, but have not yet reached it. This indicates that full magnetic saturation of the ground state has not yet been achieved. There is still some slight, yet significant, electron population of upper excited states. Thus, the conclusion from this research supporting the existence of an octahedral (cubic) site symmetry at 4.2 K remains in agreement with the results of Coufal, Lüscher, and Micklitz[68] at 4.4 K, but the crystal field separation energy ΔE_{CF} is established to be less than the 10 cm^{-1} lower bound of their results at 4.4 K. From the present study, a value of 1.1 - 1.7 cm^{-1} representing the crystal field parameter D^{OCT} of ~0.02 – 0.03 cm^{-1} is determined at 4.2 K.

The crystal field symmetry derived for Fe(0) in a krypton matrix is modeled as a very slight octahedrally distorted site having a positive crystal field parameter D^{OCT} at and near liquid helium temperature. The total energy separation ΔE_{CF} between the lower T_2 and upper A energy levels (Figure 4-1) is approximately 1.1 – 2.5 cm^{-1}. A tetragonal distortion of similar ΔE_{CF} (2.61 cm^{-1})span is a significant alternative possibility, with $F_1^{TET} = 0.015$, $F_2^{TET} = 0.087$, $B^{TET} = -0.041$. At these small magnitudes of energy, it is difficult, if not impossible, to distinguish between the two sites given the experimental uncertainty present. As the matrix is cooled to lower temperatures, below ~2.5 K, the crystal field symmetry transitions distinctly to a tetragonal symmetry model. The ΔE_{CF} increases with decreasing T, indicated by an increase in the magnitude of one or all three crystal field parameters F_1^{TET}, F_2^{TET}, and B^{TET}. The calculated energies associated with these parameters below ~2.5 K fall between ~2.8 – 7.6 cm^{-1} near 2.2 K to 7.6 – 16.3 cm^{-1} circa 1.5 K.

The region preceding the transition from the very slightly octahedral state to tetragonal symmetry with decreasing temperature is accompanied by a slight increase in the D^{OCT} crystal field parameter, indicating an increase in the energy separation between the T_2 and A energy levels. It is reasonable to expect that the crystal field parameters would change if a unit cell contraction of the Kr cage were occurring with a decrease in temperature. Increased interaction between the occupied Kr electron orbitals with the occupied d-electron orbitals of the Fe(0) atom would be an expected occurrence upon physical contraction of the surrounding lattice. Although the freezing point of Kr is 115.8 K, matrix experiments in Kr have always been lost by rearrangement mechanisms around 40 K, indicating high fluidity of the 'solid' matrix at this temperature. Atomic ABS, MCD, and MLD spectral lines disappear completely, leaving only broad UV absorption bands probably indicative of bulk metal cluster formation. The annealing of the matrices around 35 K to permit unstable site rearrangement without losing significant absorption is highly indicative of a less than rigid environment. Clear Kr matrices at liquid helium temperature (4.2 K) turn cloudy upon warming (even very slowly) to around 9 K, often resulting in broad dispersion of incident radiation in the ultraviolet region. This is probably due to bulk cluster formation within the matrix. Obviously, a physical lattice rearrangement of some type is occurring at what is considered a very low temperature (9 K).

Further studies by Coufal, Lüscher, and Micklitz[68] using electron spin resonance (ESR) spectroscopy demonstrated multiple geometry site trapping for a wide variety of atoms isolated in Ne, Ar, Kr, and Xe, including H, Li, Na, K, Cs, Ru, Cu, Au, N, P, As, Cd, Cr, Al, Ga, and I. Silver (Ag) alone has only one site geometry in all four heavy rare gas solids. Gold (Au) exhibits two different trapping sites very close in energy in Ne, but only one in Ar, Kr, and Xe. Many of the other listed atoms (vide supra) have three, four, five, and in the case of rubidium in argon, seven different trapping sites in rare gas solids. These generally are a function of the co-condensation method utilized. High-energy vaporization/deposition techniques and photolysis can enhance the appearance of multiple sites. Many or all of these additionally sites disappear on annealing the matrix, leaving predominantly the stable ground state configuration. The g-factor shifts in a particular site are generally small, usually 0.01 – 0.1 %, but sometimes as large as 3 – 4 %. Variation of the g-factor shift from one site configuration to another is typically several per cent in magnitude.

Similar behavior is seen in the Fe/Kr spectra of this study (Figure 4-9). Many of the absorption peaks show a distinct shoulder on the low energy side of the band that is attributed to an alternative higher energy trapped site. These shoulders are especially prominent after a fast, 'hot' deposition of Fe(0) atoms in the rare gas matrix. Annealing adequately causes these shoulders to diminish significantly in intensity, nearly disappearing completely.

Consideration of the physical structure of an Fe(0) atom embedded in a rare gas lattice must begin with a description of the lattice without the Fe(0) atom present. The four heavy rare gases (Ne, Ar, Kr, and Xe) all crystallize in face-centered cubic (fcc) lattices, not the expected hexagonal close-packed (hcp) lattice as He. The interatomic distance for Kr, the rare gas used in this study, is 3.94 Å.[69] The stabilization of the fcc lattice over the hcp lattice has been attributed to many-body effects beyond the primitive two-body electrostatic interaction potentials.[70] The effect is apparently due to splitting of the degenerate rare-gas d, f, and higher orbitals due to interaction with nearest neighbors. In the fcc structure, p-orbitals overlap equally with nearest neighbors. The d_{z2} and d_{x2-y2} orbitals interact directly with nearest neighbors located axially from the central rare gas atom, destabilizing these orbitals energetically. The d_{xy}, d_{xz}, and d_{yz} orbitals are directed between the nearest neighbors, still experiencing some destabilization to electron occupation, but not as much as the d_{z2} and d_{x2-y2} orbitals. This is the classic ligand field splitting of degenerate states into a lower T_2 and an upper E_g state. There is a relative stabilization of the T_2 state as compared with the E_g state. This effect is much weaker, by a factor of nearly four, in the noncentrosymmetric hcp lattice.

Beginning with the face-centered cubic lattice structure for krypton, what physical strains and modifications might be imposed by placing an Fe(0) atom in the middle of the Kr lattice? For the Kr-Kr interatomic distance of 3.94 Å in the fcc lattice, removing a single Kr atom would leave a void (hypothetically) 3.94 Å across at the center of a unit cell of twelve surrounding Kr atoms. The Fe-Fe interatomic distance is 2.48 Å. This is the atomic diameter of Fe obtained from X-ray analysis of the bulk metal. Fe(0) atoms in π-arene organometallic complexes have Fe(0) – C_{arene} bond distances of typically 2.10 Å and an Fe(0) atom to plane-of-ring distance of 1.55 Å as determined by single-crystal X-

---

ray diffraction spectroscopy.[71] Bonding to the arene rings of these compounds is via arene p-orbital overlap with partially empty Fe(0) d-orbitals. It should be noted that this is not an ideal comparison, as back π-bonding along the σ-bonded ligands also present in these complexes affects the π-arene bonding. However, these types of compounds illustrate the properties of Fe(0) atoms in a phsycial environment more similar to the rare gas lattice environment than bulk metal.

For an Fe(0) atomic diameter of 2.48 Å in a 3.94 Å central void of a Kr lattice unit cell (substitutional site), there is technically 0.73 Å of 'clearance' between the periphery of the Fe(0) (treating it as a rigid sphere) and the periphery of each Kr atom. This crude model may allow for the cubic symmetry of the surrounding Kr atoms to remain intact, balancing the Fe(0) atom at some equi-potential configuration centrally located in the unit cell. This seems unlikely, however, if the extent of the Fe(0) atom's electronic interaction allows for 'void' space between the periphery of the Fe and Kr atoms. If such is the case, it is highly conceivable that an axial distortion of the local cubic unit cell would occur to 'fill' the void, allowing some Kr atoms to move closer, while others (likely the axial Kr atoms) would disperse slightly away to permit the space-filling contraction. This could certainly support a local tetragonal environment, even if only slightly distorted, although the possibility of rearrangement to an interstitial cubic geometry is also a valid proposition.

Taking into consideration the crystallographic data for the π-arene organometallic complexes of Fe(0) (vide supra), the 2.10 Å Fe(0) – C_{arene} bond distance implies that the

---

capability of Fe(0) d-orbitals to experience an interaction with Kr atoms may extend beyond the Fe(0) atomic radius of 1.24 Å, countering any tendency for the cubic cage to collapse to lower symmetry. The extent to which vibrational modes associated with Fe(0) and particular Kr atoms in the unit cell may allow for the effective Kr diameter to be larger, especially at warmer temperatures, has been addressed by ShaksEmampour et al.[22] They checked for lattice mode vibrations which would indicate the presence of a Jahn-Teller effect and found that there was none. Given the large spin-orbit coupling constant of matrix-isolated Fe(0) atoms, no Jahn-Teller effect is expected.

For a Kr matrix at ~40 K in which visible physical changes occur at ~9K, it is not at all unreasonable to expect a significant unit cell contraction to occur on approaching superfluid helium temperature and below. Unit cell contractions are commonly observed in low temperature single crystal X-ray diffraction studies when contrasted with the same crystal structure determined at room temperature.[72] Thus it is concluded from the present study that Fe(0) atoms have only very slight interaction with the Kr matrix throughout most of the temperature range in which matrix isolation studies have been previously performed (22 – 4.2 K), existing in a nearly pure free atom lattice configuration, probably perturbed only slightly by what is predominately an octahedral distortion of just a few wavenumbers in extent. The MCD data suggests a slight octahedral distortion continues to exist and increases in magnitude as solid Kr contracts significantly at 4.2 – 3 K, beginning to 'crowd in' on the central metal atom. As depicted in Figure 4-1, an octahedral crystal field splitting with positive D^{OCT} results in A, T_1, E, and T_2 energy levels, with the T_2 lying lowest in energy. This is consistent with the experimental Mossbaüer results[67,68]. For a positive crystal field D^{OCT}, the T_2 level would be the lowest in energy. If the crystal field parameter were negative, an inversion of energy levels would exist. This was predicted from earlier data simulations by Jacobi, Schmeisser, and Kolb,[73] but cannot be supported by the data presented in this study. As shown in Figure 4-22 representing the refinement of simultaneous MCD/MLD data at ~2.1 K, the octahedral crystal field parameter $D^{OCT} = 0.06$ cm^{-1}. This results in an overall splitting between level A and T_2 of only 3.24 cm^{-1}. This would certainly be undetectable in any absorption experiment, including linear limit MCD and MLD. Application of the magnetic field Hamiltonian $\hat{\mu}_Z$ further splits these crystal field levels as depicted in the diagrams. It is from these magnetically split crystal field levels that the MCD and MLD transitions occur. It is seen in Figure 3-2 that even a small splitting of 0.97 cm^{-1} can be amplified significantly in the presence of a magnetic field, resulting in a total splitting of 22.4 cm^{-1} at 4 Tesla and 1.4 K. Although still not resolvable in practical ABS, MCD, or MLD spectra, these effects can be discerned effectively with the MCD/MLD saturation method as the simulations indicate. These methods derive from changes in the MCD/MLD bandshape as detected by **B** and T dependent moments analyses.

Since the RMS value for a tetragonal refinement at 2.1 K is approaching the octahedral RMS level (1.96% for tetragonal vs 1.56% for octahedral), it appears that continued contraction of the rare gas matrix cage is occurring and becoming more significant, causing detectable distortion on the Fe(0) atom environment which presents best as a tetragonal distortion as the temperature continues to decrease. Figure 4-23 shows the crystal field splitting for a $^5D_4$ ground state under tetragonal distortion. There are seven resulting energy levels of which two are doubly degenerate E levels. The overall splitting between the low-lying $A_1(1)$ and highest energy E(2) (at zero magnetic field) is 74.5 cm^{-1} for crystal field parameters $B^{TET} = 1.65$, $F_1^{TET} = 1.00$, $F_2^{TET} = 1.00$ at 2.1 K. As the temperature decreases, the zero field splitting under tetragonal symmetry appears to distort further under the strain of a contracting matrix cage, yet remains the dominant symmetry. The total splitting at 1.74 K is 91.0 cm^{-1}, at 1.61 K it is 95.3 cm^{-1}, and at 1.56 K it is 96.3 cm^{-1}. This model is not inconsistent with the Mossbaüer results of Coufal, Lüscher, and Micklitz,[68] as their results were obtained at and above 4.4 K, where octahedral geometry is slightly favored

Summary

The complementary techniques of MCD and MLD utilized together prove to be definitive in permitting unambiguous assignment of the electronic energy transitions particular to the Fe(0)/Kr environment. The usefulness of these combined methods in other systems of more complicated spectra to unravel unresolved and otherwise weakly absorbing transitions appears to be of great value. The method of combined MCD/MLD saturation spectroscopy to determine the site symmetry of metal atom/host matrix environments with reasonable confidence is justified by the results demonstrated herein.

Development and analysis of the randomly oriented magnetic saturation phenomenon applied to matrix-isolated metal atoms in a rare gas matrix can be thought of in three distinct stages: theoretical modeling, computer simulation, and experimental data collection/reduction. The objective has been to derive a theoretical model for the randomly oriented metal atoms located in particular geometrical lattice environments (octahedral, tetragonal, and trigonal). Utilizing these theoretical models, theoretical data points are calculated. numerically using computer simulations, and compared directly with the properly reduced experimental data obtained in the laboratory. The theoretical derivations are sound. However, there are ambiguities which appear to arise in the mathematics of the computer modeling process, specifically the minimization routine. The most serious difficulty is in distinguishing the validity of multiple solutions. These present in the form of multiple minima, corresponding to different crystal field parameters along with different energies of crystal field splitting.

The minimization routine utilized, Powell's multi-dimensional method,[66] is a widely used and successful optimization routine. The philosophy behind the application of Powell's method involves invoking a local perturbation at a local minimum by moving a small, finite distance away from it. The routine then proceeds to determine a minimum from this new location. If a new and distinct minimum is discovered, it becomes the new local extreme. If not, the routine returns to the previously discovered minimum. Depending on the starting point coordinates input to the routine and the step size in relation to the width and frequency of actual minimum wells, the success of the routine may not locate all or especially the most extreme minima. The difficulties encountered in the pursuit of extreme minima in the present study bear out this deficiency.

Press et al.[66] discuss briefly recently developed optimization methods for finding global minima in the presence of undesired local minima. The methods are termed 'simulated annealing methods', and utilization of them has resulted in solutions of problems previously regarded as insoluble. The most significant problem in minimization routines is the generator of random changes in the system configuration. Most routines suffer from the inefficiency of proposing uphill moves at times when downhill moves still are the most practical move. Press et al. suggest solutions to the random cgange generator problem involving an 'annealing' method, similar to thermodynamic temperature annealing. The efficiency of the routine suffers initially, in favor of accuracy, only to become more efficient as hypothetical solutions are discarded as invalid. Future improvements to the modeling software should be considered with these particular methods as a viable option for determining more accurately the true extreme minimum.

It is concluded that Fe(0) atoms in a Krypton matrix reside normally in a geometrical environment that has almost no discernible effect on their electronic energy levels at 'normal' matrix temperatures (> 4.2 K), presenting as a slight octahedrally distorted site geometry. The energy levels can be perturbed further, however, by extreme cooling of the matrix to superfluid helium temperature. The resulting tetragonal symmetry environment presents itself with a crystal field splitting of ~8 - 16 cm^{-1}. Since the optical band width of the $^5P_3 \leftarrow {}^5D_4$ transition is 186 cm^{-1} FWHM for the absorption band and 136 cm^{-1} for the MCD and MLD bands, it is impossible to detect this splitting within the absorption band directly. This conclusion has been extracted from mathematically modeling the magnetization locus as it varies with T and **B**. The transition goes from a nearly free atom environment above 4 K down to near 3.5 K, collapsing to lower tetragonal symmetry below approximately 3.5 K. A steady increase in the crystal field splitting and separation energy ΔE_{CF} as the temperature decreases is readily explained by a contracting rare gas cage environment.

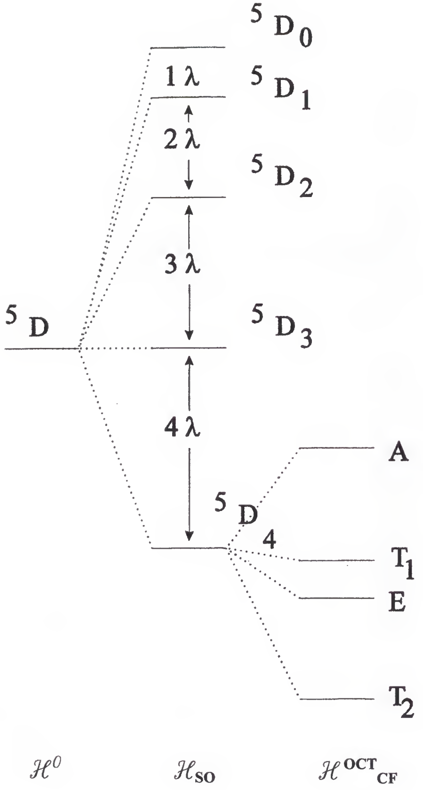

Figure 4-1. Splitting of Fe(0) by spin-orbit (SO) and octahedral crystal field (CF) perturbations. $\lambda = 104\ \text{cm}^{-1}$. The crystal field splitting is exaggerated.

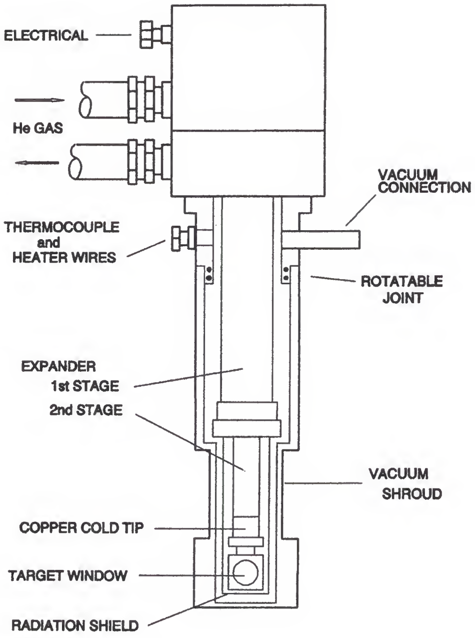

Figure 4-2. Diagram of Air Products closed-cycle helium cryostat. $T_{min} \cong 10\text{-}12$ K.

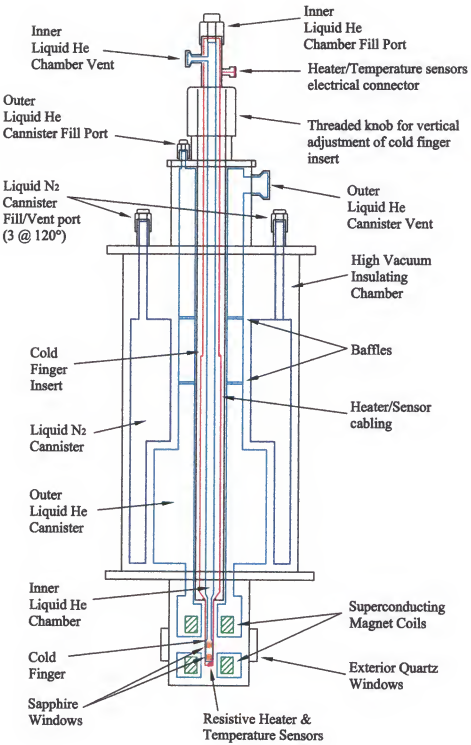

Figure 4-3. Diagram of Oxford superconducting split-coil magnet / liquid helium cryostat. Designed by M. Vala and manufactured by Oxford Instruments Co., Ltd., Oxford, England. Not shown in the drawing are the magnet power supply connectors and the high vacuum chamber valve assembly.

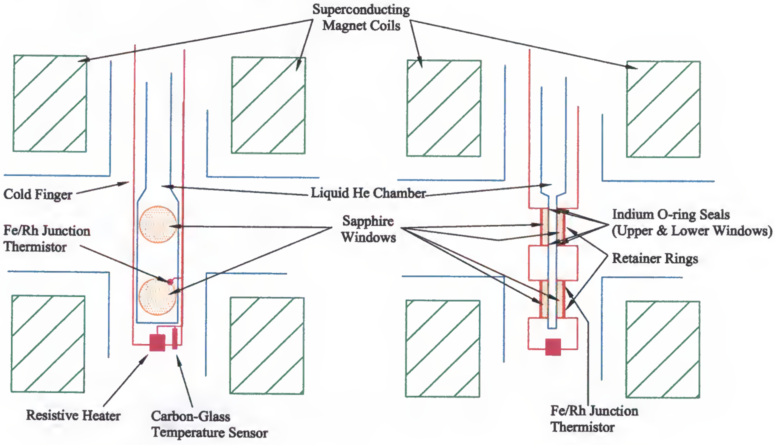

Relative Cold Finger Rotation 0°

Relative Cold Finger Rotation 90°

Figure 4-4. Expanded view of Oxford Instruments magnet/cryostat cold finger. Diagram illustrates the liquid He cooling of the dual sapphire window sets along with the location of the resistive heater (not utilized in these experiments) and the Carbon-Glass and Fe/Re thermistors.

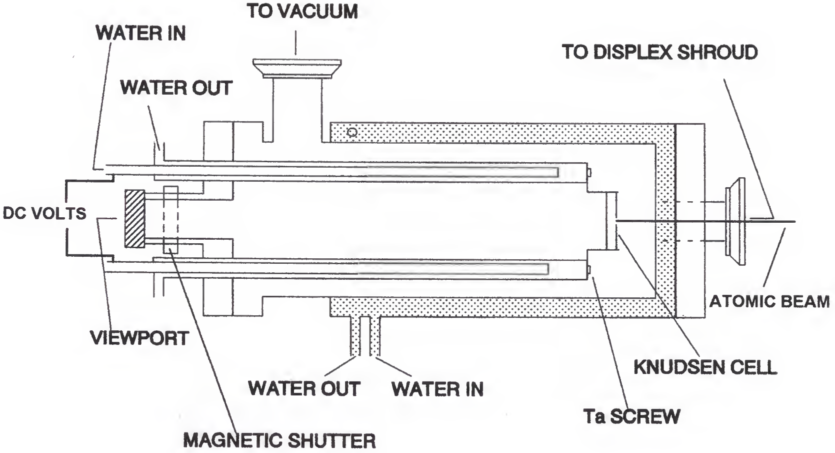

Figure 4-5. Plan view of furnace and Knudsen cell assembly for generating atomic beam.

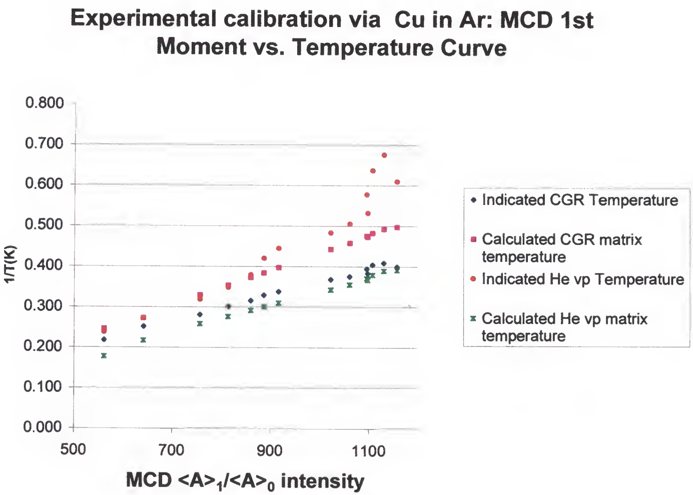

Figure 4-6. Temperature calibration data curves derived from a moments analysis. A matrix of Cu(0) atoms isolated in an Ar matrix deposited on the lower set of sapphire windows was utilized.

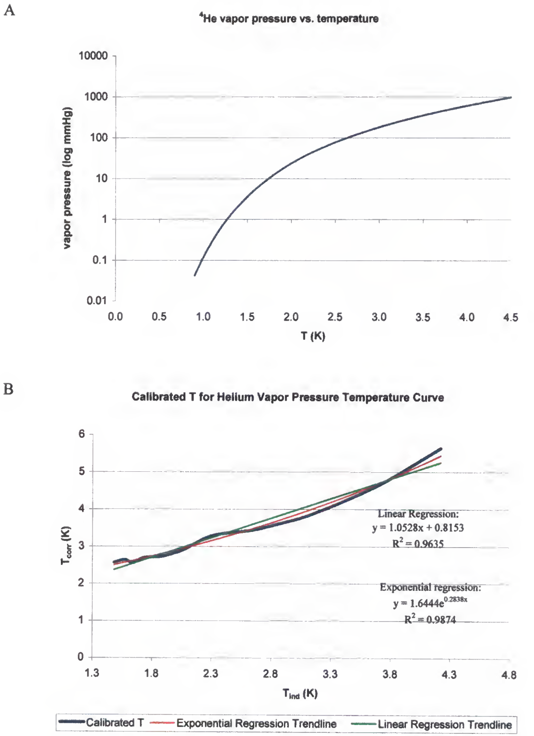

Figure 4-7. Superfluid ^{4}He vapor pressure calibration. A) ^{4}He vapor pressure vs. temperature curve illustrating T-dependence of ^{4}He in superfluid state. B) Graph illustrating calibrated ^{4}He temperature curve as derived from moments measurements of Cu in Ar relative to the temperature derived from the measured ^{4}He vapor pressure according to Figure 4-7 A.

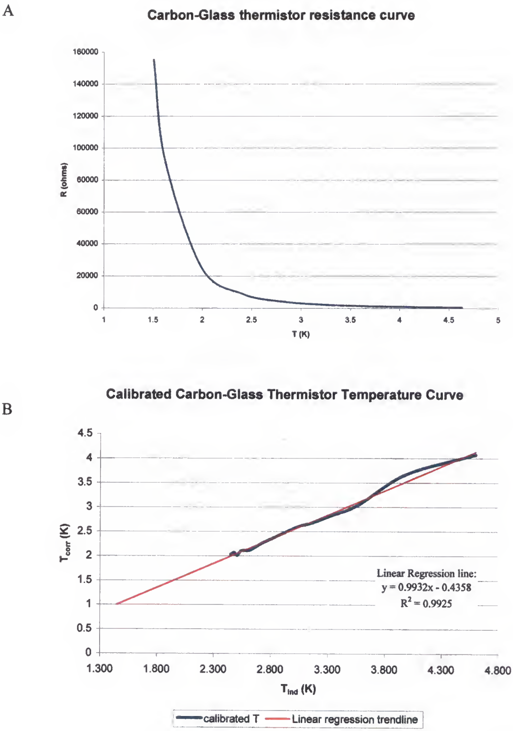

Figure 4-8. Carbon-Glass thermistor calibration. A) Carbon-Glass thermistor (CGR) temperature curve illustrating factory-calibrated T-dependence of window. B) Graph illustrating laboratory-calibrated CGR temperature curve as derived from moments measurements of Cu in Ar relative to the temperature derived from the measured CGR temperature according to Figure 4-8 A.

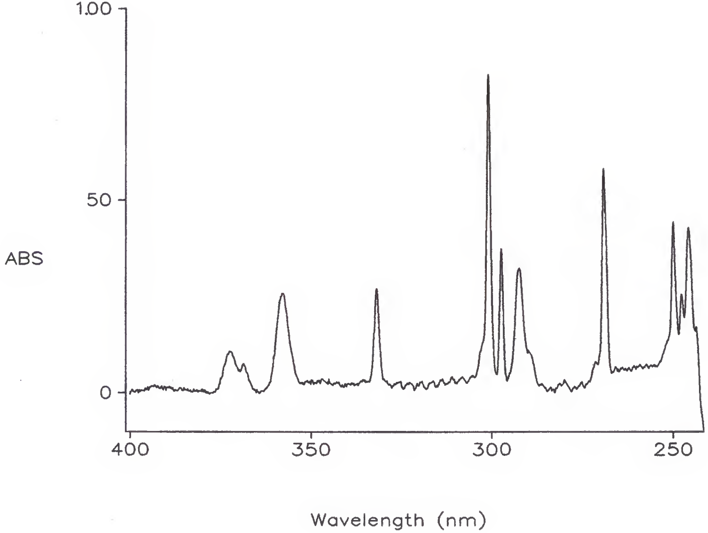

Figure 4-9. Absorption spectrum of Fe(0) atoms isolated in krypton matrix.

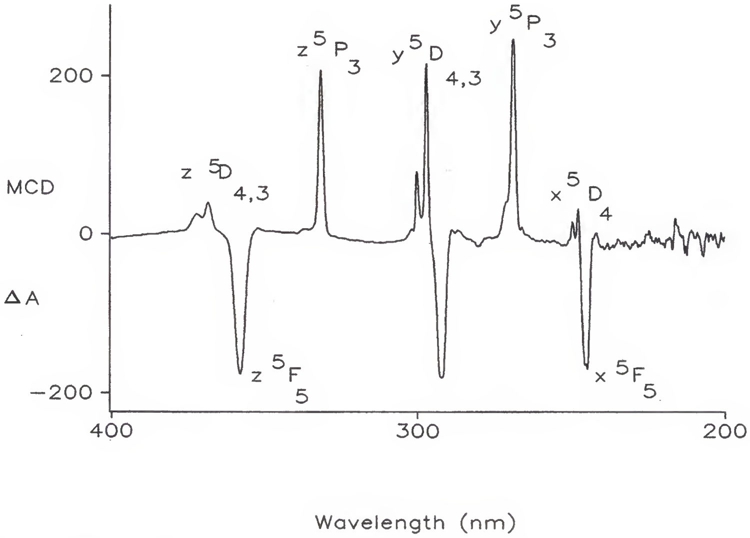

Figure 4-10. Magnetic circular dichroism (MCD) spectrum of Fe(0) atoms isolated in krypton matrix.

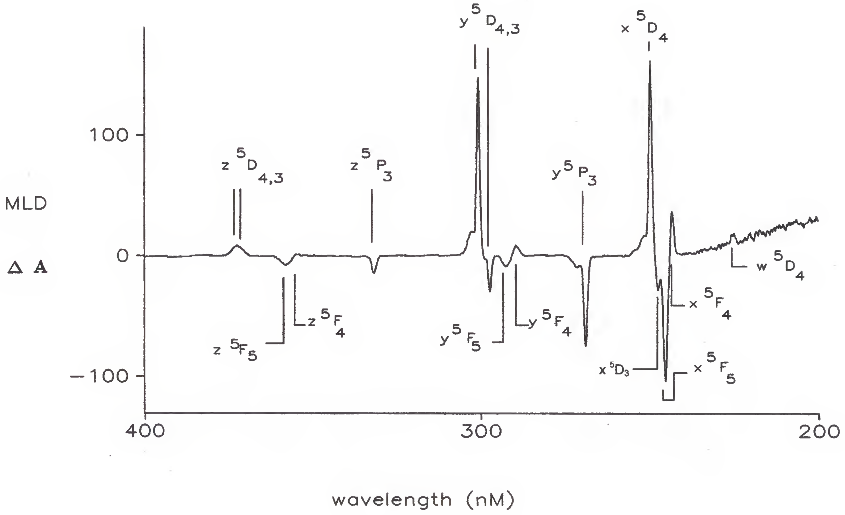

Figure 4-11. Magnetic linear dichroism (MLD) spectrum of Fe(0) atoms isolated in a krypton matrix.

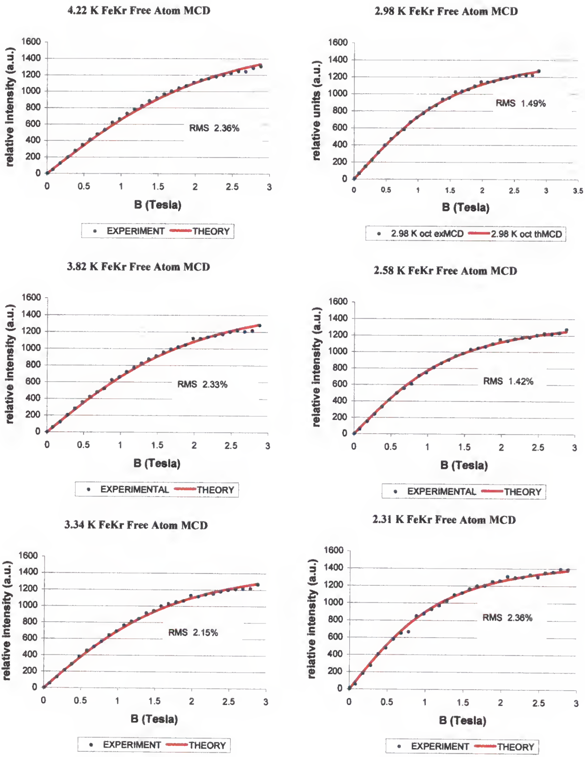

4.22 K FeKr Free Atom MCD

2.98 K FeKr Free Atom MCD

3.82 K FeKr Free Atom MCD

2.58 K FeKr Free Atom MCD

3.34 K FeKr Free Atom MCD

2.31 K FeKr Free Atom MCD

Figure 4-12. Fe(0) atoms in Kr free atom MCD vs **B** experimental and theoretical plots.

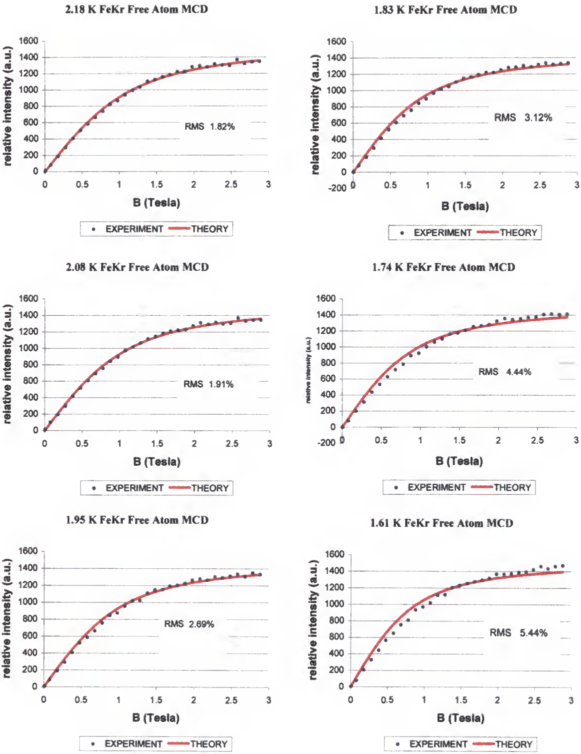

2.18 K FeKr Free Atom MCD

1.83 K FeKr Free Atom MCD

2.08 K FeKr Free Atom MCD

1.74 K FeKr Free Atom MCD

1.95 K FeKr Free Atom MCD

1.61 K FeKr Free Atom MCD

Figure 4-12. (continued)

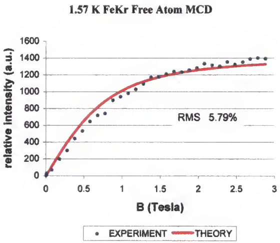
1.57 K FeKr Free Atom MCD

Figure 4-12. (continued)

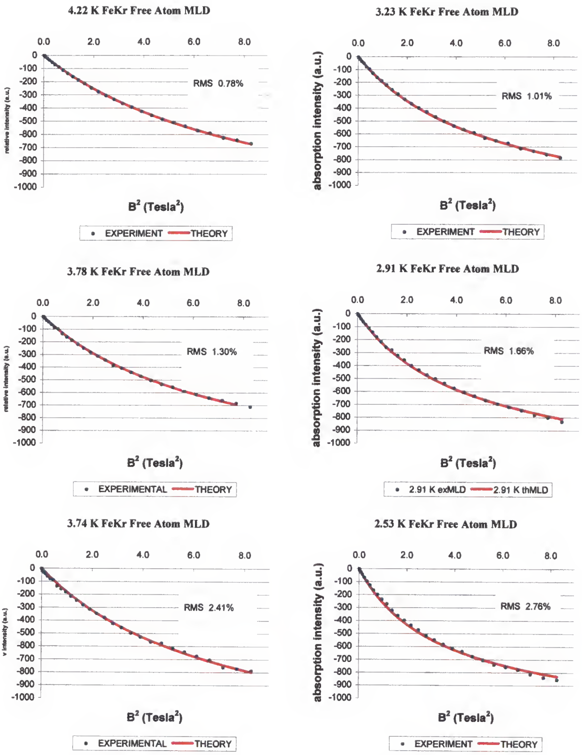

Figure 4-13. Fe(0) atoms in Kr free atom MLD vs B^2 experimental and theoretical plots.

2.29 K FeKr Free Atom MLD

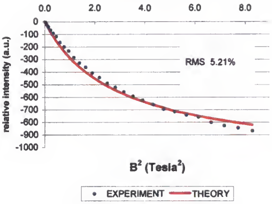

1.79 K FeKr Free Atom MLD

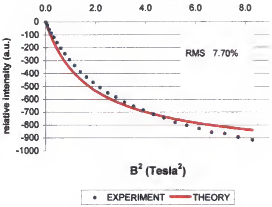

2.11 K FeKr Free Atom MLD

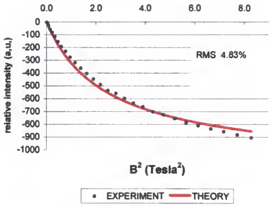

1.74 K FeKr Free Atom MLD

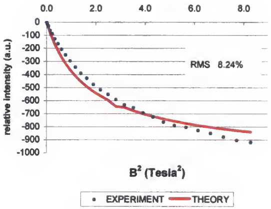

1.91 K FeKr Free Atom MLD

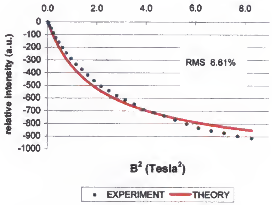

1.68 K FeKr Free Atom MLD

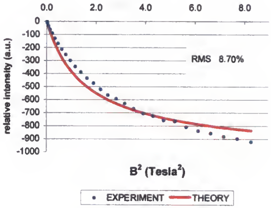

Figure 4-13. (continued)

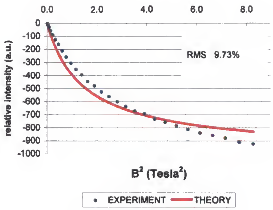
1.61 K FeKr Free Atom MLD

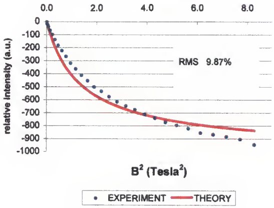
1.55 K FeKr Free Atom MLD

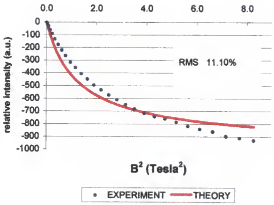
1.48 K FeKr Free Atom MLD

Figure 4-13. (continued)

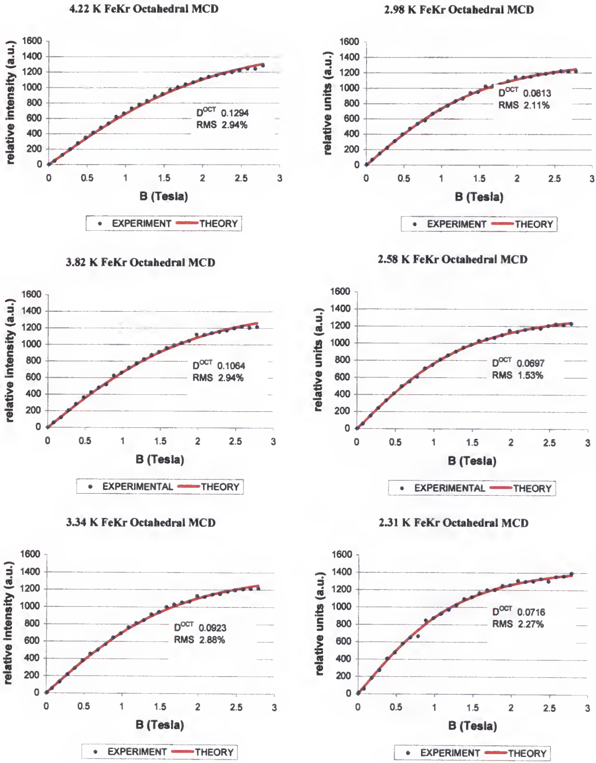

Figure 4-14. Fe(0) atoms in Kr octahedral MCD vs **B** experimental and theoretical plots. One increment for numerical theta angle integration.

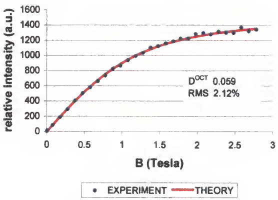
2.18 K FeKr Octahedral MCD

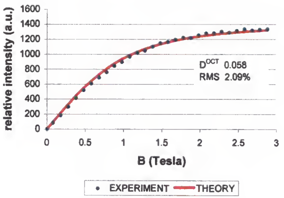
1.83 K FeKr Octahedral MCD

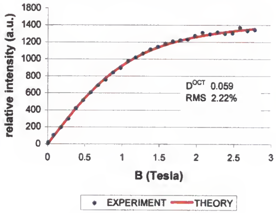
2.08 K FeKr Octahedral MCD

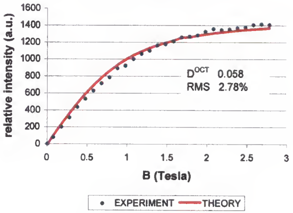
1.74 K FeKr Octahedral MCD

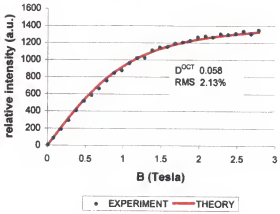
1.95 K FeKr Octahedral MCD

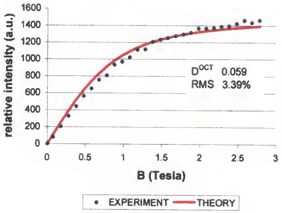
1.61 K FeKr Octahedral MCD

Figure 4-14. (continued)

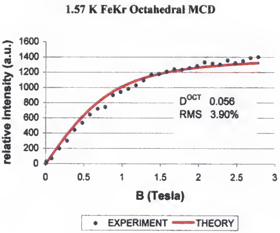

Figure 4-14. (continued)

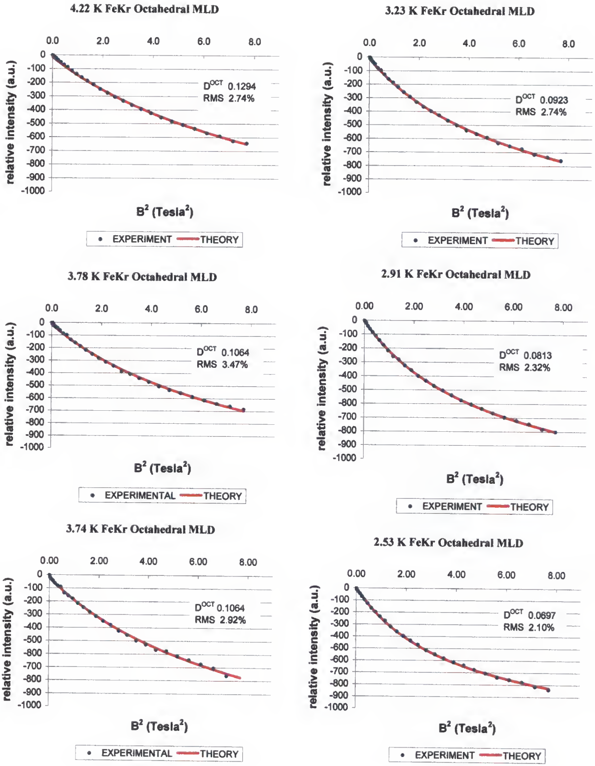

Figure 4-15. Fe(0) atoms in Kr octahedral MLD vs B^2 experimental and theoretical plots.

2.29 K FeKr Octahedral MLD

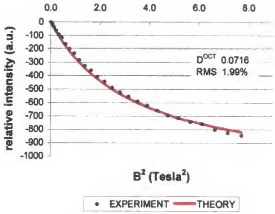

1.79 K FeKr Octahedral MLD

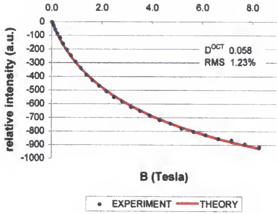

2.11 K FeKr Octahedral MLD

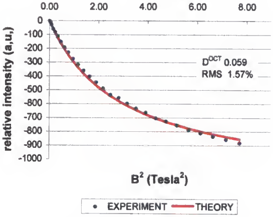

1.74 K FeKr Octahedral MLD

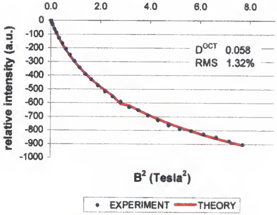

1.91 K FeKr Octahedral MLD

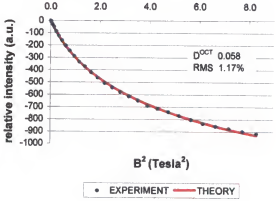

168 K FeKr Octahedral MLD

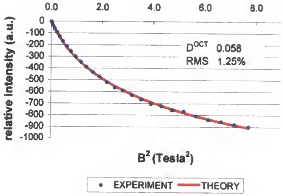

Figure 4-15. (continued)

1.61 K FeKr Octahedral MLD

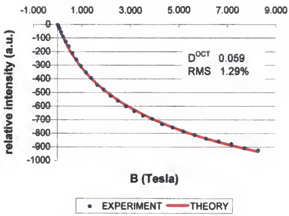

1.55 K FeKr Octahedral MLD

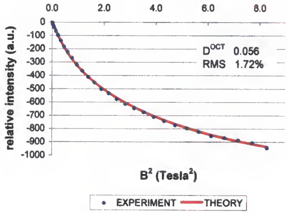

1.48 K FeKr Octahedral MLD

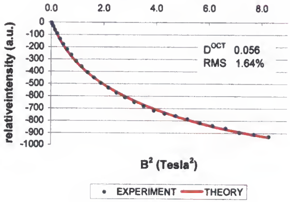

Figure 4-15. (continued)

4.22 K FeKr Tetragonal MCD

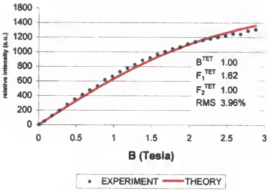

3.82 K FeKr Tetragonal MCD

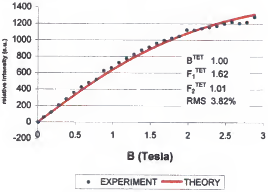

3.34 K FeKr Tetragonal MCD

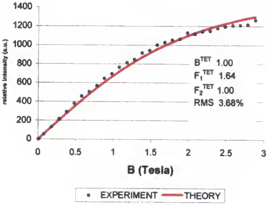

2.98 K FeKr Tetragonal MCD

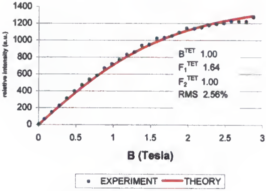

2.58 K FeKr Tetragonal MCD

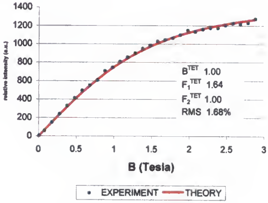

2.31 K FeKr Tetragonal MCD

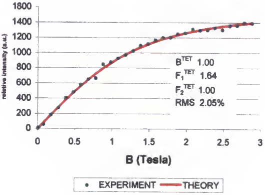

Figure 4-16. Fe(0) atoms in Kr tetragonal MCD vs. **B** experimental and theoretical plots. Initial input parameters to minimization routine: $F_1^{TET} = F_2^{TET} = B^{TET} = 1.0$.

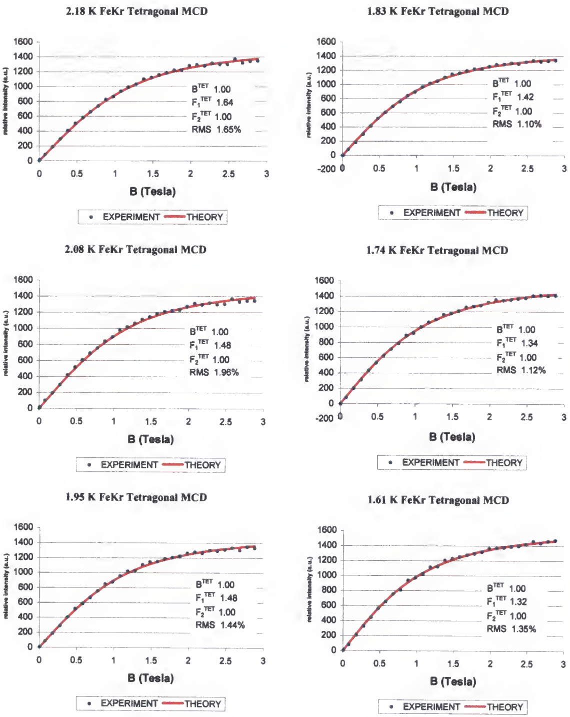

2.18 K FeKr Tetragonal MCD

1.83 K FeKr Tetragonal MCD

2.08 K FeKr Tetragonal MCD

1.74 K FeKr Tetragonal MCD

1.95 K FeKr Tetragonal MCD

1.61 K FeKr Tetragonal MCD

Figure 4-16. (continued)

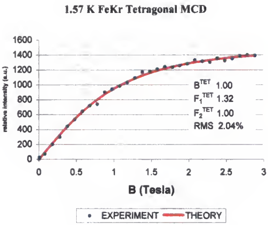

1.57 K FeKr Tetragonal MCD

Figure 4-16. (continued)

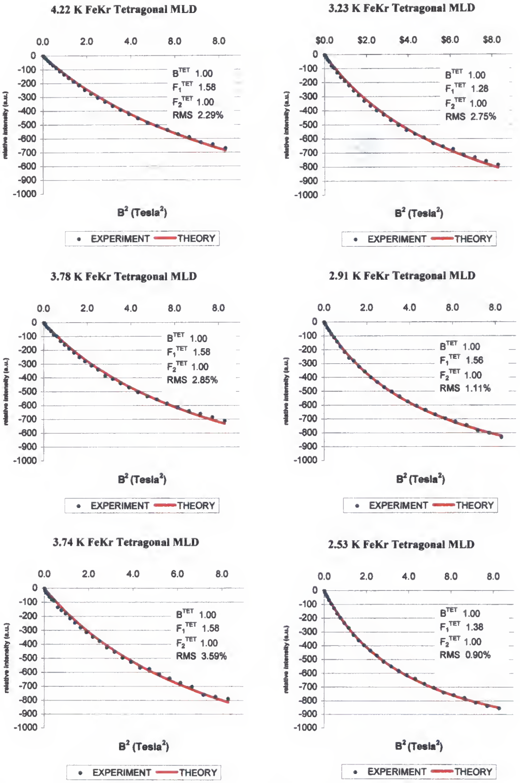
4.22 K FeKr Tetragonal MLD

3.23 K FeKr Tetragonal MLD

3.78 K FeKr Tetragonal MLD

2.91 K FeKr Tetragonal MLD

3.74 K FeKr Tetragonal MLD

2.53 K FeKr Tetragonal MLD

Figure 4-17. Fe(0) atoms in Kr tetragonal MLD vs. $\mathbf{B}^2$ experimental and theoretical plots. Initial input parameters to minimization routine: $F_1^{TET} = F_2^{TET} = B^{TET} = 1.0$.

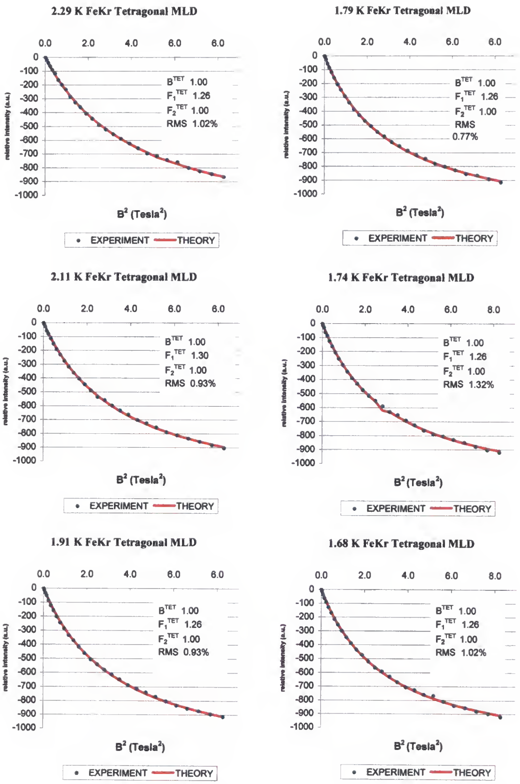

2.29 K FeKr Tetragonal MLD

1.79 K FeKr Tetragonal MLD

2.11 K FeKr Tetragonal MLD

1.74 K FeKr Tetragonal MLD

1.91 K FeKr Tetragonal MLD

1.68 K FeKr Tetragonal MLD

Figure 4-17. (continued)

1.61 K FeKr Tetragonal MLD

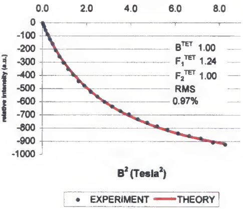

1.55 K FeKr Tetragonal MLD

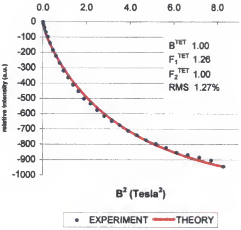

1.48 K FeKr Tetragonal MLD

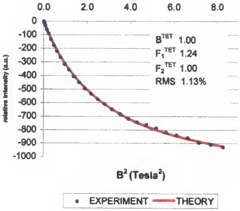

Figure 4-17. (continued)

4.22 K FeKr Trigonal MCD

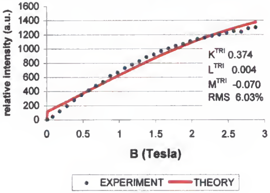

2.98 K FeKr Trigonal MCD

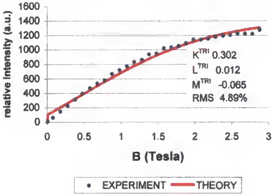

3.82 K FeKr Trigonal MCD

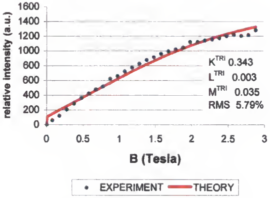

2.58 K FeKr Trigonal MCD

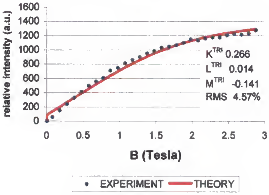

3.34 K FeKr Trigonal MCD

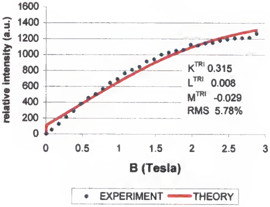

2.31 K FeKr Trigonal MCD

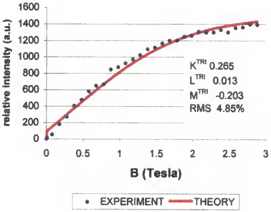

Figure 4-18. Fe(0) atoms in Kr trigonal MCD vs. **B** experimental and theoretical plots. Initial input parameters to minimization routine: $F_1^{TET} = F_2^{TET} = B^{TET} = 1.0$.

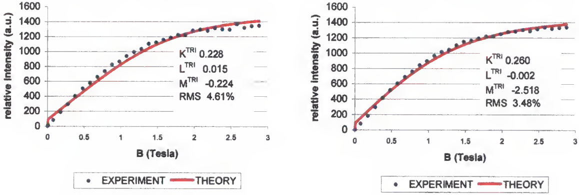

2.18 K FeKr Trigonal MCD

1.83 K FeKr Trigonal MCD

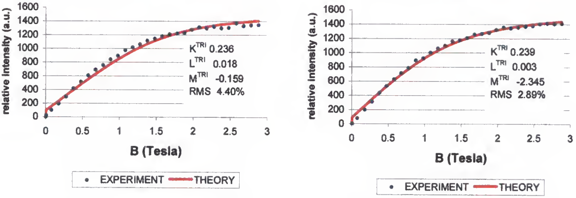

2.08 K FeKr Trigonal MCD

1.74 K FeKr Trigonal MCD

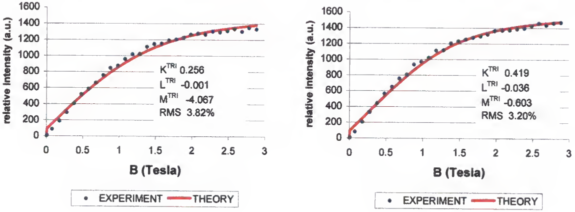

1.95 K FeKr Trigonal MCD

1.61 K FeKr Trigonal MCD

Figure 4-18. (continued)

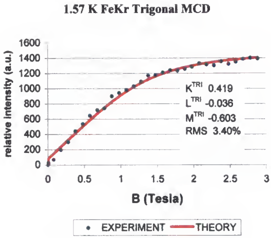

Figure 4-18. (continued)

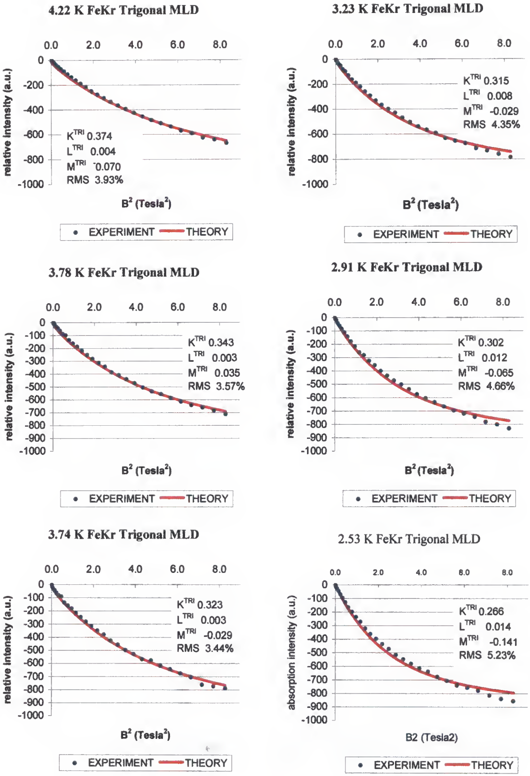
4.22 K FeKr Trigonal MLD

3.23 K FeKr Trigonal MLD

3.78 K FeKr Trigonal MLD

2.91 K FeKr Trigonal MLD

3.74 K FeKr Trigonal MLD

2.53 K FeKr Trigonal MLD

Figure 4-19. Fe(0) atoms in Kr trigonal MLD vs. $\mathbf{B}^2$ experimental and theoretical plots. Initial input parameters to minimization routine: $F_1^{TET} = F_2^{TET} = B^{TET} = 1.0$.

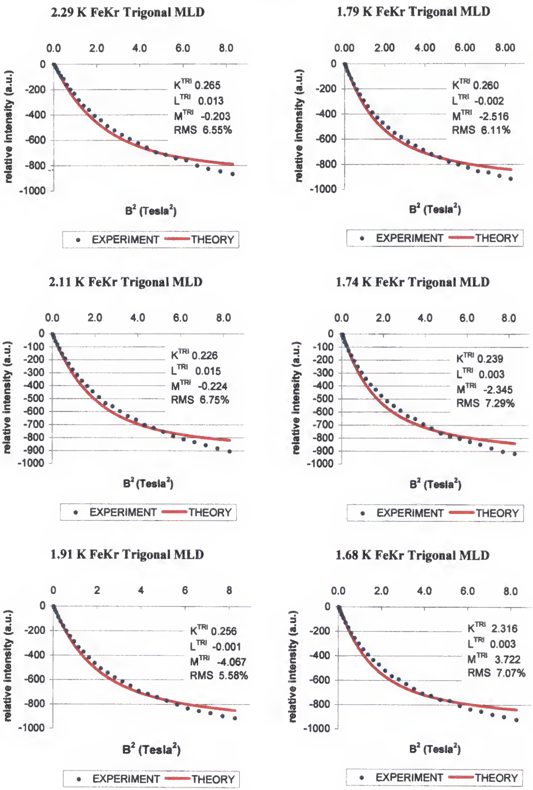

Figure 4-19. (continued)

1.61 K FeKr Trigonal MLD

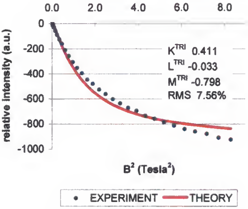

1.55 K FeKr Trigonal MLD

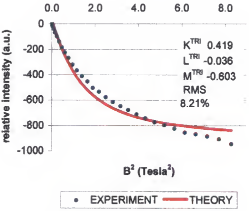

1.48 K FeKr Trigonal MLD

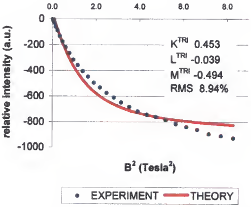

Figure 4-19. (continued)

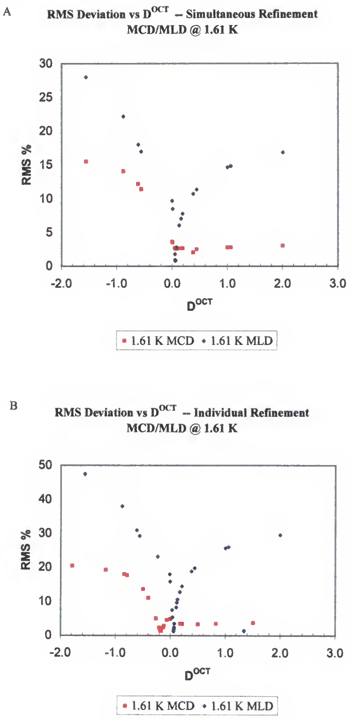

Figure 4-20. RMS vs. D^{OCT} plots for actual MCD and MLD refinements at 1.61 K. A) MCD and MLD refined simultaneously. B) MCD and MLD refined individually.

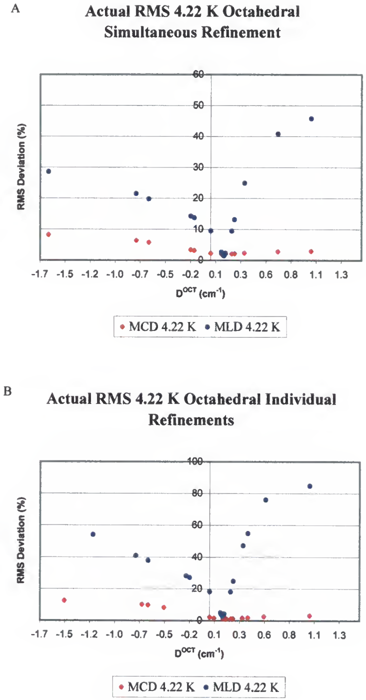

Figure 4-21. RMS vs. D^{OCT} plots for actual MCD and MLD refinements at 4.22 K. A) MCD and MLD refined simultaneously. B) MCD and MLD refined individually.

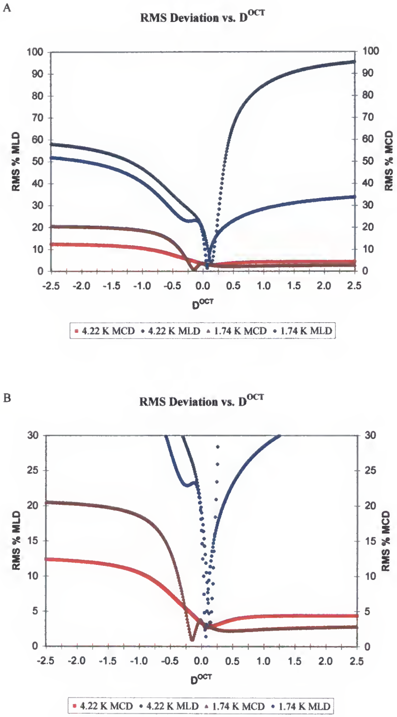

Figure 4-22. The results of a structured incrementing of the D^{OCT} values at 1.74 K and 4.22 K for MCD and MLD. The minimization routine is not utilized. Instead, the D^{OCT} value is set to a specific value, the theoretical MCD and MLD are calculated, then the RMS deviation is determined at that value. D^{OCT} is then incremented to the next step and the process repeated. A) Vertical scale 0-100%; B) expanded vertical scale.

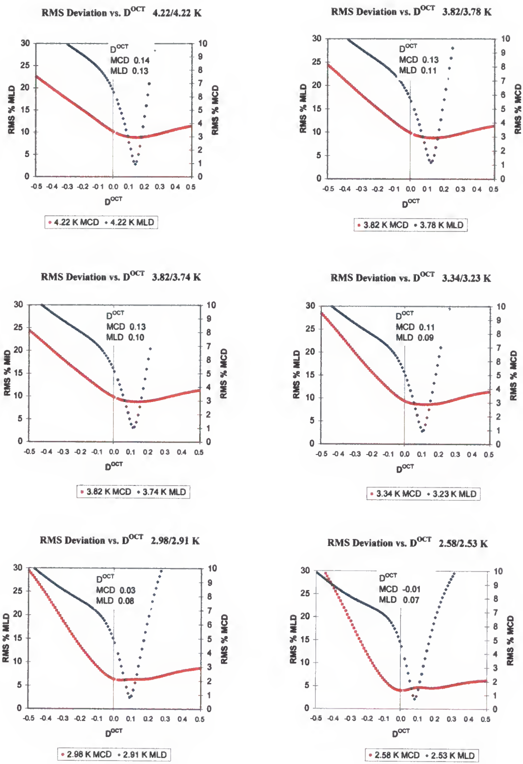

RMS Deviation vs. D^{OCT} 4.22/4.22 K

RMS Deviation vs. D^{OCT} 3.82/3.78 K

RMS Deviation vs. D^{OCT} 3.82/3.74 K

RMS Deviation vs. D^{OCT} 3.34/3.23 K

RMS Deviation vs. D^{OCT} 2.98/2.91 K

RMS Deviation vs. D^{OCT} 2.58/2.53 K

Figure 4-23. Results of structured incrementing of D^{OCT} performed on all the data sets between 4.22 K and 1.48 K for octahedral geometry. Numerical theta integration is over one step only.

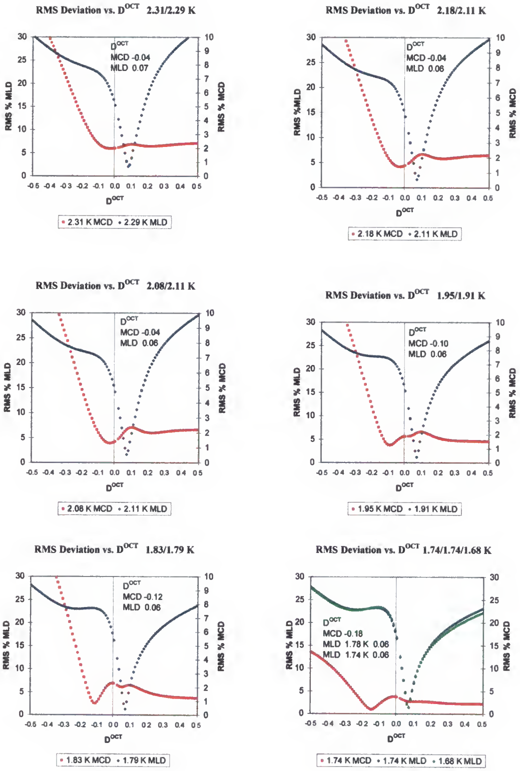
RMS Deviation vs. D^{OCT} 2.31/2.29 K

RMS Deviation vs. D^{OCT} 2.18/2.11 K

RMS Deviation vs. D^{OCT} 2.08/2.11 K

RMS Deviation vs. D^{OCT} 1.95/1.91 K

RMS Deviation vs. D^{OCT} 1.83/1.79 K

RMS Deviation vs. D^{OCT} 1.74/1.74/1.68 K

Figure 4-23. (continued)

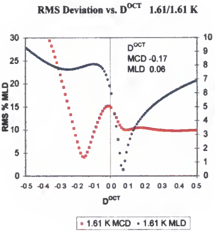

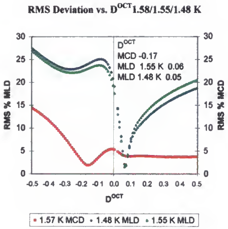

Figure 4-23. (continued)

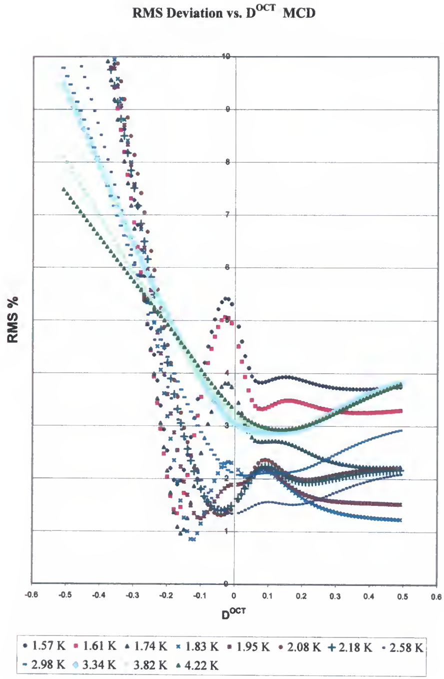

Figure 4-24. Superimposed graphs for the MCD plots of Figure 4.23 for easier comparison.

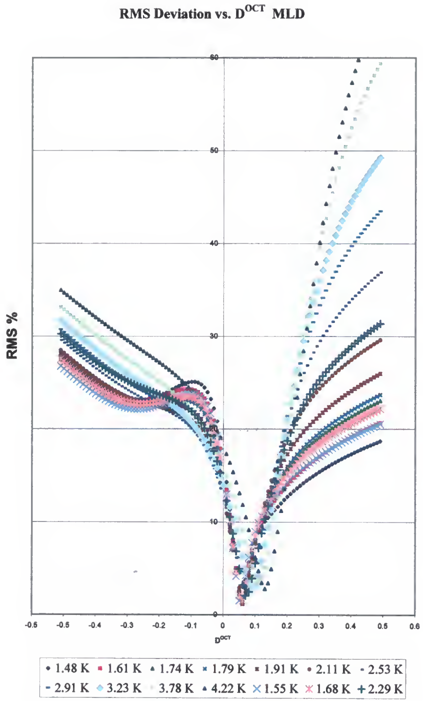

Figure 4-25. Superimposed graphs for the MLD plots of Figure 4.23 for easier comparison.

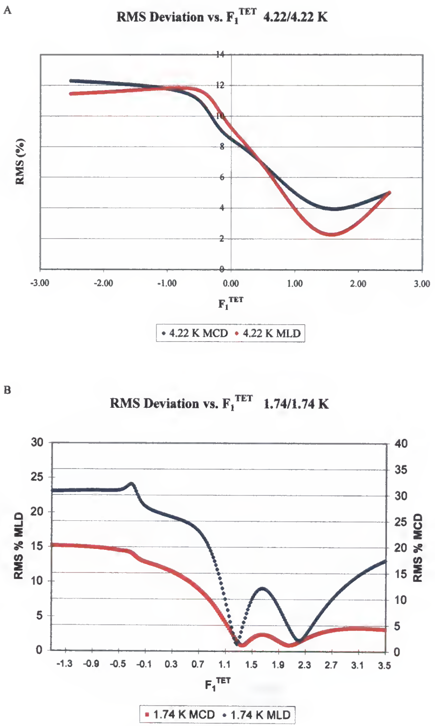

Figure 4-26. The results of incrementing along one dimension (F_1^{TET}) of the tetragonal solution for the 4.22 K and 1.74 K MCD and MLD data sets. The other two dimensions (F_2^{TET} and B^{TET}) were maintained at the constant value of 1.000 cm^{-1}. The F_1^{TET} increment spacing was 0.02 cm^{-1} and each cycle was calculated over 250 theta increments between 0 and $\pi/2$.

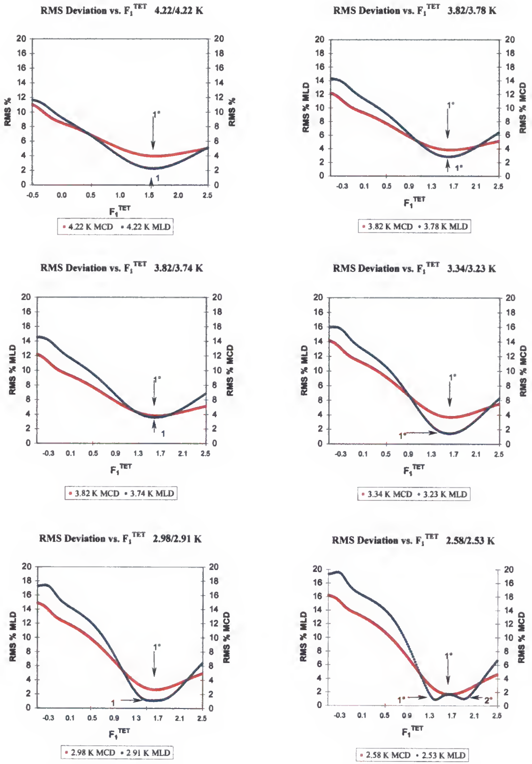

Figure 4-27. Plots of structured incrementing over all data sets for tetragonal symmetry. The minimization routine was bypassed and F_1^{TET} parameter was incremented from –0.5 to +2.5 in increments of 0.02 cm^{-1} while holding the F_2^{TET} and B^{TET} crystal field parameters constant at 1.00.

RMS Deviation vs. F_1^{TET} 2.31/2.29 K

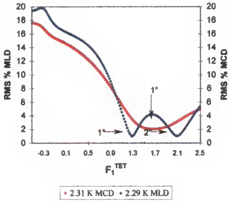

RMS Deviation vs. F_1^{TET} 2.18/2.11 K

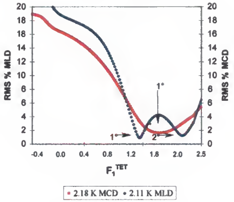

RMS Deviation vs. F_1^{TET} 2.08/2.11 K

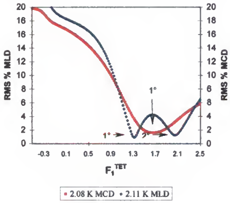

RMS Deviation vs. F_1^{TET} 1.95/1.91 K

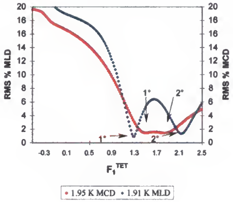

RMS Deviation vs. F_1^{TET} 1.83/1.79 K

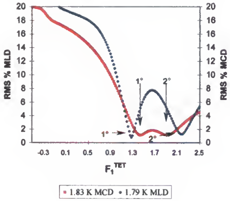

RMS Deviation vs. F_1^{TET} 1.74/1.74 K

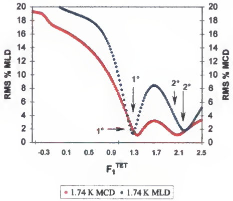

Figure 4-27. (continued)

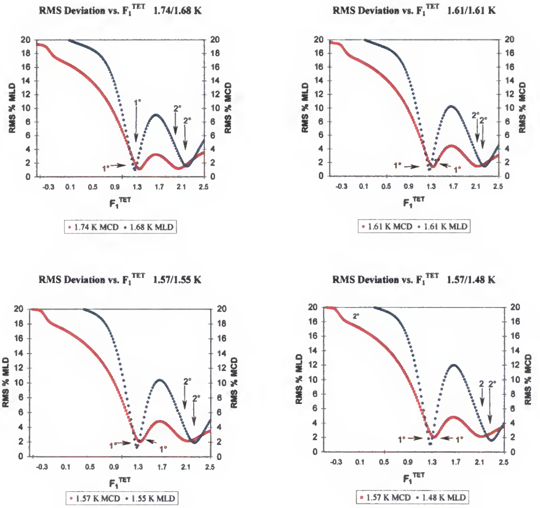

Figure 4-27. (continued)

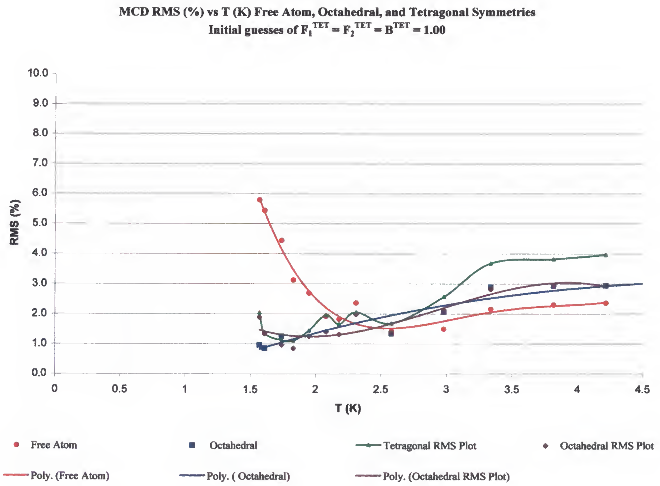

Figure 4-28. Simultaneous plots of MCD refinement data for all geometries based on numerically integrating theta over $\pi/2$ in one step for octahedral symmetry and initial starting parameters of $F_1^{TET} = F_2^{TET} = B^{TET} = 1.00$ for tetragonal and trigonal symmetry. Numerical integration was over 250 steps for tetragonal and trigonal geometries.

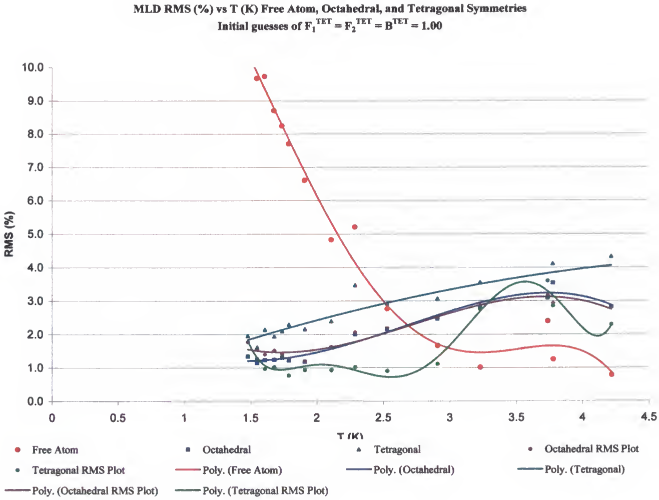

Figure 4-29. Simultaneous plots of MLD refinement data for all geometries based on numerically integrating theta over π/2 in one step for octahedral symmetry and initial starting parameters of $F_1^{TET} = F_2^{TET} = B^{TET} = 1.00$ for tetragonal and trigonal symmetry. Numerical integration was over 250 steps for tetragonal and trigonal geometries.

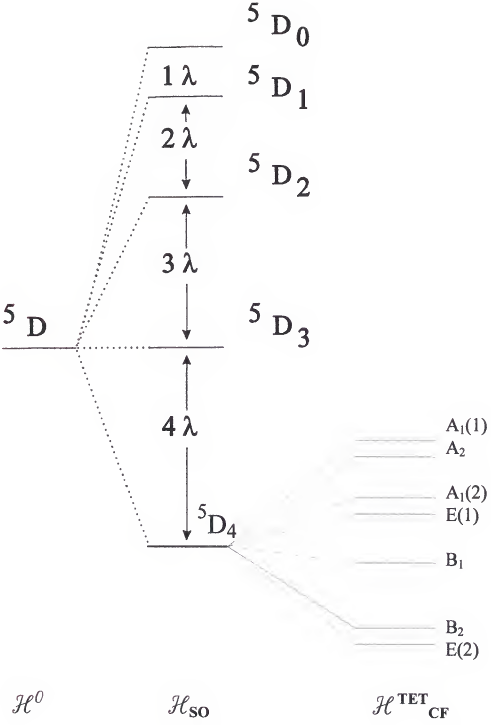

Figure 4-30. Splitting of Fe(0) by spin-orbit (SO) and tetragonal crystal field (CF) perturbations. $\lambda = 104\ cm^{-1}$. The crystal field splitting is exaggerated.

4.22 K FeKr Tetragonal MCD

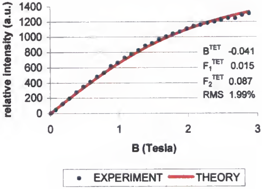

2.98 K FeKr Tetragonal MCD

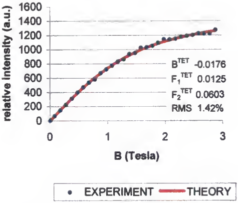

3.82 K FeKr Tetragonal MCD

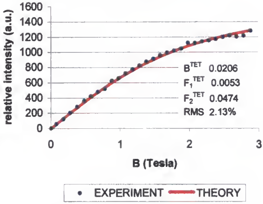

2.58 K FeKr Tetragonal MCD

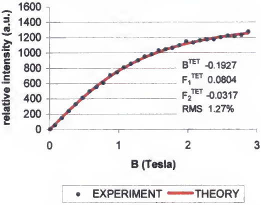

3.34 K FeKr Tetragonal MCD

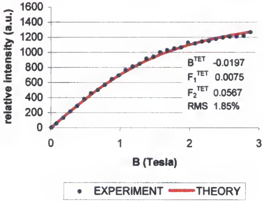

2.31 K FeKr Tetragonal MCD

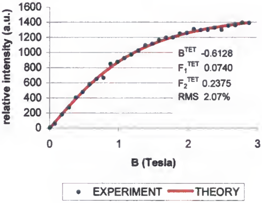

Figure 4-31. Fe(0) atoms in Kr tetragonal MCD vs. B experimental and theoretical plots. Initial input parameters to minimization routine: $F_1^{TET} = F_2^{TET} = B^{TET} = 0.05$.

2.18 K FeKr Tetragonal MCD

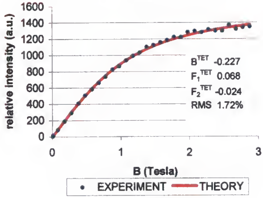

1.83 K FeKr Tetragonal MCD

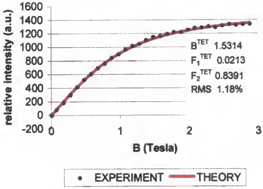

2.08 K FeKr Tetragonal MCD

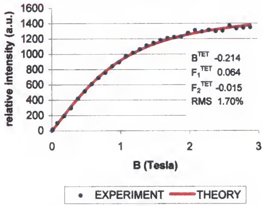

1.74 K FeKr Tetragonal MCD

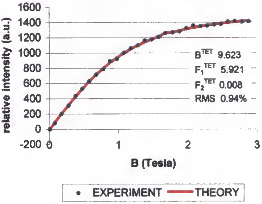

1.95 K FeKr Tetragonal MCD

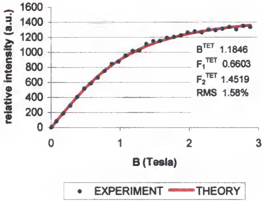

1.61 K FeKr Tetragonal MCD

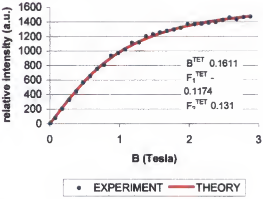

Figure 4-31. (continued)

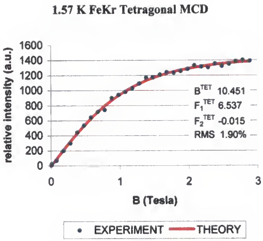

Figure 4-31. (continued)

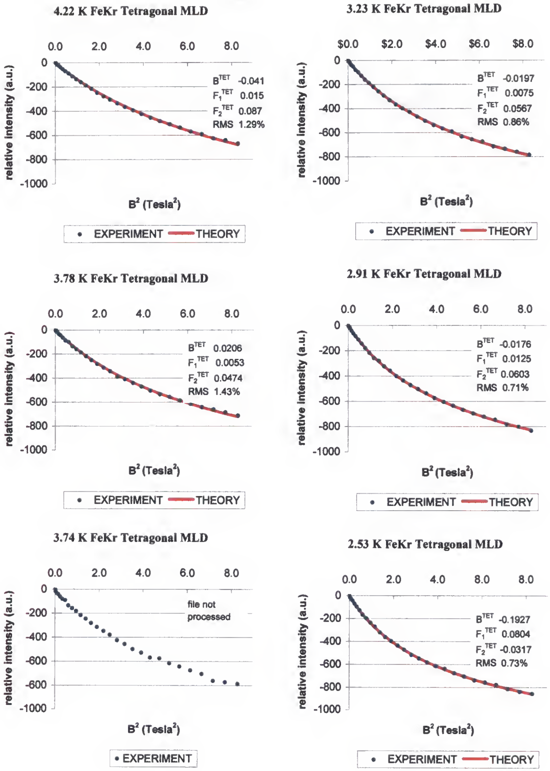

Figure 4-32. Fe(0) atoms in Kr tetragonal MLD vs. B2 experimental and theoretical plots. Initial input parameters to minimization routine: $F_1^{TET} = F_2^{TET} = B^{TET} = 0.05$.

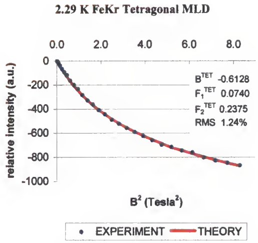

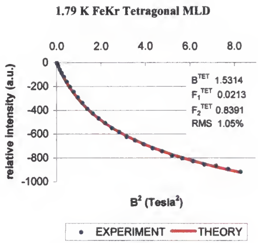

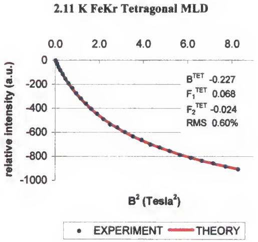

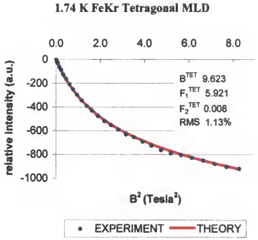

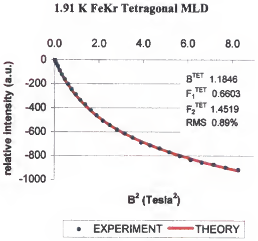

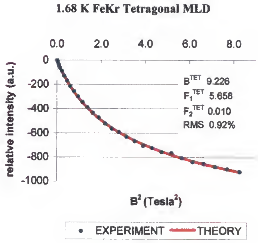

Figure 4-32. (continued)

1.61 K FeKr Tetragonal MLD

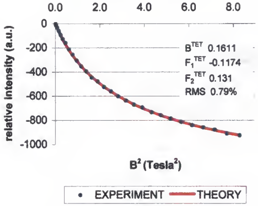

1.55 K FeKr Tetragonal MLD

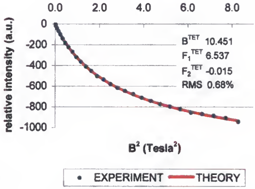

1.48 K FeKr Tetragonal MLD

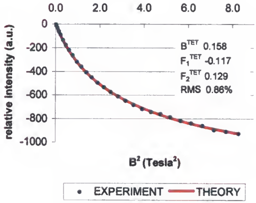

Figure 4-32. (continued)

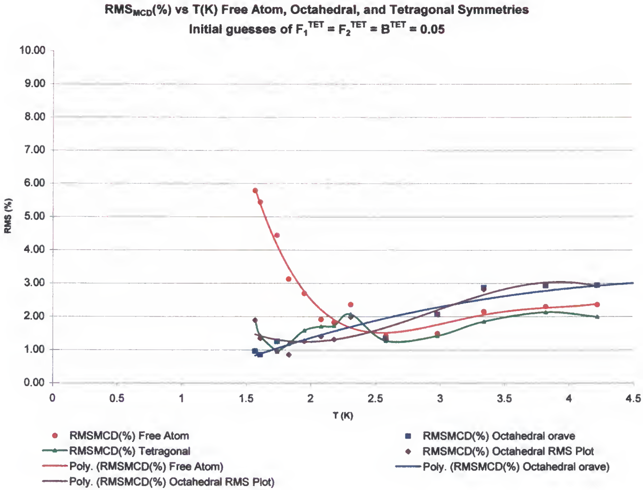

Figure 4-33. Simultaneous plots of MCD refinement data for all geometries based on numerically integrating theta over π/2 in one step for octahedral symmetry and initial starting parameters of $F_1^{TET} = F_2^{TET} = B^{TET} = 0.05$ for tetragonal and trigonal symmetry. Numerical integration was over 250 steps for tetragonal and trigonal geometries.

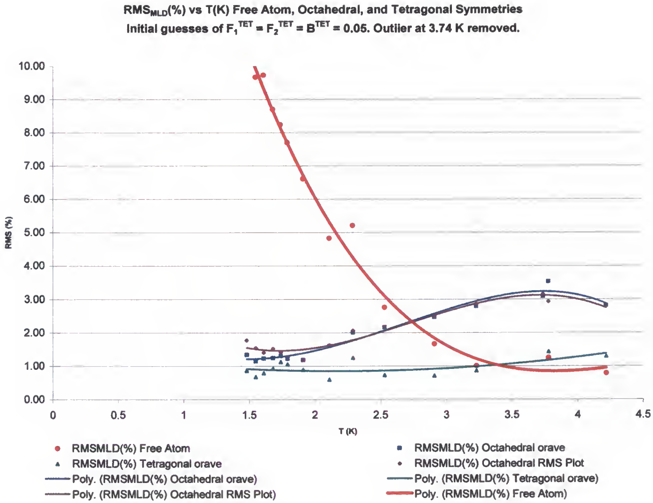

Figure 4-34. Simultaneous plots of MLD refinement data for all geometries based on numerically integrating theta over $\pi/2$ in one step for octahedral symmetry and initial starting parameters of $F_1^{TET} = F_2^{TET} = B^{TET} = 0.05$ for tetragonal and trigonal symmetry. Numerical integration was over 250 steps for tetragonal and trigonal geometries.

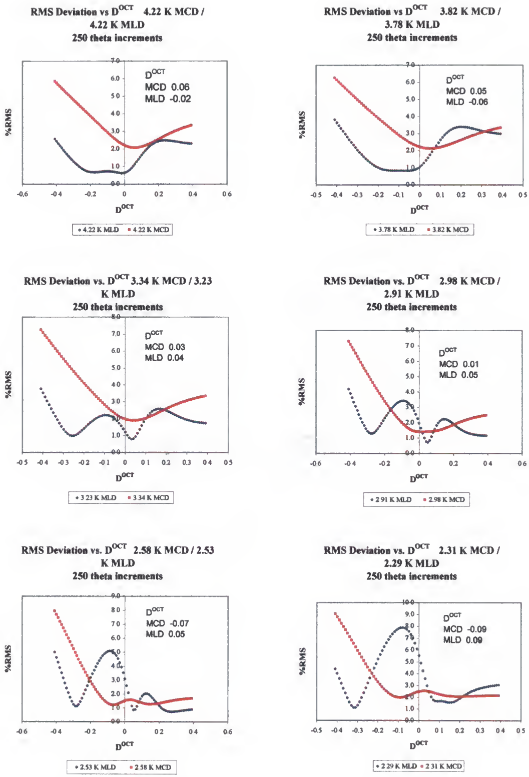

Figure 4-35. Plots of structured incrementing of the MCD and MLD data under octahedral symmetry processing 250 steps of numerical integration from 0 to π/2. The range is for D^{OCT} from -0.5 to +0.5 in 0.01 increments.

RMS Deviation vs. D^{OCT} 2.18 K MCD /
2.11 K MLD
250 theta increments

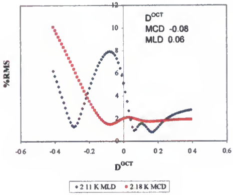

RMS Deviation vs. D^{OCT} 2.08 K MCD /
2.11 K MLD
250 theta increments

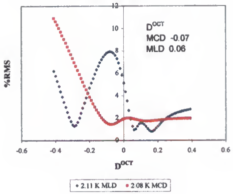

RMS Deviation vs. D^{OCT} 1.95 K MCD /
1.91 K MLD
250 theta increments

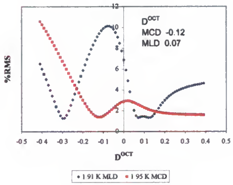

RMS Deviation vs. D^{OCT} 1.83 K MCD /
1.79 K MLD
250 theta increments

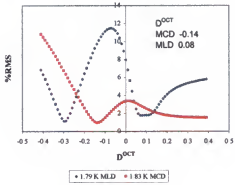

RMS Deviation vs. D^{OCT} 1.74 K MCD /
1.74 K MLD
250 theta increments

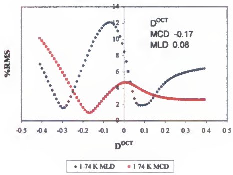

RMS Deviation vs. D^{OCT} 1.74 K MCD /
1.68 K MLD
250 theta increments

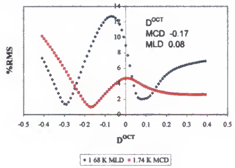

Figure 4-35. (continued)

RMS Deviation vs. D^{OCT} 1.61 K MCD / 1.61 K MLD
250 theta increments

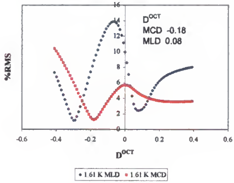

RMS Deviation vs. D^{OCT} 1.57 K MCD / 1.55 K MLD
250 theta increments

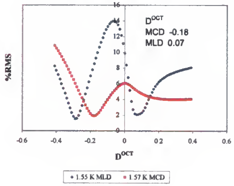

RMS Deviation vs. D^{OCT} 1.57 K MCD / 1.48 K MLD
250 theta increments

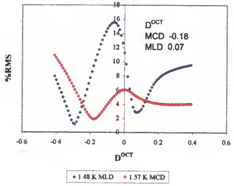

Figure 4-35. (continued)

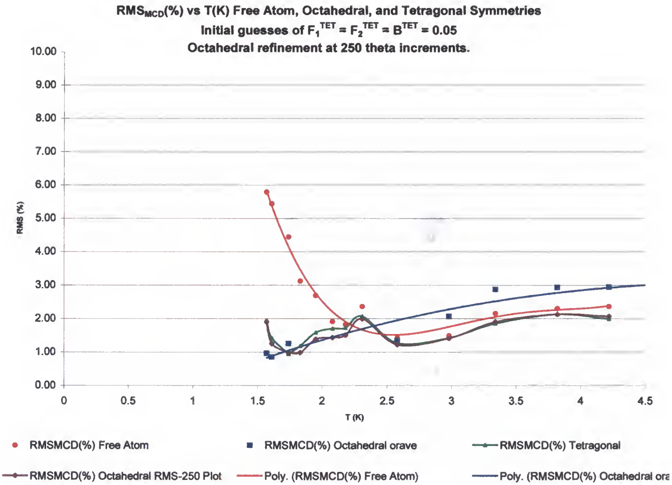

Figure 4-36. Simultaneous plots of MLD refinement data for principal geometries based on numerically integrating theta over π/2 in 250 steps for octahedral symmetry and initial starting parameters of $F_1^{TET} = F_2^{TET} = B^{TET} = 0.05$ for tetragonal symmetry. Numerical integration was over 250 steps for tetragonal geometry.

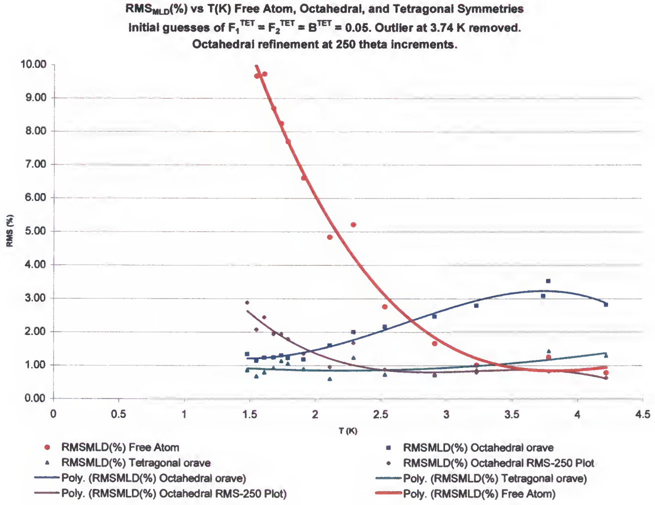

Figure 4-37. Simultaneous plots of MLD refinement data for principal geometries based on numerically integrating theta over π/2 in 250 steps for octahedral symmetry and initial starting parameters of $F_1^{TET} = F_2^{TET} = B^{TET} = 0.05$ for tetragonal symmetry. Numerical integration was over 250 steps for tetragonal geometry.

CHAPTER 5
THE MCD AND MLD OF Ni(0) ATOMS IN ARGON AND KRYPTON MATRICES

Introduction

A great deal of absorption data has been acquired on matrix-isolated metal atoms using the heavy rare gases (neon, argon, krypton, and xenon), along with other solid low temperature matrix substrates (N_2, SF_6, CH_4, etc.[2,18]). All of the atomic metal species studied to date have correlated very well with the gas-phase atomic line spectra of Moore.[11] Typically, red or blue shifts in the transition frequencies occur relative to the gas phase due to matrix effects, but the structure and frequency separations remain largely intact. The absorption spectrum of the Fe(0) atoms from the $^5D_4$ ground state discussed in Chapter 4 is an excellent example. Figure 5-1 illustrates the absorption spectrum of Fe(0) atoms matrix-isolated in krypton at 4.2 K along with the gas-phase ultraviolet/visible (UV/Vis) spectrum from 400 – 200 nm synthesized from Moore's data.[11] The correlation between the transitions is obvious. The matrix-isolated Fe(0) atomic transitions all exhibit a red shift in Kr relative to the gas phase due to matrix effects.

The absorption spectrum of Ni(0) atoms in rare gas matrices has been known for some time. It is expected that Ni(0) atoms isolated in rare-gas matrices should behave similarly as the other metals. Figure 5-2 shows the absorption spectrum of Ni(0) atoms matrix-isolated in argon and krypton contrasted with the Ni(0) atomic gas phase UV/Visible absorption spectrum from the $^3F_4$ ground state, again synthesized from Moore's data.[11] The difference in the two spectra is conspicuous. It is possible the three intense transitions in the gas-phase spectrum residing in the UV region around 230 nm exist in the broadened band structure near 230 nm in the matrix-isolated spectrum. Given the number and nature of the structure of all the bands present in the matrix-isolated spectrum, to draw such a conclusion is purely speculative. Assignment of the electronic transitions using the shifted gas phase spectral transitions cannot be made in a straightforward manner as had been done with many previous metal-rare-gas matrices. Several other absorption bands appear which cannot be accounted for by a gas phase ground state of $^3F_4$.

Jacobi, Schmeisser, and Kolb[73] proposed an inversion of a low-lying $^3D_3$ electronic state residing 205 cm^{-1} above the gas phase $^3F_4$ ground state. Condensation into a solid matrix could reasonably result in interaction between the unshielded 4s electrons of the $^3F_4$ $3d^84s^2$ configuration and the lattice atoms, providing higher stability for a $^3D_3$ $3d^94s^1$ configuration. Figure 5-3 compares the matrix-isolated UV/Visible absorption spectrum from this study with the synthesized gas-phase line spectrum from Moore's data[11] for a $^3D_3$ ground state configuration. The correlation between the two spectra is readily apparent.

Measurement of the magnetic circular dichroism (MCD) spectrum of Ni(0) atoms in Ar, Kr, and Xe matrices by Grinter and Stern[38] and Breithaupt et al[74] provided support for the inversion-of-states hypothesis. Further research by Barrett, Graham, and Grinter[75] along with laser-induced emission studies by Celluci and Nixon[76] demonstrated the simultaneous existence of both $^3D_3$ and $^3F_4$ states in the same matrix. The four spectra of Figure 5-4 illustrate various mixtures of Ni(0) atoms in the $^3D_3$ and $^3F_4$ gas-phase ground states. The mixture containing 99% $^3D_3$ and 1% $^3F_4$ (Figure 5-4 B) compares well with the Ni/Ar spectrum of Figure 5-3 A, while the 80% $^3D_3$ / 20% $^3F_4$ mixture of Figure 5-4 C is more representative of the Ni/Kr mixture of Figure 5-3 B.

The assignments of electronic transitions specific to particular environments remained vague due to the inability to resolve overlapping bands. A magnetic linear dichroism (MLD) study has been made of Ni(0) atoms in Ar matrix to take advantage of the complementarity of MCD and MLD spectral transitions which have specific signs of differential absorption (Table 4-1). The MLD spectra coupled with ABS/MCD spectra of Ni(0) atoms in argon and krypton confirm the presence of both ground states and permit absolute assignment of the transitions attributable to $^3D_3$ and those attributable to $^3F_4$. The results and conclusion of the MLD study of the Ni(0) electronic states are reported in the section below on the electronic state assignments of Ni(0) atoms in argon.

It is of interest to establish the physical nature of the separate ground state sites. To address this concern, a magnetic saturation study of Ni(0) atoms isolated in Kr matrix, similar to that done on Fe(0) in Chapter 4, was conducted on representative transitions from both isolable ground state configurations, the normal $^3F_4$ gas-phase ground state and the matrix-stabilized $^3D_3$ ground state. The temperature and magnetic field saturation dependence of the $z^3P_2 \leftarrow {}^3D_3$ transition at 338.7 nm and the $y^3G_5 \leftarrow {}^3F_4$ transition at 235.2 nm were recorded. Mathematical simulations of the data were calculated via computer modeling of the Ni(0) atomic environment for both ground state configurations via the methods presented in Chapter 3, again focusing on the free atom, octahedral, tetragonal, and trigonal symmetry models. The results and conclusions formulated about the existing site symmetry are reported in a following section which addresses the MCD and MLD saturation spectroscopy of Ni(0) atoms in krypton.

Electronic State Assignments of Ni(0) in Argon

Experimental

The experimental approach was similar to that for Fe(0) in Kr in Chapter 4. High purity powdered Ni metal (Spex, 99.98 % purity) was resistively heated in an Al_2O_3 Knudsen cell (Figure 4-6) to ~1640 °C for 3 hours. The Al_2O_3 cylinder encasing the Ni powder was itself supported inside a tantalum (Ta) cell which provided the conductive path for the Knudsen cell vaporization. Al_2O_3 was utilized due to the reactive nature of nickel metal at high temperatures which has a strong tendency to spontaneously alloy with other metals. This proved to be the primary decay mode of the supporting Ta cell, sometimes after even only a few hours of operation. The effusing atomic Ni beam was mixed axially with Ar gas (Matheson, 99.9995 % purity) and co-condensed on a 0.75 inch diameter calcium fluoride (CaF_2) window at 4.2 K. The Oxford superconducting split coil magnet / cryostat (Figures 4-3 and 4-4) was utilized for these experiments. The deposition window was CaF_2, not sapphire as in the experiments of Chapter 4.

The matrix was annealed at ~25 K for one hour. Temperature monitoring of the matrix temperature was via a carbon-glass thermistor adjacent to the CaF_2 window. The Ni/Ar matrix was analyzed via absorption (ABS), MCD, and MLD spectroscopy (Figures 1-1, 1-2, and 1-6) to ascertain the presence of dual ground states and clarify the electronic state assignments due to each transition. Absorption and MCD scans were acquired from 400-200 nm. Due to acquisition difficulties in the UV region below 250 nm, the MLD was only acquired reliably from 400-250 nm. Signal averaging of each data point was performed over 16 acquisition cycles. The magnetic field strength was 0.29 and 1.58 T for the MCD, and 3.0 T for the MLD scans.

Results

The ABS and MCD spectra of Ni(0) atoms isolated in Ar matrix are illustrated in Figure 5-5. The MLD spectrum is presented in Figure 5-6 along with an MCD spectrum acquired after additional annealing of the matrix to show the complementary nature of the MCD/MLD technique. The magnetic field strength was increased to 1.58 T to compensate for the deterioration of the matrix by the additional annealing. Table 5-1 lists the observed and predicted transition positions and signs of the MCD and MLD spectra along with the gas phase transitions for Ni atoms in a $^3D_3$ ground state.[11] All bands demonstrate $\mathcal{C}$-term (MCD) or $\mathcal{G}$-term (MLD) temperature dependence. The signs of the transitions are determined according to the allowed transitions, ΔJ = 0,±1, and the theoretical signs of MCD and MLD associated with ΔJ (Table 4-1). The *gf* values from gas phase absorptions[77] (Table 5-1) are multiplied by the theoretical values of the $\mathcal{C}_0/\mathcal{D}_0$ MCD parameters and $\mathcal{G}_0/\mathcal{D}_0$ MLD parameters via the AMCOR method[8,77-79] to give simulated ABS, MCD, and MLD spectra for a $^3D_3$ ground state (Figure 5-7). Gaussian bandshapes and bandwidths of 4.0 nm were employed to simulate normal line broadening under actual experimental conditions. The simulated spectra without simulated broadening would be represented by a stick diagram. There are obvious differences in the sign and intensity of most of the major transitions. For example, the z^3P_2 transition near 353 nm (gas phase) is strongly positive in the MCD, yet opposite in sign in the MLD while retaining similar intensity. The strong y $^3D_3$ MLD transition at 300 nm (gas phase) is predicted to be positive in both the MCD and MLD, yet its oscillator strengths from Table 5-1 (0.87 vs. 1.96) show its predicted intensity in the MCD to be approximately

Table 5-1. Gas phase absorption positions, observed argon matrix MCD and MLD positions and signs, and predicted relative intensities for MCD and MLD bands for Ni atoms with a $^3D_3$ ground state.

	Gas Phase Absorption			Observed in Argon matrix				Theory	
Assignment	λ (nm)	$\bar{\nu}^a$ (cm^{-1})	gf^b	λ^c (nm)	$\bar{\nu}$ (cm^{-1})	MCD sign	MLD sign	$(C_0/D_0)gf^d$	$(G_0/D_0)gf^e$
z^5D_2	367.4	27210	0.0027	--	--			- 0.011	- 0.0049
z^5G_4	358.8	27863	0.004	--	--			- -0.12	- 0.0030
z^3P_2	352.5	28364	0.93	332.8^{MCD}	30039	pos	neg	3.72	- 1.67
z^5F_4	346.2	28879	0.44	$\sim 325(s)^{MCD,MLD}$	30760	neg	neg	- 1.32	- 0.33
z^3F_3	343.4	29116	0.21	--	--			0.21	0.47
z^3F_4	341.5	29276	0.94	$320.0^{MCD,MLD}$	31241	neg	neg	- 2.82	- 0.071
z^3D_3	339.3	29464	0.29	315.5^{MLD}	31687	--	pos	0.29	0.65
z^5F_3	337.4	29628	0.017	--	--			0.017	0.048
z^3D_2	336.8	29683	0.0022	--	--			0.0098	- 0.0040
z^3F_2	328.7	30414	0.0032	--	--			0.0138	- 0.0058
z^3G_4	324.9	30775	0.0168	--	--			- 0.0204	- 0.0051
z^1F_3	324.3	30826	0.054	--	--			0.054	0.0029
z^1D_2	320.0	31237	0.0025	310^{MCD}	32249	pos	neg	0.01	- 0.0045
y^3F_4	305.1	32768	0.74	$290.0^{MCD,MLD}$	34473	neg	neg	- 2.25	- 0.56
y^3F_3	303.8	32907	0.31	288^{MLD}	34712	--	pos	0.31	0.26
y^3D_3	300.2	33296	0.87	284.5^{MCD}	35139	pos	pos	0.87	1.96
z^1G_4	299.4	33385	0.12	--	--			- 0.36	- 0.09
y^3F_2	299.3	33406	0.079	284.5^{MCD}	35139	pos?	--	0.28	- 0.12
y^3D_2	294.4	33958	0.079	280^{MCD}	35705	pos	neg?	0.28	- 0.12

Table 5-1. continued

	Gas Phase Absorption			Observed in Argon matrix				Theory	
Assignment	λ (nm)	$\bar{\nu}^a$ (cm^{-1})	gf^b	λ^c (nm)	$\bar{\nu}$ (cm^{-1})	MCD sign	MLD sign	$(C_0/D_0)gf^d$	$(G_0/D_0)gf^e$
y^1F_3	282.1	35434	0.04	268.6^{MCD}	37219	pos	--	0.04	0.09
y^1D_2	274.7	36396	0.019	261.0^{MCD}	38303	pos	--	0.046	- 0.026
w^3D_3	234.9	42563	0.136	--	--			0.136	0.28
x^3F_3	230.1	43450	0.42	--	--			0.42	0.95
x^1F_3	227.2	44001	0.037	--	--			0.037	0.061
y^3G_4	226.6	44110	0.0258	--	--			- 0.057	- 0.012
w^3D_2	225.8	44270	0.076	--	--			0.264	- 0.12
w^3F_3	225.4	44360	0.102	--	--			0.102	0.25
x^3P_2	215.8	46318	0.24	--	--			0.96	- 0.43

[a] Adapted from: Charlotte E. Moore. "Atomic Energy Levels As Derived From the Analyses of Optical Spectra", Vol. II 24Cr - 41Nb, pp. 97-100, National Bureau of Standards, Aug 15, 1952

[b] Adapted from: M. C. E. Huber and R. J. Sandeman. Oscillator strengths of ultraviolet Ni-I lines from Hook method and absorption measurements in a furnace. Astron Astrophys **86** (1-2), 95-104, 1980

[c] Wavelengths from MCD or MLD spectra indicated by superscript notation.

[d] In units of g_A, g factor of ground state.

[e] In units of g^2_A.

one-half of its intensity in the MLD. It is this difference in sign and structure that will be exploited to unambiguously assign the electronic transition states.

A similar analysis was performed for the gas phase transitions originating from a $^3F_4$ ground state[11]. Table 5-2 contains the gas phase data along with the predicted and observed MCD/MLD spectral transitions from a $^3F_4$ state. Figure 5-8 shows simulated spectra illustrating the energy and sign of the MCD transitions in the UV region based on gas phase transitions due to the different ground states, $^3D_3$ and $^3F_4$. The simulations were generated via the AMCOR method for Gaussian bandwidths of 0.5 and 2.0 nm.

The absorption and MCD spectra obtained are in generally close agreement with previously reported spectra.[7,36,38,80] There are differences in the ultraviolet (UV) range. The spectra can be divided into two separate regions: the long wavelength UV region from 370-250 nm, and the short wavelength UV region from 250 – 200 nm. Three specific characterizations can be made about the predicted MCD transitions from the dual ground states.

- Transitions from $^3F_4$ are expected to be very weak in the 370-250 nm range with the exception of transitions to z^3D_3 and z^3G_5 states, but several strong and very strong transitions are predicted in the high energy region below 250 nm (x^3F_3, x^3D_3, y^3G_5).
- Transitions from $^3D_3$ are expected to be numerous and strong in the lower energy region (370- 250 nm), with several moderate bands in the UV.
- $^3D_3$ transitions below 250 nm should all be positive in sign.

The simulated MCD and MLD spectra in Figures 5-7 and 5-8 illustrate the transitions due to $\Delta J = +1$ for negative MCD and MLD signals, $\Delta J = 0$ for positive MCD

Table 5-2. Gas phase absorption positions, observed argon matrix MCD and MLD positions, signs, and predicted relative intensities for MCD and MLD bands for Ni atoms with a $^3F_4$ ground state

Gas Phase Absorption				Observed in Argon matrix				Theory	
Assignment	λ (nm)	$\bar{\nu}^a$(cm^{-1})	gf^b	λ^c (nm)	$\bar{\nu}$ (cm^{-1})	MCD sign	MLD sign	$(C_0/D_0)gf^d$	$(G_0/D_0)gf^e$
z^5G_5	362.5	27580	0.0033					- 0.013	- 0.0046
z^5G_4	356.2	28068	0.002					0.002	0.0177
z^5F_5	350.3	28542	0.0017					- 0.0047	- 0.0024
z^5F_4	343.7	29084	0.065					0.065	0.25
z^3F_3	341.0	29321	0.0039					0.02	- 0.011
z^3F_4	339.1	29481	0.085					0.085	0.33
z^3D_3	337.0	29669	0.204					1.02	- 0.56
z^3G_5	323.3	30923	0.091	306.5	32617	neg		- 0.36	- 0.13
z^3G_4	322.7	30980	0.003					0.003	0.012
z^1F_3	322.2	31031	0.0126					0.063	- 0.0450
y^3F_4	303.2	32973	0.0148					0.0148	0.067
y^3F_3	301.9	33112	0.056					0.23	- 0.13
y^3D_3	298.4	33501	0.034					0.17	- 0.094
y^1F_3	280.5	35639	0.0049					0.035	- 0.013
y^1D_1	247.7	40361	0.0266					0.083	- 0.056
x^3F_4	234.8	42585	0.766	--	--			0.766	0.64
x^3D_3	234.6	42621	1.29	237	42181	pos		6.45	- 3.55
y^3G_5	232.0	43090	6.16	233.5	42813	neg		- 24.64	- 8.62
x^3F_3	229.0	43655	1.15	227.5	43942	pos		5.75	- 3.16

Table 5-2. Continued

	Gas Phase Absorption			Observed in Argon matrix				Theory	
Assignment	λ (nm)	$\bar{\nu}$[a](cm^{-1})	gf[b]	λ[c] (nm)	$\bar{\nu}$ (cm^{-1})	MCD sign	MLD sign	$(C_0/D_0)gf$[d]	$(G_0/D_0)gf$[e]
x^1F_3	226.1	44263	0.059	--	--			0.25	- 0.14
y^3G_4	225.5	44315	0.076	--	--			0.076	0.25
v^3D_3	212.6	47030	0.024	--	--			0.12	- 0.076

[a] Adapted from: Charlotte E. Moore. "Atomic Energy Levels As Derived From the Analyses of Optical Spectra", Vol. II, 24Cr - 41 pp. 97-100, National Bureau of Standards, Aug 15, 1952

[b] Adapted from: M. C. E. Huber and R. J. Sandeman. Oscillator strengths of ultraviolet Ni-I lines from Hook method and absorptic measurements in a furnace. Astron Astrophys **86** (1-2), 95-104, 1980

[c] Wavelengths from MCD or MLD spectra indicated by superscript notation.

[d] In units of g_A, g factor of ground state.

[e] In units of g^2_A.

and MLD transitions, and $\Delta J = -1$ for positive MCD and negative MLD. Thus the simulated MLD spectrum (Figure 5-7) for a $^3D_3$ ground state predicts the intense $z^3P_2 \leftarrow {}^3D_3$ transition to be negative in sign, opposite from the positive MCD $z^3P_2 \leftarrow {}^3D_3$ transition. The predicted transitions to z^5F_4 and z^3F_4 are both negative in the MLD, as in the MCD, while the underlying z^3F_3 and nearby z^3D_3 are both positive in the MCD and MLD. The relative intensities for these five bands are significantly different in the MCD than the MLD, presenting as a significant change in the predicted pattern in the region of those transitions. The relative intensities for these peaks are collected in Table 5-3. The distinct variation in structure caused by the marked difference in intensity of the $^3F_4 \leftarrow {}^3D_3$ transition in the MCD as compared to the MLD is easily discerned in the predicted spectra of Figure 5-7. Similarly, the intensity differences between MCD and MLD transitions in the 290-310 nm region of the simulated gas phase spectra cause a significant variation in the peak structure, despite the fact that the signs of the four dominant transitions in that region are the same for the MCD and MLD: two are positive and two are negative (Table 5-1).

Table 5-3 Relative intensities for the predicted MCD and MLD gas phase transitions between 339 and 352 nm

		Theoretical Intensity		
Assignment	$(C_0/D_0)gf$ [a]	normalized	$(G_0/D_0)gf$ [a]	normalized
z^3P_2	3.72	17.7	-1.67	-5.1
z^5F_4	-1.32	-6.3	-0.33	-1.0
z^3F_3	0.21	1.0	0.47	1.4
z^3F_4	-2.82	-13.4	-0.71	-2.2
z^3D_3	0.29	1.4	0.65	2.0

[a] Values extracted from Table 5-2

Comparison of the simulated spectra in Figures 5-7 and 5-8 with the actual MCD and MLD spectra of Figures 5-5 and 5-6 results in a straightforward assignment of the electronic transitions from the $^3D_3$ ground state (Table 5-1) based on the complementary methods presented.Assessment of the MCD/MLD spectra of Figures 5-5 and 5-6 readily permits associating the $^3D_3$ ground state configuration with the low energy bands in the region of 350 – 270 nm. The excited state assignments are indicated in Figure 5-5 and Table 5-1. The positive z^5P_2 (332.8 nm), negative z^5F_4 (324.8 nm), and negative z^3F_4 (320.0 nm) MCD $\mathcal{C}$-terms are assigned to transitions from a $^3D_3$ ground state. These peaks similarly fit the prescribed MLD pattern for $^3D_3$: negative, negative, and negative, respectively. A spin-forbidden transition to the z^5F_4 state accounts for the 324.8 nm absorption band, and precludes observation of expected weakly positive transitions (z^5F_3 and z^3D_3). The intensity of this spin-forbidden transition is evidence for the extent of spin-orbit coupling present. A weak negative transition at 306.5 nm in the MCD is unaccounted for by a $^3D_3$ ground state.

Since predictions from gas phase data indicate no negative transitions should occur in the high energy UV region for a $^3D_3$ ground state, it is apparent from the strong negative MCD transition at 233.5 nm that something other than a $^3D_3$ state is responsible. The predicted spectral transitions for MCD in this region for a $^3F_4$ ground state (Figure 5-8 and Table 5-2) mimic directly the observed spectra, corrected for an energy shift due to metal-matrix interaction.[76] Further consideration of the $^3F_4$ ground state predicts that a moderately intense positive transition at a gas phase energy of 337.9 nm and a moderately intense negative transition at 323.3 nm should occur. A positive band is not seen, but if present would most likely be unresolved from the $^3D_3$ transitions in the region. Allowing for a matrix shift from the gas phase data, the 306.5 nm negative peak could be the $z^3G_5 \leftarrow {}^3F_4$ transition. Annealing the matrix sufficiently results in complete disappearance of the spectral transitions attributable to the $^3F_4$ ground state. Conversely, irradiation of the $^3P_2$ band powers the regeneration of the $^3F_4$ ground state atoms, as evidenced by growth of the negatively signed x $^3G_5$ band.[38] A new weakly positive transition at 310 nm is seen in the annealed matrix (dominant $^3D_3$ ground state) which has been assigned as $z^1D_2 \leftarrow {}^3D_3$. This transition is considered to be always present, just submerged under the stronger 306.5 nm $z^3G_5 \leftarrow {}^3F_4$ transition prior to annealing. The weak negative MLD signal seen at this same location after annealing corroborates this assignment.

Discussion

Complementary MCD/MLD spectral analysis applied to the complex spectra of Ni(0) atoms isolated in an argon matrix has revealed the dual ground state nature of the spectra. The demonstrated superposition of spectra isolable to transitions from each of two ground states, $^3D_3$ and $^3F_4$, corroborate the hypotheses predicting the existence of both ground states.[5,6] All of the observed transitions except the $z^5F_4 \leftarrow {}^3D_3$ transition at 325 nm can be explained in terms of the simultaneous presence of both these ground states. The strong $z^5F_4 \leftarrow {}^3D_3$ transition at 325 nm is not allowed [i.e., is spin-forbidden] via spectroscopic selection rules, and is attributable to strong spin-orbit coupling between the Ni(0) atom and its surrounding heavy atom lattice[6,17]. The coupling is most certainly with the nearby z^3F_4 allowed electronic state at 320.0 nm.

Sequential acquisition of MCD and MLD spectra of matrix-isolated species, previously substantiated as a valid technique for absolute assignment of electronic state transitions, has proven definitive in unraveling the complex spectra of Ni atoms in argon matrices. Extension of these results to confirm the similarly complex nature of Ni atoms isolated in krypton and xenon is straightforward.

MCD and MLD Saturation Spectroscopy of Ni(0) in a Krypton Matrix

Having now confirmed the presence of both Ni(0) $^3D_3$ and $^3F_4$ stable ground states in Ar matrix by complementary MCD/MLD spectroscopy, the determination of the lattice site symmetry of these ground states has now been determined. The MCD/MLD saturation method (presented in Chapter 3 and utilized on Fe(0) in Chapter 4) has been applied to Ni(0) atoms isolated in solid krypton matrix. Ni(0)/Kr matrices display the same multiple ground state spectra as Ni(0) atoms in argon.[38,74-76] The electronic transitions are red-shifted slightly relative to argon matrices due to the larger radius of interaction of krypton lattice atoms compared to argon atoms. The transition $z^3P_2 \leftarrow {}^3D_3$ at 338.7 nm and the transition $y^3G_5 \leftarrow {}^3F_4$ at 235.2 nm will be characterized by the saturation methods.

Experimental

Data acquisition for Ni(0) atoms in krypton was accomplished over two separate and distinct experiments, due to the amount of time required to conduct the scans and the limited supply of liquid helium available at a given time. During the first experimental study, the $^3D_3$ ground state was studied by obtaining absorption, MCD and MLD spectra for the $z^3P_2 \leftarrow {}^3D_3$ transition at 338.7 nm. In the second set of experiments, data for the $^3F_4$ ground state absorption, MCD and MLD were acquired for the $y^3G_5 \leftarrow {}^3F_4$ transition at 235.2 nm. In each experiment, the sample matrix was prepared identically according to the following method. Atomic beam deposition of Ni metal (SPEX, powdered, 99.98 % purity) was made in Kr matrix (Matheson, 99.9996 % purity) on a sapphire window for the MCD/MLD saturation studies, utilizing the Oxford superconducting magnet / cryostat (Figures 1-1, 1-2, 1-3, 4.-3 and 4-4). The Knudsen furnace technique was used to create the Ni atomic beam (Figure 4-5), again confining the powdered Ni metal in an Al_2O_3 cylinder supported in a Ta cell. The Ni(0) beam was co-deposited with Kr gas for 100 minutes at 1670-1720 °C. The matrix was annealed at 35 K for one hour prior to data collection. Temperature monitoring was via a carbon-glass thermistor adjacent to the sapphire window and calibrated vs. Cu/Kr moments determination (Figures 4-6 and 4-8). ABS, MCD, and MLD scans were acquired from 400-200 nm at 4.22 K (Figure 5-9). Signal averaging (16 cycles) was performed for each data point. The magnetic field strength was 1.0 T for the MCD scan in Figure 5-10 and 0.6 T for the MLD scan.

The MCD experiment was conducted in accordance with the diagrams of Figures 1-1 and 1-2. For the $z^3P_2 \leftarrow {}^3D_3$ transition at 338.7 nm, the monochromator was scanned from 365.0 – 315.0 nm in 0.1 nm increments while digitizing the bandshape via a PC utilizing a data acquisition card with an analog-to-digital converter. Signal averaging (16 cycles) was performed on each data point prior to computer storage. The bandshape was also recorded on a chart recorder for backup. Absorption bandshapes were recorded simultaneously with the MCD to correct for any matrix decay or other matrix effects (as diamagnetic impurities). Scans were conducted incrementally over a magnetic field range of 0.0 – 3.01 T and across the temperature range 4.38 – 2.26 K for a total of 110 individual MCD bandshape scans.

Upon completion of the MCD data acquisition, the Oxford magnet / cryostat was isolated from the high vacuum system and rotated 90° to obtain MLD data on the same $z^3P_2 \leftarrow {}^3D_3$ transition. The equipment used is given in Figures 1-1 and 1-6. Scans from 355.0 – 315.0 nm were acquired simultaneously for MLD and absorption to conduct moments analyses. Scans were conducted incrementally over a magnetic field range of 0 to 3.64 T and a temperature range 4.09 – 1.73 K for a total of 238 individual MLD scans. Again, each data point was signal averaged 16 cycles prior to computer storage.

A second set of MCD/MLD acquisition experiments was on a different Ni(0)/Kr matrix prepared in the same fashion as the previous matrix. The $y^3G_5 \leftarrow {}^3F_4$ transition at 235.2 nm was monitored during this second study. Simultaneous ABS/MCD and ABS/MLD scans were averaged (16 cycles) and digitized for computer storage. The scan range was 250.0 – 220.0 nm. The data was simultaneously plotted on a chart recorder for backup. Scans were conducted incrementally over a magnetic field range of 0.0 – 3.64 T and a temperature range of 3.91 – 1.48 K for a total of 162 individual MCD bandshape scans. MLD scans were obtained for this same transition across the magnetic field range of 0.0 – 3.64 T and the temperature range 4.00 – 2.58 K. A total of 71 MLD scans were acquired.

Data Reduction and Refinement

Digitization and recording of the bandshapes for simultaneous ABS/MCD and ABS/MLD allows the band moments representing shifts in the bandshape structure to be calculated. The total integrated area under each band, (the zeroth moment) is the only moment of interest when compensating for any matrix decay or other matrix effects. The zeroth moment of MCD (or MLD) is divided by the zeroth absorption moment for each pair of ABS/MCD (or ABS/MLD) bandshapes. The simultaneous acquisition of absorption and MCD (or MLD) spectra for moments analyses compensates for any change in the barycenter of the bandshape due to temperature-dependent population differences in the MCD and MLD ground states that may cause a physical shift of the center frequency of the band.

The magnetization data is the band peak intensity at a given magnetic field and temperature. As previously described (Chapter 4), the monochromator was tuned to the peak MCD or MLD intensity at ~ 1 T and 4.2 K. The magnetic field was then ramped from 0.0 – 3.0 T and back again in increments of ~ 0.1 or 0.2 T and the temperature varied from 4.2 – 1.5 K without adjusting the monochromator. Thus the recorded magnetization scans tracked the peak intensity at a single wavelength, i.e., the wavelength of maximum intensity at ~ 1 T and 4.2 K. Having acquired the entire bandshape in the Ni(0)/Kr scans of this study as a function of magnetic field and temperature, magnetization parameters are easily extracted from the bandshape by measuring the peak intensity relative to the baseline. Since the peak intensity is measured directly from the bandshape, any drift in the center frequency due to a change in barycenter is avoided. Employing the fully integrated band area avoids this difficulty.

The variation in the reduction method for the magnetization contrasted with the moments ratios is small (~0.5 – 3 %), but not negligible. Both magnetization and moments-reduced raw data were analyzed for the $^3D_3$ MLD results. Reduced data for the Magnetization scans only was analyzed for the $^3D_3$ MCD and $^3F_4$ MCD and MLD spectra. The MLD raw data for the $z^3P_2 \leftarrow {}^3D_3$ transition was reduced to a set of thirteen magnetization intensity data sets and eight moments-ratio data sets continuously scaled across each series by the associated absorption intensity or integrated band area. The $^3D_3$ MCD data was reduced to twelve sets of magnetization scans, scaled similarly. The $^3F_4$ raw data generated nine MCD and four MLD data sets for further analysis. One of the MCD data sets (at 3.91 K) was deemed invalid after it was discovered instrument scale settings had been improperly calibrated during the data acquisition process.

Results

$^3D_3$ ground State Configuration of Ni(0)

The ABS, MCD, and MLD scans of the Ni(0)/Kr matrix are shown in Figure 5-10. Symmetry modeling refinements were performed on all the corrected raw data points for both ground state configurations within a given temperature set using the free atom, octahedral, tetragonal, and trigonal symmetry models. The results for the refinement of the $^3D_3$ ground state environment are illustrated in Figures 5-10 – 5-17 and collected in Tables 5-4 through 5-9. It is seen at once from the data of Table 5-4 and Figures 5-10 and 5-11 that the free atom optimization of Ni/Kr in the $^3D_3$ ground state results in severe disagreement between the experimental data and the free atom model. The range of RMS deviation for the MCD free atom data is 4.36 - 6.16 %, and for the MLD magnetization data it is 7.55 – 20.23 %. The results of the refinements utilizing continuously scaled moments data are included in Table 5-4, and shows a similar trend of high RMS deviation, ranging from 8.40 – 20.48 %.

The octahedral model (Table 5-5 and Figures 5-12 and 5-13) provides equally poor results for the MCD data, while the MLD data (both magnetization-based and moments-based) demonstrates an improved agreement between the experimental data and the octahedral theoretical model, but still does not support an octahedral symmetry environment for the $^3D_3$ Ni atoms. The MCD RMS results range from ~ 3.9 – 6.5 %, and the MLD ranges 2.4 – 5.6 % for the magnetization-based data and 2.8 – 4.3 % for the moments-based data. Note the close agreement of the calculations based on magnetization data with those based on the moments-ratio data. The calculated D^{OCT} and energy separation between the corresponding crystal field split energy levels of a $^3D_3$ octahedral state (ΔE) compare very well with each other, showing no preference for either data type. This is highly supportive of the use of magnetization scans for site symmetry analysis via magnetic saturation methods.

Table 5-4. Free atom refinement parameters for the $^3D_3$ MCD and MLD experimental data sets

Number of			Magnetization Data		Moments Data
Data Points	T_{MCD}(K)	T_{MLD}(K)	RMS_{MCD} (%)	RMS_{MLD} (%)	RMS_{MLD} (%)
30/22	4.38	4.09	5.15	7.55	8.40
30/22	3.90	4.09	6.16	7.55	---
16/18	3.39	3.47	5.62	10.28	---
16/18	3.06	2.96	5.23	10.10	8.87
16/18	2.84	2.75	4.68	9.92	---
16/18	2.67	2.75	5.15	9.92	---
16/18	2.59	2.53	4.70	10.63	10.94
16/18	2.48	2.53	4.50	10.63	---
16/18	2.41	2.38	5.59	12.43	11.87
16/18	2.33	2.38	4.39	12.43	---
16/18	2.30	2.38	4.84	12.43	---
16/18	2.26	2.18	4.36	14.92	---
16/18	---	2.06	---	13.95	13.53
16/18	---	1.98	---	14.09	---
16/18	---	1.89	---	14.31	14.18
16/18	---	1.82	---	15.28	---
16/18	---	1.76	---	18.54	15.72
16/18	---	1.73	---	20.23	20.48

Consideration of the MCD and MLD data refined under tetragonal symmetry (Tables 5-6 and 5-7 and Figures 5-14 and 5-15) demonstrates poor results again for the MCD data (RMS: 5.78 – 7.95 %), but a marked improvement in agreement for the MLD magnetization-based data (1.2 – 4.4 %, with the 4.4 % result at 1.73 K appearing as an outlier among the rest of the tetragonal MLD refinement data). Moments-based refinement under tetragonal symmetry gives RMS values of 0.99 – 2.95 %. The agreement between the tetragonal crystal field parameters (F_1^{TET}, F_2^{TET}, and B^{TET}) and ΔE for the magnetization-based and moments-based data sets is reasonable, but not

Table 5-5. Octahedral refinement parameters for the $^3D_3$ MCD and MLD data sets

Number of Data Points	MCD T(K)	MLD T(K)	Magnetization Data					Moments Data		
			MCD RMS (%)	MLD RMS (%)	D_{MCD}^{OCT}	D_{MLD}^{OCT}	MLD ΔE (cm^{-1})	MLD RMS (%)	MLD D^{OCT}	MLD ΔE (cm^{-1})
30/22	4.38	4.09	4.88	3.35	-5.46	2.35	42.2	3.31	2.65	47.6
30/22	3.90	4.09	6.47	3.35	-4.47	2.35	---	---	---	---
16/18	3.39	3.47	5.44	2.68	-3.87	1.97	35.4	---	---	---
16/18	3.06	2.96	5.64	3.32	-3.46	1.45	26.1	4.29	1.49	26.8
16/18	2.84	2.75	5.05	4.14	-3.29	1.27	22.8	---	---	---
16/18	2.67	2.75	4.99	4.14	-3.04	1.27	---	---	---	---
16/18	2.59	2.53	3.88	3.94	-2.98	1.12	20.1	3.78	1.12	20.2
16/18	2.48	2.53	4.52	3.94	-2.91	1.12	---	---	---	---
16/18	2.41	2.38	4.17	3.55	-2.71	1.07	19.2	3.73	1.05	18.8
16/18	2.33	2.38	4.57	3.55	-2.80	1.07	---	---	---	---
16/18	2.30	2.38	3.90	3.55	-2.69	1.07	---	---	---	---
16/18	2.26	2.18	4.03	3.15	-2.73	1.00	17.9	---	---	---
16/18	---	2.06	---	3.65	---	0.89	16.0	4.01	0.88	15.8
16/18	---	1.98	---	4.35	---	0.83	14.9	---	---	---
16/18	---	1.89	---	3.71	---	0.79	14.1	4.03	0.78	14.1
16/18	---	1.82	---	5.58	---	0.77	13.9	---	---	---
16/18	---	1.76	---	2.38	---	0.85	15.2	3.22	0.77	13.8
16/18	---	1.73	---	5.09	---	0.88	15.8	2.84	0.89	16.1

Note: Numerical theta integration used 250 increments from 0 to $\pi/2$

Table 5-6. Tetragonal refinement parameters for the $^3D_3$ MCD and MLD data sets reduced by continuous scaling of the magnetization data

Number of Data Points	T_{MCD}(K)	T_{MLD}(K)	RMS_{MCD} (%)	RMS_{MLD} (%)	F_1^{TET}	F_2^{TET}	B_{MLD}^{TET}	ΔE_{MLD} (cm^{-1})
30/22	4.38	4.09	5.78	2.68	1.22	-0.57	0.05	18.4
30/22	3.90	4.09	7.95	2.68	---	---	---	---
16/18	3.39	3.47	6.37	2.30	1.21	0.06	0.02	16.0
16/18	3.06	2.96	7.39	1.18	0.49	-1.05	2.32	15.1
16/18	2.84	2.75	7.22	1.42	0.44	-0.92	2.09	13.4
16/18	2.67	2.75	6.95	1.42	---	---	---	---
16/18	2.59	2.53	5.98	1.58	0.64	-0.56	0.06	10.8
16/18	2.48	2.53	6.99	1.58	---	---	---	---
16/18	2.41	2.38	6.02	2.21	0.66	0.05	0.06	8.6
16/18	2.33	2.38	7.24	2.21	---	---	---	---
16/18	2.30	2.38	6.32	2.21	---	---	---	---
16/18	2.26	2.18	6.72	2.68	-0.32	0.74	1.39	13.5
16/18	---	2.06	---	1.33	0.53	-0.59	2.44	10.4
16/18	---	1.98	---	2.96	0.53	0.05	0.56	6.5
16/18	---	1.89	---	1.21	0.52	-0.74	-0.23	11.4
16/18	---	1.82	---	3.29	0.49	-0.60	2.00	11.5
16/18	---	1.76	---	1.26	0.56	-0.49	1.16	9.2
16/18	---	1.73	---	4.36	0.61	-0.80	2.71	15.5

Table 5-7. Tetragonal refinement parameters for the $^3D_3$ MCD and MLD data sets reduced by continuous scaling of the moments data

Number of Data Points	T_{MCD}(K)	T_{MLD}(K)	RMS_{MLD} (%)	F_1^{TET}	F_2^{TET}	B_{MLD}^{TET}	ΔE (cm^{-1})
30/22	4.38	4.09	2.95	1.51	0.06	0.03	19.8
30/22	3.90	4.09	---	---	---	---	---
16/18	3.39	3.47	---	---	---	---	---
16/18	3.06	2.96	1.86	0.61	-0.69	2.12	8.5
16/18	2.84	2.75	---	---	---	---	---
16/18	2.67	2.75	---	---	---	---	---
16/18	2.59	2.53	1.64	0.65	-0.56	0.05	8.2
16/18	2.48	2.53	---	---	---	---	---
16/18	2.41	2.38	2.00	0.63	0.05	0.06	12.3
16/18	2.33	2.38	---	---	---	---	---
16/18	2.30	2.38	---	---	---	---	---
16/18	2.26	2.18	---	---	---	---	---
16/18	---	2.06	1.28	0.53	-0.59	2.21	8.8
16/18	---	1.98	---	---	---	---	---
16/18	---	1.89	0.99	0.47	-0.53	0.42	7.1
16/18	---	1.82	---	---	---	---	---
16/18	---	1.76	1.18	0.52	-0.76	-0.18	11.3
16/18	---	1.73	2.85	0.64	0.05	0.07	8.2

exceptional. Tetragonal symmetry, weighting the more sensitive MLD data refinement, is distinctly a possibility as the prevailing geometry for the $^3D_3$ ground state.

Tables 5-8 and 5-9 and Figures 5-16 and 5-17 contain the trigonal refinement data. It can be seen that the MCD results remain poor under this refinement geometry also, ranging 4.5 – 6.6 %. The MLD results for both data types are reasonably low, indicating the trigonal geometry as similar in possibility to the tetragonal environment as the dominant geometry for $^3D_3$ Ni atoms in krypton. The RMS range of the MLD magnetization-based results is 1.04 – 4.88 %, with the 1.73 K data set again appearing as an outlier. The moments-based data refinements range 1.26 – 3.10 %. Again the separation energy (ΔE) and crystal field parameters (K^{TRI}, L^{TRI}, M^{TRI}) for both MLD data sets are comparable, indicating the cross-compatibility of the refinement method for either

Table 5-8. Trigonal refinement parameters for the $^3D_3$ MCD and MLD data sets reduced by continuous scaling of the magnetization data

Number of Data Points	T_{MCD}(K)	T_{MLD}(K)	RMS_{MCD} (%)	RMS_{MLD} (%)	K^{TRI}	L^{TRI}	M^{TRI}	ΔE (cm^{-1})
30/22	4.38	4.09	6.39	2.71	-0.49	1.58	0.11	44.8
30/22	3.90	4.09	7.57	2.71				
16/18	3.39	3.47	6.59	2.30	0.27	2.00	0.05	47.0
16/18	3.06	2.96	6.27	1.04	-0.76	1.35	-1.34	21.0
16/18	2.84	2.75	5.56	1.27	-0.65	0.93	-0.76	13.3
16/18	2.67	2.75	5.73	1.27				
16/18	2.59	2.53	4.88	1.61	-0.56	0.71	-0.06	20.1
16/18	2.48	2.53	5.05	1.61				
16/18	2.41	2.38	5.29	2.23	-0.64	1.05	0.22	35.0
16/18	2.33	2.38	4.80	2.23				
16/18	2.30	2.38	4.75	2.23				
16/18	2.26	2.18	4.53	3.63	2.49	0.10	0.04	30.7
16/18	---	2.06	---	1.81	2.12	0.05	0.05	25.9
16/18	---	1.98	---	3.08	2.03	0.05	0.05	25.1
16/18	---	1.89	---	1.39	1.97	0.05	0.05	24.3
16/18	---	1.82	---	3.71	1.92	0.05	0.05	23.7
16/18	---	1.76	---	1.50	2.18	0.05	0.05	27.2
16/18	---	1.73	---	4.88	2.26	0.05	0.05	28.2

Table 5-9. Trigonal refinement parameters for the $^3D_3$ MCD and MLD data sets reduced by continuous scaling of the moments data

Number of Data Points	T_{MCD}(K)	T_{MLD}(K)	RMS_{MLD} (%)	K^{TRI}	L^{TRI}	M^{TRI}	ΔE (cm^{-1})
30/22	4.38	4.09	3.00	0.35	1.69	-0.13	35.2
30/22	3.90	4.09	---	---	---	---	---
16/18	3.39	3.47	---	---	---	---	---
16/18	3.06	2.96	1.72	-0.70	1.27	-1.26	19.7
16/18	2.84	2.75	---	---	---	---	---
16/18	2.67	2.75	---	---	---	---	---
16/18	2.59	2.53	1.66	-0.59	0.77	0.02	23.4
16/18	2.48	2.53	---				
16/18	2.41	2.38	2.01	-0.68	1.06	0.33	37.7
16/18	2.33	2.38	---	---	---	---	---
16/18	2.30	2.38	---	---	---	---	---
16/18	2.26	2.18	---	---	---	---	---
16/18	---	2.06	1.75	2.08	0.05	0.05	25.7
16/18	---	1.98	---	---	---	---	---
16/18	---	1.89	1.26	1.94	0.05	0.05	24.0
16/18	---	1.82	---	---	---	---	---
16/18	---	1.76	1.41	1.98	0.05	0.05	24.5
16/18	---	1.73	3.10	2.33	0.05	0.05	29.1

magnetization or moments-ratio based input data. ΔE varies from 24 – 45 cm^{-1} for the magnetization-based refinements and from 24 – 38 cm^{-1} for the moments-based refinements.

In four cases for the tetragonal refinement (temperatures 2.53, 2.41, 1.98, and 1.73 K) one or two of the crystal field parameters ends up refining near its starting point (0.05 in all cases). The situation is worse for the trigonal refinements, where all of the lowest temperature data sets from 2.18 – 1.73 K result in solutions with two of the crystal field parameters near or equal to the starting parameters. This same finding was observed in the Fe(0) minimization results of Chapter 4.

Figure 5-18 illustrates the $^3D_3$ ground state RMS deviation values as a function of temperature for all geometry models except the free atom model. One free atom point is plotted high in the figure, but the remainder are off scale high. The free atom and octahedral models are obviously excluded in preference for the competing tetragonal and trigonal symmetry models.

$^3F_4$ Ground State Configuration of Ni(0)

The MCD and MLD spectra in the ultraviolet region for the $^3F_4$ ground state Ni(0) atomic transitions in krypton are reproduced in Figure 5-19. The principal transitions in this region provide more evidence of the ability of the complementary MCD/MLD technique to unambiguously resolve most electronic state assignments by comparing their expected sign of transition with the observed MCD or MLD spectrum. The previously described Ni/Ar study of this chapter failed to address the complementary assignment of the $^3F_4$ ground state MLD transitions due to the poor character of the sample spectrum in the ultraviolet region. The principal absorption peak in Figure 5-19 is located at 235.2

nm, as previously determined. The MLD in Figure 5-19, although showing evidence of a slightly noisy background near its high energy end, is quite dramatic in the intensity of the principal electronic transitions. The negatively signed x $^3G_5 \leftarrow {}^3F_4$ transition is dominant in both the MLD and MCD, the MCD transition being located at 234.4 nm in the krypton matrix as compared to 233.5 nm in argon, exhibiting a red shift of +0.9 nm from argon and +2.4 nm from the gas phase. Similar behavior is observed for the positive x $^3D_3 \leftarrow {}^3F_4$ transition at 238.8 nm and the positive x $^3F_3 \leftarrow {}^3F_4$ transition at 229.4 nm. Note the positive-negative-positive orientation of the signs of these three transitions, along with their intensities: moderate-strong-moderate, and compare this structure with the simulated MCD spectrum in the ultraviolet range shown in Figure 5-8. Obviously, the simulated transitions and structure from the $^3D_3$ ground state of Figure 5-8 A do not correspond. However, the simulated structure and intensities of Figure 5-8 B for the $^3F_4$ ground state UV MCD transitions are a remarkably good match. The peak at 224.0 nm corresponds well with the expected positively signed y $^3G_4 \leftarrow {}^3F_4$ MCD transition (see Table 5-2). Other weaker peaks are seen on the high energy side of the y $^3G_4$ transition, but cannot be assigned relative to the $^3F_4$ ground state.

The low energy side of the x $^3D_3$ band demonstrates some asymmetry, and may be exhibiting some MCD behavior due to transitions from the $^3D_3$ ground state which is simultaneously present in the matrix. Structure caused by the weakly positive w $^3D_3 \leftarrow {}^3D_3$ transition and x $^3F_3 \leftarrow {}^3D_3$ transitions expected to be found at 236.6 and 231.8 nm, respectively, may be responsible for this distortion (the expected positions of the transitions in krypton have been shifted +2.4 nm from the positions relative to the gas phase spectrum).

The MLD spectrum is much more intense, and the very strong and negatively signed x $^3G_5 \leftarrow {}^3F_4$ transition at 231.7 nm is largely in agreement with the behavior predicted for that transition from Table 5-2. However the bandshape appears to be skewed significantly by an underlying strongly positive-going transition, probably due to the transitions produced by Ni atoms in the alternate $^3D_3$ symmetry sites. The true location of the x $^3G_5 \leftarrow {}^3F_4$ peak may well be located to slightly lower energy. The x $^3F_3$ band at 224.0 nm on the high energy side is also negatively signed and moderate in strength, as predicted. The expected x $^3D_3$ transition is not readily observed due to a large positive-going peak which has a distinct bifurcation at its maximum intensity. It is feasible to interpret this negative-going bifurcation as originating from the x $^3D_3 \leftarrow {}^3F_4$ transition superimposed on the strong positive x $^3F_3 \leftarrow {}^3D_3$ transition and possibly also the w $^3D_3 \leftarrow {}^3D_3$ transition. The weakly negative transition at 227 nm is assigned as the x $^1F_3 \leftarrow {}^3D_3$ transition.

Figures 5-20 – 5-27 illustrate the $^3F_4$ symmetry-model refinement results, which are listed in Tables 5-10 through 5-15. Figure 5.28 is a plot of the minimization routine's RMS deviation values from Tables 5-10, 5-12, 5-14 and 5-15 as a function of temperature for all four geometries investigated. The free atom model perhaps is valid at temperatures greater than 4 K, but below 4 K in the MLD and below approximately 2.8 K in the MCD it quickly departs from the observed experimental data, and is thus excluded as a candidate for the site geometry below ~ 2.8 – 4K. It should not be ruled out as a distinct possibility at or above these temperatures. The RMS deviation values vary from 2.12 % at 3.31 K for the MCD data, passing through a minimum at 2.78 K of 1.50 %, then increasing steadily to 8.94 % at the lowest temperature of 1.48 K. The MLD RMS values

Table 5-10. Free atom refinement parameters for the $^3F_4$ MCD and MLD experimental data sets for Ni(0) atoms in Kr

Number of Data Points	T_{MCD}(K)	T_{MLD}(K)	RMS_{MCD} (%)	RMS_{MLD} (%)
17	---	4.00	---	3.56
18/18	3.31	3.28	2.12	14.92
18/18	2.78	2.78	1.50	10.94
18/18	2.62	2.58	2.03	14.51
18	2.34	---	2.63	---
18	2.14	---	3.52	---
18	1.89	---	5.46	---
18	1.66	---	5.37	---
18	1.48	---	8.94	---

Table 5-11. Octahedral refinement parameters for the $^3F_4$ MCD and MLD experimental data sets for Ni(0) atoms in Kr using one increment for numerical theta integration from 0 to $\pi/2$

Number of Data Points	MCD T (K)	MLD T (K)	MCD RMS (%)	MLD RMS (%)	D_{MCD}^{OCT}	ΔE (cm^{-1})	D_{MLD}^{OCT}	ΔE (cm^{-1})
17	---	4.00	---	40.75	---	---	-0.193	10.4
18/18	3.31	3.28	0.96	40.56	0.14	7.3	-0.140	7.6
18/18	2.78	2.78	1.38	12.12	0.65	35.1	-0.500	27.0
18/18	2.62	2.58	1.37	37.52	1.30	70.3	0.008	4.7
18	2.34	---	1.61	---	1.37	74.0	---	---
18	2.14	---	2.66	---	1.05	56.6	---	---
18	1.89	---	4.85	---	0.77	41.4	---	---
18	1.66	---	4.81	---	0.64	34.3	---	---
18	1.48	---	1.68	---	-0.23	-12.4	---	---

are even less stable, beginning at 3.56 % at 4.00 K, then climbing quickly to over 14 % through the lower temperatures.

Octahedral symmetry refinements for the MCD data initially were indicative of this geometry as a potential candidate for a stable environment, but the MLD results were unconvincing. The MCD ranged from 0.96 % at 3.31 K to 4.8 % at 1.89 and 1.66 K. The drop at 1.48 K to 1.68 % is most likely due to experimental error. The associated D^{OCT}

Table 5-12. Octahedral refinement parameters for the $^3F_4$ MCD and MLD experimental data sets for Ni(0) atoms in Kr using 250 increments for numerical theta integration from 0 to $\pi/2$

Number of Data Points	T_{MCD}(K)	T_{MLD}(K)	RMS_{MCD} (%)	RMS_{MLD} (%)	D_{MCD}^{OCT}	ΔE (cm^{-1})	D_{MLD}^{OCT}	ΔE (cm^{-1})
17	---	4.00	---	5.15	---	---	0.429	23.2
18/18	3.31	3.28	2.29	5.58	-0.040	2.2	0.359	19.4
18/18	2.78	2.78	2.41	4.74	-0.139	7.5	0.366	19.8
18/18	2.62	2.58	2.08	4.92	-0.167	9.0	0.366	19.8
18	2.34	---	2.48	---	-0.17	9.2	---	---
18	2.14	---	2.49	---	-0.18	10.0	---	---
18	1.89	---	2.12	---	-0.22	12.0	---	---
18	1.66	---	2.47	---	-0.18	9.9	---	---
18	1.48	---	2.15	---	-0.24	12.8	---	---

Table 5-13. Octahedral refinement parameters for the $^3F_4$ MCD and MLD experimental data sets for Ni(0) atoms in Kr using 1000 increments for numerical theta integration from 0 to $\pi/2$

Number of Data Points	T_{MLD}(K)	RMS_{MCD} (%)	RMS_{MLD} (%)	D_{MCD}^{OCT}	ΔE (cm^{-1})	D_{MLD}^{OCT}	ΔE (cm^{-1})
18	4.00	---	4.87	---	---	0.427	23.0
18	3.28	---	5.41	---	---	0.356	19.3
18	2.78	---	4.56	---	---	0.365	19.7
18	2.58	---	4.77	---	---	0.364	19.7

parameters and separation energies vary widely, with energies ranging from –12 to +74 cm^{-1}. The MLD results refined to very large values of RMS deviation, ranging from 12 – 41 %, although the D^{OCT} crystal field parameters associated with these refinements are reasonable in magnitude and closely grouped. The energies of separation are narrower also, ranging from 4.7 – 27.0 cm^{-1}.

Consideration of the difficulties observed in the refinements of Chapter 4 led to a further investigation of the extent to which the number of steps utilized in the numerical integration of the minimization routine over the angle 0 - $\pi/2$ affects the results. Such an effect was known, and predicted, for the lower symmetry model, but the pseudo-isotropic model had been regarded as not prone to serious deviations by assuming it to be totally isotropic. The MCD and MLD data sets for the $^3F_4$ Ni(0) atoms in krypton were reprocessed utilizing 250 increments for the numerical integration of theta in one set of refinements (Table 5-12). The MLD data set was also processed utilizing 1000 increments in an additional set of refinements. These data are contained in Table 5-13.

It is evident that the use of only a single increment for the octahedral data model results in very poor refinement of the MLD data sets. Using 250 increments for both the MCD and MLD produces much better results in the case of the MLD RMS deviations, but slightly worse for the MCD. The MLD refinement RMS deviations now range from 4.74 – 5.58 % and the MCD from 2.08 – 4.38 %. Inspection of the D^{OCT} values indicates much better consistency among the individual temperature data sets, although the sign is opposite between the MCD and MLD refinements. The crystal field separation energy is much more stable and reasonable within each data group, ranging from 2.2 – 22 cm^{-1} for the MCD and from 19.4 – 23.2 cm^{-1} for the MLD. Increasing the number of increments to 1000 for the four MLD data sets shows a further decrease in the refinement errors, now ranging 4.77 – 5.41 %, while the D^{OCT} and separation energy parameters vary by less than 0.5 % from their values using 250 increments. It is necessary to refine data using octahedral symmetry in the same manner as the lower symmetry tetragonal and trigonal models where theta is routinely numerically integrated over 250 or more increments as a matter of necessity. The hypothesis that the pseudo-isotropic octahedral model can be treated as totally isotropic is rejected. Reasoning from Watanabe's development of the equivalent operators[57] (Equations 3-9, 3-10, and 3-11), it is noted that the crystal field perturbation that Watanabe introduces is an electric field generated by the superposition of six isolated point charges, located at the vertices of an octahedron for the octahedral symmetry equivalent operator. This electric field is not itself isotropic, but varies between local maxima at the vertices and local minima midway between the vertices. A rotation of an octahedral vertex away from the parallel or perpendicular axis of a magnetic field in which it is embedded causes a perturbation in the MLD similar to that seen for the lower symmetry geometries and addressed Chapter 3.

The octahedral model can now be considered a serious candidate for the existing site geometry of the Ni(0) atoms in krypton at temperatures near or below 4 K. Tetragonal symmetry is also a realistic possibility, as Figure 5-28 shows, tracking very close to the octahedral results. The tetragonal MCD values are reasonably stable throughout the entire temperature span, ranging from 2.23 – 2.74 %. The energies associated with these refinements vary from ~ 2 – 25 cm^{-1}. The MLD RMS values are higher, but also stable across the temperature range, varying between 4.40 and 5.28 %. The crystal field energies are greater in the MLD than for the MCD refinements, ranging from 39.3 – 55.0 cm^{-1}.

The trigonal model is excluded at higher temperatures, but improves rapidly with decreasing temperature, becoming the favorite symmetry model below ~2.7 K in the MCD. The MCD trigonal RMS values are from 7.66 % at 3.31 K to 1.95 % at 1.48 K. The crystal field energies are low and tightly grouped for the MCD trigonal model, lying between 5.9 – 11.0 cm^{-1}. At ~2.5 K in the MLD, the trigonal model is very near both the octahedral and tetragonal RMS values, and is approaching at a sharp slope indicating it may become the dominant geometry below 2.5 K. Premature loss of the sample matrix precluded acquisition of MLD data below 2.58 K for the $^3F_4$ ground state transitions, rendering it impossible to conclude the behavior of the system below 2.5 K based on MLD analysis alone.

Discussion

The data plots of Figures 5-18 and 5-28 for all geometry models of both the $^3D_3$ and the $^3F_4$ ground states of Ni(0) atoms in krypton matrices are not totally conclusive, but do permit boundaries to be set on the actual site geometry model for each ground state configuration. The y $^3G_5 \leftarrow {}^3F_4$ transition is contaminated by an underlying x $^3F_3 \leftarrow {}^3D_3$ transition from the $^3D_3$ ground state that was not completely removed by the annealing process. Thus, error is introduced into the experimental data by the associated MCD and MLD differential absorptions for these transitions, which is superimposed on the $^3F_4$ ground state transition. The corresponding *gf* values for the x $^3F_3 \leftarrow {}^3D_3$ transition are 0.42 (units of g) in the MCD and 0.95 (units of g^2) in the MLD. Thus the MLD contamination is expected to be twice the magnitude of the MCD. The physical structure of the MCD y$^3G_5 \leftarrow {}^3F_4$ bandshape is little different from the theoretically-predicted structure, indicating little contamination by the underlying x $^3F_3 \leftarrow {}^3D_3$ transition. The MLD structure is less agreeable with the predicted model, however, and is probably reflecting the larger MLD contribution of the x $^3F_3 \leftarrow {}^3D_3$ transition. For this particular analysis, the MCD results are concluded to be more reliable than the MLD results as a consequence of this contamination.

Similar to the case of Fe(0) in Kr, Ni(0) atoms in Kr may substitutionally occupy a 'void' left by a krypton atom, or may interstitially 'crowd' in between surrounding lattice cage Kr atoms. The normal face-centered cubic structure of the Kr lattice cage would leave a hypothetical 3.94 Å 'hole' were a single Kr atom to be removed. The covalent radius of Ni(0) in bulk metal is 2.84 Å, significantly smaller than the void. The outer d and s- orbitals, and higher levels, have radial functions which extend beyond thes covalent radius however, to some extent, and the interaction between these outer orbitals and the surrounding Kr lattice atoms ultimately determines the stability of the local system. Repulsive interaction between the outer 4s electron shell (containing two electrons) of the Ni(0) $^3F_4$ ground state with the surrounding krypton outer electron shell (fully occupied) is to be expected. the consequence would be a destabilization of the 4s energy level, causing it to raise in potential energy. In Fe(0), the next available electronic angular momentum state is the $^5F_5$ ($3d^7$ 4s) at ~ +7000 cm^{-1} above the $^5D_4$ gas-phase ground state. For Ni(0), the next available energy level ($^3D_3$ $3d^9$ 4s) is only 204 cm^{-1} above the $^3F_4$ ground state. It is not surprising that destabilization of the 4s level to electron occupation may favor movement of an electron to the lower-energy 3d level. This distortion apparently is a consequence of the Kr lattice interaction with the Ni(0) atom, reflected by the different site geometries. The 3F4 site geometry experiences only minimal interaction with the Kr lattice cage, while the 3D3 site is geometrically distorted to a significant degree.

The behavior of transitions from the $^3D_3$ state is clearly not described by a free atom environment or an octahedral crystal field. The MLD saturation spectra clearly point to a stable geometry environment consistent with a tetragonal or trigonal crystal field lattice environment. The tetragonal refinement RMS deviation values indicate a slight preference for a tetragonal model, but the extent of experimental error present in the raw data sets precludes reaching this conclusion. The MCD results are also inconclusive, so that no inferences about a geometry preference can be deduced from them. The crystal field energies for both the tetragonal and trigonal geometries range from 6.5 to 47 cm^{-1}, although consideration of the tetragonal symmetry independently shows it is favored as the lower energy system, ranging from 6.5 – 19.8 cm^{-1} while the trigonal energies range 13.3 – 47.0 cm^{-1}. It is concluded that the $^3D_3$ ground state of Ni(0) atoms in a krypton matrix is probably tetragonal in nature at temperatures at and below 4 K, with a crystal field energy of approximately 10 – 20 cm^{-1}, favored only slightly over trigonal symmetry.

The $^3F_4$ site symmetry configuration is undoubtedly free atom or very slightly octahedral in the vicinity of 4 K and above. Figure 5-28 clearly distinguishes the free atom and trigonal model results from the tetragonal and octahedral results. Below 4 K, however, the free atom model becomes highly inconsistent with the observed spectral data, and a clear preference is shown for an octahedral symmetry by both the MCD and MLD data. The associated crystal field energies of 2 – 23 cm^{-1} are small and would not be evident in the spectral bandwidths observed. The close tracking of the tetragonal results with the octahedral is to be expected. Consideration of equations 3-9 and 3-10 demonstrate the relation between the octahedral and tetragonal models. The equivalent operator describing the crystal field perturbation to the Hamiltonian for tetragonal symmetry is a subset of the octahedral equivalent operator. If the geometry is truly octahedral, then both operators should provide the same end result. Only in the case where the geometry is tetragonal would the tetragonal refinement result in RMS deviation values less than the octahedral math model.

Further cooling of the matrix to below 3 K demonstrates an increased preference for trigonal symmetry. The transition occurs near 2.8 K for the MCD data. The corresponding crystal field energies are significantly lower than for the tetragonal model, ranging from 5.9 – 11.0 cm^{-1}. Although data below 2.5 K was not acquired for the MLD due to experimental difficulties, extrapolation for the trend in the trigonal model as the temperature decreases indicates it is competing directly with the octahedral/tetragonal model near 2.5 K. Continuation below 2.5 K could very well result in a similar plot as for the MCD data of Figure 5-28 where the trigonal model is slightly favored below 2.8 K.

Transition from one geometry (generally high symmetry) to a lower symmetry model has been observed in other instances, as in the Fe(0) study of Chapter 4 and the Ni(0) $^3D_3$ study of this chapter. The phenomenon is consistent in its progression from higher symmetry to lower symmetry, and the associated crystal field parameters often indicate a smooth change reflecting an increase in the crystal field separation energy with decreasing temperature. The consistent deterioration of the free atom model with temperature in all studies accomplished so far is supportive of the contention that the rare gas lattice cage contracts with decreasing temperature. This results in an increasing physical interaction between atomic d-electrons and the rare gas shell electrons, severely destabilizing the free atom model relative to the other crystal field stabilized interactions proposed. It is not surprising to see a temperature dependent variation of the minimization stability for a particular crystal field geometry in these data.

It is concluded that the dominant $^3F_4$ site symmetry at and above approximately 4 K is free atom or slightly octahedral in nature. Reduction of the matrix temperature results in lattice cage compression of the krypton atoms surrounding the Ni(0) atom, increasing the inter-electron interactions, causing a distortion of the site geometry to lower trigonal symmetry in the vicinity of 2.5 – 2.8 K. Trigonal symmetry the remains the dominant lattice model below 2.5 K.

Summary

The advantage of using complementary MCD/MLD spectroscopy to absolutely assign complex electronic transitions has been demonstrated on Ni(0) atoms in argon and corroborated by the analogous krypton spectra. MCD and MLD saturation spectroscopy methods were then applied successfully to ascertain the site symmetry of Ni(0) atoms isolated in a krypton matrix. The $^3F_4$ ground state is largely uninfluenced by the surrounding heavy atoms at temperatures above 2.5 –2.8 K, existing in a free atom state or a weak octahedral potential field. The stabilized $^3D_3$ excited state resides in a higher energy tetragonal symmetry environment, indicative of interaction between the 3d-electrons of the Ni(0) atoms with the surrounding Kr atoms comprising the lattice cage. It is this physical interaction of the electric potential fields that stabilizes the matrix-isolated $^3D_3$ atoms relative to the gas phase.

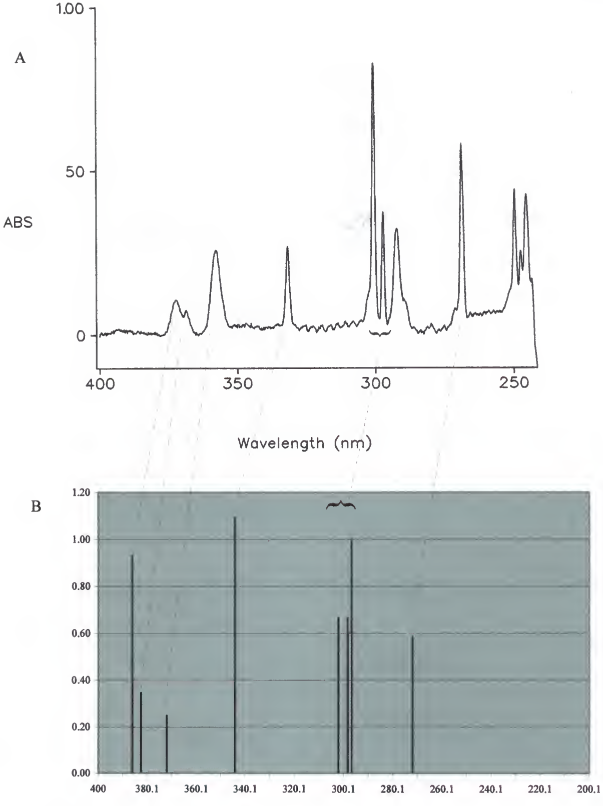

Figure 5-1. Comparison of absorption spectrum of Fe(0) atoms in argon with Fe(0) gas phase atomic transitions from the $^5D_4$ ground state. A) Absorption in argon. B) Gas phase line spectrum.

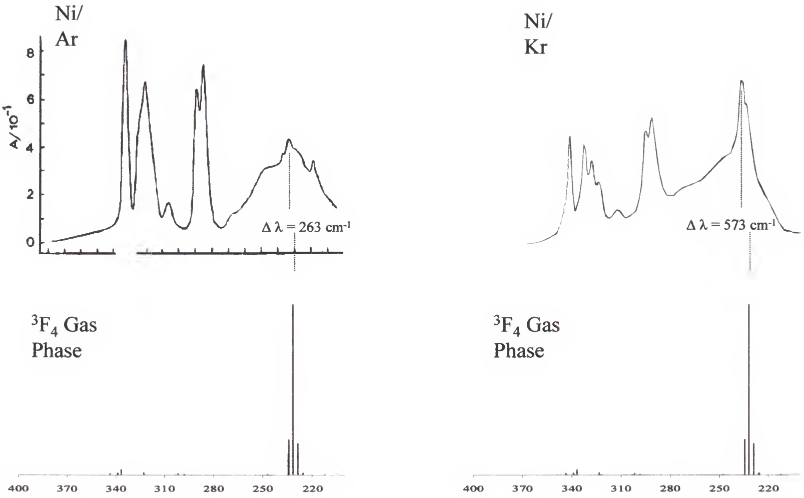

Figure 5-2. The absorption spectrum of Ni(0) atoms matrix-isolated in argon and krypton contrasted with the Ni(0) atomic gas phase UV/Visible absorption spectrum from the $^3F_4$ ground state.

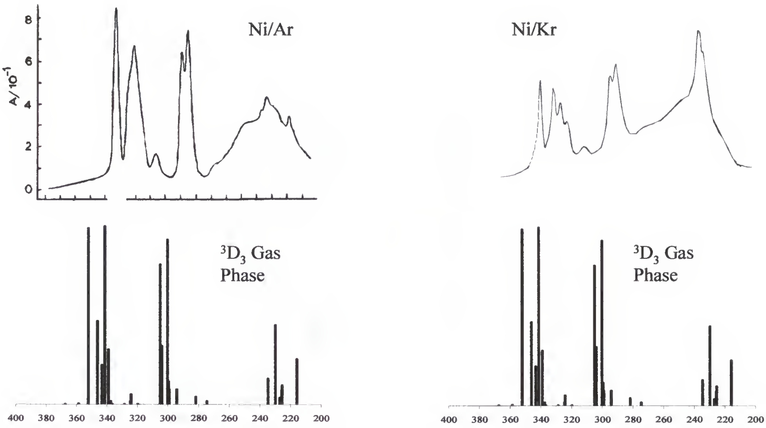

Figure 5-3. The absorption spectrum of Ni(0) atoms matrix-isolated in argon and krypton contrasted with the Ni(0) atomic gas phase UV/Visible absorption spectrum from the $^3D_3$ ground state.

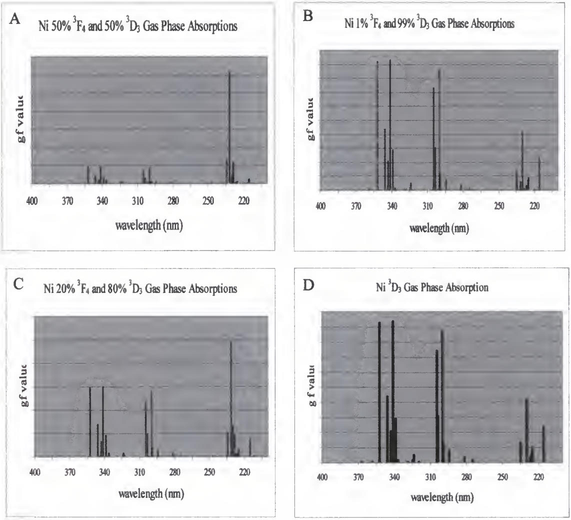

Figure 5-4. Various mixtures of the gas-phase $^3F_4$ Ni(0) ground state transitions with those originating from a $^3D_3$ ground state. A) 50% $^3F_4$ and 50% $^3D_3$. B) 1% $^3F_4$ and 99% $^3D_3$. C) 20% $^3F_4$ and 80% $^3D_3$. D) 100% $^3D_3$.

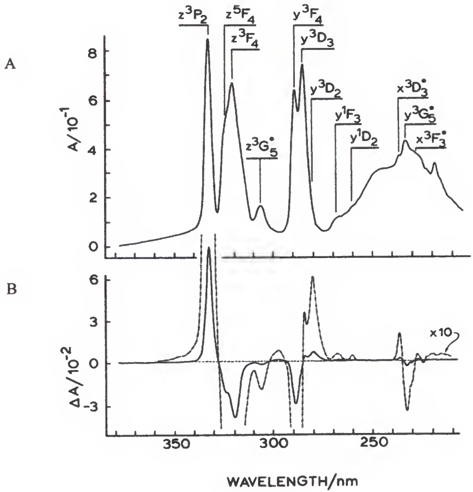

Figure 5-5. Absorption and MCD spectrum of Ni (0) atoms isolated in an argon matrix. A) Absorption spectrum at 4.2 K. States labeled with black dots are assigned to transitions from the $^3F_4$ ground state. B) Magnetic circular dichroism (MCD) spectrum at 4.2 K and 0.29 Tesla. (—) solid line, on scale; (---) dotted line, scale X 10.

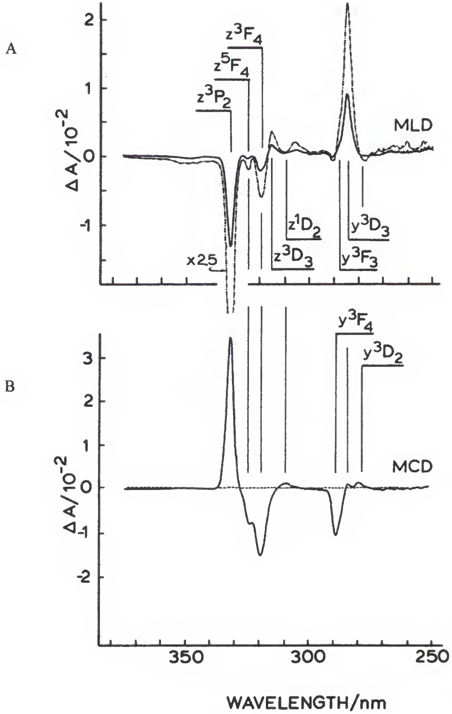

Figure 5-6. Magnetic linear dichroism (MLD) and magnetic circular dichroism (MCD) spectra of Ni(0) atoms isolated in argon matrix. A) MLD spectrum at 4.2 K and 3.0 T (additionally annealed ~ 10 min at 25 K). B) MCD spectrum at 4.2 K and 1.58 T.

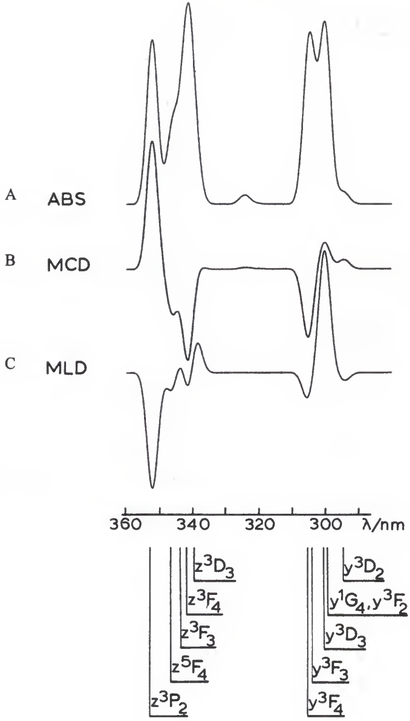

Figure 5-7. Simulated spectra for gas phase Ni(0) with a $^3D_3$ ground state. A) Absorption (ABS). B) MCD. C) MLD. Gaussian bandshapes with 4.0 nm bandwidth were utilized. State assignments are listed beneath the figures.

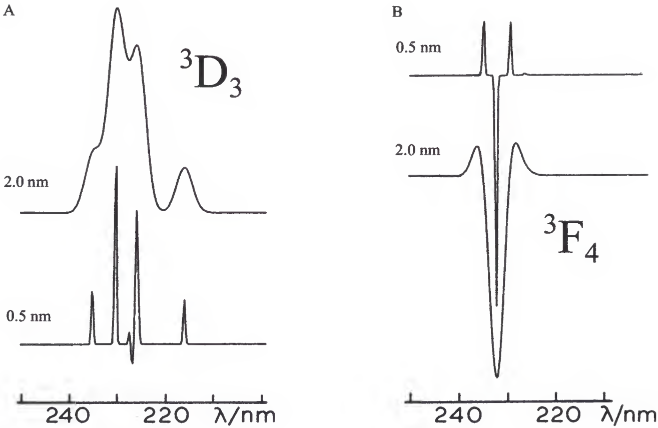

Figure 5-8. Simulated MCD spectra in the ultraviolet region for gas phase Ni(0) atoms. Gaussian band widths utilized are 0.5 nm and 2.0 nm. A) Spectrum for a $^3D_3$ ground state configuration. B) Spectrum for a $^3F_4$ ground state configuration.

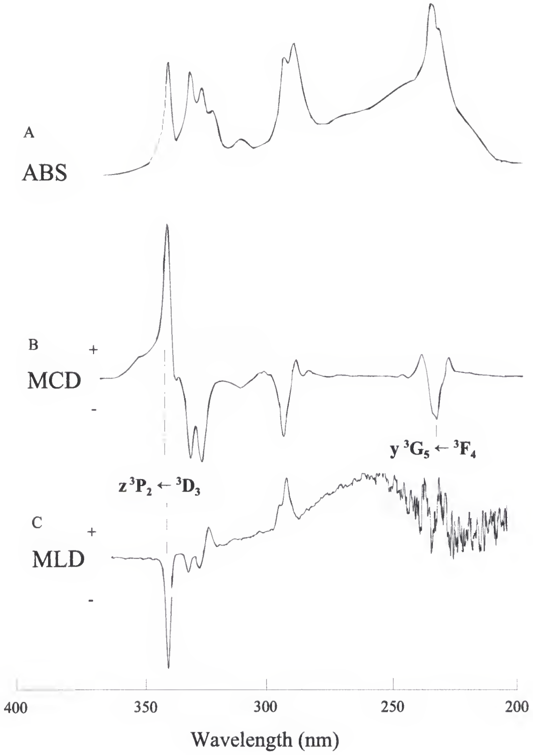

Figure 5-9. Absorption, MCD, and MLD spectra for Ni(0) in Kr with both $^3D_3$ and $^3F_4$ ground states at 4.2 K. A) Absorption (ABS). B) MCD at 1.0 T. C) MLD at 0.6 T. State assignments are indicated for the transitions $z^3P_2 \leftarrow {}^3D_3$ at 338.7 nm and $y^3G_5 \leftarrow {}^3F_4$ at 235.2 nm.

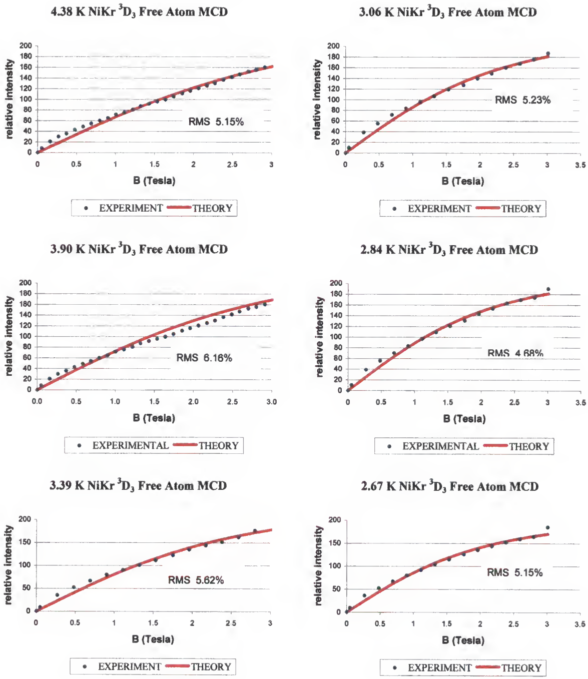

4.38 K NiKr $^3D_3$ Free Atom MCD

3.06 K NiKr $^3D_3$ Free Atom MCD

3.90 K NiKr $^3D_3$ Free Atom MCD

2.84 K NiKr $^3D_3$ Free Atom MCD

3.39 K NiKr $^3D_3$ Free Atom MCD

2.67 K NiKr $^3D_3$ Free Atom MCD

Figure 5-10. Ni(0) atoms in Kr free atom MCD vs. **B** experimental and theoretical plots for $^3D_3$ ground state

2.59 K NiKr $^3D_3$ Free Atom MCD

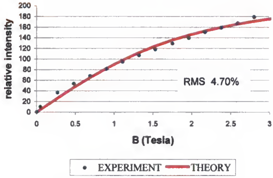

2.33 K NiKr $^3D_3$ Free Atom MCD

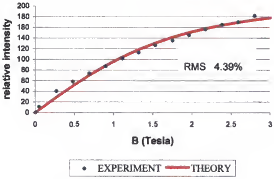

2.48 K NiKr $^3D_3$ Free Atom MCD

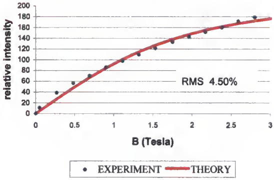

2.30 K NiKr $^3D_3$ Free Atom MCD

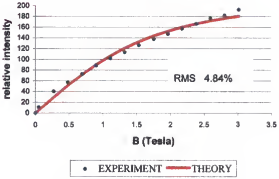

2.41 K NiKr $^3D_3$ Free Atom MCD

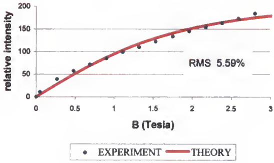

2.26 K NiKr $^3D_3$ Free Atom MCD

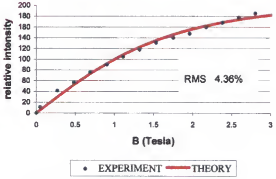

Figure 5-10. (continued)

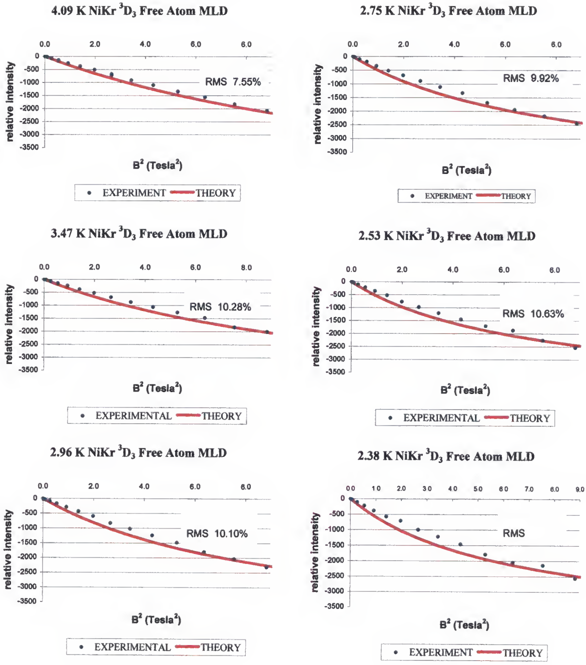

Figure 5-11. Ni(0) atoms in Kr free atom MLD vs. B^2 experimental and theoretical plots for $^3D_3$ ground state.

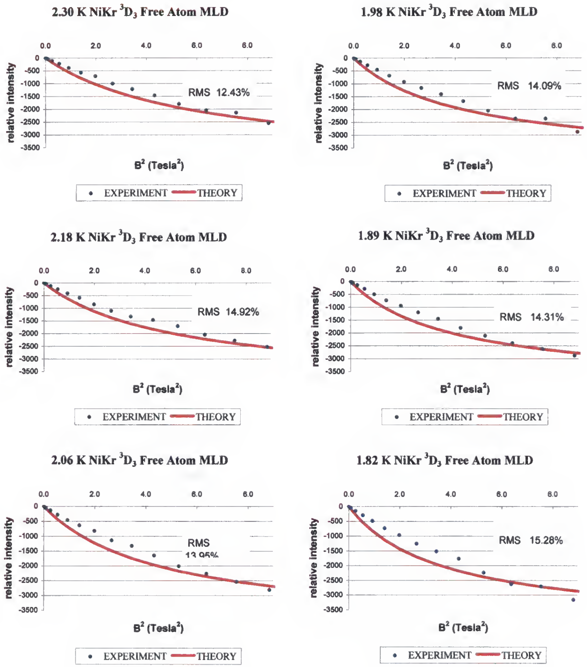

Figure 5-11. (continued)

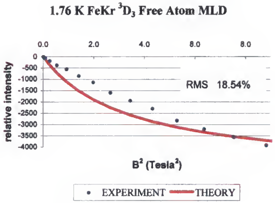

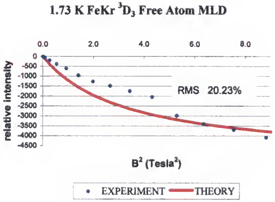

Figure 5-11. (continued)

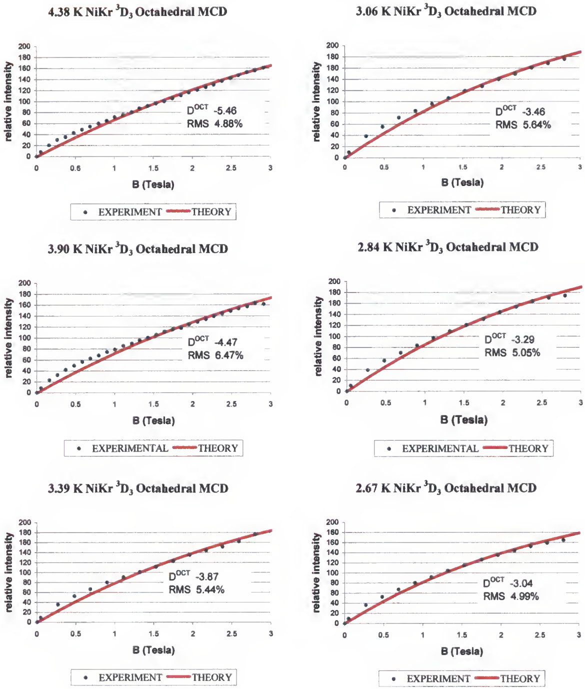

Figure 5-12. Ni(0) atoms in Kr octahedral MCD vs. **B** experimental and theoretical plots for $^3D_3$ ground state

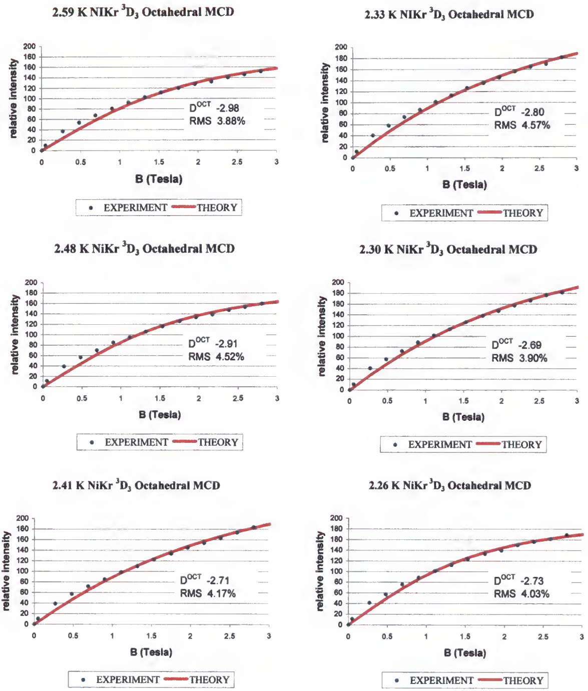

Figure 5-12. (continued)

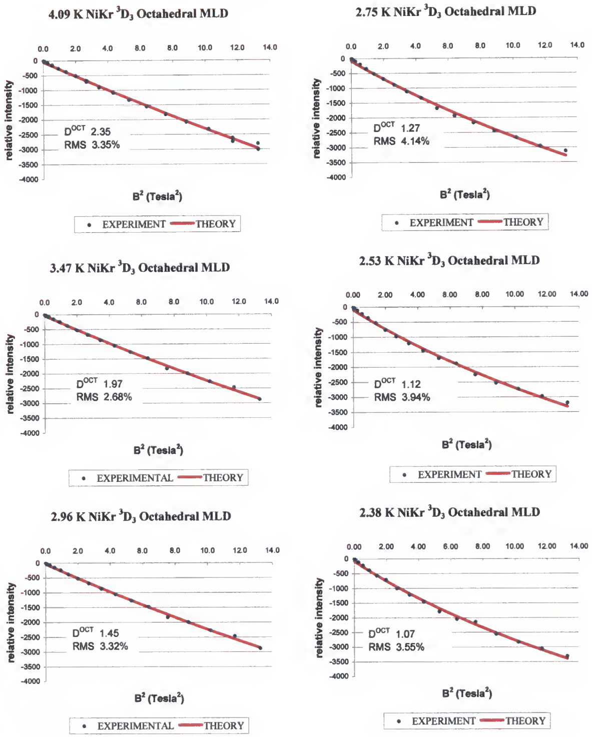

4.09 K NiKr $^3D_3$ Octahedral MLD

2.75 K NiKr $^3D_3$ Octahedral MLD

3.47 K NiKr $^3D_3$ Octahedral MLD

2.53 K NiKr $^3D_3$ Octahedral MLD

2.96 K NiKr $^3D_3$ Octahedral MLD

2.38 K NiKr $^3D_3$ Octahedral MLD

Figure 5-13. Ni(0) atoms in Kr octahedral MLD vs. **B**^{2} experimental and theoretical plots for $^3D_3$ ground state

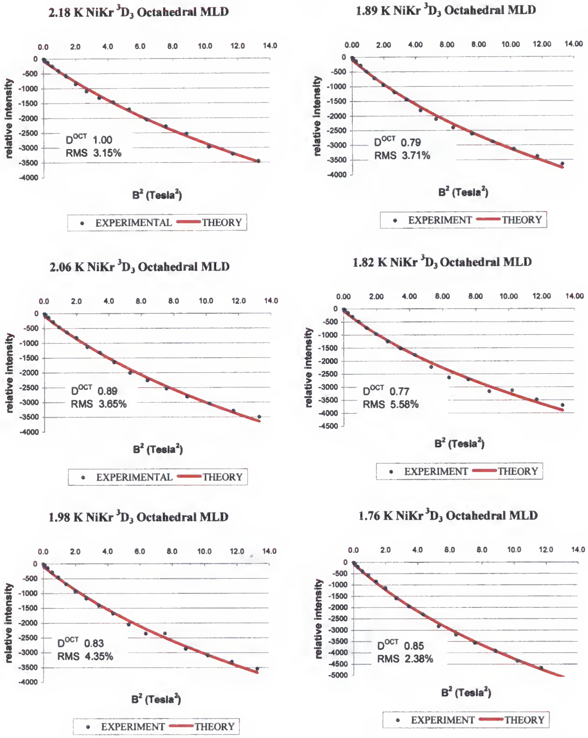

Figure 5-13. (continued)

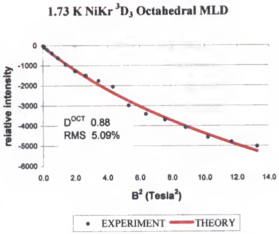

Figure 5-13. (continued)

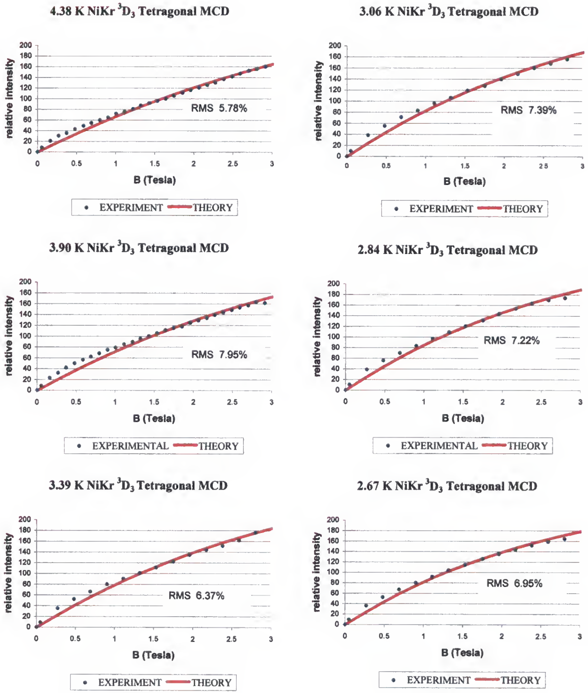

Figure 5-14. Ni(0) atoms in Kr tetragonal MCD vs. B experimental and theoretical plots for $^3D_3$ ground state

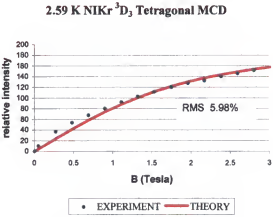

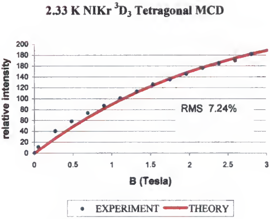

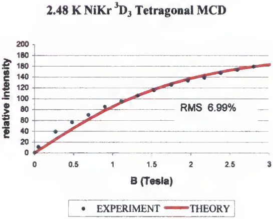

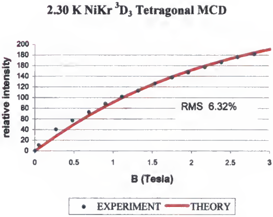

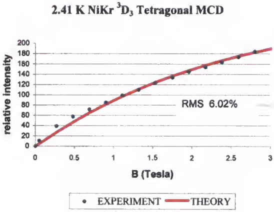

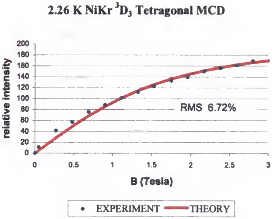

Figure 5-14. (continued)

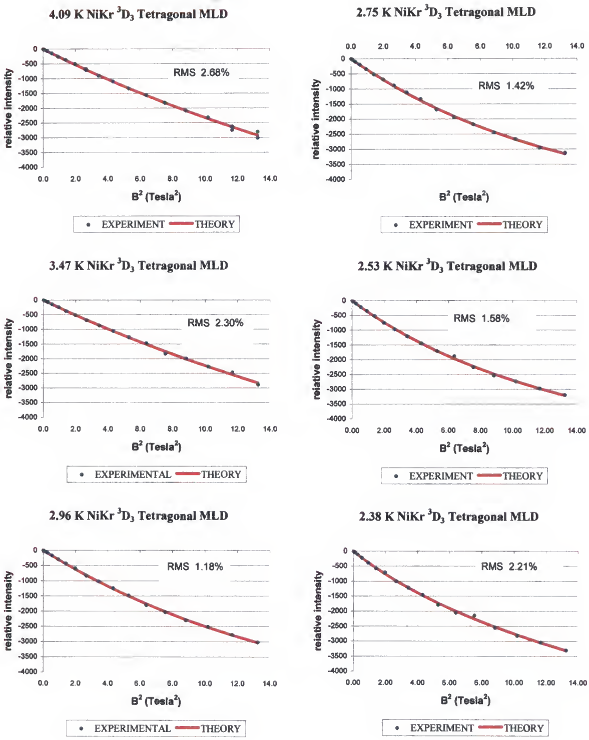

4.09 K NiKr $^3D_3$ Tetragonal MLD

2.75 K NiKr $^3D_3$ Tetragonal MLD

3.47 K NiKr $^3D_3$ Tetragonal MLD

2.53 K NiKr $^3D_3$ Tetragonal MLD

2.96 K NiKr $^3D_3$ Tetragonal MLD

2.38 K NiKr $^3D_3$ Tetragonal MLD

Figure 5-15. Ni(0) atoms in Kr tetragonal MLD vs. $\mathbf{B}^2$ experimental and theoretical plots for $^3D_3$ ground state

2.18 K NiKr $^3D_3$ Tetragonal MLD **1.89 K NiKr $^3D_3$ Tetragonal MLD**

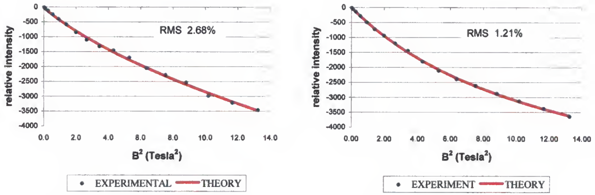

2.06 K NiKr $^3D_3$ Tetragonal MLD **1.82 K NiKr $^3D_3$ Tetragonal MLD**

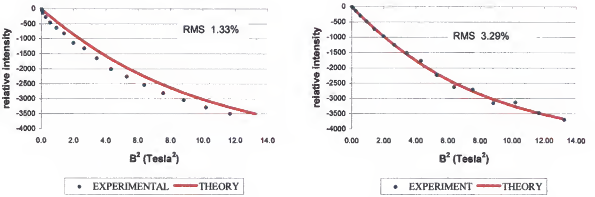

1.98 K NiKr $^3D_3$ Tetragonal MLD **1.76 K NiKr $^3D_3$ Tetragonal MLD**

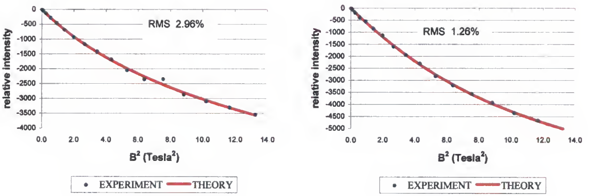

Figure 5-15. (continued)

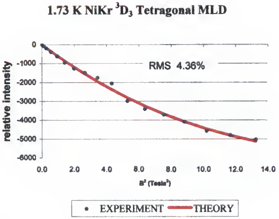

Figure 5-15. (continued)

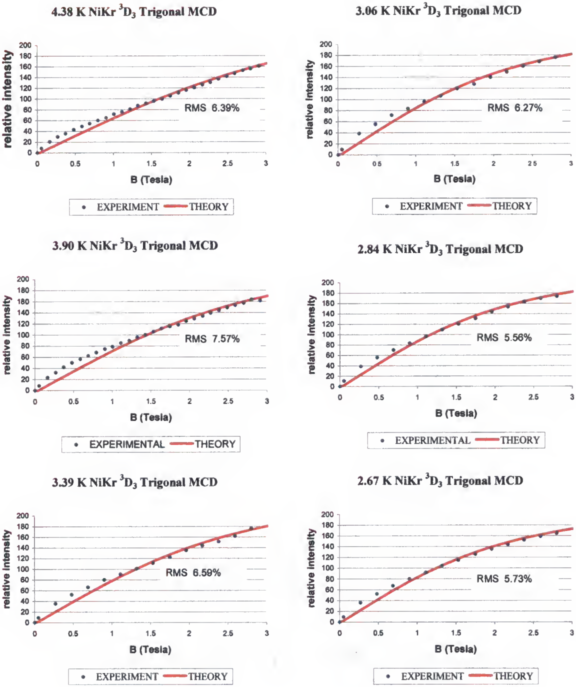

Figure 5-16. Ni(0) atoms in Kr trigonal MCD vs. **B** experimental and theoretical plots for $^3D_3$ ground state

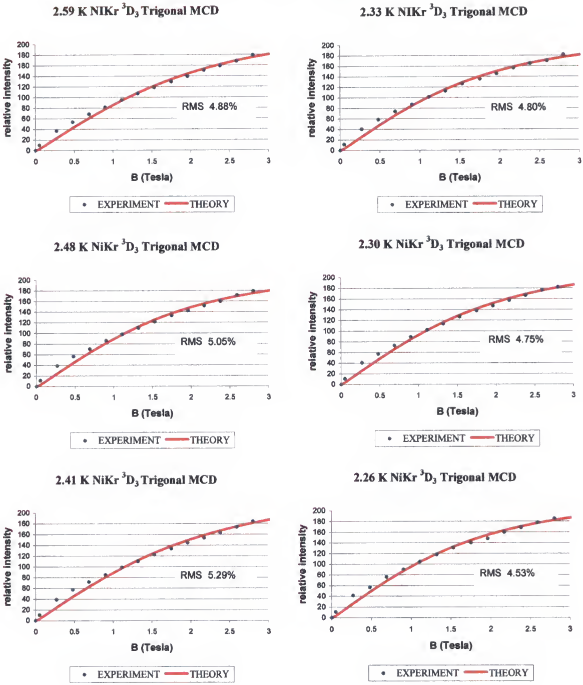

Figure 5-16. (continued)

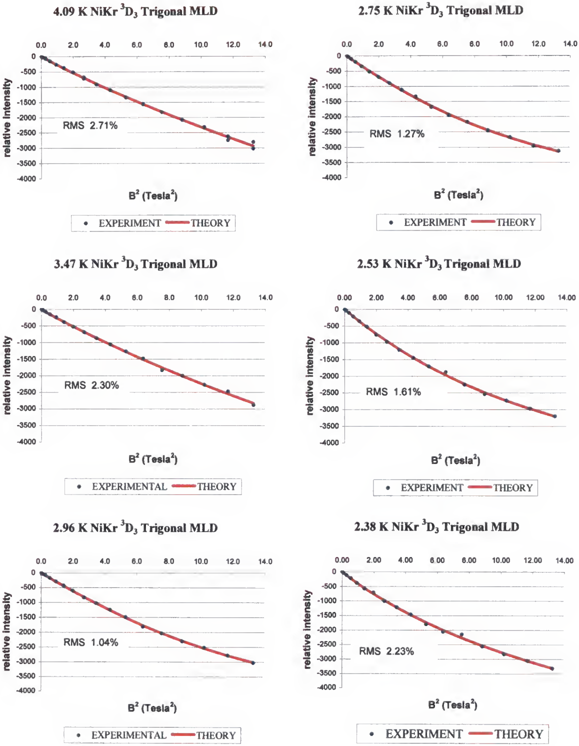

Figure 5-17. Ni(0) atoms in Kr trigonal MLD vs. **B**^{2} experimental and theoretical plots for $^3D_3$ ground state

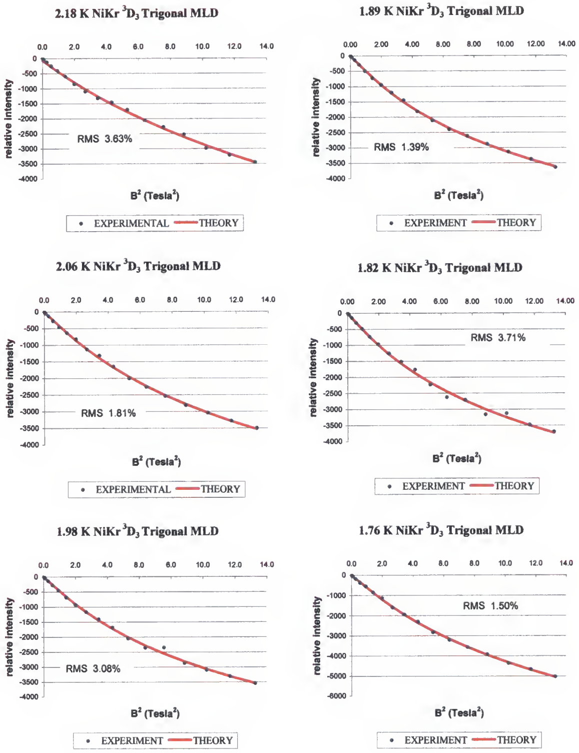

Figure 5-17. (continued)

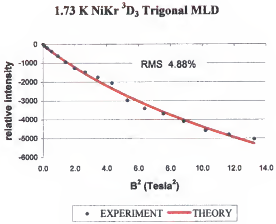

Figure 5-17. (continued)

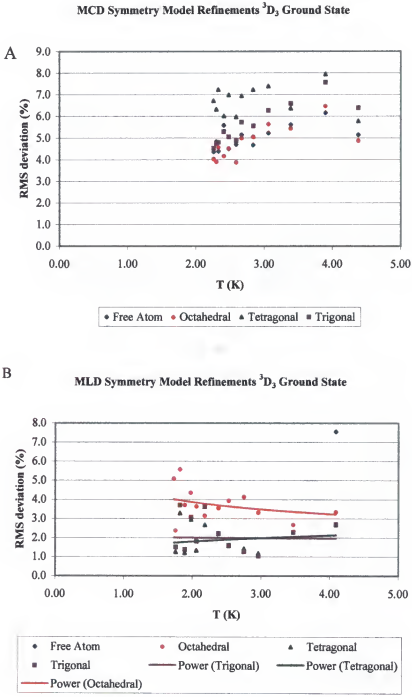

Figure 5-18. RMS deviation values as a function of temperature for all four geometry models for a $^3D_3$ ground state. A) MCD results. B) MLD results. Note that the free atom model illustrates only one data point at 4.09 K, 7.5 % due to the expansion of the scale. The remainder of the free atom data is off scale. Also in B), trendlines are calculated from a power series in Microsoft Excel. They are for visual reference only.

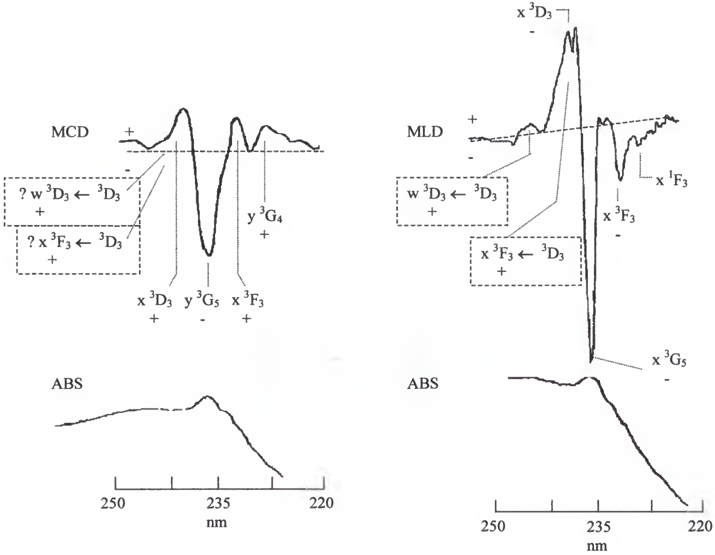

Figure 5-19. Absorption, MCD, and MLD spectra of the principal ultraviolet transitions of Ni(0) atoms in krypton from the $^3F_4$ ground state. A) MCD (upper) and ABS (lower) spectra at 3.64 T and 1.48 K. B) MLD (upper) and ABS (lower) spectra at 2.75 T and 4.00 K. Dashed line is the zero field MCD or MLD. Transitions from a $^3D_3$ ground state are indicated in the dashed box.

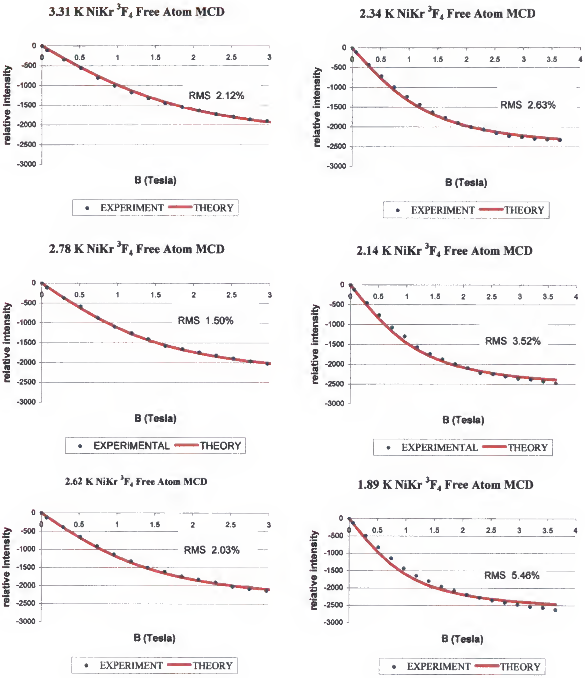

3.31 K NiKr $^3F_4$ Free Atom MCD

2.34 K NiKr $^3F_4$ Free Atom MCD

2.78 K NiKr $^3F_4$ Free Atom MCD

2.14 K NiKr $^3F_4$ Free Atom MCD

2.62 K NiKr $^3F_4$ Free Atom MCD

1.89 K NiKr $^3F_4$ Free Atom MCD

Figure 5-20. Ni(0) atoms in Kr free atom MCD vs. **B** experimental and theoretical plots for $^3F_4$ ground state

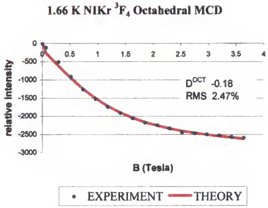

1.66 K NIKr $^3F_4$ Octahedral MCD

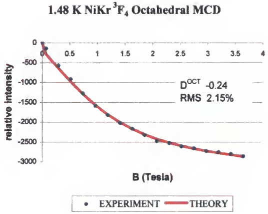

1.48 K NiKr $^3F_4$ Octahedral MCD

Figure 5-20. (continued)

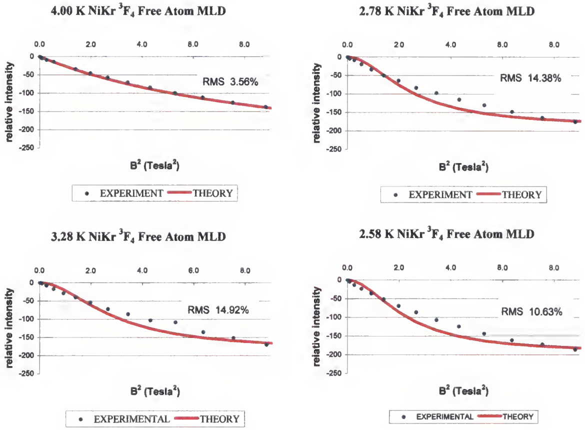

Figure 5-21. Ni(0) atoms in Kr free atom MLD vs. **B**^{2} experimental and theoretical plots for $^3F_4$ ground state

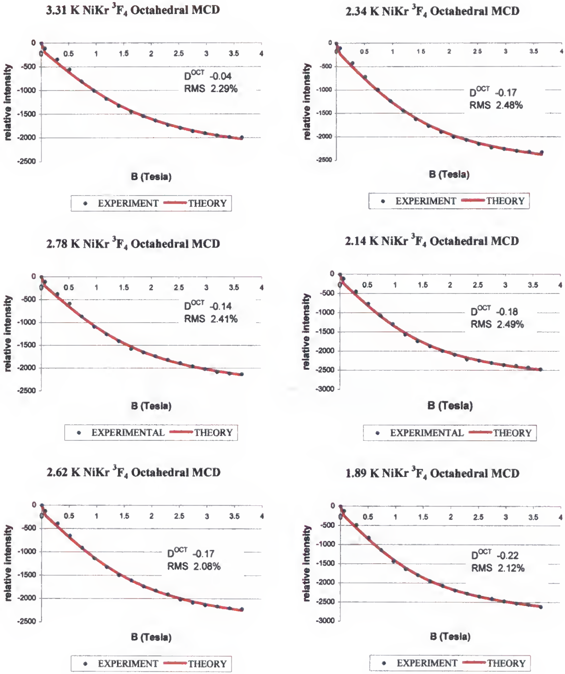

3.31 K NiKr $^3F_4$ Octahedral MCD

2.34 K NiKr $^3F_4$ Octahedral MCD

2.78 K NiKr $^3F_4$ Octahedral MCD

2.14 K NiKr $^3F_4$ Octahedral MCD

2.62 K NiKr $^3F_4$ Octahedral MCD

1.89 K NiKr $^3F_4$ Octahedral MCD

Figure 5-22. Ni(0) atoms in Kr octahedral MCD vs. **B** experimental and theoretical plots for $^3F_4$ ground state

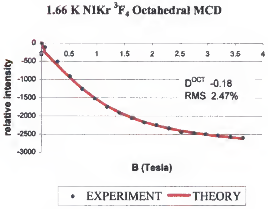

1.66 K NiKr $^3F_4$ Octahedral MCD

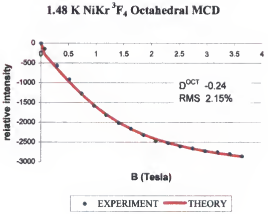

1.48 K NiKr $^3F_4$ Octahedral MCD

Figure 5-22. (continued)

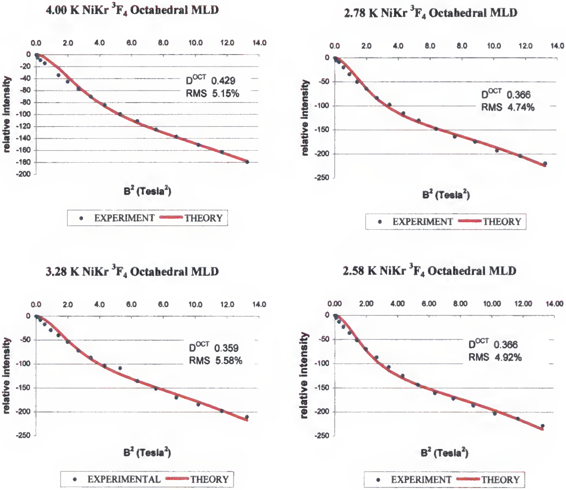

4.00 K NiKr $^3F_4$ Octahedral MLD

2.78 K NiKr $^3F_4$ Octahedral MLD

3.28 K NiKr $^3F_4$ Octahedral MLD

2.58 K NiKr $^3F_4$ Octahedral MLD

Figure 5-23. Ni(0) atoms in Kr octahedral MLD vs. $\mathbf{B}^2$ experimental and theoretical plots for $^3F_4$ ground state

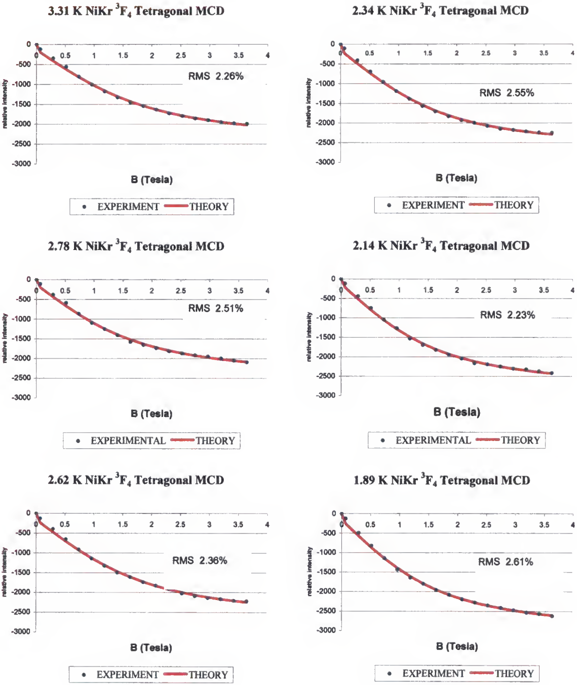

3.31 K NiKr $^3F_4$ Tetragonal MCD

2.34 K NiKr $^3F_4$ Tetragonal MCD

2.78 K NiKr $^3F_4$ Tetragonal MCD

2.14 K NiKr $^3F_4$ Tetragonal MCD

2.62 K NiKr $^3F_4$ Tetragonal MCD

1.89 K NiKr $^3F_4$ Tetragonal MCD

Figure 5-24. Ni(0) atoms in Kr tetragonal MCD vs. **B** experimental and theoretical plots for $^3F_4$ ground state

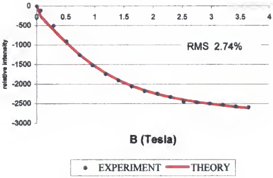
1.66 K NIKr $^3F_4$ Tetragonal MCD

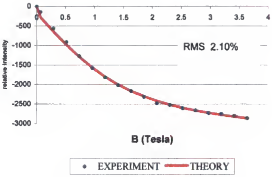
1.48 K NiKr $^3F_4$ Tetragonal MCD

Figure 5-24. (continued)

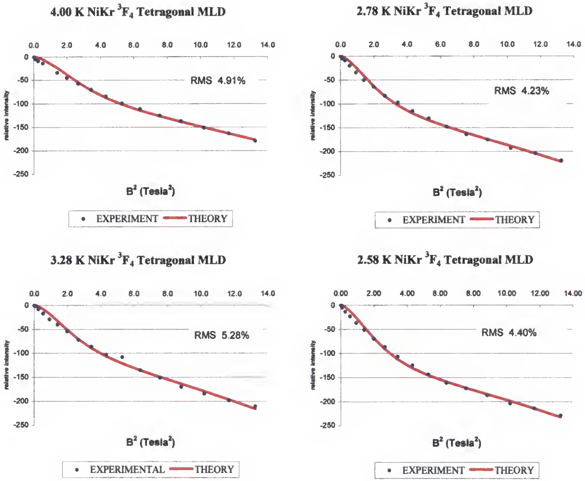

4.00 K NiKr $^3F_4$ Tetragonal MLD

2.78 K NiKr $^3F_4$ Tetragonal MLD

3.28 K NiKr $^3F_4$ Tetragonal MLD

2.58 K NiKr $^3F_4$ Tetragonal MLD

Figure 5-25. Ni(0) atoms in Kr tetragonal MLD vs. $\mathbf{B}^2$ experimental and theoretical plots for $^3F_4$ ground state

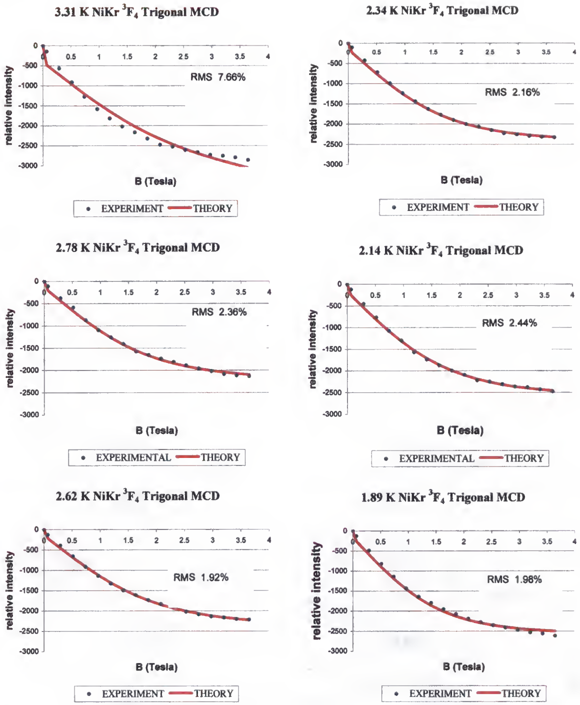

Figure 5-26. Ni(0) atoms in Kr trigonal MCD vs. **B** experimental and theoretical plots for $^3F_4$ ground state

1.66 K NIKr $^3F_4$ Trigonal MCD

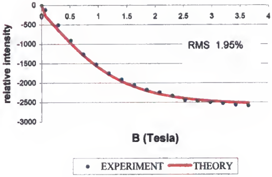

1.48 K NiKr $^3F_4$ Trigonal MCD

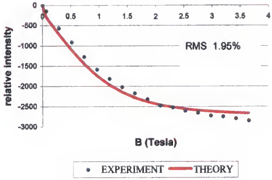

Figure 5-26. (continued)

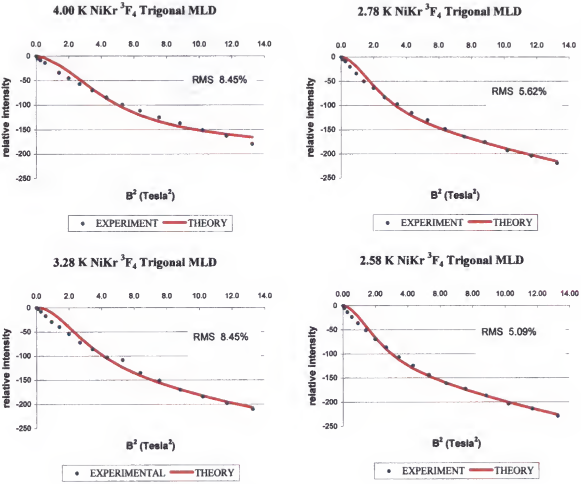

Figure 5-27. Ni(0) atoms in Kr trigonal MLD vs. **B**^{2} experimental and theoretical plots for $^3F_4$ ground state

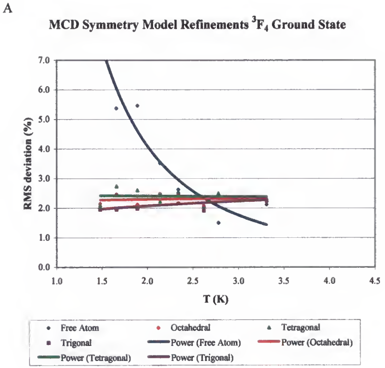

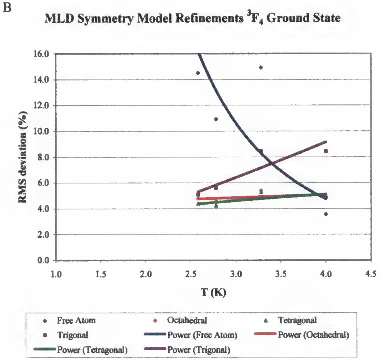

Figure 5-28. RMS deviation values as a function of temperature for all four geometry models for a $^3F_4$ ground state. A) MCD results. B) MLD results. In B, trendlines are drawn calculated from a power series in Microsoft Excel. They are for visual reference only.

CHAPTER 6
CONCLUSIONS

The techniques of magnetic circular dichroism (MCD) and magnetic linear dichroism (MLD) spectroscopy have been successfully applied to low-temperature matrix-isolated systems of Fe(0) and Ni(0) in argon and /or krypton. The absolute assignments of electronic state transitions for zero-valent Fe in solid krypton and Ni atoms isolated in solid argon and krypton at and below liquid He temperature have been determined. The different selection rules applicable to MCD vs. MLD transitions along with differing transition intensities demonstrates the usefulness of sequential MCD/MLD for resolving transitions which may be otherwise unresolved or even unobservable by either of the techniques alone. Additionally, sequential application of the techniques of magnetic circular and magnetic linear dichroism saturation spectroscopy was achieved on these systems. Extension beyond the linear limits of MCD and MLD allows determination of the geometrical site symmetry of the embedded metal atom with high confidence levels.

The measurement of the MLD spectrum of $^5D_4$ Fe(0) in krypton was the first demonstrated application of the MLD technique to matrix-isolated species and corroborated the assignments previously made by MCD spectroscopy. Several previously unobserved bands were detected in the MLD spectrum and assigned accordingly (Figure 6-1 A). The MLD technique was then applied to Ni(0) atoms isolated in an argon matrix to aid in the controversial assignment of the electronic absorptions thought to be attributable to two different isolable ground state configurations of Ni(0) in rare gas matrices. These energy states are ~205 cm^{-1} apart in the gas phase: the normal low energy $^3F_4$ and the higher energy $^3D_3$. The electronic assignments of transitions from these states were assigned unambiguously by applying the selection rules of the sequential MCD and MLD technique. Thus, the validity of the dual ground state hypothesis (Figure 6-1 B) is established.

The experimental technique within the linear limit region of MCD and MLD involved low magnetic fields (~0.5 Tesla) and temperatures above liquid He temp (12-30 Kelvin). Extension to the non-linear regime of MCD/MLD saturation spectroscopy (magnetic field to 4 Tesla and temperatures to ~1.5 Kelvin) provided excellent data for establishing the site symmetries of the solute atoms in the Kr matrices with high confidence for the single Fe(0) site and the dual Ni(0) sites.

Extensive theoretical development to apply the analyses to symmetry point groups lower than pseudo-isotropic was accomplished. FORTRAN and C++ software was written to calculate the theoretical MCD/MLD absorptions at various symmetries. Refinement of the theoretical fit to the experimental data yields both the actual site symmetry and the extent of splitting attributable to the crystal field effect resulting from the symmetry. The unexpected appearance of a temperature dependent crystal field splitting is seen and explained relative to unit cell contraction of the Kr matrix cage on cooling below liquid He temperature.

Figure 6-2 depicts the very slight octahedral geometry ("near" free atom) found to exist in the vicinity of liquid helium temperature (4.2 K) for Fe(0) atoms in solid krypton. The crystal field separation energy, ΔE_{CF}, in this temperature region is approximately 1 –

3 cm^{-1}. As the matrix temperature is cooled further to superfluid-helium state, there is an unexpected increase in ΔE_{CF}, representing an increase in the octahedral crystal field parameter, D^{OCT}. This parameter indicates the extent of distortion exerted on the Fe(0) atom's outer atomic energy levels under an octahedral symmetry model by the Kr lattice atoms.

Consideration of lower symmetry models indicates a better correlation with a tetragonal symmetry environment at and below approximately 3.5 K, with energies ranging from ~ 3 cm-1 up to ~16 cm^{-1} as the temperature decreases. The crystal field parameters F_1^{TET}, F_2^{TET}, and B^{TET} remain low, ranging from ~ -0.4 – + 0.5 cm^{-1}. They are somewhat fluxional, probably due more to experimental uncertainty than any difficulty in the theoretical model.

The dual nature of the Ni(0) atomic ground states in krypton presents as isolable $^3F_4$ and $^3D_3$ ground state configurations. Investigation of the nature of the site geometry associated with each ground state was performed by examining the behavior of specific ultraviolet and visible energy transitions occurring from each ground state using the newly-developed MCD/MLD saturation spectroscopic methods. The intensity and bandshape of these transitions, the y $^3G_5 \leftarrow {}^3F_4$ at 235.2 nm and the z $^3P_2 \leftarrow {}^3D_3$ at 338.7 nm, were recorded over the temperature ranges of 4.0 – 1.5 K and 4.4 – 1.7 K, respectively. The magnetic field was varied from 0 to 3.64 T.

The site symmetry of the $^3F_4$ ground state Ni(0) atoms isolated in krypton is determined to be similar in nature to the Fe(0)/Kr system, existing in a "near" free-atom environment exhibiting a very slight octahedral symmetry distortion on the $^3F_4$ Ni(0) atomic energy levels at and near liquid helium temperature (Figure 6-3) . The crystal field energy at these temperatures is derived as ~ 2 cm^{-1} for the MCD data and ~ 23 cm^{-1} for the MLD data. The MLD results are considered less reliable as a consequence of contamination by the underlying x $^3F_3 \leftarrow {}^3D_3$ transition relative to the MCD results. At a temperature near 2.8 – 2.5 K the site geometry distorts to lower trigonal symmetry, exhibiting a crystal field energy at approximately 6 cm^{-1} which increases steadily to approximately 11 cm^{-1} at 1.48 K.

The stabilization of the $^3D_3$ Ni(0) atomic ground state relative to the $^3F_4$ ground state is reflected in a distinct tetragonal site symmetry at and near liquid helium temperature which distorts to trigonal symmetry in the vicinity of 3 K and below (Figure 6-4). The crystal field separation energy ranges from approximately 24 – 38 cm^{-1}.

The presence of a slight octahedral distortion for both Fe(0) and Ni(0) atoms in their normal gas-phase ground state configurations when isolated in solid Kr is indicative of little interaction with the surrounding Kr lattice. Whether the site is substitutional or interstitial in nature cannot be determined from this data. Disruption of the face-centered cubic structure of the krypton lattice is probable in the instances of noncubic symmetry environments for the Fe(0) and Ni(0) atoms. Since the covalent radii of both Fe(0) and Ni(0) atoms from X-ray analysis of the bulk metal are less than the void created by removing a single Kr atom, axial distortion of the Kr lattice cage in the vicinity of the zero-valent metal atoms is not an unreasonable expectation.

Sequentially-applied MCD and MLD spectroscopy has been demonstrated to be definitive in aiding the absolute assignment of electronic state transitions for Fe(0) and Ni(0) atoms isolated in solid rare-gas matrices. Extension of this technique to other metal atoms, and especially to metal ions, clusters, and cluster ions isolated in rare-gas matrices is practical and should provide new details about the electronic structure of these species. Further application of the methods of sequential MCD/MLD saturation spectroscopy enables an understanding of the interactions of the outer atomic electronic levels of Ni(0) and Fe(0) with the surrounding Kr substrate. Utilizing this technique to analyze the interactions of other isolated atoms, clusters, and ions with a variety of substrates has the potential for providing of wealth of information regarding the basic science underlying impurities doped in crystalline solids, and may prove have a practical application in the semiconductor industry.

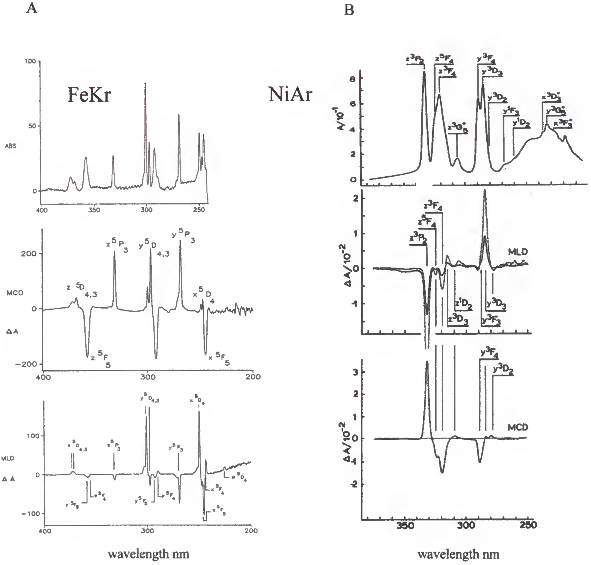

Figure 6-1. Absorption (ABS), MCD, and MLD spectra of Fe(0) and Ni(0) isolated in solid krypton. A) Fe(0) in Kr. B) Ni(0) in Kr. In B), states marked with a dot (•) originate from the $^3F_4$ ground state. All others are from the $^3D_3$ ground state.

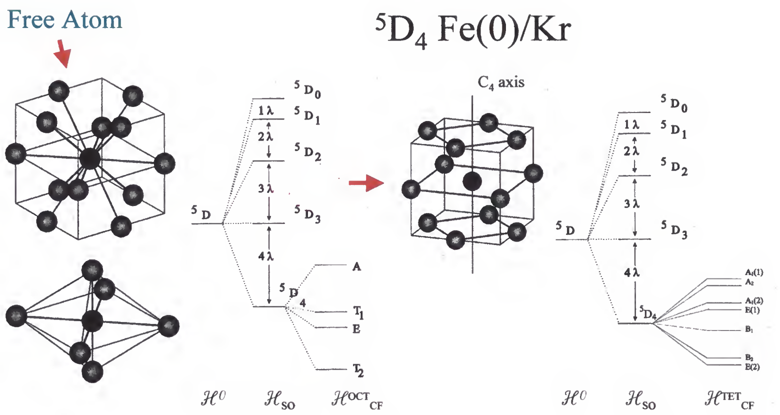

Figure 6-2. Site symmetry configuration of $^5D_4$ ground state Fe(0) atoms matrix-isolated in solid krypton at 4.20 – 1.48 K. The symmetry at near liquid He temperature is 'near' free atom, being slightly perturbed octahedrally. On further cooling, the symmetry environment collapses to tetragonal symmetry.

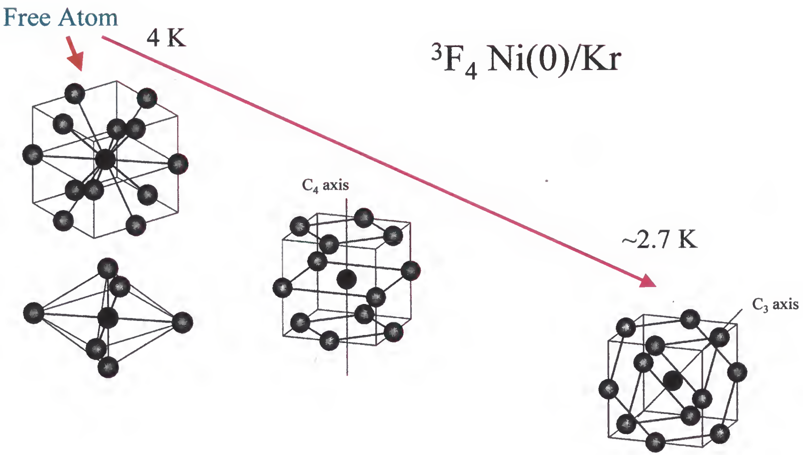

Figure 6-3. Site symmetry configuration of $^3F_4$ ground state Ni(0) atoms matrix-isolated in solid krypton at 4.00 – 1.48 K. The symmetry at near liquid He temperature is ‘near’ free atom, being slightly perturbed octahedrally or tetragonally. On further cooling to ~2.7 K, the symmetry environment collapses to trigonal symmetry.

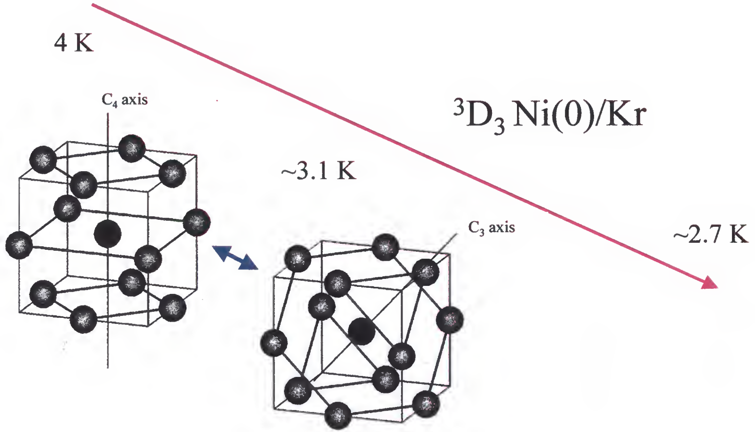

Figure 6-4. Site symmetry configuration of $^3D_3$ ground state Ni(0) atoms matrix-isolated in solid krypton at 4.38 – 1.73 K. The symmetry at near liquid He temperature distinctly tetragonal, collapsing to trigonal symmetry on further cooling below ~3.1 K.

APPENDIX
MATHEMATICAL MODELING SOFTWARE IN C^{++}

```
//PROGRAM orave.cpp
//
//Karen L.Jensen  Sep 07 2002        0852
//
//Translated into C++ from FORTRAN77/VS2 source code originally written in 1993. Original author
//of base code was Robert Pellow in 1990 with additional extensions by Bryce Williamson.
//Extensive routines were added in this version to enable modeling of randomly oriented
//'supermolecules' via Euler transformation of the MCD and MLD equations.
//Several routines from Numerical Recipes in C++ are utilized [William H. Press, Saul A. Teukolsky,
//William T. Vetterling, and Brian P. Flannery, "Numerical Recipes in C++", Second Edition, Cambridge
//University Press, Cambridge (2002).] The source code is not included in the following code list as it
//copyrighted material. The Numerical Recipes routines utilized are: powell.cpp, jacobi.cpp, brent.cpp,
//f1dim.cpp, linmin.cpp, and mnbrak.cpp. Additionally, several data types created by the Numerical
//Recipes authors have been utilized ... specifically the vector and matrix data type definitions defined by
//the nr.h header file [also not listed].
//
//
//Contrary to C++ convention, I am retaining the variable names in uppercase letters to be compatible
//with the FORTRAN 77/VS2 software version of this program.
//
//This code list is setup for minimization of an MLD data set for Ni(0) atoms in a ³D₃ ground state
//configuration using octahedral symmetry.
//

#include <iostream>
#include <fstream>
#include <cstdio>
#include <iomanip>
#include <cstdlib>
#include <cstring>
#include <cctype>
#include <cmath>
#include <ctime>
#include "nr.h"
using namespace std;

//Function prototype
DP func(Vec_I_DP &p);

void zeeman(const int JI,const int JF,Vec_IO_DP &TPZMAN,Vec_IO_DP &TMZMAN,Vec_IO_DP
&TZZMAN,
                        Vec_IO_DP &TJMP,Vec_IO_DP &TJMM,Vec_IO_DP &TJMZ,
                        Vec_IO_DP &TJMP2,Vec_IO_DP &TJMM2,Vec_IO_DP &TJMZ2);

void NR::powell(Vec_IO_DP &p, Mat_IO_DP &xi, const DP ftol, int &iter,
        DP &fret, DP func(Vec_I_DP &));
```

```
void crysteig(int jinit,char *geom[13],Mat_I_DP &BASIS,Vec_IO_DP &CFE,Vec_I_DP
&Pparm);//prototype for crystal field energy calcs

void NR::jacobi(Mat_IO_DP &a, Vec_O_DP &d, Mat_O_DP &v, int &nrot);
double power(double x, int n);
void scalem(Vec_DP &exmcd,Vec_DP &exmld,Vec_DP &thmcd,Vec_DP &thmld,double &sumc,double
&suml,const int nexmcd, const int nexmld, char *runStat[4]);

//Global variables

        //Fundamental variable declarations and initializations
        //'also in 'filedata.inp'

        int i,j,bufCoeff(9),NDIM(3),cycle(0);
        const int bufSize1(9),bufSize2(500),bufSize3(60);
        const double pi(3.14159265358979);

        int JI(0),JF(0), CRYSTAL(0),NEXmcd(0),NEXmld(0),NEXmax(0),ITER(0.);
        int NSC1(0),NSC2(0),NSC3(0),NSC4(0),NSL1(0),NSL2(0),NSL3(0),NSL4(0);
        int IDG(0),NFLAG(0),NXTAL(0),INDEX(0),THEITV(0),qv(0),Pinc(0);
        long t0,t1;

        double G(0.),FTOL(0.),FRET(0.),THEINC(0),ttotal(0.),Pinit(1.),Pintvl(0.);

        Vec_DP P3d(1.,NDIM);//change P tp P3d for 3d case
        Vec_DP P1d(1.,1);//create P1d for 1d case

        char caseType,tempStr[20];
        char *MCDDATA[bufSize3],*MLDDATA[bufSize3],*runStat[4];
        char
*COEFF[bufSize3],*COEFFFAT[bufSize3],*COEFFOCT[bufSize3],*COEFFTRI[bufSize3],
*geom[bufSize3];
        char
*FLSTR1[bufSize3],*FLSTR2[bufSize3],*FLSTR3[bufSize3],*FLSTR4[bufSize3],*FLSTR5[bufSize3],*I
D[5],*rmsState[4];

        // Open file for initial parameter input
        // ID: MCD,MLD, or Both. Type in the option as given to the left.. mixed,lower or uppercase.
        // JI: Initial J state.    JF: Final J state. COEFF: Basis eigenvectors for geometry.
        // geom: Crystal field geometry-- FREE ATOM, OCTAHEDRAL, tetragonal,OR TRIGONAL.
        // FLSTR1: standard hard-copy output file. FLSTR2: theorectical MCD outputfile.
        // FLSTR3: Theoretical MLD output file.    FLSTR4: P parameter/ RMS output file.
        // MCDDATA: Experimental MCD data. MLDDATA: Experimental MLD data. G: Lande G
factor.
        // THEITV: No.of theta increments over 0 to 2 pi [ie,interval THEINC is (2pi-0)/THEITV].
        // P[0],P[1],P[2]: Starting point for Direction Set Method minimization via Powell's method.
        // reference Chapter 10 Numerical Recipes in C++. P[] is a 'guess' ( 1,0,0 for 1D octahedral,
        // 1,1,1 for 3D tetragonal or trigonal).  FTOL: tolerance level for minimization thru Powell.
        // No less than SQRT of computer's double float limit of error (typically 1e-08 for double
        // precision roundoff error limit of 1e-16). See NR, Chapters 2 and 10.
        //

        double THETA(0.),THETA1(0.),THETA2(pi/2),SCN=0.0,SCD=0.0;

        //MCD specific
        double SCALMC(0.),EXMAXMCD(0.),SIGMAMCD(0.),DTEMCD(0.);
        double SCALEMCD=0.0,SMMCD=0.0,FRETNORMMCD=0.0;

        Vec_DP SIGMCD(0.,bufSize2),DELTAMCD(0.,bufSize2);
        Vec_DP
TC(0.,bufSize2),BFC(0.,bufSize2),EXMCD(0.,bufSize2),THMCD(0.,bufSize2),THnormMCD(0.,bufSize2
),THSCMCD(0.,bufSize2);

        //MLD specific
        double SCALML(0.),EXMAXMLD(0.),SIGMAMLD(0.),DTEMLD(0.);
        double SCALEMLD=0.0,SMMLD=0.0,FRETNORMMLD=0.0;

        Vec_DP SIGMLD(0.,bufSize2),DELTAMLD(0.,bufSize2);
        Vec_DP
TL(0.,bufSize2),BFL(0.,bufSize2),EXMLD(0.,bufSize2),THMLD(0.,bufSize2),THnormMLD(0.,bufSize2),
THSCMLD(0.,bufSize2);

        //Common to MCD and/or MLD
        Vec_DP D(0.,bufSize1),CFE(0.,bufSize1);
        Vec_DP TPZMAN(0.,bufSize1),TMZMAN(0.,bufSize1),TZZMAN(0.,bufSize1);
        Vec_DP TJMP(0.,bufSize1),TJMM(0.,bufSize1),TJMZ(0.,bufSize1);
        Vec_DP TJMP2(0.,bufSize1),TJMM2(0.,bufSize1),TJMZ2(0.,bufSize1);

        Mat_DP A(0.,bufSize1,bufSize1), Basis(0.,bufCoeff,bufCoeff),C(0.,bufSize1,bufSize1);
        Mat_DP  V(0.,bufSize1,bufSize1),XI(0.,NDIM,NDIM), TH(0.,100),Pcalc(0.,NDIM);
        Mat3D_DP ZEEMAN(bufSize1,bufSize1,1001);        //This zeeman matrix will need to be
expanded to 100001 !!

int main()

{
        t0=time(0);
        time_t t0Str;
        time (&t0Str);
        clock_t start,finish;
        start=clock();
        cout<<"Start time: "<<t0<<" seconds."<<endl<<endl;
        cout<<ctime(&t0Str)<<endl<<endl<<endl;

        ifstream datainput;

/*      datainput.open ("filedata.inp",ios::in);
        if (!datainput)
        {
                cerr <<"File "<<datainput<<" could not be opened.\n";
                        exit(1);
        }

//      datainput
>>*ID>>JI>>JF>>*geom>>*COEFFOCT>>*COEFFTRI>>*FLSTR1>>*FLSTR2>>*FLSTR3
//
>>*FLSTR4>>*MCDDATA>>*MLDDATA>>G>>THEITV>>P[0]>>P[1]>>P[2]>>FTOL;
        datainput.close();

        // End initial parameter input
```

```
*/
        *ID="mld",JI=4,JF=5,*geom="octahedral",*COEFFFAT="d:/nikr3f4/3f4_data/coefffat.for",*CO
EFFOCT="d:/nikr3f4/3f4_data/COEFF4D4.txt";
        *COEFFTRI="d:/nikr3f4/3f4_data/COEFF4D3.txt",*FLSTR1="d:/nikr3f4/3f4_data/oct/nikr3d3o
ct400mldscl1.0001.out";
        *FLSTR2="d:/nikr3f4/3f4_data/oct/nikr3d3theooct400mldscl1.0001.mcd",*FLSTR3="d:/nikr3f4/
3f4_data/oct/nikr3d3theooct400mldscl1.0001.mld";
        *FLSTR4="d:/nikr3f4/3f4_data/oct/nikr3d3oct400mldscl1.0001.rms",*FLSTR5="d:/nikr/3D3_dat
a/oct/nikr3d3oct400mldscl1.0001.Prms";
        *MCDDATA="d:/nikr3f4/3f4_data/nikr3f4mcdmagscl1.214.dat",*MLDDATA="d:/nikr3f4/3f4_d
ata/nikr3f4mldmagscl1.400.dat",G=1.33,THEITV=1;
        P3d[0]=0.05,P3d[1]=0.05,P3d[2]=0.05,FTOL=0.0001,*COEFF="COEFF",*rmsState="off",Pinit=
.30,Pinc=120,Pintvl=.005,*runStat="off";

/*
        *ID="mcd",JI=3,JF=2,*geom="tetragonal",*COEFFFAT="d:/nikr3d3/3d3_data/coefffat.for",*CO
EFFOCT="d:/nikr3d3/3d3_data/COEFF3D4.txt";
        *COEFFTRI="d:/nikr3d3/3d3_data/COEFF3D3.txt",*FLSTR1="d:/nikr3d3/3d3_data/magnetizati
on/tet/nikr3d3tet226mcd.0250.out";
        *FLSTR2="d:/nikr3d3/3d3_data/magnetization/tet/nikr3d3tet226mcd.0250.mcd",*FLSTR3="d:/ni
kr3d3/3d3_data/magnetization/tet/nikr3d3tet226mcd.0250.mld";
        *FLSTR4="d:/nikr3d3/3d3_data/magnetization/tet/nikr3d3tet226mcd.0250.rms",*FLSTR5="d:/ni
kr/3D3_data/magnetization/tet/nikr3d3tet226mcd.0250.Prms";
        *MCDDATA="d:/nikr3d3/3d3_data/nikr3d3mcdmag.226.dat",*MLDDATA="d:/nikr3d3/3d3_dat
a/nikr3d3mldmag.409.dat",G=1.33,THEITV=250;
        P3d[0]=0.05,P3d[1]=0.05,P3d[2]=0.05,FTOL=0.0001,*COEFF="COEFF",*rmsState="off",Pinit=
.30,Pinc=120,Pintvl=.005,*runStat="off";
*/

//      FLSTR5="testout.dat";
//      FLSTR5+=ctime(&t0Str);
//      FLSTR5+=".";
//      FLSTR5+=_itoa(t0,tempStr,10);

//      cout<<"FLSTR5= "<<FLSTR5<<endl<<endl;

/*      cout<<"\nInput number of theta intervals to process: ";
        cin>>THEITV;
        cout<<endl<<endl;
*/
        if (_strnicmp(*ID,"MCD",5)==0) caseType='C';
        if (_strnicmp(*ID,"MLD",5)==0) caseType='L';
        if (_strnicmp(*ID,"BOTH",5)==0) caseType='B';

        THEINC=(THETA2-THETA1)/THEITV;

        if (_strnicmp(*geom,"octahedral",13)==0)
        {
                P1d[0]=P3d[0];
                NDIM=1;
                cout<<"P1d0= "<<P1d[0]<<endl;
        }

        else cout<<"P3d0= "<<P3d[0]<<"P3d1= "<<P3d[1]<<"P3d2= "<<P3d[2]<<endl;
```

```
// Declare input and output files. Open files for output.

        fstream  infileMCD,infileMLD,infileCOEFF,inTestMCD,inTestMLD;

        ofstream outfile01 (*FLSTR1,ios::out);
        ofstream outfile02 (*FLSTR2,ios::out);
        ofstream outfile03 (*FLSTR3,ios::out);
        ofstream outfile04 (*FLSTR4,ios::out);
        ofstream outfile05 (*FLSTR5,ios::out);

//Write pertinent information to output text file

        outfile01<<"Start time: "<<t0<<" seconds."<<endl<<endl;
        outfile01<<ctime(&t0Str)<<endl<<endl;
        outfile02<<ctime(&t0Str)<<endl<<endl;
        outfile03<<ctime(&t0Str)<<endl<<endl;
        outfile04<<ctime(&t0Str)<<endl<<endl;
        outfile05<<ctime(&t0Str)<<endl<<endl;

        outfile01<<*MCDDATA<<setw(20)<<*MLDDATA<<endl<<endl;
        outfile02<<*MCDDATA<<setw(20)<<*MLDDATA<<endl<<endl;
        outfile03<<*MCDDATA<<setw(20)<<*MLDDATA<<endl<<endl;
        outfile04<<*MCDDATA<<setw(20)<<*MLDDATA<<endl<<endl;
        outfile05<<*MCDDATA<<setw(20)<<*MLDDATA<<endl<<endl;

        outfile01 <<"\nMCD/MLD CRYSTAL FIELD ITERATION ROUTINE --
"<<setw(15)<<*MCDDATA<<setw(15)<<*MLDDATA<<endl
                              <<"MCD/MLD PROGRAM orave.cpp ORIENTATIONAL AVERAGING
ROUTINE\n\n"<<endl;

        cout << "Data input parameters from file 'filedata.inp'"
                << "\n\nID = "<<*ID<< "\nJI = "<<JI<<"\nJF = "<<JF<<"\ngeom = "<<*geom
                <<"\nCOEFFOCT = "<<*COEFFOCT<<"\nCOEFFTRI =
"<<*COEFFTRI<<"\nFLSTR1 = "<<*FLSTR1
                <<"\nFLSTR2 = "<<*FLSTR2<<"\nFLSTR3 = "<<*FLSTR3<<"\nFLSTR4 =
"<<*FLSTR4
                <<"\nMCDDATA = "<<*MCDDATA<<"\nMLDDATA = "<<*MLDDATA<<"\nG =
"<<G<<"\nTHEITV = "<<THEITV;
        if (_strnicmp(*geom,"octahedral",13)==0)
                cout<<"\nP1d[0] = "<<P1d[0]<<endl<<endl;
        else
                cout<<"\nP3d[1] = "<<P3d[0]<<"\nP3d[2] = "<<P3d[1]<<"\nP3d[3] =
"<<P3d[2]<<"\nFTOL = "<<FTOL<<endl<<endl;

        outfile01 << "Data input parameters from file 'filedata.inp'"
                << "\n\nID = "<<*ID<< "\nJI = "<<JI<<"\nJF = "<<JF<<"\ngeom = "<<*geom
                <<"\nCOEFFOCT = "<<*COEFFOCT<<"\nCOEFFTRI =
"<<*COEFFTRI<<"\nFLSTR1 = "<<*FLSTR1
                <<"\nFLSTR2 = "<<*FLSTR2<<"\nFLSTR3 = "<<*FLSTR3<<"\nFLSTR4 =
"<<*FLSTR4
                <<"\nMCDDATA = "<<*MCDDATA<<"\nMLDDATA = "<<*MLDDATA<<"\nG =
"<<G<<"\nTHEITV = "<<THEITV;
        if (_strnicmp(*geom,"octahedral",13)==0)
                outfile01<<"\nP1d[0] = "<<P1d[0]<<endl<<endl;
        else
```

```
                outfile01<<"\nP3d[1] = "<<P3d[0]<<"\nP3d[2] = "<<P3d[1]<<"\nP3d[3] =
"<<P3d[2]<<"\nFTOL = "<<FTOL<<endl<<endl;

        outfile01<<"----------------------------------------------------------------------"<<endl<<endl;

        if (_strnicmp(*geom,"octahedral",13)==0)

        outfile05<<"P1d[0]"<<setw(10)<<"rmsMCD"<<setw(10)<<"P1d[0]"<<setw(10)<<"rmsMLD"<<
endl<<endl;
        else

        outfile05<<"P3d[0]"<<setw(7)<<"P3d[1]"<<setw(7)<<"P3d[2]"<<setw(10)<<"rmsMCD"<<setw(
12)<<"P3d[0]"<<setw(7)<<"P3d[1]"<<setw(7)<<"P3d[2]"<<setw(10)<<"rmsMLD"<<endl<<endl;

//Open MCD and MLD raw data files and input data Temperature, Magnetic field strength, and
//Experimental MCD or MLD intensities to arrays TC[i], BFC[i], EXMCD[i], TL[i], BFL[i], EXMLD[i]

        switch (caseType)
        {
                case 'C':
                case 'B':
                default:

                        infileMCD.open (*MCDDATA,ios::in);
                        outfile01<<"MCD Input Filename: "<<*MCDDATA<<endl<<endl;

        outfile01<<setw(12)<<"TC[i]"<<setw(10)<<"BFC[i]"<<setw(10)<<"EXMCD[i]"<<endl;
                        outfile01<<"eof = "<<infileMCD.eof()<<endl;

                        while (infileMCD.eof()==0)
                        {
                                infileMCD >> TC[NEXmcd] >> BFC[NEXmcd] >>
EXMCD[NEXmcd];
                                if (EXMAXMCD<abs(EXMCD[NEXmcd]))
                                        EXMAXMCD=EXMCD[NEXmcd];

                                outfile01
<<setw(5)<<NEXmcd<<setw(7)<<TC[NEXmcd]<<setw(10)<<BFC[NEXmcd]<<setw(10)<<EXMCD[NE
Xmcd]<<endl;
                                NEXmcd++;
                        }
                        NEXmcd-=1;
                        outfile01<<"\nEXMAXMCD = "<<EXMAXMCD<<endl<<endl<<endl;
                        infileMCD.close();

                        if (caseType=='C')
                        {
                                outfile01<<endl<<endl;
                                break;
                        }

                case 'L':

                        infileMLD.open (*MLDDATA,ios::in);
                        outfile01<<"MLD Input Filename: "<<*MLDDATA<<endl<<endl;
```

```
	outfile01<<setw(12)<<"TL[i]"<<setw(10)<<"BFL[i]"<<setw(10)<<"EXMLD[i]" << endl;

//				for (i=0;i<NEX;i++)
				while (infileMLD.eof()==0)
				{
					infileMLD >> TL[NEXmld] >> BFL[NEXmld] >>
EXMLD[NEXmld];

					if (abs(EXMAXMLD)<abs(EXMLD[NEXmld]))
						EXMAXMLD=EXMLD[NEXmld];

					outfile01
<<setw(5)<<NEXmld<<setw(7)<<TL[NEXmld]<<setw(10)<<BFL[NEXmld]<<setw(10)<<EXMLD[NEX
mld] << endl;
					NEXmld++;
				}
				NEXmld-=1;
				outfile01<<"\nEXMAXMLD = "<<EXMAXMLD<<endl<<endl<<endl;
				infileMLD.close();

				break;
	}

	((NEXmcd>NEXmld)?(NEXmax=NEXmcd):(NEXmax=NEXmld));

	cout<<"NEXmcd = "<<NEXmcd<<setw(12)<<"NEXmld = "<<NEXmld<<setw(12)<<"NEXmax
= "<<NEXmax<<endl<<endl;
	outfile01<<"NEXmcd = "<<NEXmcd<<setw(12)<<"NEXmld =
"<<NEXmld<<setw(12)<<"NEXmax = "<<NEXmax<<endl<<endl;

	outfile01<<"-------------------------------------------------------------------"<<endl<<endl;

//Section for inputting test data files of MCD and MLD data to be used as theoretical files
//for testingroutines. Arrays to be filled are: THMCD[i], THMLD[i]. These arrays are filled
//in the normal courseof the program by the theroretical calculations prior to scaling. The
//scaled arrays are THSCMCD[i] and THSCMLD[i]. The MCD file will be stored as 'TestMCD.dat' and the
//corresponding MLDfile is 'TestMLD.dat'
//
//To use this section for running against dummy theoretical data, uncomment the following block.
//
//IT IS IMPERATIVE THAT THIS BLOCK BE COMMENTED OUT FOR NORMAL COMPILATION
OF THE PROGRAM FOR USE IN
//REAL DATA SETS TO CALCULATE REAL THEORETICAL DATA !!!!!!(actually,it would all be
overwritten
//eventually,but don't do it anyway !!)
//
//BEGIN BLOCK OF DUMMY TEST DATA READ-IN
//*****************************************************************************************
************
/*
	inTestMCD.open ("TestMCD.dat",ios::in);
	inTestMLD.open ("TestMLD.dat",ios::in);

	outfile01 <<"Dummy Theoretical Test Data\n\n\n";
	outfile01 <<setw(5)<<"i"<<setw(7)<<"TC[i]"<<setw(10)<<"BFC[i]"<<setw(10)<<"THMCD[i]"
```

```
        <<"\t\t"<<setw(7)<<"TL[i]"<<setw(10)<<"BFL[i]"<<setw(10)<<"THMLD[i]" << endl;

        for (i=0;i<NEXmcd;i++)
        {
                inTestMCD >> THMCD[i];
                outfile01
<<setw(5)<<i+1<<setw(7)<<TC[i]<<setw(10)<<BFC[i]<<setw(10)<<THMCD[i]<<endl;
        }

        for (i=0;i<NEXmld;i++)
        {
                inTestMLD >> THMLD[i];

        outfile01<<setw(5)<<i+1<<setw(7)<<TL[i]<<setw(10)<<BFL[i]<<setw(10)<<THMLD[i] <<
endl;
        }
        inTestMCD.close();
        inTestMLD.close();

        outfile01<<"----------------------------------------------------------------------"<<endl<<endl;
*/
//**************************************************************************************
************
//END BLOCK OF DUMMY TEST DATA

//Assign proper Eigenvalues for input geometry from 'coeff.for' [octahedral/tetragonal]
//or 'coefftri.for' for trigonal symmetry. Add routine to do free atom calcs also.

        if (_strnicmp(*geom,"free atom",13)==0)
        {

                *COEFF=*COEFFFAT;
        }

        else if ((_strnicmp(*geom,"octahedral",13)==0)||(_strnicmp(*geom,"tetragonal",13)==0))
        {
                *COEFF=*COEFFOCT;
        }

        else if (_strnicmp(*geom,"trigonal",13)==0)
        {
                *COEFF=*COEFFTRI;
        }

        else if
((_strnicmp(*geom,"octahedral",13)!=0)&&(_strnicmp(*geom,"tetragonal",13)!=0)&&(_strnicmp(*geom,"
trigonal",13)!=0))
        {
                cout <<"\ngeom = "<<*geom<<"\tCOEFF = "<<*COEFF
                        <<"\n\nError in input geometry designation --- must be FREE ATOM,
OCTAHEDRAL,TERAHEDRAL, or TRIGONAL"
                        <<"\nupper or lower case acceptable,but not mixed case.\n\n";

                NR::nrerror("Error in input geometry designation");
        }
```

```
//Read in crystal field coefficients dependent on geometry. octahedral or tetragonal: coeff.for; trigonal:
coefftri.for

        infileCOEFF.open (*COEFF,ios::in);

        outfile01           <<"\n\nEIGENVECTOR FILE -- "<<*COEFF<<"\nCRYSTAL FIELD
EIGEVECTORS (ref Butler):"<<endl;
        outfile01   <<"Matrix dimensions: "<<bufCoeff<<" x "<<bufCoeff<<endl<<endl;
        outfile01<<setiosflags(ios::fixed|ios::showpoint);
        outfile01<<setprecision(6);

                for (i=0; i<bufCoeff;i++)
                        for (j=0;j<bufCoeff;j++)
                        {
                                infileCOEFF >> Basis[i][j];
                                outfile01<<setw(11)<<Basis[i][j];
                                if ((j==bufCoeff-1))
                                        outfile01<<endl;
                        }
                outfile01<<endl;

        infileCOEFF.close();

        outfile01<<"\n\n----------------------------------------------------------------------------------------------------
-"<<endl;
        outfile01<<"---------------------------------------------------------------------------------------------------
"<<endl<<endl;

        //Zeeman vector calculations

        zeeman(JI,JF,TPZMAN,TMZMAN,TZZMAN,TJMP,TJMM,TJMZ,TJMP2,TJMM2,TJMZ2);

        outfile01<<"OUTPUT OF orave.cpp"<<endl;
        outfile01<<"\n\n\t3JM ZEEMAN ELEMENTS: "<<endl;
        outfile01           <<"\n\nTPZMAN Vector -- "<<endl;

                for (i=0; i<bufSize1;i++)
                                outfile01<<setw(10)<<TPZMAN[i];

                outfile01           <<"\n\nTMZMAN Vector -- "<<endl;

                for (i=0; i<bufSize1;i++)
                                outfile01<<setw(10)<<TMZMAN[i];

                outfile01           <<"\n\nTZZMAN Vector -- "<<endl;

                for (i=0; i<bufSize1;i++)
                                outfile01<<setw(10)<<TZZMAN[i];

                outfile01<<"\n\n--------------------------------------------------------------------------------------
---"<<endl<<endl;

                outfile01<<"\n\n\t3JM VALUES calculated for delta J = "<<JF-JI<<endl;

                outfile01           <<"\n\nTJMP Vector -- "<<endl;
                for (i=0; i<bufSize1;i++)
                                outfile01<<setw(10)<<TJMP[i];

                outfile01       <<"\n\nTJMM Vector -- "<<endl;

                for (i=0; i<bufSize1;i++)
                                outfile01<<setw(10)<<TJMM[i];

                outfile01       <<"\n\nTJMZ Vector -- "<<endl;

                for (i=0; i<bufSize1;i++)
                                outfile01<<setw(10)<<TJMZ[i];

        outfile01<<"\n\n----------------------------------------------------------------------------------------------------
"<<endl<<endl;

        outfile01<<"\n\n\t3JM       SQUARED VALUES calculated for delta J = "<<JF-JI<<endl;

                outfile01       <<"\n\nTJMP2 Vector -- "<<endl;

                for (i=0; i<bufSize1;i++)
                                outfile01<<setw(10)<<TJMP2[i];

                outfile01       <<"\n\nTJMM2 Vector -- "<<endl;

                for (i=0; i<bufSize1;i++)
                                outfile01<<setw(10)<<TJMM2[i];

                outfile01       <<"\n\nTJMZ2 Vector -- "<<endl;

                for (i=0; i<bufSize1;i++)
                                outfile01<<setw(10)<<TJMZ2[i];

                outfile01<<"\n\n------------------------------------------------------------------------------------------------
---"<<endl<<endl;

//Assign matrix XI[i][j] to unit vectors i,j,k for NDIM dimensions.
//This is starting direction set for powell
        for (i=0;i<NDIM;i++)
                XI[i][i]=1.;

//Multi-dimensional optimization routine NR::powell
//uses direction set method.
//Routine to step thru P values calculating RMS deviation at each P increment.

        if (_strnicmp(*rmsState,"on",4)==0)
        {
                ITER=9999;
                P1d[0]=P3d[0]=Pinit;
                for (i=0;i<=Pinc;i++)
                {
                        if (_strnicmp(*geom,"octahedral",13)==0)
                        {
                                NR::powell(P1d,XI,FTOL,ITER,FRET,func);
                                P1d[0]-=Pintvl;
                        }
                        else
                        {
                                NR::powell(P3d,XI,FTOL,ITER,FRET,func);
                                P3d[0]-=Pintvl;
                        }
                }
        }
        else

        {
                if (_strnicmp(*geom,"octahedral",13)==0)
                        NR::powell(P1d,XI,FTOL,ITER,FRET,func);
                else
                        NR::powell(P3d,XI,FTOL,ITER,FRET,func);
        }


//Output theoretical values and refinement parameters here, along with results of comparison with
//experimental data
//
        outfile01<<"\n\n-----------------------------------------------------------------------------------------------
-"<<endl;
        outfile01<<"----------------------------------------------------------------------------------------------
"<<endl<<endl;
        outfile01<<"   RRRR    EEEE    SSSS    U  U    L      TTTTTTT    SSSS"<<endl
                <<"    R  R    E       S       U  U    L       T       S  "<<endl
                <<"    RRRR     EEE     SSSS    U  U    L       T       SSSS"<<endl
                <<"    R  R    E         S    U  U    L       T        S"<<endl
                <<"    R    R   EEEE    SSSS    UUUUU    LLLLL    T      SSSS"<<endl;
        outfile01<<"\n---------------------------------------------------------------------------------------------
"<<endl;
        outfile01<<"----------------------------------------------------------------------------------------------
"<<endl<<endl;
        outfile01<<"\n\nRESULTS:"<<endl<<endl;
        outfile01<<"Scale factor for MCD:"<<SCALEMCD<<"\tMLD: "<<SCALEMCD<<endl<<endl;
        outfile01 <<setw(5)<<"
"<<setw(7)<<"TC[i]"<<setw(15)<<"BFC[i]"<<setw(15)<<"EXMCD[i]"<<setw(15)<<"THMCD[i]"<<set
w(15)<<"SIGMA"<<endl;

        outfile02<<"\n\nRESULTS:"<<endl<<endl;
        outfile02<<"Scale factor for MCD:"<<SCALEMCD<<"\tMLD: "<<SCALEMCD<<endl<<endl;
        outfile02 <<setw(5)<<"
"<<setw(7)<<"TC[i]"<<setw(15)<<"BFC[i]"<<setw(15)<<"EXMCD[i]"<<setw(15)<<"THMCD[i]"<<set
w(15)<<"SIGMA"<<endl;

        outfile01<<setiosflags(ios::fixed|ios::showpoint);
        outfile01<<setprecision(2);

        outfile02<<setiosflags(ios::fixed|ios::showpoint);
        outfile02<<setprecision(2);

        outfile03<<setiosflags(ios::fixed|ios::showpoint);
        outfile03<<setprecision(2);

        for (i=0;i<NEXmcd;i++)
        {
// Remove once scaling routine is built
                THSCMCD[i]=THMCD[i];
                SIGMCD[i]=EXMCD[i]-THMCD[i];
// ************************************
                outfile01
<<setw(5)<<i+1<<setw(7)<<TC[i]<<setw(15)<<setprecision(3)<<BFC[i]<<setw(15)<<setprecision(2)<<E
XMCD[i]<<setw(15)<<THSCMCD[i]<<setw(15)<<SIGMCD[i]<<endl;
                outfile02
<<setw(5)<<i+1<<setw(7)<<TC[i]<<setw(15)<<setprecision(3)<<BFC[i]<<setw(15)<<setprecision(2)<<E
XMCD[i]<<setw(15)<<THSCMCD[i]<<setw(15)<<SIGMCD[i]<<endl;
        }
/*
        if (_strnicmp(*geom,"octahedral",13)==0)
{
cout<<setw(15)<<"RMS MCD: "<<rmsMCD<<endl<<endl;
outfile01<<setw(15)<<"RMS MCD: "<<rmsMCD<<endl<<endl;
cout<<"SUMMLD= "<<SUML<<setw(15)<<"RMS MLD: "<<rmsMLD<<endl<<endl;
cout<<"No. intervals: "<<THEITV<<endl<<endl<<endl;
outfile01<<"SUMMLD= "<<SUML<<setw(15)<<"RMS MLD: "<<rmsMLD<<endl<<endl;
outfile01<<"No. intervals: "<<THEITV<<endl<<endl<<endl;
cout<<"SUM= "<<SUM<<setw(10)<<"RMS: "<<rmsTot<<setw(10)<<"P1d0= "<<P1d[0]<<endl<<endl;
outfile01<<"SUM= "<<SUM<<setw(10)<<"RMS: "<<rmsTot<<setw(10)<<"P1d0=
"<<P1d[0]<<endl<<endl;
}

else
{
cout<<"SUMMCD= "<<SUMC<<setw(15)<<"RMS MCD: "<<rmsMCD<<endl<<endl;
outfile01<<"SUMMCD= "<<SUMC<<setw(15)<<"RMS MCD: "<<rmsMCD<<endl<<endl;
cout<<"SUMMLD= "<<SUML<<setw(15)<<"RMS MLD: "<<rmsMLD<<endl<<endl;
cout<<"No. intervals: "<<THEITV<<endl<<endl<<endl;
outfile01<<"SUMMLD= "<<SUML<<setw(15)<<"RMS MLD: "<<rmsMLD<<endl<<endl;
outfile01<<"No. intervals: "<<THEITV<<endl<<endl<<endl;
cout<<"SUM= "<<SUM<<setw(10)<<"RMS: "<<rmsTot<<setw(10)<<"P3d0=
"<<P3d[0]<<setw(10)<<"P3d1= "<<P3d[1]<<setw(10)<<"P3d2= "<<P3d[2]<<endl;
outfile01<<"SUM= "<<SUM<<setw(10)<<"RMS: "<<rmsTot<<setw(10)<<"P3d0=
"<<P3d[0]<<setw(10)<<"P3d1= "<<P3d[1]<<setw(10)<<"P3d2= "<<P3d[2]<<endl;
}

*/      outfile01<<endl<<endl;
        outfile03<<"\n\nRESULTS:"<<endl<<endl;
        outfile03<<"Scale factor for MCD:"<<SCALEMCD<<"\tMLD: "<<SCALEMCD<<endl<<endl;
        outfile01<<setw(5)<<"
"<<setw(7)<<"TL[i]"<<setw(15)<<"BFL[i]"<<setw(15)<<"EXMLD[i]"<<setw(15)<<"THMLD[i]"
<<setw(15)<<"SIGMA"<< endl;
        outfile03<<setw(5)<<"
"<<setw(7)<<"TL[i]"<<setw(15)<<"BFL[i]"<<setw(15)<<"EXMLD[i]"<<setw(15)<<"THMLD[i]"
<<setw(15)<<"SIGMA"<< endl;
        for (i=0;i<NEXmld;i++)
        {
                THSCMLD[i]=THMLD[i];
                SIGMLD[i]=EXMLD[i]-THMLD[i];

        outfile01<<setw(5)<<i+1<<setw(7)<<TL[i]<<setw(15)<<setprecision(3)<<BFL[i]<<setw(15)<<s
etprecision(2)<<EXMLD[i]<<setw(15)<<THSCMLD[i]<<setw(15)<<SIGMLD[i] << endl;
```

```
        outfile03<<setw(5)<<i+1<<setw(7)<<TL[i]<<setw(15)<<setprecision(3)<<BFL[i]<<setw(15)<<s
etprecision(2)<<EXMLD[i]<<setw(15)<<THSCMLD[i]<<setw(15)<<SIGMLD[i] << endl;
        }
        outfile01           <<"\nMCD: SMMCD = "<<SMMCD<<"\tMLD: SMMLD =
"<<SMMLD<<endl<<endl
                            <<"\nMCD: sigma = "<<SIGMAMCD<<"\tMLD: sigma =
"<<SIGMAMLD<<endl<<endl
                            <<"\n\nSum of data points within each listed sigma range:\n\n"
                            <<"\t"<<setw(10)<<"MCD"<<"\t\t"<<setw(16)<<"MLD"<<endl
                            <<"\t  1sigma = "<<setw(3)<<NSC1<<"\t\t 1 sigma =
"<<setw(3)<<NSL1<<endl
                            <<"\t  2sigma = "<<setw(3)<<NSC2<<"\t\t 2 sigma =
"<<setw(3)<<NSL2<<endl
                            <<"\t  3sigma = "<<setw(3)<<NSC3<<"\t\t 3 sigma =
"<<setw(3)<<NSL3<<endl
                            <<"\t>3 sigma = "<<setw(3)<<NSC4<<"\t\t>3 sigma =
"<<setw(3)<<NSL4<<endl<<endl<<endl;

        outfile01<<"-------------------------------------------------------------------------------------------
"<<endl<<endl;

        cout << "\n\n";

        t1=time(0);
        ttotal=(t1-t0)/60.;
        finish=clock();
        double duration=(finish - start) / CLOCKS_PER_SEC/60;

        cout<<setprecision(2)<<"Run time: "<<ttotal<<" minutes."<<endl<<endl;
        outfile01<<"Run time: "<<ttotal<<" minutes."<<endl<<endl;
        outfile04<<"Run time: "<<ttotal<<" minutes."<<endl<<endl;
        cout<<"CPU time: "<<duration<<" minutes."<<endl<<endl;
        outfile01<<"CPU time: "<<duration<<" minutes."<<endl<<endl;
        outfile04<<"CPU time: "<<duration<<" minutes."<<endl<<endl;

        cout<<"\a\a\a\a\a";

        return 0;
}

//Function func definition
//Can be called from orave.cpp,
        DP func(Vec_I_DP &P)

{
        int INDEX(0),i,j,k,l(1),n(1),m1,m2,mp,nrot(0);
        const double uB=0.4669;
        double
TK(0.),TERM0(0.),TERM1(0.),TERM2(0.),THMCD1(0.),THMLD1(0.),THMLD2(0.),THMCD2(0.);
        double
CTHETA(0.),STHETA(0.),C2THETA(0.),S2THETA(0.),DEL1THET(0.),DEL2THET(0.),DEL3THET(0.)
;
        double
TCSSN1(0.),TCSSN2(0.),TCSSN3(0.),TSIN(0.),TSIN1(0.),TSIN2(0.),TSIN3(0.),TCOS1(0.),TCOS2(0.);
        double returnVal(0.),returnValMCD(0.),returnValMLD(0.);
        double rmsMLD(0.),rmsMCD(0.),rmsTot(0.);
        double SUM(0.),SUMC(0.),SUML(0.);

        Vec_IO_DP Pcalc(0.,3),BOLTZ(0.,2*JI+1);
        ofstream outfile04 (*FLSTR4,ios::app);
        ofstream outfile05 (*FLSTR5,ios::app);
//Compare Pcalc (calculated P parameters) to P parameters passed from calling routine.

        if (_strnicmp(*geom,"octahedral",13)==0)
        {
                if (Pcalc[0]==P[0])
                return P[0];
                        for (i=0;i<NDIM;i++)
                Pcalc[i]=P[i];

        //      call crysteig
cout<<"function -- octahedral"<<endl;
        crysteig(JI,geom,Basis,CFE,P);
        }

        else
        {
        if ((Pcalc[0]==P[0])&&(Pcalc[1]==P[1])&&(Pcalc[2]==P[2]))
                return P[0];
                for (i=0;i<NDIM;i++)
                Pcalc[i]=P[i];

        //      call crysteig
cout<<"function -- non-octahedral"<<endl;
        crysteig(JI,geom,Basis,CFE,P);
        }

        INDEX++;

        int mult=2*JI+1;
        double RMM=-G*uB*sqrt(JI*(2*JI+1)*(JI+1));
        double Z(0.);

// while loop to perform theoretical MCD anc MLD calculations NEX times
        while (l<=NEXmax)
        {
                THMLD2=0.;
                THMCD2=0.;

// while loop to perform weighted orientational averaging for each increment of THETA
                while (n<=THEITV+1)
                {
                        THETA=THETA1+(n-1)*THEINC;
                        CTHETA=cos(THETA);
                        STHETA=sin(THETA);
                        C2THETA=pow(CTHETA,2.);
                        S2THETA=pow(STHETA,2.);
                        DEL1THET=C2THETA-S2THETA/2;
                        DEL2THET=S2THETA/4-C2THETA/2;
                        DEL3THET=STHETA/sqrt(2.);
```

```
            if (NFLAG==0)
            {
                for (j=0;j<mult;j++)
                    for (i=0;i<mult;i++)
                    {
                        A[i][j]=0.;
                        for (k=0;k<mult;k++)
                        {
                            int IM=k-JI;

    TERM0=Basis[i][k]*Basis[j][k]*CTHETA*TZZMAN[k];
                            if (k<mult)

    TERM1=Basis[i][k]*Basis[j][k+1]*TMZMAN[k];
                            else TERM1=0.;
                            if (k>1)
                                TERM2=Basis[i][k]*Basis[j][k-
1]*TPZMAN[k];
                            else TERM2=0.;
                            A[i][j]+=power(-1.,(JI-
IM))*(DEL3THET*(TERM1-TERM2)+TERM0);
                        }
                        ZEEMAN[i][j][n]=A[i][j];
                    }
            }

            if ((caseType=='B')||(caseType=='L'))
            for (j=0;j<mult;j++)
                for (i=0;i<mult;i++)
                {
                    if (i==j)
                        A[i][j]=BFL[l]*RMM*ZEEMAN[i][j][n]+CFE[i];
                    else A[i][j]=BFL[l]*RMM*ZEEMAN[i][j][n];
                }

            if (caseType=='C')
            for (j=0;j<mult;j++)
                for (i=0;i<mult;i++)
                {
                    if (i==j)
                        A[i][j]=BFC[l]*RMM*ZEEMAN[i][j][n]+CFE[i];
                    else A[i][j]=BFC[l]*RMM*ZEEMAN[i][j][n];
                }

//Function call to NR::jacobi to diagonalize eigenvalue matrix elements
            NR::jacobi(A,D,V,nrot);

            for (k=0;k<mult;k++)
                for (j=0;j<mult;j++)
                {
                    C[j][k]=0.;
                    for (i=0;i<mult;i++)
                        C[j][k]+=V[i][j]*Basis[i][k];
                }

    //MLD calcs
```

```
                        if (l<=NEXmld)
                        {
                                TK=log(2)*TL[l];
                                Z=0.;
                                THMLD1=0.;

                                for (j=0;j<mult;j++)
                                {
                                        BOLTZ[j]=exp(-D[j]/TK);
                                        Z+=BOLTZ[j];
                                }

                                for (i=0;i<mult;i++)
                                        for (mp=0;mp<mult;mp++)
                                                for (m1=0;m1<mult;m1++)
                                                {
                                                        if (m1==mp)

        TCSSN1=power(C[i][m1],2)*DEL1THET*TJMZ2[m1];
                                                        else TCSSN1=0.;
                                                        if (m1==(mp+1))

        TCSSN2=power(C[i][m1],2)*DEL2THET*TJMM2[m1];
                                                        else TCSSN2=0.;
                                                        if (m1==(mp-1))

        TCSSN3=power(C[i][m1],2)*DEL2THET*TJMP2[m1];
                                                        else TCSSN3=0.;
                                                        TSIN=0.;

                                                        for (m2=0;m2<mult;m2++)
                                                        {
                                                                if ((m1==(mp+1))&&(m2==(mp-
1)))

        TSIN1=C[i][m1]*C[i][m2]*1.5*S2THETA*TJMM[m2]*TJMP[m1];
                                                                else TSIN1=0.;
                                                                TSIN+=TSIN1;
                                                        }

        THMLD1+=STHETA*(BOLTZ[i]*(TCSSN1+TCSSN2+TCSSN3-TSIN))/Z;

                                                }
                                THMLD2+=THMLD1;
                        }

        //MCD calcs
                        if (l<=NEXmcd)
                        {
                                TK=log(2)*TC[l];
                                THMCD1=0.;
                                Z=0.;
                                for (j=0;j<mult;j++)
                                {
                                        BOLTZ[j]=exp(-D[j]/TK);
                                        Z+=BOLTZ[j];
```

```
                }

                for (i=0;i<mult;i++)
                    for (mp=0;mp<mult;mp++)
                        for (m1=0;m1<mult;m1++)
                        {
                            if (m1==(mp-1))

    TCOS1=power(C[i][m1],2)*CTHETA*TJMM2[m1];
                            else TCOS1=0.;
                            if (m1==(mp+1))

    TCOS2=power(C[i][m1],2)*CTHETA*TJMP2[m1];
                            else TCOS2=0.;
                            if (m1==mp)
                            {
                                TSIN=TSIN1=TSIN2=TSIN3=0.;

                                for (m2=0;m2<mult;m2++)
                                {

    TSIN1=C[i][m1]*C[i][m2]*sqrt(2.)*STHETA*TJMZ[m1];
                                    if (TSIN1!=0.)
                                    {
                                        if (m2==(mp-1))

    TSIN2=TJMM[m2];

                                        else TSIN2=0.;
                                        if (m2==(mp+1))

    TSIN3=TJMP[m2];

                                        else TSIN3=0.;
                                    }

    TSIN+=TSIN1*(TSIN2+TSIN3);

                                }
                            }
                            else TSIN=0.;


    THMCD1+=STHETA*(BOLTZ[i]*(TCOS1-TCOS2+TSIN))/Z;
                        }

                THMCD2+=THMCD1;
            }

            n++;
        }

// End inner while loop(THEITV)

        NFLAG=1;
        THMLD[l]=THMLD2;
        THMCD[l]=THMCD2;
```

```
                        n=1;
                        l++;
                        cout<<".";
                }
        cout<<endl;
        // End outer while loop (NEX)

                        scalem(EXMCD,EXMLD,THMCD,THMLD,SUMC,SUML,NEXmcd,NEXmld,runStat);

                        SUM=SUMC+SUML;
                        returnValMCD=sqrt(SUMC/(2*NEXmcd-1));
                        returnValMLD=sqrt(SUML/(2*NEXmld-1));
                        returnVal=sqrt(SUM/(NEXmcd+NEXmld-1));

        //adding RMS normalized scaling
                SCALEMCD=SCALEMLD=0.;
                SCN=SCD=SUM=SUMC=SUML=0.;
                cout<<"exmaxmld= "<<EXMAXMLD<<setw(15)<<"exmaxmcd= "<<EXMAXMCD<<endl;
                for(i=0;i<NEXmld;i++)
                {
                        SCN+=(EXMLD[i]/EXMAXMLD)*THMLD[i];
                        SCD+=power(THMLD[i],2);
                }

                SCALEMLD=SCN/SCD;
                for(i=0;i<NEXmld;i++)
                {
                        THnormMLD[i]=SCALEMLD*THMLD[i];
                        SUML+=power((THnormMLD[i]-(EXMLD[i]/EXMAXMLD)),2);
                }
                cout<<setprecision(6)<< "SCALEMLD= "<<SCALEMLD<<setprecision(2)<<setw(15)<<"SCN=
        "<<SCN<<setw(15)<<"SCD= "<<SCD<<endl;
                SCN=SCD=0.;
                for(i=0;i<NEXmcd;i++)
                {
                        SCN+=(EXMCD[i]/EXMAXMCD)*THMCD[i];
                        SCD+=power(THMCD[i],2);
                }
                SCALEMCD=SCN/SCD;
                for(i=0;i<NEXmcd;i++)
                {
                        THnormMCD[i]=SCALEMCD*THMCD[i];
                        SUMC+=power((THnormMCD[i]-(EXMCD[i]/EXMAXMCD)),2);
                }
                cout<<setprecision(6)<< "SCALEMCD= "<<SCALEMCD<<setw(15)<<setprecision(2)<<"SCN=
        "<<SCN<<setw(15)<<"SCD= "<<SCD<<endl;

        //RMS fix
                double SUMC1(0.),SUML1(0.),SUMT(0.);
                SUM=SUMC=SUML=0.;
                for(i=0;i<NEXmcd;i++)
                {
                        SUMC+=power((THMCD[i]-EXMCD[i]),2);
                        SUMC1+=power(EXMCD[i],2);
                }
```

```
		for(i=0;i<NEXmld;i++)
		{
			SUML+=power((THMLD[i]-EXMLD[i]),2);
			SUML1+=power(EXMLD[i],2);
		}

		SUM=SUMC+SUML;
		SUMT=SUMC1+SUML1;

//			double rmsMLD=sqrt(SUML/(NEXmld-1))*100.;
//			double rmsMCD=sqrt(SUMC/(NEXmcd-1))*100.;
//			double rmsTot=sqrt(SUM/(NEXmld+NEXmcd-1))*100.;

			rmsMLD=sqrt(SUML/(NEXmld-1))*100./sqrt(SUML1/(NEXmld-1));
			rmsMCD=sqrt(SUMC/(NEXmcd-1))*100./sqrt(SUMC1/(NEXmcd-1));
			rmsTot=sqrt(SUM/(NEXmld+NEXmcd-1))*100./sqrt(SUMT/(NEXmld+NEXmcd-1));

//end addition

cout<<"\nCheckpoint func return"<<setiosflags(ios::fixed|ios::showpoint)<<setprecision(6)<<endl;
outfile04<<"\nCheckpoint func return"<<setiosflags(ios::fixed|ios::showpoint)<<setprecision(6)<<endl;

for (i=0;i<2*JI+1;i++)
{
		cout<<"CFE["<<i+1<<"] = "<<setw(15)<<CFE[i]<<endl;
		outfile04<<"CFE["<<i+1<<"] = "<<setw(15)<<CFE[i]<<endl;
}

++cycle;
cout<<endl<<endl<<"cycle no.: "<<cycle<<endl<<endl;
outfile04<<endl<<endl<<"cycle no.: "<<cycle<<endl<<endl;
cout.precision(4);
outfile04.precision(4);

if (_strnicmp(*geom,"octahedral",13)==0)
{
cout<<"SUMMCD= "<<SUMC<<setw(15)<<"returnValMCD= "<<returnValMCD<<setw(15)<<"RMS
MCD: "<<rmsMCD<<endl<<endl;
outfile04<<"SUMMCD= "<<SUMC<<setw(15)<<"returnValMCD=
"<<returnValMCD<<setw(15)<<"RMS MCD: "<<rmsMCD<<endl<<endl;
outfile05<<P[0]<<setw(10)<<rmsMCD<<setw(10)<<P[0]<<setw(10)<<rmsMLD<<endl;
cout<<"SUMMLD= "<<SUML<<setw(15)<<"returnValMLD= "<<returnValMLD<<setw(15)<<"RMS
MLD: "<<rmsMLD<<endl<<endl;
cout<<"No. intervals: "<<THEITV<<endl<<endl<<endl;
outfile04<<"SUMMLD= "<<SUML<<setw(15)<<"returnValMLD=
"<<returnValMLD<<setw(15)<<"RMS MLD: "<<rmsMLD<<endl<<endl;
outfile04<<"No. intervals: "<<THEITV<<endl<<endl<<endl;
cout<<"SUM= "<<SUM<<setw(15)<<"returnVal= "<<returnVal<<setw(10)<<"RMS:
"<<rmsTot<<setw(10)<<"P1d0= "<<P[0]<<endl<<endl;
outfile04<<"SUM= "<<SUM<<setw(15)<<"returnVal= "<<returnVal<<setw(10)<<"RMS:
"<<rmsTot<<setw(10)<<"P1d0= "<<P[0]<<endl<<endl;
}

else
{
```

```
cout<<"SUMMCD= "<<SUMC<<setw(15)<<"returnValMCD= "<<returnValMCD<<setw(15)<<"RMS
MCD: "<<rmsMCD<<endl<<endl;
outfile04<<"SUMMCD= "<<SUMC<<setw(15)<<"returnValMCD=
"<<returnValMCD<<setw(15)<<"RMS MCD: "<<rmsMCD<<endl<<endl;
outfile05<<P[0]<<setw(7)<<P[1]<<setw(7)<<P[2]<<setw(10)<<rmsMCD<<setw(12)<<P[0]<<setw(7)<<
P[1]<<setw(7)<<P[2]<<setw(10)<<rmsMLD<<endl;
cout<<"SUMMLD= "<<SUML<<setw(15)<<"returnValMLD= "<<returnValMLD<<setw(15)<<"RMS
MLD: "<<rmsMLD<<endl<<endl;
cout<<"No. intervals: "<<THEITV<<endl<<endl<<endl;
outfile04<<"SUMMLD= "<<SUML<<setw(15)<<"returnValMLD=
"<<returnValMLD<<setw(15)<<"RMS MLD: "<<rmsMLD<<endl<<endl;
outfile04<<"No. intervals: "<<THEITV<<endl<<endl<<endl;
cout<<"SUM= "<<SUM<<setw(15)<<"returnVal= "<<returnVal<<setw(10)<<"RMS:
"<<rmsTot<<setw(10)<<"P3d0= "<<P[0]<<setw(10)<<"P3d1= "<<P[1]<<setw(10)<<"P3d2=
"<<P[2]<<endl;
outfile04<<"SUM= "<<SUM<<setw(15)<<"returnVal= "<<returnVal<<setw(10)<<"RMS:
"<<rmsTot<<setw(10)<<"P3d0= "<<P[0]<<setw(10)<<"P3d1= "<<P[1]<<setw(10)<<"P3d2=
"<<P[2]<<endl;
}

	return rmsTot;
}

//PROGRAM Zeeman.cpp
//zeeman.cpp
//
//Calculate Zeeman parameters and JM values for delta J = 0,+1,-1

#include <iostream>
#include <fstream>
#include <cstdio>
#include <iomanip>
#include <cstdlib>
#include <cmath>
#include "nr.h"

void zeeman(const int JI,const int JF,Vec_IO_DP &TPZMAN,Vec_IO_DP &TMZMAN,Vec_IO_DP
&TZZMAN,
				Vec_IO_DP &TJMP,Vec_IO_DP &TJMM,Vec_IO_DP &TJMZ,
				Vec_IO_DP &TJMP2,Vec_IO_DP &TJMM2,Vec_IO_DP &TJMZ2)
{
	int IM(0);
//	const int bufSize1=TPZMAN.size();
	const int bufSize1=9;

	double DENSQR = sqrt(2*JI*(2*JI+1)*(JI+1));

	double JIIM[bufSize1],JIIMP[bufSize1],JIIMM[bufSize1];

	for (IM=0;IM<bufSize1;IM++)
	{
		JIIM[IM]=IM-JI;
		JIIMP[IM]=JI+JIIM[IM];
		JIIMM[IM]=JI-JIIM[IM];

		TPZMAN[IM]=pow(-1.,JIIMM[IM]+1)*sqrt((JIIMM[IM]+1)*JIIMP[IM])/DENSQR;
```

```
        TMZMAN[IM]=pow(-1.,JIIMM[IM])*sqrt(JIIMM[IM]*(JIIMP[IM]+1))/DENSQR;
        TZZMAN[IM]=pow(-1.,JIIMM[IM])*sqrt(2.)*JIIM[IM]/DENSQR;

    }
//Calculate JM values, delta J=0,-1, +1

    switch (JF-JI)
    {
        case -1: for (IM=0;IM<bufSize1;IM++)
                {
                    DENSQR=sqrt(2*JI*(2*JI+1)*(2*JI-1));
                    TJMP[IM]=pow(-1.,3*JI+JIIM[IM])*sqrt((JIIMP[IM]-
1)*(JIIMP[IM]))/DENSQR;

                    TJMM[IM]=pow(-1.,JIIMM[IM])*sqrt((JIIMM[IM]-
1)*JIIMM[IM])/DENSQR;

                    TJMZ[IM]=pow(-
1.,JIIMM[IM])*sqrt(2*JIIMP[IM]*JIIMM[IM])/DENSQR;
                }
        break;

        case 0:  for (IM=0;IM<bufSize1;IM++)
                {
                    TJMP[IM]=TPZMAN[IM];
                    TJMM[IM]=TMZMAN[IM];
                    TJMZ[IM]=TZZMAN[IM];
                }
        break;

        case 1:  for (IM=0;IM<bufSize1;IM++)
                {
                    DENSQR=sqrt((2*JI+1)*(2*JI+2)*(2*JI+3));
                    TJMP[IM]=pow(-
1.,JIIMM[IM])*sqrt((JIIMM[IM]+1)*JIIMM[IM]+2)/DENSQR;
                    TJMM[IM]=pow(-
1.,3*JI+JIIM[IM])*sqrt((JIIMP[IM]+1)*(JIIMP[IM]+2))/DENSQR;
                    TJMZ[IM]=pow(-1.,JIIMM[IM]-
1)*sqrt((JIIMP[IM]+1)*(JIIMM[IM]+1))/DENSQR;
                }
        break;
    }

    for (IM=0;IM<bufSize1;IM++)
    {

        TJMP2[IM]=TJMP[IM]*TJMP[IM];
        TJMM2[IM]=TJMM[IM]*TJMM[IM];
        TJMZ2[IM]=TJMZ[IM]*TJMZ[IM];
    }


    return;

}

//PROGRAM crysteig.cpp
//crysteig.cpp
```

```
//
//Function to compute crystal field energies based on geometry type.
//I'll try this first using a reference to the vector I need to access after 'return' --- CFE[]
//which contains the calculated crystal field energies. I'll use modern variable conventions here (lower case)
//except I'll use uppercase for arrays and vectors
//
//***THIS ROUTINE IS CURRENTLY ONLY VALID FOR JI=4 (Fe(0))!!! THE J+ AND J-
EXPANSIONS ARE TO +- 4. THEY NEED TO
//RESTRICTED TO +- 3 FOR ji=3 IN THE Ni(0) CASE.
//

#include <iostream>
#include <fstream>
#include <cstdio>
#include <iomanip>
#include <cstdlib>
#include <cmath>
#include "math.h"
#include "nr.h"

using namespace std;

void crysteig(int jinit,char *geom[13],Mat_I_DP &BASIS,Vec_IO_DP &CFE,Vec_I_DP &Pparm)
{
        int i,j,k,n;
        int mult=2*jinit+1;
        double coeff1,coeff2;

//error check for apropriate geometry in variable 'geom' to be used in this routine
        if ((_strnicmp(*geom,"free
atom",13)!=0)&&(_strnicmp(*geom,"octahedral",13)!=0)&&(_strnicmp(*geom,"tetragonal",13)!=0)&&(_
strnicmp(*geom,"trigonal",13)!=0))
                NR::nrerror("Geometry input error to function 'crysteig'");

                if (_strnicmp(*geom,"free atom",13)==0)
                {
                        for (n=0;n<mult;n++)
                                CFE[n]=0.;
                        return;
                }

        double m=0;
        coeff1=Pparm[0]/60;                                                             //assign values to
coefficients

        if (_strnicmp(*geom,"octahedral",13)==0)
                        coeff2=Pparm[0]/12;

        else coeff2=Pparm[1]/12;

//Octahedral & Tetragonal geometry crystal field calculations occur here
        if (_strnicmp(*geom,"trigonal",13)!=0)
        {
                for (n=0;n<mult;n++)
                {
                        CFE[n]=0.;
                        for(i=0;i<mult;i++)
                                for (j=0;j<mult;j++)
                                {
                                        if ((BASIS[n][i]*BASIS[n][j])==0.)
                                                continue;
                                        if (i==j)
                                        {
                                                m=i-jinit;

        CFE[n]+=coeff1*BASIS[n][i]*BASIS[n][j]*(35.*pow(m,4.)-30.*jinit*(jinit+1.)*m
                                                                *m+25.*m*m-
6.*jinit*(jinit+1.)+3.*jinit*jinit*pow(jinit+1.,2.));
                                        }
                                        else
                                        if (i==j+4)
                                        {
                                                m=j-jinit;

        CFE[n]+=0.5*coeff2*BASIS[n][i]*BASIS[n][j]*pow((jinit-m)*(jinit-m-1)*(jinit-m-2)
                                                                *(jinit-m-
3)*(jinit+m+1)*(jinit+m+2)*(jinit+m+3)*(jinit+m+4),0.5);
                                        }
                                        else
                                        if (i==j-4)
                                        {
                                                m=j-jinit;

        CFE[n]+=0.5*coeff2*BASIS[n][i]*BASIS[n][j]*pow((jinit+m)*(jinit+m-1)*(jinit+m-2)
                                                                *(jinit+m-3)*(jinit-m+1)*(jinit-
m+2)*(jinit-m+3)*(jinit-m+4),0.5);
                                        }
                                }
//If geometry is octahedral, CFE calculation stops here.
//If geometry is Tetragonal, additional CFE summations follow.
                        if (_strnicmp(*geom,"tetragonal",13)==0)
                        {
                                for (k=0;k<mult;k++)
                                {
                                        m=k-jinit;
                                        CFE[n]+=(Pparm[2]/3)*BASIS[n][k]*BASIS[n][k]*(3*m*m-
jinit*(jinit+1));
                                }
                        }
                }

                return ;
        }

        else
        {
                for (n=0;n<mult;n++)
                {
                        CFE[n]=0.;
                        for (i=0;i<mult;i++)
                                for(j=0;j<mult;j++)
                                {
                                        if ((BASIS[n][i]*BASIS[n][j])==0.)
                                                continue;

                                        if (i==j)
                                        {
                                                m=i-jinit;

        CFE[n]+=BASIS[n][i]*BASIS[n][j]*((Pparm[0]/3)*(3*m*m-jinit*(jinit+1))
                                                            +(Pparm[1]/60)*(35.*pow(m,4.)-
30*jinit*(jinit+1.)*m*m+25*m*m-6*jinit*(jinit+1)
                                                            +3*jinit*jinit*(jinit+1)*(jinit+1)));
                                        }

                                        else
                                        if (i==j+3)
                                        {
                                                m=j-jinit;

        CFE[n]+=(Pparm[2]/12)*BASIS[n][i]*BASIS[n][j]*(2*m+3)*pow((jinit-m)*(jinit-m-1)
                                                            *(jinit-m-
2)*(jinit+m+1)*(jinit+m+2)*(jinit+m+3),0.5);
                                        }
                                        else
                                        if (i==j-3)
                                        {
                                                m=j-jinit;

        CFE[n]+=(Pparm[2]/12)*BASIS[n][i]*BASIS[n][j]*(2*m-3)*pow((jinit+m)*(jinit+m-1)
                                                            *(jinit+m-2)*(jinit-m+1)*(jinit-
m+2)*(jinit-m+3),0.5);
                                        }

                                }
                        }

        return ;
        }
}

//PROGRAM scalem.cpp
//scalem.cpp
//
//Routine to scale calculated theoretical MCD/MLD data (THMCD[nex] and THMLD[nex])
//to experimental data (EXMCD[nex] and EXMLD[nex]) priorto least-squares correlation
//analysis
//KLJensen        August 2002

#include  <iomanip>
#include <cstdlib>
#include <cmath>
#include "math.h"
#include "nr.h"

using namespace std;
```

```
void scalem(Vec_DP &exmcd,Vec_DP &exmld,Vec_DP &thmcd,Vec_DP &thmld,double &suml,double
&sumc,const int nexmcd,const int nexmld, char *runStat[4])
{
        int i,nexmax;
        double scalen(0.),scaled(0.),scalml(0.),scalmc(0.),sum(0.);
        ((nexmcd>nexmld)?(nexmax=nexmcd):(nexmax=nexmld));

        for(i=0;i<nexmld;i++)
        {
                scalen+=exmld[i]*thmld[i];
                scaled+=pow(thmld[i],2.);
        }

        scalml=scalen/scaled;
        scalen=scaled=0.;

//cout<<"Ex vs. Th prior to scaling"<<endl;
        for(i=0;i<nexmcd;i++)
        {
                scalen+=exmcd[i]*thmcd[i];
                scaled+=pow(thmcd[i],2.);
        }

        scalmc=scalen/scaled;

        cout<<"Ex vs. Th after scaling"<<setprecision(2)<<setiosflags(ios::fixed|ios::showpoint)<<endl;

        for (i=0;i<nexmcd;i++)
        {
                thmcd[i]=scalmc*thmcd[i];
                sumc+=pow((thmcd[i]-exmcd[i]),2.);
        }

                for (i=0;i<nexmld;i++)
        {
                thmld[i]=scalml*thmld[i];
                suml+=pow((thmld[i]-exmld[i]),2.);
        }

        sum=sumc+suml;
//      for (i=0;i<20;i++)
//              cout<<"exmcd["<<i<<"]="<<exmcd[nexmcd-
20+i]<<setw(12)<<"thmcd[i]="<<thmcd[nexmcd-20+i]<<setw(12)<<"exmld[i]="<<exmld[nexmld-
20+i]<<setw(12)<<"thmld[i]="<<thmld[nexmld-20+i]<<endl;

        if (_strnicmp(*runStat,"on",4)==0)
        {
                ofstream outfile06 ("data.out",ios::out);

                outfile06<<"data.out"<<endl<<endl;
                for (i=0;i<nexmax;i++)

        outfile06<<exmcd[i]<<setw(12)<<thmcd[i]<<setw(12)<<exmld[i]<<setw(12)<<thmld[i]<<endl;

                cin>>i;
        }
```

```
          cout<<"\nscalmc= "<<scalmc<<setw(15)<<"scalml= "<<scalml<<endl;
//        cout<<"scalen= "<<scalen<<setw(15)<<"scaled= "<<scaled<<endl;
//        cout<<"sum= "<<sum<<setw(15)<<"suml= "<<setw(15)<<suml<<setw(15)<<"sumc=
"<<sumc<<endl;
}

//PROGRAM power.cpp
//power.cpp
// Recursive function to compute integral powers of a double
// value - first argument is a double value, and the second
// argument is a power index.

#include <iostream>
#include <fstream>
#include <cstdio>
#include <iomanip>
#include <cstdlib>
#include <cmath>
#include "math.h"
#include "nr.h"

using namespace std;

using namespace std;

double power(double x, int n)
{
  if(n<0)
  {
    cout << endl
        << "Negative index, program terminated.";
    exit(1);
  }
  if(n)
    return x*power(x, n-1);
  else
    return 1.0;
}
```

REFERENCE LIST

1. Whittle E, Dows DA, Pimentel GC. Matrix isolation method for the experimental study of unstable species. J Chem Phys 1954; 22: 1943.

2. Moskovitz M, Ozin GA, editors. Cryochemistry. New York: J. Wiley and Sons; 1976.

3. Muetterties EL, Krause MJ. Catalysis by molecular-metal clusters. Angew Chem Int Edit 1983; 22: 135.

4. Ozin GA, Mitchell SA. Ligand-free metal-clusters. Angew Chem Int Edit 1983; 22: 674.

5. Szcepanski J, Roser D, Personette W, Eyring M, Pellow R, Vala M. Infrared spectrum of matrix-isolated naphthalene radical cation. J Phys Chem 1992; 96: 7876.

6. Meyer B. Low temperature spectroscopy. Amsterdam: Elsevier; 1971.

7. Mann DM, Broida HP. Ultraviolet absorption spectra of transition metal atoms in rare-gas matrices. J Chem Phys 1971; 55: 84.

8. Carstens DHW, Brashear W, Eslinger DR, Gruen DM. Correlation between gaseous atomic spectra and absorption spectra of atoms isolated in noble-gas matrices. Appl Spectrosc 1972; 26: 184.

9. Mowery RL, Miller JC, Krausz ER, Schatz PN, Jacobs SM, Andrews L. Magnetic circular dichroism of the $^1S \rightarrow {}^1P$ transition of Mg atoms in noble gas matrices. J Chem Phys 1979; 70: 3920.

10. Zeringue K, ShakhsEmampour J, Rivoal JC, and Vala M. Atom-matrix interactions: an MCD study of copper atoms in argon. J Chem Phys 1983; 78: 2231.

11. Moore, CE. Atomic energy levels. Washington, DC: United States Department of Commerce, National Institute of Standards; 1958 Volume II; 24Cr-41Nb; Circular 467; p. 49-110.

12. Forstmann F, Kolb DM, Leutloff D, Schulze W. Analysis of matrix-induced changes in optical spectra of matrix-isolated noble-metal atoms. J Chem Phys 1977; 66: 2806.

13. McCarty, Jr M, Robinson GW. Environmental perturbations on foreign atoms and molecules in solid argon, krypton, and xenon. Mol Phys 1959; 2: 415.

14. Opik U, Pryce MHL. Studies of the Jahn-Teller effect. 1. A survey of the static problem. Proc R Soc London Ser. A 1957; 238: 425.

15. Moskovitz M, Hulse JE. The UV-visible spectra of copper atoms isolated in various matrices. J Chem Phys 1981; 75: 2904.

16. Radonovich LJ, Zuerner EC, Efner HF, Klabunde KJ. Stereochemistry of η^6-bis(1,4-diflurobenzene)vanadium(0). Inor Chem 1976; 15: 2976.

17. Klabunde KJ, Anderson B, Bader M, Radonovich LJ. Pi-arene complexes of nickel(II) stabilized by sigma-bonded pentafluorophenyl ligands. Homogeneous arene hydrogenation catalysis and unusually labile pi-arene ligands. J Am Chem Soc 1978; 100: 1313.

18. Clark RJH, Hester RE. Spectroscopy of matrix isolated species. New York: J. Wiley and Sons; 1989.

19. Armstrong S, Grinter R, McCombie J. Magnetic circular dichroism study of the $^2S \rightarrow {}^2P$ spectrum of matrix-isolated copper atoms. J Chem Soc Farad T 2 1981; 77 (1): 123.

20. Brittain R, Powell D, Voigtman E, Vala M. Measurement of magnetic circular dichroism of matrix-isolated high temperature molecules. Rev Sci Instrum 1980; 51: 905.

21. Brittain R, Powell D, Kreglewski M, Vala M. The magnetic circular dichroism spectrum of matrix-isolated TaO. Chem Phys 1980; 54: 71.

22. ShakhsEmampour J, Pyzalski R, Vala M, Rivoal JC. Magnetic circular dichroism study of matrix-isolated iron atoms. J Phys-Paris 1984; 45: 953.

23. Vanzee RJ, Li S, Hamrick YM, Weltner W. ESR of Co, Rh, Ir trimers and diatomic ions. Chem Phys Lett 1992; 195 (2-3): 241.

24. Vala M, Zeringue K, ShakhsEmampour J, Rivoal JC, Pyzalski R. Magnetic circular dichroism studies of matrix-isolated atoms: excited state spin-orbit coupling constant reduction of copper in the noble gases. J Chem Phys 1984; 80: 2401.

25. Vala M, Pyzalski R, ShakhsEmampour J, Eyring M, Pyka J, Tipton T, Rivoal JC. Moment analysis for absorption and magnetic circular dichroism bands of atomic *P* ← *S* transitions: application to matrix-isolated chromium. J Chem Phys 1987; 86: 5951.

26. Roser D, Pellow R, Eyring M, Vala M. Spin-orbit splitting and Jahn-Teller effect in rare gas matrix-isolated Ag and Au atoms – a magnetic circular dichroism study. Chem Phys 1992; 166: 393.

27. Stephens PJ. Theory of magnetic circular dichroism. J Chem Phys 1970; 52: 3489.

28. Stephens PJ. Magnetic circular dichroism. In: Prigogine I, Rice SA, editors. Advances in chemical physics. 35: 197. New York: J. Wiley and Sons; 1976.

29. Kreglewski M, Vala M. Theory of magnetic linear dichroism. Application to matrix-isolated atomic transitions. J Chem Phys 1981; 74: 5411.

30. Condon EU, Shortley GH. The theory of atomic spectra. London: Cambridge University Press; 1957.

31. Vala M, Brittain RD, and David Powell D. Matrix-isolated NbO – a magnetic circular dichroism investigation. Chem Phys 1985; 93: 147.

32. Rivoal JC, Vala M. Moment analysis of matrix-enhanced forbidden transitions: application to Cr atoms isolated in Kr and Xe matrices. J Chem Phys 1987; 86: 5958.

33. Piepho SB, Schatz PN. Group theory in spectroscopy with applications to magnetic circular dichroism. New York: John Wiley and Sons; 1983.

34. Lorraine P, Corson D. Electromagnetic fields and waves. San Francisco: W. H. Freeman and Company; 1970.

35. Jackson JD. Classical Electrodynamics. Second Edition. New York: John Wiley and Sons; 1975.

36. Klotzbücher W, Ozin GA. Reinvestigation of optical spectra of nickel, palladium, and platinum atoms in noble-gas matrices. Inorg Chem 1976; 15: 292.

37. Moskovitz M, Hulse JE. Ultraviolet-visible spectra of diatomic, triatomic, and higher nickel clusters. J Chem Phys 1977; 66: 3988.

38. Grinter R, Stern DR. Electronic and magnetic circular dichroism spectra of matrix-isolated nickel atoms. J Chem Soc Farad T 2 Part 7 1983; 79: 1011.

39. Schroeder W, Grinter R, Schnittenlacher W, Rotermund HH, Kolb DM. The electronic spectra of matrix-isolated nickel atoms – the coexistence of the $^3D_3$ and $^3F_4$ ground states in Ar, Kr, and Xe. J Chem Phys 1985; 82: 1623.

40. Pellow R. Matrix isolation spectroscopy: magnetic circular and linear dichroism [dissertation]. Gainesville (FL): University of Florida; 1990.

41. Roser D. Magnetic circular dichroism and absorption spectroscopy of matrix isolated transition metal atoms [dissertation]. Gainesville (FL): University of Florida; 1992.

42. Banwell CN. Fundamentals of molecular spectroscopy. New York: McGraw-Hill Publishing Co.; 1972.

43. Schatz PN, A.J. McCaffery AJ. Faraday effect. Q Rev Chem Soc 1969; 23: 552.

44. Power EA, Thirunamachandran T. Circular dichroism – general theory based on quantum electrodynamics. J Chem Phys 1974; 60: 3695.

45. Chen GC, Yang JT. 2-point calibration of circular dichrometer with d-10-camphorsulfonic acid. Anal Lett 1977; 10: 1195.

46. McCaffery AJ, Mason SF. The electronic spectra, optical rotatory power, and absolute configuration of metal complexes. The dextro-tris (ethylenediamine)cobalt(III) ion.Mol Phys 1963; 6: 359.

47. Kemp JC. Piezo-optical birefringence modulators – new use for a long-known effect. J Opt Soc Am 1969; 59 (1): 950.

48. Kemp JC, Macek JH, Nehring FW. Induced atomic orientation, an efficient mechanism for magnetic circular polarization. Astrophys J 1984; 278: 863.

49. Osborne GA, Stephens PJ. Magnetic circular dichroism of impurities in solids – allowed electronic transitions and LiF F-center. J Chem Phys 1972; 56: 609.

50. Henry CH, Schnatterly SE, Slichter CP. Effect of applied fields on optical properties of color centers. Phys Rev 1965; 137 (2A): A583.

51. Mort J, Lüty F, Frederick C. Brown FC. Faraday rotation and spin-orbit splitting of F center in alkali halides. Phys Rev 1965; 137 (2A): A566.

52. Harris DC, Bertolucci MD. Symmetry and spectroscopy. Toronto: Oxford University Press; 1978.

53. Van Vleck JH. The dipolar broadening of magnetic resonance lines in crystals. Phys Rev 1948; 74: 1168.

54. Pellow R, Vala M. Magnetic circular dichroism and magnetic linear dichroism of randomly oriented linear molecules. Molecular Phys 1989; 68(4): 893.

55. Vala M, Rivoal J, Grisolia C, Pyka J. Magnetic linear dichroism of matrix-isolated iron atoms. J Chem Phys 1985; 82(9): 4376.

56. Butler PH. Point group symmetry applications. New York: Plenum Press; 1981.

57. Watanabe H. Operator methods in ligand field theory. Englewood (NJ): Prentice-Hall; 1966.

58. Goldstein H. Classical Mechanics. reading (MA): Addison-Wesley Pub. Co.; 1981.

59. Griffith JS. The irreducible tensor method for molecular symmetry groups. Englewood (NJ) Prentice-Hall; 1962.

60. Wigner EP. Group Theory. New York: Academic Press; 1959.

61. Lignieres J. Rapport de stage. Paris, France. Universite Paris VI, Juin (1987).

62. Micklitz H, Barrett PH. Temperature dependence of optical absorption lines from iron atoms in a krypton matrix. Phys Rev 1971; B4: 3845.

63. McKenzie MT, Epting MA, Nixon ER. Visible and near-infrared fluorescence spectra of Fe atoms in argon matrices. J Chem Phys 1982; 77: 735.

64. Rivoal JC, Zoueu J, Blanchard X, Nahoum R, Eyring M, Pyka J, Vala M. Magnetic circular and linear dichroism saturation studies: determination of the "crystal field" splitting in krypton and xenon matrix-isolated iron atoms. J Chem Phys 1994; 101(4): 2684.

65. Graham R, Grinter R. Magnetic circular dichroism spectroscopy and magnetization studies of iron atoms isolated in krypton matrices. J Chem Phys 1989; 91: 6677.

66. Press WH, Teukolsky SA, Vetterling WT, Flannery BP. Numerical recipes in C^{++}. 2nd ed. Cambrigde (MA): Cambridge University Press; 2002.

67. Montano PA, Barrett PH, Shanfield Z. Magnetic hyperfine interaction of iron monomers and dimmers isolated in an argon matrix. J Chem Phys 1976; 64: 2896.

68. Coufal H, Lűscher E, Micklitz H. Electron spin and nuclear gamma resonance studies of rare gas matrix-isolated atoms and ions. In: Coufal H, Lűscher E, Micklitz H., editors. Rare gas solids. In: Springer tracts in modern physics. Berlin: Springer-Verlag; 1984. Vol. 103; p. 1-57.

69. Slater JC. Introduction to chemical physics. New York: Dover Publications; 1939.

70. Niebel KF, Venables JA. The crystal structure problem. In: Klein ML, Venables JA, editors. Rare gas solids. New York: Academic Press; 1976. p. 558-589.

71. Eyring MW. Bonding in diene-ML_2 and arene-ML_2 complexes: stereochemistry and structure of two arene-ML_2 complexes of Fe(0) and two diene-ML_2 complexes of Ni(0) [thesis]. Grand Forks (ND): University of North Dakota; 1982.

72. Radonovich LJ, Eyring MW, Groshens TJ, Klabunde KJ. Synthesis, chemistry, and structure of a new pi-arene complex of iron(0), (eta-6-toluene)(2,2′-bipyridine)irn(0) – structural evidence for extensive pi back-bonding to 2,2′-bipyridine. J Am Chem Soc 1982; 104: 2816.

73. Jacobi K, Schmeisser D, Kolb DM. Photoemission from matrix-isolated nickel atoms. Chem Phys Lett 1980; 69: 113.

74. Breithaupt B, Hulse JE, Kolb DM, Rotermund HH, Schroeder W, Schrittenlacher W. A matrix-induced change in the electronic ground state of nickel atoms isolated in rare gases. Chem Phys Lett 1983; 95: 513.

75. Barrett CP, Graham RG, Grinter R. The electronic ground state of matrix-isolated nickel atoms. Chem Phys 1984; 86: 199.

76. Celluci TA, Nixon ER. Study of low-lying electronic states of Ni atoms in solid inert gas matrices. J Chem Phys 1984; 81: 1174.

77. Huber MCE, Sandeman RJ. Oscillator-strengths of ultraviolet Ni-I lines from Hook-method and absorption-measurements in a furnace. Astron Astrophys 1980; 86: 95.

78. Kreglewski M, Vala M. Absorption and magnetic circular dichroism spectra of matrix-isolated Ta atoms. Chem Phys 1981; 56: 381.

79. Gruen DM. Spectroscopic identification and characterization of matrix-isolated atoms. In: Moskovits M, Ozin GA, editors. Cryochemistry. New York: John Wiley and Sons; 1976. p. 441-491.

80. Moskovits M, Hulse JE. Ultraviolet-visible spectra of diatomic, triatomic, and higher nickel clusters. J Chem Phys 1977; 66: 3988.

BIOGRAPHICAL SKETCH

Karen L. Jensen was born in Uniontown, Pennsylvania, in 1951. She attended Lakeview High School in Winter Garden, Florida, graduating in 1969. She received a Bachelor of Science degree with a major in chemistry from the University of North Dakota in 1978, followed by a Master's Degree in Physical Chemistry in 1982, also from the University of North Dakota. She attended graduate school at the University of Florida from 1982 to 1984, then again from 1989 to 1993. She has worked in both state and federal government, along with private industry. She was employed at Kennedy Space Center during the mid-1980's and was an integral part of the launch operations team for space shuttle launches, including Challenger's last flight. She returned to the University of Florida in 2001 to complete her graduate education, pursuing a Ph.D. in Physical Chemistry.

I certify that I have read this study and that in my opinion it conforms to acceptable standards of scholarly presentation and is fully adequate, in scope and quality, as a dissertation for the degree of Doctor of Philosophy.

Martin T. Vala

Martin T. Vala, Chair
Professor of Chemistry

I certify that I have read this study and that in my opinion it conforms to acceptable standards of scholarly presentation and is fully adequate, in scope and quality, as a dissertation for the degree of Doctor of Philosophy.

William Weltner Jr.

William Weltner, Jr.
Professor of Chemistry

I certify that I have read this study and that in my opinion it conforms to acceptable standards of scholarly presentation and is fully adequate, in scope and quality, as a dissertation for the degree of Doctor of Philosophy.

Kathryn R. Williams

Kathryn R. Williams
Scholar of Chemistry

I certify that I have read this study and that in my opinion it conforms to acceptable standards of scholarly presentation and is fully adequate, in scope and quality, as a dissertation for the degree of Doctor of Philosophy.

Samuel O. Colgate

Samuel O. Colgate
Professor of Chemistry

I certify that I have read this study and that in my opinion it conforms to acceptable standards of scholarly presentation and is fully adequate, in scope and quality, as a dissertation for the degree of Doctor of Philosophy.

E. Dwight Adams

E. Dwight Adams
Professor of Physics

This dissertation was submitted to the Graduate Faculty of the Department of Chemistry in the College of Liberal Arts and Sciences and to the Graduate School and was accepted as partial fulfillment of the requirements for the degree of Doctor of Philosophy.

May 2003

Dean, Graduate School